Fatigue life assessment for civil infrastructures using Bayesian filtering-based algorithms

Thesis submitted to the
Indian Institute of Technology Mandi
For the award of the degree

of

Doctor of Philosophy

by

Eshwar Kuncham

Under the guidance of

Dr. Subhamoy Sen

School of Civil and Environmental Engineering
INDIAN INSTITUTE OF TECHNOLOGY MANDI
September 2023

CERTIFICATE

This is to certify that the thesis entitled **Fatigue life assessment for civil infrastructures using Bayesian filtering-based algorithms**, submitted by **Eshwar Kuncham** to the Indian Institute of Technology Mandi, is a record of bona fide research work under my supervision and we consider it worthy of consideration for the award of the degree of Doctor of Philosophy of the Institute.

11/08/23

Date: 11-08-2023

Dr. Subhamoy Sen

(Supervisor)

Dr. Subhamoy Sen
Associate Professor
i4S IIT MANDI
Indian Institute of Technology,
Mandi, Kamand-175075 (HP)

DECLARATION

I certify that

1. The work contained in the thesis is original and has been done by myself under the general supervision of my supervisor.
2. The work has not been submitted to any other Institute for any degree or diploma.
3. I have followed the guidelines provided by the Institute in writing the thesis.
4. I have conformed to the norms and guidelines given in the Ethical Code of Conduct of the Institute.
5. Whenever I have used materials (data, theoretical analysis, and text) from other sources, I have given due credit to them by citing them in the text of the thesis and giving their details in the references.
6. Whenever I have quoted written materials from other sources, I have put them under quotation marks and given due credit to the sources by citing them and giving required details in the references.

Eshwar Kuncham

Roll no. D19047

School of Civil and Environmental Engineering

Indian Institute of Technology Mandi

Date: 29-09-2023

Curriculum Vitae

Mr. Eshwar Kuncham is a PhD research scholar at the Indian Institute of Technology Mandi, Himachal Pradesh, India. He holds a bachelor's degree in civil engineering and a master's degree in structural engineering, both completed in 2015 and 2017, respectively, from Jawaharlal Nehru Technological University Hyderabad. During his academic journey, he acquired valuable research experience at both the Indian Institute of Technology Patna and the Indian Institute of Technology Mandi. Subsequently, in February 2020, he enrolled in a PhD program at the Indian Institute of Technology Mandi.

Throughout his PhD, he focused on developing Bayesian filter-based algorithms for predicting the Remaining Useful Life of bridge structures. These algorithms leverage available sensor data while considering uncertainty in measurement and various loading conditions, including mechanical and thermo-mechanical, vehicles. To address the challenges of computational and instrumentation density costs, he also developed an algorithm that integrates substructure predictor models with Bayesian filters.

Over the time of his research journey, he has honed his expertise in real-life structural health monitoring. This includes proficiency in high-end numerical modelling through coding or software, utilization of filtering-based structural health monitoring approaches, and handling diverse sensor types such as accelerometers and strain sensors (both wired and wireless), data acquisition systems, anemometers, and more.

His primary research interests lie in the areas of Structural Health Monitoring, Inverse Problems, Fatigue Life Prediction, Bayesian filtering, etc. He is enthusiastic about contributing to addressing the social problem by developing and implementing practical solutions for health assessment and prediction of remaining useful life of civil and mechanical structures.

List of Journal Publications

1. **Kuncham, E**., Aswal, N., Sen, S., and Mevel, L. Bayesian monitoring of substructures under unknown interface assumption, 2023. **Mechanical Systems and Signal Processing**.

2. **Kuncham, E.**, Sen, S., Kumar, P., and Pathak, H. An online model-based fatigue life prediction approach using extended Kalman filter, 2022. **Theoretical and Applied Fracture Mechanics**.

3. Hoda, Md. A., **Kuncham, E.**, and Sen, S. Response and input time history dataset and numerical models for a miniaturized 3D shear frame under damaged and undamaged conditions, 2022. **Data in Brief**.

4. Aswal, N., **Kuncham, E.**, Sen, S., and Mevel, L. Health assessment of high dimensional structures under spatial thermal variation using localized estimation approach. Mechanical Systems and Signal Processing. (*under review*)

5. **Kuncham, E.**, and Sen, S. Fatigue assessment of bridges using interacting filtering approach with sub-structured predictor model based on current health. Journal of Bridge Engineering. (*under review*)

6. Faridi, Md. A., **Kuncham, E.**, Roy, K., and Singhal, V. Operational modal analysis of a bridge under ambient excitation using limited roving sensors. Journal of Civil Structural Health Monitoring. (*under review*)

7. Hoda, Md A., **Kuncham, E.**, and Sen, S. Enhanced high-resolution structural crack detection using hybrid interacting Particle-Kalman filter. (h-IPKF). Structures. (*under review*)

8. **Kuncham, E.**, Hoda, Md A., and Sen, S. Force estimation in bridge substructure boundary under vehicle loading using interacting filtering approach. International Journal of Advances in Engineering Sciences and Applied Mathematics. (*under review*)

9. Shereena, O.A, **Kuncham, E.**, Sen, S., Jain, P. C., and Mevel, L. Mitigating high dimensionality in damage identification for plate-like structures through substructuring with interacting filtering-based approaches. Engineering Structures. (*under preparation*)

Book Chapter/Lecture Notes

1. **Kuncham, E.**, and Pasupuleti, V. D. K. Progressive Collapse Analysis of Two Dimensional Reinforced Concrete Framed Structure, 2019. **Advances in Intelligent Systems and Computing**.

2. Chilakalapallii, R. V., Palvai, P., **Kuncham, E**., and Pasupuleti, V. D. K. Lateral Response Reduction of Tall Buildings Using Portal Frame as TMD, 2020. **Lecture Notes in Civil Engineering**.

Conference

1. OA, Shereena., Sen, S., Aswal, N., **Kuncham, E**., and Mevel, L. Monitoring a sparsely observed high dimensional structures with virtual sensor-based identification framework defined in lagged time domain. **IOMAC 2024**. Naples, Italy. (*submitted*)

2. Rashid, S., **Kuncham, E**., and Sen, S. Integration of numerical and experimental approaches for ultrasonic wave propagation-based damage detection. **CARRS 2023**. IIT Hyderabad, India. (*submitted*)

3. Aswal, N., **Kuncham, E**., Sen, S., and Mevel, L. Subdomain Fault Isolation for Linear Parameter Varying Systems through Coupled Marginalized Particle and Kitanidis Filters. 22nd **IFAC World Congress 2023**. Yokohama, Japan.

4. **Kuncham, E**., Hoda, Md A., and Sen, S. Identifying the cracks in beam structures using a simplified substructure technique. 4th **SICE 2022**. IIT Hyderabad, India.

5. **Kuncham, E**., Hoda, Md A., and Sen, S. Force estimation in bridge substructure boundary under vehicle loading using interacting filtering approach. 67th **ISTAM 2022**. IIT Mandi, India.

6. Hoda, Md A., **Kuncham, E**, and Sen, S. Detection of edge crack in beam-like structure modelled as rotational spring by using Bayesian filtering. 67th **ISTAM 2022**. IIT Mandi, India.

7. **Kuncham, E**., and Sen, S. Development of computationally efficient health benchmarking approach for a bridge structure by coupling substructuring technique within interacting filtering approach. 10th **EWSHM 2022**. Palermo, Italy.

8. Aswal, N., **Kuncham, E**., Sen, S., and Mevel, L. Robust Interacting Particle-Kalman Filter based structural damage estimation using dynamic

strain measurements under non-stationary excitation - an experimental study. 10th **SHMII 2021**, Porto, Portugal. - (*online*)

9. **Kuncham, E.**, and Sen, S. Damping Estimation in Composites Structures: An Inverse Damping Modelling Technique. **NDE 2019**. Bengaluru, India.
10. **Kuncham, E.**, and Pasupuleti, V. D. K. Structural Vibration During Progressive Collapse. **ICVOP 2017**. IIT Guwahati, India.
11. **Kuncham, E.**, and Pasupuleti, V. D. K. Progressive Collapse Analysis of Three-Dimensional Reinforced Concrete Structures. **ICEE 2017**. Padang, Indonesia.

Acknowledgment

I extend my heartfelt gratitude and appreciation to all those who have played a significant role in the successful completion of my doctoral journey.

First and foremost, I am deeply indebted to my esteemed supervisor, Dr. Subhamoy Sen, for believing in me and providing me with the opportunity to pursue my dreams. Their unwavering guidance, encouragement, and invaluable insights throughout this research endeavor have been instrumental in shaping my ideas and refining my work, for which I am sincerely grateful. What sets my supervisor apart is our unique relationship, where we engage in heated discussions on the research topic during the first half, and then, in the evening, forget everything and share a cup of tea. This open and supportive environment has allowed me to discuss freely about research ideas.

I extend my appreciation to Dr. Himanshu Pathak and Dr. Laurent Mevel, who contributed to my research and academic growth as coauthors.

I would like to express my sincere thanks to both past and present members of my Doctoral Committee: Dr. Sandip Saha, Dr. Himanshu Pathak, Dr. Rajendra Ray, Dr. Rajesh Ghosh, and Dr. Vishal Singh Chauhan for their valuable feedback and commitment to the improvement of this research.

I am also thankful to my research lab colleagues, including Smriti, Pramod, Neha, Naveen, Ashish, Kshitij, Moumita di, Maninder, Arman, Sumit, Armanul, Shereena, Nikhil, and Rohit for fostering a great work environment. All the past and current members associated with the i4S lab were great to work with.

I would like to thank different friend groups like the Telugu group (Pramod, Ravi, Jeevitha, etc.), the Badminton group (Varun, Yadu, Manohar anna, etc.), and the hiking and trekking group (Neha, Rishikanth, etc.) for making my journey fun, stress-free, and physically active throughout my PhD.

My deepest gratitude goes to my family for their unwavering love, encouragement, and belief in my capabilities.

Last but not least, I thank my dostulu Sunny, Siddiq, and Shravan for their dostana and moral support throughout this challenging journey. Their encouragement and understanding have been a constant source of motivation during both the highs and lows of my doctoral pursuit.

Abstract

Engineering structures, including bridges, undergo fatigue loads over time, leading to material degradation, reduced resistance, and increased risk of failure. Regular local inspections or structural health monitoring (SHM) are crucial to identify potential failures and predict fatigue life. However, challenges arise in predicting the remaining useful life (RUL) of structures, such as limited data, large structural dimensions, and estimating vehicle-induced loading. This study addresses these challenges by employing Bayesian filtering-based SHM frameworks for fatigue life prediction. Two conditions are considered: structures with visible fatigue cracks and those without visible cracks. Cost-efficient and practical detection algorithms are developed for both conditions. In structures without visible cracks, RUL estimation utilizes Miner's rule and the S-N curve of the material, using stress data obtained through SHM. For structures with visible cracks, RUL estimation focuses on crack length prognosis based on crack growth history. The updated Paris model is used to simulate fatigue crack propagation, with model parameters estimated using SHM data while accounting for uncertainties.

For the structures with visible cracks and available crack growth history, an online model-based approach is proposed to provide a probabilistic estimate for fatigue life by jointly inferring fatigue parameters from available SHM data using a Joint Extended Kalman Filter (JEKF). The effectiveness of the proposed method is validated through numerical studies on two fracture scenarios: edge and center cracks in a finite plate subjected to mechanical and thermal loading conditions. Additionally, numerical simulations are performed to study the RUL for a welded joint of a bridge based on its worst operational scenario. To validate the accuracy of the proposed approach, an experimental study is conducted on compact tension (CT) specimens, confirming its consistency in estimating fatigue model parameters and subsequently predicting the RUL.

Further, to address the practical challenges in infrastructure fatigue monitoring, wherein the structures are high-dimensional enhancing computational and instrumentation expenses, probabilistic substructure monitoring approaches powered by interacting filtering algorithms, such as particle and ensemble Kalman filters (IP-EnKF) are employed to focus on critical segments or members of the structure, thereby reducing computational complexity and improving efficiency. The efficiency of the algorithm in estimating substructural health is rigorously demonstrated through both numerical and experimental studies. Further, the unknown substructure boundary forces, required for estimating the fatigue life of the substructure, are also reconstructed through post-processing. Numerical experiments conducted on a bridge structure modelled with vehicle-structure interaction aspect validate the proposed method. Several real-life experiments are also done wherein the damage is however required to be simulated in its calibrated digital twin.

Moreover, a similar substructure algorithm is employed to estimate the RUL of a crack-free bridge structure. Numerical experiments are conducted on a reinforced concrete box girder bridge, considering vehicle-bridge interaction. A parametric analysis investigates the relationships between the FDI and factors such as surface roughness, vehicle speed, weight, and category, with the aim of identifying dominant stimuli. The results demonstrate an accurate estimation of health parameters and RUL. Additionally, a novel decomposed approach for RUL estimation is developed, enabling the mapping of traffic information to fatigue damage without the need for costly simulations. A case study is presented, focusing on a reinforced concrete box girder bridge in Kamand, Himachal Pradesh, India, to highlight the practical applicability of the approach in real-world scenarios.

Keywords: *Fatigue, structural health monitoring, remaining useful life, limited data, large structural dimensions, Bayesian filters, critical element, substructure, vehicle-bridge interaction.*

Contents

List of Tables

List of Figures

Abbreviations

HI	Health Index
FDI	Fatigue Damage Accumulation Index
ϵ-N	Strain-Life
b/w	between
dof	Degree of Freedom
snr	Signal-to-Noise Ratio
v/s	versus
ASTM	American Society for Testing Materials
BRO	Border Roads Organisation
CDM	Cumulative Damage Model
COD	Crack Opening Displacement
DT	Digital Twin
EKF	Extended Kalman Filter
EnKF	Ensemble Kalman Filter
FDD	Frequency Domain Decomposition
FEM	Finite Element Method
FIU	Florida International University
FN	False Negative
FP	False Positive
GDE	Governing Differential Equation
HCF	High Cycle Fatigue
IPEnKF	Interacting Particle Ensemble Kalman Filters
JEKF	Joint Extended Kalman Filter
LCF	Low Cycle Fatigue
LEFM	Linear Elastic Fracture Mechanics
LI	Life Index
MSMD	Moving Spring Mass Damper
MTS	Maximum Tangential Stress
NDE/T	Non-Destructive Evaluation/Testing

PF	Particle Filter
PSD	Power Spectral Density Function
RC	Reinforced Concrete
RMSE	Root Mean Square Error
RUL	Remaining Useful Life
SCF	Stress Concentration Factor
SHM	Structural Health Monitoring
SIF	Stress Intensity Factor
S-N	Stress-Life
SWGN	Stationary White Gaussian Noise
TN	True Negative
TP	True Positive
UKF	Unscented Kalman Filter
VHCF	Very High Cycle Fatigue
VLCF	Very Low Cycle Fatigue
XFEM	eXtended Finite Element Method

Chapter 1

Preamble

PhD research problems are typically derived from social challenges. Similarly, my research problem draws inspiration from the remarkable longevity of the Victoria Bridge in Mandi, Himachal Pradesh which has maintained its structural integrity for a staggering 143 years (1877-2020) of service life. To safeguard the heritage structure and avoid catastrophic failure, the bridge function has been shut down in 2020. The decision was however abrupt and appeared to me as necessary but not well-informed. This intrigued my interest in pursuing what factors affect the service life of a structure, and how to estimate and predict the accurate life of a civil structure using modern techniques so that an informed decision can be taken to safeguard the interest of its users. Throughout this research process, I have encountered numerous challenges such as limited data, large structural dimensions, and estimating the vehicle-induced loading which I addressed in different chapters of this thesis for predicting the accurate life of a civil structure.

1.1 Introduction

The service phase is the most crucial period in the lifespan of civil engineering structures, and monitoring its safety and serviceability is therefore necessary during its operation, especially for large structures. During this phase, construction materials degrade over time due to mechanical factors such as ageing, prolonged cyclic loading, unanticipated loads (e.g. earthquakes, cyclones), and physio-chemical factors, such as steel corrosion and concrete carbonation. As a result of material degradation, the capacity, and durability of the structure degrade. This eventually leads to a decrease in the structural reliability while increasing the probability of failure over time Chen (2018). To address such risks, structural health monitoring (SHM) has emerged as an efficient approach that harnesses information from the measured responses sampled from a network of well-placed sensors attached all over the structure.

Material degradation, whether due to ageing-related decay from a prolonged operation or sudden damage caused by natural disasters such as earthquakes, eventually affects structural stiffness. Sudden damage can result in abrupt and catastrophic structural failure, offering limited time for inspection or maintenance. On the other hand, ageing-related decay occurs gradually, providing sufficient time to identify the causes of stiffness degradation. As a result, the objectives of SHM approaches and associated uncertainties differ significantly for these two types of damage. When dealing with sudden damage, the primary aim is to detect its occurrence and, if possible, localize the affected area. In contrast, for structures experiencing slow deterioration, the focus shifts to prognosis. This study specifically targets the latter type of structural deterioration, and the algorithms employed are tailored to suit this objective.

The gradual deterioration of material caused by repeated cyclic loading is commonly known as material fatigue, and the duration it takes for the material to render the structure inoperable is referred to as the fatigue life of the structure. One of the key challenges in this context is predicting the fatigue life while considering the limited measured structural responses and computational resources available. Since fatigue failure can have catastrophic consequences, leading to significant loss of lives, property damage, and economic disruption, it is crucial to accurately and reliably predict the fatigue life for the design, maintenance, and overall safety of bridge structures.

To estimate fatigue life, monitoring fatigue can be accomplished using standard SHM frameworks. These frameworks involve instrumenting the structure to gather responses that can be used to make inferences about fatigue. The assessment of fatigue through SHM is crucial for predicting future performance and making cost-effective decisions regarding inspections, maintenance, repairs, and replacements. However, various factors such as material characteristics, load history, and environmental conditions introduce uncertainties of unknown magnitudes into the estimation process. This necessitates the use of probabilistic approaches, such as the Bayesian filter, rather than traditional deterministic approaches, to predict fatigue life accurately in complex structures exposed to real-life uncertainties from diverse sources Kuncham et al. (2022).

The focus of this study is on estimating the fatigue life of bridges, with the solutions specifically designed for this type of structure while considering their generalization capability. Significant progress has been made in this field, but challenges remain due to limited data availability, the need to monitor large structural dimensions, and the incorporation of uncertainties related to vehicle-induced loading. This thesis explores these challenges and proposes solutions to develop a more reliable and efficient approach for estimating fatigue life in complex structures.

1.2 Background

Bridges are highly vulnerable to fatigue, exacerbated by environmental factors that contribute to material degradation. These structures experience cyclic loads from traffic, wind, and other sources, and they are designed with a safety margin below their structural capacity. Despite these precautions, fatigue failures can still occur during normal operation over an extended period, often due to unforeseen complexities rather than extreme events such as overloading. Fatigue-induced cracks develop gradually in materials after prolonged service, initially having no significant impact on the overall behaviour of the structure. However, once cracks initiate, they can propagate rapidly and uncontrollably, leading to sudden and catastrophic fractures Metallurgy (1986). The absence of clear warning signs or performance deterioration makes fatigue failures challenging to detect or incorporate into maintenance schedules.

To address fatigue failures, comprehensive investigations are necessary to comprehend the material and mechanical behaviour of components subjected to simulated operational conditions involving cyclic loads. These studies provide valuable insights into the fatigue performance of the components.

1.2.1 Instances of significant fatigue

During the 19th century, fatigue in engineering structures presented a perplexing phenomenon characterized by imperceptible damage and sudden, unforeseen failures. However, in the 20th century, researchers made notable strides in understanding the initiation of fatigue mechanisms in engineering materials. Ye et al. (2014) revealed that repeated loading could initiate the formation of microcracks, which would subsequently propagate and ultimately result in structural failure.

A few significant incidents exemplify the hazards of fatigue in engineering, drawing upon examples from both historical and modern events. The Great Molasses Flood of 1919 Julia (2019), which resulted from a failure of a steel tank, (see Figure 1.1a) and the engine failures of a Boeing 777 in 2021 Pilar (2021), all demonstrate the influence of fatigue in the materials involved (see Figure 1.1b). These incidents underscore the importance of comprehending fatigue properties and the necessity for proper engineering design and maintenance.

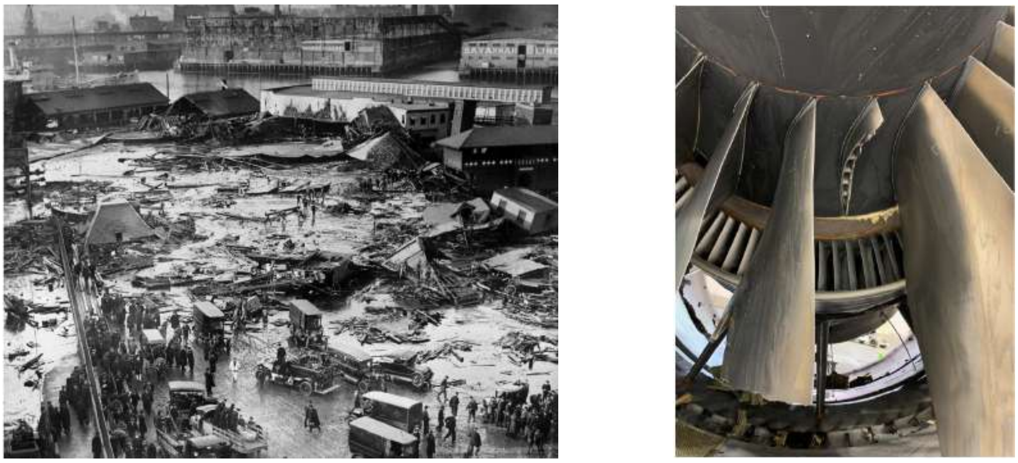

(a) Boston Molasses Flood Julia (2019).

(b) Boeing 777 engine Pilar (2021).

Figure 1.1: Fatigue failures in the materials.

1.2.2 Significance of fatigue in bridge structures

The collapse of the Silver Bridge in 1967 (see Figure 1.2), resulting in the tragic loss of 46 lives, raised concerns about the fatigue reliability of bridges Lichtenstein (1993). This incident triggered a significant shift in bridge inspection practices and the implementation of safety measures by the US government. The Silver Bridge possessed distinctive design features, including high-tension eye-bar chains, a unique anchorage system, and rocker towers. The bridge's failure highlighted the perilous combination of stress concentrations and fatigue, as well as the significance of structural redundancy. A small flaw in one of the eye bars, subjected to repetitive loading over several decades, led to rapid crack propagation and the eventual collapse of the bridge. The absence of redundancy in both the eye-bar connection and the overall structure contributed to the catastrophic failure Lichtenstein (1993).

Figure 1.2: Silver bridge collapse due to fracture Matt (2017).

Subsequent bridge failures in the 20^{th} and 21^{st} centuries, including the I-35 truss bridge in Minneapolis in 2007, the Ponte Morandi cable-stayed bridge in Italy in 2018 (see Figures 1.3), the Florida international university (FIU) pedestrian bridge in Miami (see Figures 1.4), Florida in 2018, and the Nanfang'ao steel single-arch bridge in Taiwan in 2019, has further emphasized the importance of bridge design and maintenance practices. These incidents have raised concerns not only regarding the frequency of inspections but also the identification of potential vulnerabilities in bridge structures.

Figure 1.3: I-35 W bridge collapse due to fatigue cracking David (2017).

The series of bridge failures witnessed in recent decades has exposed the limitations of conventional bridge monitoring, which primarily focuses on diagnostic steps. Such an approach is insufficient for effectively evaluating the safety of these vital infrastructures. To ensure the integrity of ageing structures and prevent catastrophic collapses caused by subtle and hard-to-detect damage, new methods for bridge monitoring are required. These methods should prioritize

Figure 1.4: FIU pedestrian bridge collapse due to extensive cracking John (2019).

prognosis and incorporate specific considerations in bridge design.

To accomplish this goal, it is crucial to investigate the primary causes of bridge failures, including design deficiencies, construction issues, detailing problems, and material shortcomings. By identifying potential failure mechanisms associated with each cause, it becomes possible to develop innovative approaches in bridge design and monitoring. The objective is to minimize the risk of future bridge collapses and enhance the overall safety of these structures.

1.3 Degradation process

Fatigue primarily arises from prolonged exposure to cyclic operational forces, and its effects become more significant when accompanied by other forms of ageing-related material deterioration. The process of ageing-related degradation is influenced by a range of physical and environmental factors that are unique to each structure. These factors can induce changes in the chemical composition of materials, subsequently affecting their mechanical and physical properties. As a result, these changes diminish the lifespan of the structure, requiring prompt repairs Gonzalez et al. (2020) to extend its fatigue life.

1.3.1 Degradation due to environmental factors

High humidity poses an ongoing challenge for civil structures constructed with reinforced concrete and steel. When these materials come into contact with moisture, corrosion issues are initiated through electrochemical reactions. This gradual process leads to the formation of rust and the degradation of the materials. The impact of corrosion on the reinforcement steel of a pier is depicted in Figure 1.5a, where the loss of the protective coating and reduced cross-sectional area result in a deterioration of the mechanical capacity. Similarly, unprotected structural steel can experience widespread rusting, as shown in Figure 1.5b. This oxidation reaction affects all components susceptible to corrosion, causing significant damage Gonzalez et al. (2020).

(a) Reinforced concrete steel structure Mohammed (2015).

(b) Steel structure Patricia (2014).

Figure 1.5: Degradation due to corrosion in civil structures.

1.3.2 Degradation due to physical factors

Wear is another gradual degradation process that occurs due to physical forces, particularly from vehicle traffic traversing the main deck. The friction generated during braking and acceleration contributes to wear and tear on the structure. Bridges with piers exposed to water flow also experience wear due to friction. Although traffic flow typically causes minimal wear on the deck, any road defects can lead to increased wear and damage. Bridges with simply supported girders often require construction joints between supports, which, if poorly constructed, can result in the formation of bumps. Figure 1.6a showcases a common issue with a construction joint that can be avoided by employing appropriate joint procedures and industry-standard materials Gonzalez et al. (2020).

Ultimately, when such material degradation processes get coupled with fatigue-induced deterioration resulting from alternating forces, the ultimate collapse of the structure becomes unavoidable. With each load cycle, fatigue progressively diminishes the material's fatigue life, increasing its brittleness until failure occurs. This degradation can remain undetected until the actual failure happens, even if the resulting stress remains below the yield point. Figure 1.6b showcases the growth of a crack due to cyclic stress loads, where no yielding zones are observed in the beam, signifying a sudden crack failure.

(a) Bridge expansion joint damaged David (2017).

(b) Fatigue crack growth in steel beam Rob (2021).

Figure 1.6: Degradation due to wear and fatigue in civil structures.

1.3.3 Typical protection and mitigation strategies

During the design phase, preventive measures can be taken to address material deterioration, including corrosion and wear Hernandez-Duque et al. (1995). Applying epoxy coatings to isolate structural steel from moisture contact and utilizing protective coatings for concrete reinforcement help preserve the structure's durability. Flexible roads require extra attention to mitigate wear, while reinforced concrete piers exposed to water flow need additional protective coatings for reinforcing bars. However, fatigue degradation cannot be fully eliminated in structures subjected to cyclic loads below the material's yielding stress.

Acknowledging that reactive measures may not be practical for structures subjected to severe repetitive loading and of high economic/social importance, it is essential to consider proactive approaches to mitigate risks and reduce costs. Implementing a reactive repair protocol could lead to significant infrastructure downtime, while relying solely on scheduled maintenance without sufficient information may result in additional and unnecessary expenses. Therefore, adopting a proactive approach becomes imperative. In this regard, utilizing SHM strategies to estimate fatigue can offer an efficient alternative. SHM provides valuable insights for timely maintenance and proactive decision-making, allowing for more effective risk mitigation.

1.4 Evolution of fatigue comprehension

Fatigue is the term used to describe the process of crack initiation, formation, and propagation in a material due to repeated loading. It occurs when cracks develop from tiny material faults caused by the repetitive nature of the applied load, and these cracks gradually grow with each loading cycle. The crack propagation continues until it reaches a critical level, where the stress intensity factor (SIF) exceeds the fracture toughness of the material. At this point, rapid crack propagation occurs, often leading to the complete fracture of the structure.

In 1829, W.A.S. Albert performed load tests on an iron chain, marking the inception of fatigue studies Collins (1993). The emergence of fatigue failures in railway axles during the early 19^{th} century prompted the first significant investigation into cyclic loading effects. Numerous machine components underwent millions of cycles at stress levels below the yield point, with frequent documented failures. Between 1852 and 1870, August Wöhler, a German railway engineer, established and conducted the inaugural systematic fatigue study Christian (1999).

Later, Basquin made a substantial impact by introducing a logarithmic relationship between stress and cycle number in 1910, which helped in understanding materials' behaviour under fatigue. In 1933, Palmgren described linear cumulative damage for the first time. In this concept, fatigue damage occurs when materials deteriorate under specific load conditions and gradually accumulate over time. Miner developed a mathematical approach based on Palmgren's work for quantifying cumulative damage in 1945. Based on the cumulative damage to a component, this approach provided a way to estimate its remaining fatigue life Miner (1945).

Paris made a significant discovery by proposing the theory of fatigue fracture in 1960. This theory elucidates the incremental crack growth in materials subjected to cyclic loading, resulting in the eventual failure of the component Paris

(1963). The scientific understanding of fatigue and its impact on materials has substantially advanced through these contributions and discoveries. They have made it possible to predict fatigue life, design components with greater durability, and ensure the reliability and safety of diverse structures and systems that are susceptible to cyclic loads.

1.4.1 Physics behind the fatigue failure

The fatigue failure process in materials consists of three stages: crack initiation, crack propagation, and reaching a critical crack length that leads to failure. In Region I, irreversible plastic deformation occurs due to the movement of dislocations within the material's lattice structure Callister et al. (2007). This movement leads to the formation of multiple slip planes, as illustrated in Figure 1.7, ultimately resulting in the formation of microcracks. The microcracks then continue to grow parallel to each other along crystallographic slip planes, typically in the direction of maximum shear stress or shear mode, transitioning to Region II known as crack propagation Rösler et al. (2007); Fatemi et al. (2001). Figure 1.8 provides an example of this behaviour.

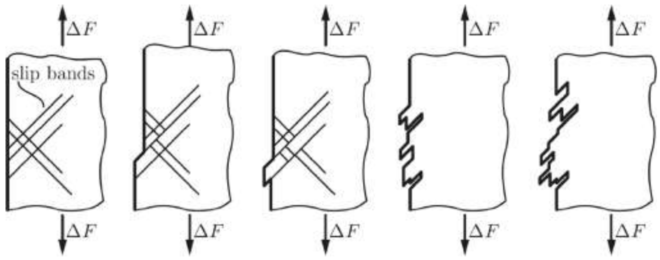

Figure 1.7: Pattern for Slip Bands Rösler et al. (2007).

As the crack propagates over successive cycles, the crack tip gradually becomes more blunted in comparison to its initial state under maximum load. In certain cases, this blunted crack tip hinders further crack growth by reducing the local concentration of stress. When the load is released or compressed, the crack surfaces rejoin, resulting in a sharpening of the crack tip, followed by the occurrence of slip once again. It is important to emphasize that the crack tip does not return to its original state, but instead progresses and widens. This cyclic process repeats with each subsequent loading cycle Metallurgy (1986). Figure 1.9 illustrates the opening of the crack and the occurrence of localized slip along the maximum shear planes, depicted by arrows.

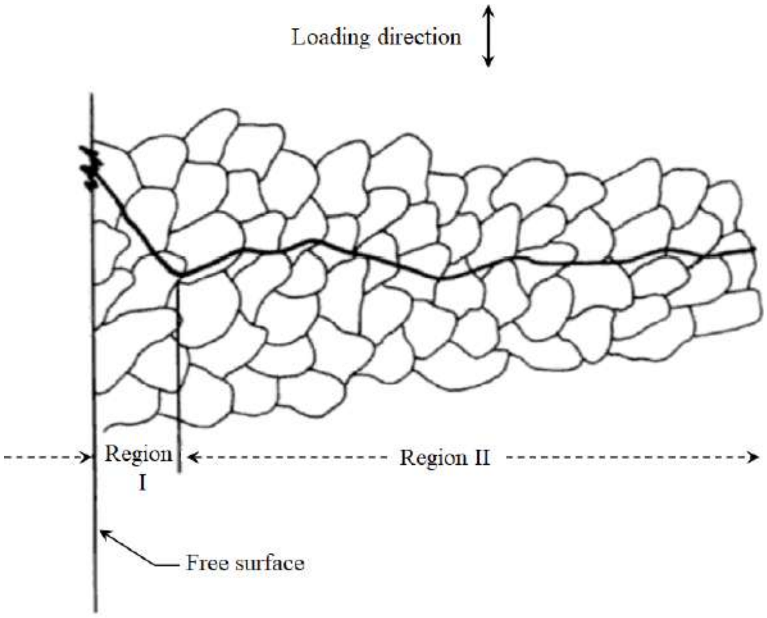

Figure 1.8: The transition from Region I (shear mode) to Region II (tensile mode) Fatemi et al. (2001).

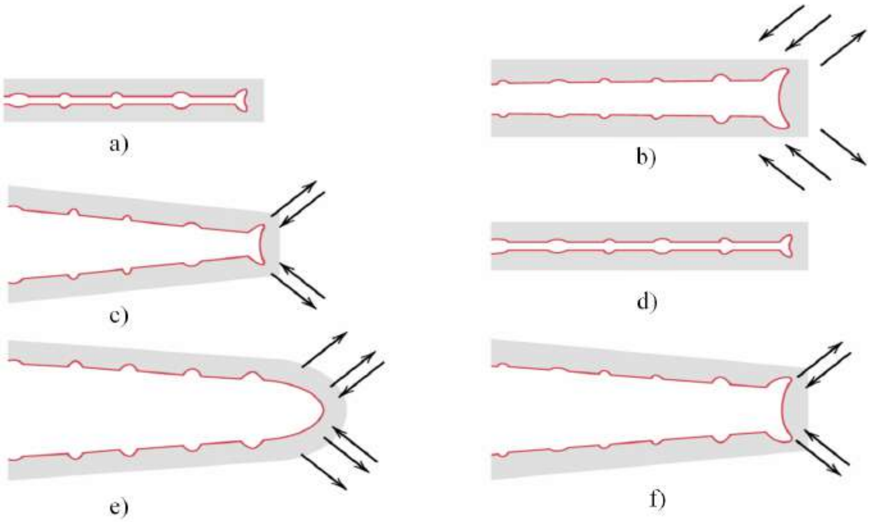

Figure 1.9: Crack growth and plastic blunting processes Metallurgy (1986).

When a crack is allowed to progress without any restrictions imposed by the mechanisms, it becomes dominant and eventually reaches a critical length or stress intensity, resulting in Region III fracture as shown in Figure 1.10. During this stage, the fracture surface appears rough or jagged. Once the critical length is attained, the crack grows rapidly and uncontrollably throughout the remaining ligament of material González-Velázquez (2020). If the material is subjected to high stresses, the crack can cause immediate separation with fracture surface features typical of tensile fractures.

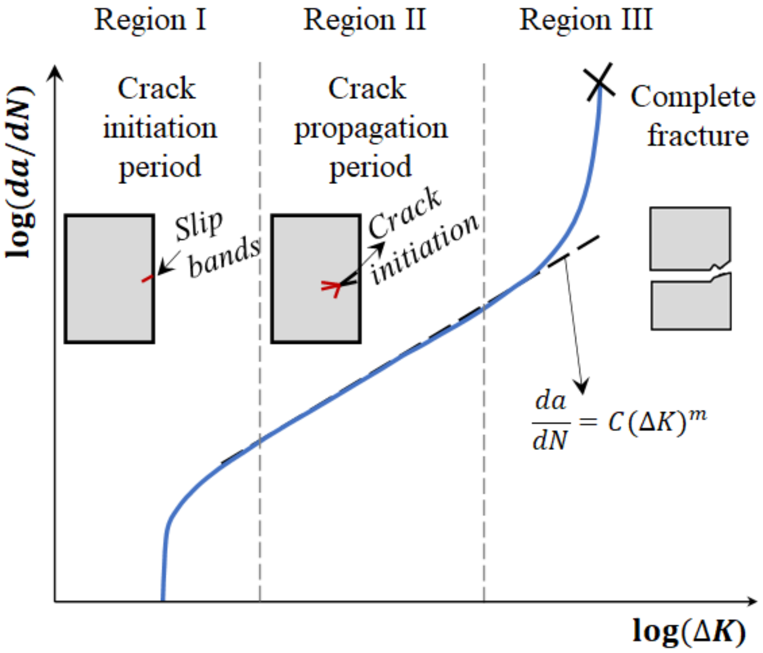

Figure 1.10: Schematic diagrams of the fatigue-failure process.

1.4.2 Structural health deterioration due to fatigue

Eventually, cyclic loading can cause deterioration in bridge structures by inducing fatigue in their material, and consequently impacting their health and strength. Fatigue initiates and propagates damage locally, impacting the global capacity of the structure and imposing limitations on the structure's operation. Figure 1.11a illustrates the reduction in residual strength due to damage growth, such as crack size in metals Anderson (2017). The design life of a structure is determined by its initial design strength and load, represented by the solid line in Figure 1.11b. The shape of the curve varies based on the material type and its properties. Failure occurs when the applied load surpasses the remaining strength or damage tolerance. By reducing the applied load below the design load, the durability and remaining life of the structure can be extended, as indicated by the dotted line, and vice versa. The same principles apply to damaged structures as well. Overall, the life of a structure can be prolonged by minimizing damage growth, reducing applied loads, and implementing appropriate maintenance and repair practices Yuan (2016).

Operational and environmental factors, along with uncertainties, however, make it challenging to define structural health in terms of age and usage. To maintain structural safety, continual in-service monitoring is essential, in order to avert catastrophic failures such as the I35 highway bridge collapse Board and

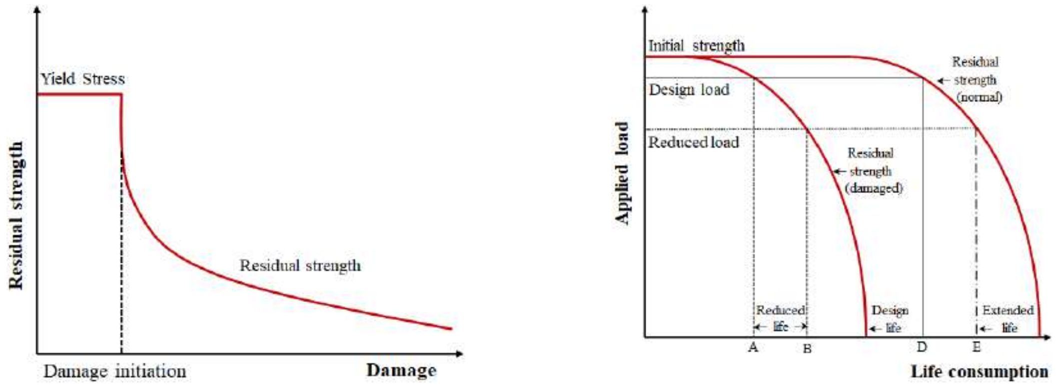

(a) Deterioration of material characteristics.

(b) Extending remaining lifespan through load reduction.

Figure 1.11: The residual strength of material undergoes variations over time Rob (2021).

Board (2008). Eventually, a monitoring initiative is required to keep track of the health of the structure and to perform prognosis studies to assess remaining service (/fatigue) life. Mere visual inspection although necessary in this regard yet is subjective and inaccurate Aktan et al. (1998), highlighting the need for rigorous and more efficient health monitoring applications.

1.5 Fatigue life

With regards to the central idea of this thesis, the concept of fatigue life here needs elaboration. According to ASTM (American Society for Testing Materials), fatigue life is defined in terms of the number of stress cycles that a specimen sustains before failure Stephens et al. (2000). For certain materials like steel and titanium, there is a theoretical stress amplitude below which the material is expected not to fail regardless of the number of cycles, referred to as the fatigue limit or endurance limit Bathias (1999). However, practical observations and extensive research conducted at higher cycle numbers indicate that fatigue limits do not exist for metals Pyttel et al. (2011); Sonsino (2007).

The analysis of fatigue is commonly divided into two regions based on the number of cycles to failure: low-cycle and high-cycle fatigue. However, recent research has further divided fatigue into four sub-regions: very low cycle fatigue (VLCF) $< 10^2$, low cycle fatigue (LCF) $10^3 - 10^5$, high cycle fatigue (HCF) $10^6 - 10^7$, and very high cycle fatigue (VHCF) $> 10^7$, which are distinguished by different damage mechanisms Kim and Hwang (2019); Karunananda et al.

(2012); Sharma et al. (2020). LCF and HCF failure is dominated by surface-initiated cracks, while subsurface crack initiation predominates in VHCF Wang et al. (2002).

1.5.1 Fatigue life prediction methods

Fatigue life prediction of a component or a system can be made through various methods. Among them, two commonly adopted approaches are the evaluation of fatigue damage and the prediction of the remaining life. The first approach uses Wöhler curve (*aka* S-N curves), to characterize material fatigue. These curves illustrate the stress (S)-cycles (N) relationship on a logarithmic scale Burhan and Kim (2018). Tests on material samples, known as coupons or specimens, apply sinusoidal stress to record cycles to failure. Coupon testing determines fatigue behaviour, while component testing offers more accuracy but limited generalizability Weibull (2013). Each test generates data points on the S-N curve, contributing to the understanding of material fatigue properties. Data censoring occurs if failure time exceeds the test duration. Statistical techniques like survival analysis and linear regression analyze fatigue data, estimate failure probabilities at different stress levels, and model stress-cycle relationships for predictions.

The second approach utilizes fracture mechanics principles and applies the crack growth equation to estimate the incremental growth of cracks with each loading cycle. Safety factors are incorporated to address uncertainties and variations associated with fatigue. The prediction of crack growth rate often involves subjecting a test specimen to multiple cycles of constant amplitude loading and monitoring changes in compliance or crack growth on the specimen's surface. ASTM International has established standardized methods for measuring crack growth rate Standard (2015).

The Paris-Erdoğan equation and similar crack growth equations are utilized to estimate the remaining lifespan of a component. These equations allow for the estimation of crack growth from an initial size of $10\mu m$ to failure, covering a significant portion of the component's fatigue life, including the initiation stage of crack growth Murakami and Miller (2005). Parameters such as stress intensity, J-integral, or crack tip opening displacement are commonly employed to establish a relationship between the conditions at the crack tip of a component and those observed in test specimens. By aligning the crack tip conditions between the component and test specimens, valuable insights into the rate of crack growth can be derived. One important advantage of crack growth methods is their ability to predict the sizes of intermediate cracks. This information is valuable for scheduling inspections on a structure to ensure safety. In contrast, S-N method only provide a life expectancy until failure without considering intermediate crack sizes. The S-N method is typically applied to small-scale, defect-free specimens, whereas real-world assets often contain flaws and micro/macro cracks.

1.5.2 Prognostic approach for RUL estimation

According to Xiongzi et al. (2011), RUL refers to the time remaining until the end of a component's useful life. Predicting RUL plays a vital role in predictive maintenance programs. Prognostic approaches provide insights into the safety, reliability, and performance of a structure under different operational scenarios. By assessing the current health state of the system, predicting damage growth, and analyzing safety risks, these approaches can forecast the success or failure of a process. Multidomain diagnostic techniques, such as system identification are employed to quantify discrepancies between the physical system and its digital representation. These discrepancies indicate damage or degradation and are utilized to generate and update risk assessments and estimates of remaining life as discussed by Saha et al. (2007). Comparing results from various operational scenarios aids in identifying the most probable scenarios for achieving successful processes.

The physical system undergoes maintenance or experiences changes in operating environments with the passage of time, which may invalidate the mathematical model as a replica of the physical structure. As shown in Figure 1.12, Bayesian inference techniques enable continuous updates of probability estimates, ensuring that the model remains as a "digital twin" of the physical system. Inverse methods are necessary to detect changes in physical systems based on sensor measurements. By comparing simulated and measured parameters, a model updater makes necessary adjustments to the mathematical model and coefficients to restore agreement between the model and the physical structure Ross (2016).

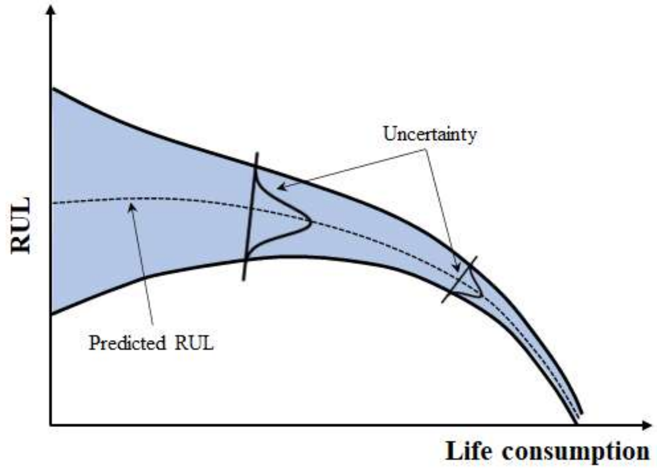

Figure 1.12: Bayesian inference improves accuracy over time with continuous probability updates.

1.6 System identification for RUL prediction

Field inspection plays a crucial role in detecting and preventing fatigue damage in bridge components, as well as assessing the uncertainties associated with fatigue processes and operational loading for the final assessment Ross (2016). To supplement visual inspection, non-destructive evaluation/testing (NDE/T) techniques such as dynamic testing, radiographic inspection, ultrasonic testing, acoustic emission monitoring, and dye penetration testing are employed Pipinato and Brühwiler (2022). However, these methods are reactive in nature and are typically initiated when there are concerns about structural health. Furthermore, they can be time-consuming, costly, and labour-intensive, particularly for large-scale bridges, resulting in significant downtime. The effectiveness of inspection programs depends on various factors, including the experience of the inspector, the type of damage being observed, the chosen NDE technique, and the potential presence of human bias Ross (2016). This highlights the necessity for efficient, reliable, and automated inspection approaches, such as SHM.

1.6.1 Purpose of SHM

SHM involves implementing a strategy to identify damage and assess the health of engineering structures by drawing inferences from the responses measured by an array of sensor networks over an extended duration. The primary objective of long-term SHM is to provide real-time information about the structural capacity considering the inevitable effects of ageing and degradation caused by operational environments Farrar and Lieven (2007) and especially after extreme events such as earthquakes or blast loading.

The objectives of an SHM strategy can be classified into five levels Farrar and Worden (2007): detection, localization, classification, quantification, and prognosis. Vibration-based damage SHM typically accomplishes the initial two levels of SHM: detection and localization while for the next two stages (classification and quantification), employment of a model becomes imperative. Prognosis, the final stage of SHM demands information from all the previous four stages as well as a predictive deterioration model and future estimates for operational loading.

Figure 1.13 showcases how advanced sensor networks and real-time data analysis tools can be utilized to evaluate the current condition of civil structures, predict their remaining lifespan, and formulate effective repair strategies. SHM aims to gather valuable information to optimize maintenance planning and ensure a dependable and cost-efficient operation. It is vital to continuously monitor and assess the performance of structures and estimate their remaining useful life for reliable operation and efficient maintenance and repair activities. Therefore, it is crucial to integrate SHM strategies with life cycle management to fine-tune structural assessment and predictions, facilitate optimal operational and maintenance practices, and prolong the lifespan of structures beyond their original design expectations.

Using SHM techniques, the health status of a structure can be evaluated by assessing damage extent and location, estimating residual strength, and analyzing applied loads. The damage indicator (cf Figure 1.14), such as crack length or fatigue cycles, can be devised to reflect the level of damage and residual strength Ross (2016). This indicator can be further periodically monitored and forecasted against a safe threshold to ensure safety. However, this task is not easy due to the presence of uncertainties in measurement, forcing, and/or environmental factors.

1.6.2 Probabilistic health assessment

The uncertainties in SHM arise from various sources, including sensor noise, ambient forcing, unaccounted environmental effects, sensor density, and model inaccuracies. Neglecting these uncertainties can result in false predictions or di-

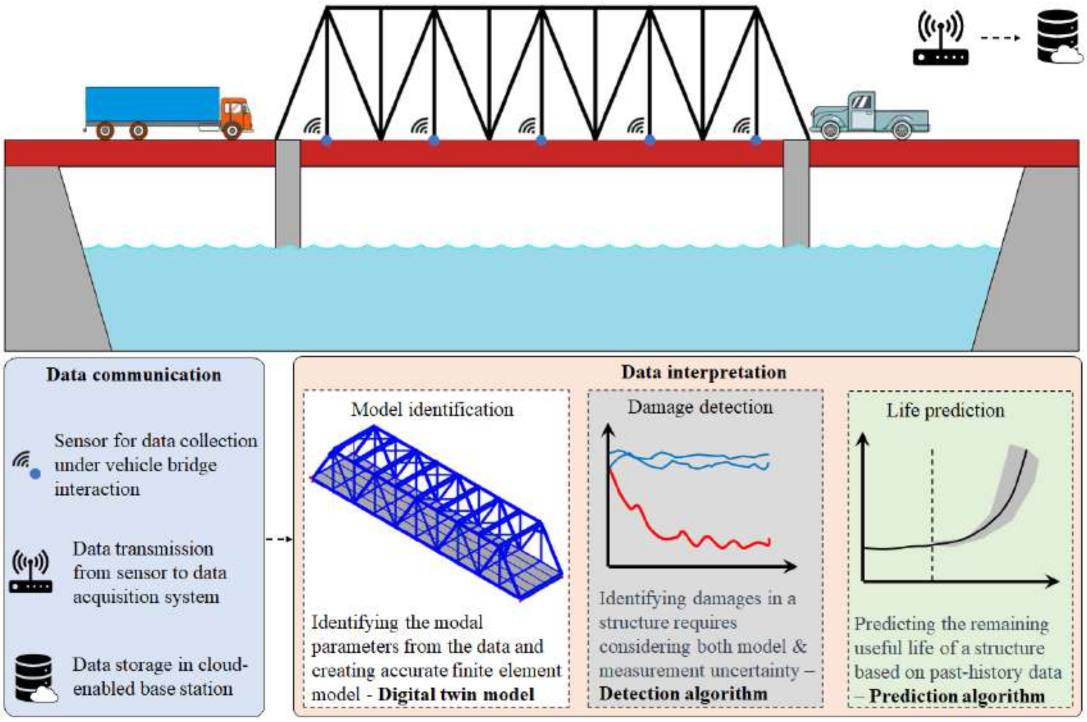

Figure 1.13: Integrated framework for health monitoring and evaluation of civil structure.

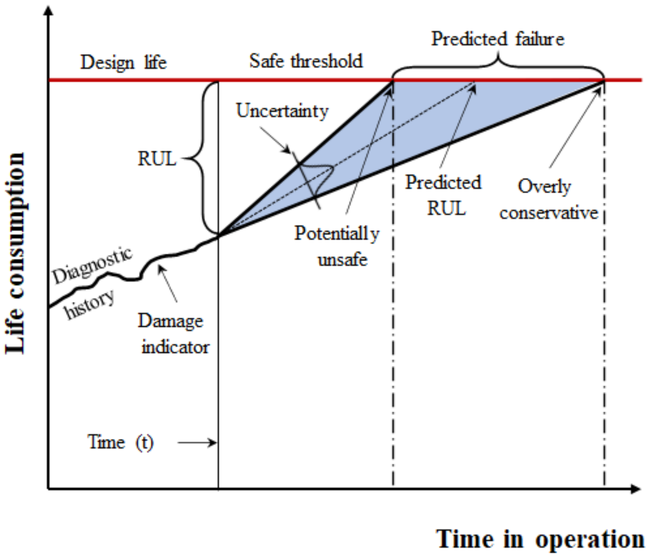

Figure 1.14: Margin errors in measurements can result in significant uncertainties in failure predictions.

vergence in estimations. The ideal SHM system aims to accurately detect damage with true positive (TP) indications, while minimizing false positive (FP) values, which lead to costly and unnecessary inspections (cf. Figure 1.15). It should also correctly differentiate true negative (TN) values indicating the absence of damage and minimize false negative (FN) values, indicating missed damage that could result in catastrophic failure. Selecting a threshold value to distinguish between damaged and undamaged states involves a trade-off between enhancing safety by increasing the probability of detecting true damage (TP rate) or reducing downtime and inspection costs by lowering the FP rate. Achieving both simultaneously requires improvement in other aspects of the system Ross (2016).

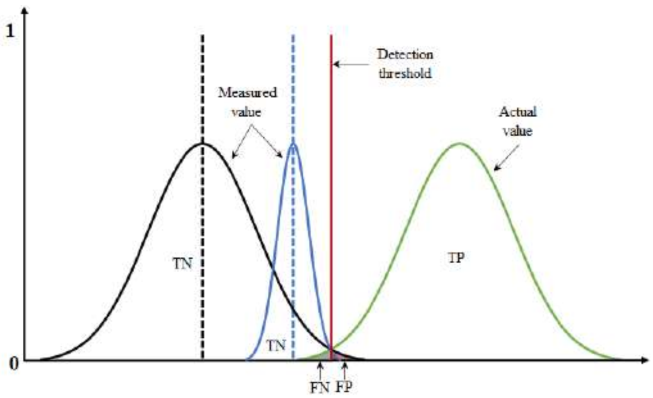

Figure 1.15: Enhancing measurement precision enhances safety predictions.

Nevertheless, the performance of any SHM algorithm while dealing with all uncertainties involved, mandates the problem to be defined in the probabilistic domain. Probabilistic methods such as Bayesian updating/filter can be used in this endeavour to deal with the unavoidable modelling inaccuracies or forcing uncertainties and measurement uncertainties separately, as discussed in detail in the following.

1.6.3 Bayesian filter

A Bayesian filter is a statistical estimator that employs Bayesian inference to estimate and predict the state of a system. By combining prior knowledge and observed data, the filter updates the probability distribution of the system's state. It continually adjusts its estimate as new measurements are obtained, considering both the measurement data and the underlying system dynamics. This enables the filter to provide more accurate and reliable estimates for the states by incorporating previous information and updating the probability distribution accordingly.

Bayesian filtering requires a state space model/formulation, which refers to the mathematical representation of dynamic systems in the probabilistic framework (Chapman-Kolomogorov equation). These models describe the evolution of the dynamic systems in terms of state dynamics detailing the relationships between the system's inputs, outputs, and internal states. The probabilistic framework, in the context of SHM, further allows to include the model inaccuracies or forcing uncertainties into this model in terms of process noise. The states are however unobserved internal variables that are further observed through a second equation, termed as measurement equation, wherein measurement uncertainty due to sensor noise can additionally be included as a noise variable.

Among several existing Bayesian filters, Kalman filter Kalman (1960), introduced by RE Kalman in 1960, is widely used for linear dynamic systems and assumes the noise as stationary white Gaussian noise (SWGN). It provides optimal estimation by recursively updating the state estimate based on measurements and system dynamics. The extended Kalman filter (EKF), which linearized the models about a current estimate, can be considered a nonlinear variant of the Kalman filter. EKF uses Taylor series expansion and updates the state estimate using nonlinear measurement equations. For the capability to handle nonlinear systems, EKF can be employed for parameter (/input) estimation which is inherently nonlinear due to the nonlinear relationship between parameters (/inputs) and measurements. However, as the dimensionality and nonlinearity increase, the performance of EKF can be affected by accumulated errors from system linearization approximations. Moreover, EKF can deal with mild non-Gaussianity, but when dealing with highly nonlinear systems, it may run into accuracy and divergence issues.

The unscented Kalman Filter (UKF) was first presented by Julier et al. in 1995 to solve the EKF's limitations. The unscented transform, which is used by UKF, computes the statistics of random variables passing through a nonlinear transformation Julier et al. (1995). In contrast to EKF, UKF uses sigma points with the unscented transform, as introduced by Wan and Van Der Merwe (2000), to approximate the mean and covariance of the updated variable more closely. Because of this, UKF is considered to be a better nonlinear estimate procedure than EKF.

Ensemble Kalman Filters (EnKF) is an ensemble-based approach that utilizes a group of model states, called an ensemble, to estimate the system state. It combines ensemble forecasting and Kalman filtering techniques to assimilate observed data into a numerical model and estimate the state of a dynamic system. In EnKF, the ensemble of model states evolves forward in time using system dynamics and is then adjusted based on available observations. This ensemble-based approach offers increased reliability and adaptability in the presence of model errors and uncertainties. EnKF is particularly suitable when working with limited data and systems with significant nonlinearities. Additionally, due to its parallelizability, EnKF can provide computational efficiency advantages for high-dimensional systems Evensen (2003).

Particle Filter (PF), also referred to as Monte Carlo filter, is a non-parametric filter that uses a collection of particles to represent the probability distribution Gordon et al. (1993). The weight of each particle reflects its likelihood. PF calculates an estimate of the system state and its uncertainty by propagating and resampling a set of particles based on system dynamics and observations. PF is widely applicable and parallelizable. However, the large sample sets required for optimal performance can make the system computationally expensive.

Although PF is known for its effectiveness in handling nonlinear problems, its computational requirements have raised concerns. As a result, interacting filtering techniques Karlsson et al. (2005); Sen and Bhattacharya (2016, 2017); Zghal et al. (2014) have emerged as an alternative approach, aiming to reduce the overall state dimension through an interactive strategy Zghal et al. (2014); Sen et al. (2021). In these techniques, the parameters are estimated using PF, while the state estimation is performed using either KF/EnKF, depending on the linearity or nonlinearity of the process model Zghal et al. (2014). Each Bayesian filter has its own strengths and is suitable for different system models and estimation scenarios. The choice of filter depends on the specific characteristics of the problem being addressed.

1.7 Research gap

Many approaches for estimating the fatigue life of civil infrastructures are offline in nature Kwon et al. (2012); Adasooriya and Siriwardane (2014); Mohammadi et al. (1998), requiring complete measured data to determine the Remaining Useful Life (RUL). In contrast, online algorithms provide flexibility by utilizing data as it becomes available. Bayesian filtering-based approaches enable the use of prior information or beliefs about fatigue model parameters and their evolution, even in the absence of measured data.

Typically, the Paris law model is used to represent fatigue crack propagation. However, it is not suitable for typical bridge structures that experience both tensile and compressive stresses in their members and joints. The Paris Law assumption contradicts this behaviour. Under compressive stress, crack propagation is reversed due to the crack closure effect. Therefore, the predictor model must account for both effects to accurately estimate the fatigue life of a bridge or its components.

To comprehensively investigate high-dimensional structures like bridges, numerous sensors and costly high-dimensional support models are required to monitor the entire domain Wu et al. (2019); Sharma and Sen (2021). This can lead to computationally expensive, ill-posed problems, resulting in divergent and sometimes infeasible results due to the processing of extensive sensor data and computational demands of high-dimensional models. However, it is important to note that fatigue is a localized weakening process that can be efficiently monitored through localized monitoring Marques et al. (2018). By identifying and independently monitoring the fatigue-critical subdomain, which represents the area of interest, the expenses related to instrumentation and computation can be reduced accordingly, while still estimating the RUL of the entire bridge.

1.7.1 Objectives and scope

The primary objective of this dissertation is to develop a precise and cost-effective approach for predicting the RUL of civil infrastructures. To accomplish this objective, the following specific objectives have been defined, focusing on RUL estimation using SHM techniques, physical models, and filter-based techniques.

1. Develop Bayesian filter-based algorithms for RUL estimation in the presence of cracks, utilizing available SHM data and incorporating model and measurement uncertainties.

2. Create a fatigue life assessment technique based on substructure monitoring, aiming to establish a distributed and cost-effective approach for fatigue monitoring in structures without cracks.

3. Develop an RUL estimation approach specifically designed for substructures with visible cracks.

4. Implement substructure-based SHM techniques considering vehicle-structure interaction forces, enabling a direct approach for RUL estimation based on vehicle counts without the need for expensive model simulations.
5. Validate the proposed approaches through numerical and real experiments, emphasizing their application to bridge structures.

The scope of this research is to investigate and propose solutions for RUL prediction in bridge infrastructures, focusing on crack detection, fatigue life assessment, vehicle-induced loads, and component-wise monitoring through substructuring. The proposed methods will be validated through rigorous experimentation, with an emphasis on their practical implementation in bridge structures.

1.7.2 Organization of thesis

The thesis consists of seven purpose-driven chapters. Chapter 1 serves as an introduction, addressing the problem statement, fatigue terminology, fatigue life prediction methods, SHM, associated uncertainties, and the importance of the Bayesian filter. The chapter also outlines the objectives of the thesis. The second chapter conducts a comprehensive review of existing methodologies and factors influencing fatigue life prediction for bridge structures. The significance of an algorithm for automated SIF calculation and its validation is emphasized.

Chapter 3 focuses on the development of a filter-based real-time algorithm for estimating RUL in the presence of cracks using available SHM data. This chapter aims to provide a reliable method for predicting the remaining lifespan of structures with cracks.

In the fourth chapter, a novel standalone substructure monitoring technique is introduced, which allows for component-wise estimation of high dimensional structures. The chapter provides a comprehensive overview and validation of this technique, highlighting its effectiveness and accuracy.

The fifth chapter presents an improvisation of the proposed substructure estimation approach to address fatigue life estimation of a bridge structure with a visible crack and available crack growth time history. The dissertation also discusses similar studies and relevant improvisations for RUL estimation in bridge structures where the crack may be absent, visible, or measurable in its sixth chapter. This chapter explores various scenarios and adapts the proposed algorithms accordingly. For all the proposed algorithms, extensive validation studies through numerical and real experiments have been undertaken whenever necessary, demonstrating their effectiveness, accuracy, precision, and promptness. The algorithms' noise sensitivity, robustness against force, and damage severity are also evaluated.

Finally, Chapter 7 summarizes the research findings, discusses the challenges encountered during the study, and suggests potential future research avenues. This chapter provides a comprehensive conclusion to the thesis, highlighting the contributions made and areas for further exploration.

1.7.3 Major contributions

This dissertation contributes to the field of prognostics by proposing a method for predicting the RUL of bridge structures using the SHM framework. The key contributions of this research are outlined below:

- Development of an online model-based real-time prognosis algorithm powered by a Joint-Extended Kalman filter (JEKF) estimation approach. This algorithm enables the prediction of the service life of structural components based on available data, facilitating proactive maintenance and optimal resource allocation.
- Introduction of a substructure technique for component-wise monitoring to reduce computational workload and instrumentation requirements. By employing an Interacting Particle-Ensemble Kalman filters (IPEnKF) algorithm Aswal et al. (2021b) and an output injection technique Zhang and Zhang (2018); Sen et al. (2021), the proposed approach isolates the subdomain of interest for health estimation without the need to consider the rest of the structure.
- Application of the substructure estimation approach to reconstruct forces at the substructure boundary under vehicle-induced vibration, and further estimate the fatigue life using the crack growth time history. By considering the dynamic effects of vehicles, the algorithm provides a comprehensive understanding of fatigue behaviour under realistic operational scenarios.

- Integration of component-wise health assessment framework to real-time RUL estimation that focuses specifically on the fatigue-critical location and estimates the fatigue life of the structure conditioned on the current health state even in the absence of cracks.

Finally, this research offers novel methods and techniques for RUL prediction and fatigue life assessment, enhancing the field of structural prognostics and enabling informed decision-making for the maintenance and management of bridge structures.

1.7.4 Publications

The publications that have been accepted and submitted based on dissertation work:

Journal papers

1. **Kuncham, E**., Aswal, N., Sen, S., & Mevel, L. (2023). Bayesian monitoring of substructures under unknown interface assumption. **Mechanical Systems and Signal Processing**, 193, 110269.
2. **Kuncham, E**., Sen, S., Kumar, P., & Pathak, H. (2022). An online model-based fatigue life prediction approach using extended Kalman filter. **Theoretical and Applied Fracture Mechanics**, 117, 103143.
3. Hoda, M. A., **Kuncham, E**., & Sen, S. (2022). Response and input time history dataset and numerical models for a miniaturized 3D shear frame under damaged and undamaged conditions. **Data in Brief**, 45, 108692.
4. Aswal, N., **Kuncham, E**., Sen, S., and Mevel, L. Health assessment of high dimensional structures under spatial thermal variation using localized estimation approach. Mechanical Systems and Signal Processing. (*under review*)
5. **Kuncham, E**., and Sen, S. Fatigue assessment of bridges using interacting filtering approach with sub-structured predictor model based on current health. Journal of Bridge Engineering. (*under review*)

6. Hoda, Md A., **Kuncham, E.**, and Sen, S. Enhanced high-resolution structural crack detection using hybrid interacting Particle-Kalman filter. (h-IPKF). Structures. (*under review*)
7. **Kuncham, E.**, Hoda, Md A., and Sen, S. Force estimation in bridge substructure boundary under vehicle loading using interacting filtering approach. International Journal of Advances in Engineering Sciences and Applied Mathematics. (*under review*)
8. Shereena, O.A, **Kuncham, E.**, Sen, S., Jain, P. C., and Mevel, L. Mitigating high dimensionality in damage identification for plate-like structures through substructuring with interacting filtering-based approaches. Engineering Structures. (*under preparation*)

Conference papers

1. Aswal, N., **Kuncham, E.**, Sen, S., & Mevel, L. Subdomain fault isolation for linear parameter varying systems through coupled marginalized particle and Kitanidis filters. 22nd **IFAC World Congress 2023**. Japan.
2. **Kuncham, E.**, and Sen, S. Development of computationally efficient health benchmarking approach for a bridge structure by coupling substructuring technique within interacting filtering approach. 10th **EWSHM 2022**. Italy.
3. Aswal, N., **Kuncham, E.**, Sen, S., & Mevel, L. Robust Interacting Particle-Kalman Filter based structural damage estimation using dynamic strain measurements under non-stationary excitation - an experimental study. 10th **SHMII 2021**. (*online*).
4. **Kuncham, E.**, Hoda, Md A., and Sen, S. Force estimation in bridge substructure boundary under vehicle loading using interacting filtering approach. 67th **ISTAM 2022**. India.
5. Hoda, Md A., **Kuncham, E**, & Sen, S. Detection of edge crack in a beam-like structure modeled as rotational spring by using Bayesian filtering. 67th **ISTAM 2022**. India.
6. **Kuncham, E.**, Hoda, Md A., and Sen, S. Identifying the cracks in beam structures using a simplified substructure technique. 4th **SICE 2022**. India.

Chapter 2

Integrating SHM techniques and numerical SIF simulation for fatigue analysis in structures

In order to achieve the overarching goal of accurately predicting the service life of civil structures, I have set specific objectives that will be addressed in each chapter. To ensure accuracy, the most effective approach is to enhance your understanding and explore various methods for predicting the fatigue life of structures. Additionally, it is important to understand the factors that influence fatigue life, such as SIF, temperature, and random loading. Lastly, an automated approach is devised to calculate SIFs for complex systems without demanding complete fracture mechanics simulation. The same is validated using standard and complex specimens under mechanical and thermomechanical loadings.

2.1 Standard fatigue analysis methods

Two major factors have been observed to be impactful in the improvement of fatigue analysis techniques. Of them, the first one is allowing designers and engineers useful, simple-to-implement, affordable approaches to fatigue analysis, and the second one is to assure the practicality of the employed approach in matching the actual observation data. Fatigue processes are typically divided into two distinct stages: initiation and propagation. There exist well-established methods to monitor fatigue within each of these stages. In this regard, the stress-life (S-N), strain-life (ϵ-N), and fracture mechanics approaches for fatigue analysis are discussed in this chapter. Although there is considerable overlap between these strategies, each has a distinct application area Ye et al. (2014).

2.1.1 Stress-life (S-N) approach

The stress-life approach is commonly used to predict long fatigue life when stresses and strains remain within the elastic range. This approach disregards the differentiation between crack initiation and propagation and instead focuses on the overall lifespan or time to failure of a structural component. It relies on S-N curves, which depict the relationship between stress range and fatigue failure. These curves are generated by subjecting the test materials to repeated applications of constant-amplitude stresses until visible cracking occurs. To construct these curves, numerous experiments are conducted on the material under consideration, subjecting it to various stress levels. However, conducting fatigue tests can be expensive and time-consuming, and incorporating the resulting fatigue data into curves also requires a significant amount of time.

To address these challenges, fatigue analytical models have been developed to combine theoretical concepts with observed data, enabling more accurate predictions for future observations. Wöhler's original research made significant contributions to the investigation of fatigue failure in railway axles and the estimation of fatigue strength based on experimental data, particularly for the German Railway Industry. His work established the connection between applied stress, cycles to failure, and the concept of fatigue limit, further enhancing the understanding of fatigue behaviour across different materials Al-Rubaie (2008).

Several S-N approaches are commonly employed for predicting fatigue life, distinguished by the stress analysis of the structural details. The three fundamental types are the nominal stress approach, hot spot stress approach, and effective notch stress approach Fricke (2003); Radaj (1996).

Nominal stress approach

The nominal stress approach is widely used to assess fatigue life in steel bridges and is incorporated in contemporary codes and standards Standard (1980); on Bridges (1990). This approach considers the average stress within the component cross-section, focusing on overall stress distribution, including high stress around welded joints. However, it does not consider local stress variations. The nominal stress determination/computation is typically carried out by any standard methods, for instance, finite element modelling analysis or linear elastic structural mechanics. Accurate measurement can be achieved by strategically placing strain gauges outside the stress concentration field of the welded joint.

Despite its wide usage, the nominal stress approach has its own limitations. It may not be suitable for cases of challenging load characterization and complex structural joints Xiao and Yamada (2004). It also overlooks the dimensional fluctuations in specific structural features, impacting the accuracy of fatigue life predictions Poutiainen et al. (2004). Caution should be exercised when applying the nominal stress approach to certain steel bridge elements, as concerns about prediction accuracy may arise.

Due to the above limitations, alternative strategies like hot spot stress or effective notch stress approaches can be considered when the issues of load characterization, complex geometry etc. arise. These techniques provide more precise evaluations of complex features and account for stress concentration effects. While the nominal stress approach is frequently used, its accuracy and suitability for specific bridge components should be thoroughly examined and evaluated.

Hot spot stress approach

The hot spot stress approach offers higher precision compared to nominal stress analysis when conducting fatigue analysis of complex welded connections. Guidelines and recommendations provided by the International Institute of Welding assist in accurately determining hot spot stress in welded connections. Steel bridges consist of various welded plate-type structural components, such as longitudinal and transverse ribs, floor beams and stringers, and joints between main girders and floor beams. Extensive research on the fatigue behaviour of welded joints and the foundations of fatigue strength measurement have combinedly resulted in the development of design guidelines and applications Gurney (1979); van Delft (1981); Hobbacher et al. (2016).

In the hot spot stress approach, fatigue cracks are prone to initiate at weld toes, which experience the highest local pressures. Determining the hot spot stress involves multiplying the nominal stress by the stress concentration factor (SCF), wherein SCF is obtained can be obtained through finite element analysis, strain gauge measurements, or empirical methods Pilkey and Pilkey (1997). Finite element methods(FEM) facilitate the estimation of SCFs by providing precise information on the positions, orientations, and magnitudes of high stresses. Strain gauges play a vital role in accurately measuring the SCF, requiring careful placement optimization based on finite element simulations of typical details Kaczinski et al. (1997); Barth and Bowman (2001); Tsakopoulos and Fisher (2002); Connor (2004); Al-Emrani (2005); Connor and Fisher (2006).

Various approaches and techniques, considering stress gradients and nonlinearities, have been proposed to assess hot spot stress at different welded joints. Early studies focused on relating fatigue strength to local stress near the weld toe and have a longstanding history in evaluating hot spot stress for fatigue Radaj (1996). Over time, the hot spot stress approach has gained wider acceptance and is encouraged in national and international codes and standards Committee et al. (1994); API (2005); IIW (2000); File (1998). While the application of this approach to predict fatigue life and design in different welded steel structures has received less attention, its use in evaluating fatigue in welded plate joints within steel structures, particularly cable-supported steel bridges, has generated significant interest Chan et al. (2005, 2003).

Effective Notch Stress Approach

The effective notch stress approach offers an alternative strategy for predicting the initiation life of a crack at the root of a notch, specifically in the high-cycle regime. Radaj et al. (2006); Radaj (1990) developed this approach, focusing on fracture initiation and early growth in the high-cycle regime. Zhang and Richter (2000) proposed novel strategies for numerically predicting fatigue life in spot-welded structures, considering the interaction between notch stress and SIF.

Sonsino et al. (2012) explored the applicability of the notch stress concept in different industrial sectors, using reference radii of 1 mm for thick-walled connections and 0.05 mm for thin-walled welded steel connections. Aygül et al. (2013) conducted a comparative study on widely used welded joints in steel bridges, evaluating the accuracy of nominal, hot spot, and effective notch stress approaches. The results indicated that the effective notch stress approach only marginally improved fatigue strength calculations despite requiring a more complex modeling effort in computation.

2.1.2 Fracture mechanics approach

The fracture mechanics approach is commonly used to estimate the propagation life of an initial crack. Linear elastic fracture mechanics (LEFM) connects the growth of a crack with the number of fatigue cycles, allowing engineers and researchers to study crack behaviour and predict its progression over time. This enables the estimation of fatigue life and helps in designing stronger and safer structures. Paris' law is a widely used tool in fatigue research for calculating fracture growth rates Paris (1963).

The application of fracture mechanics techniques in assessing bridge fatigue conditions has been extensively studied. Fisher (1984) examined fatigue crack occurrences in steel bridges using fracture mechanics concepts and case studies. Agerskov and Nielsen (1999) investigated fatigue damage accumulation in steel bridges under random loads, utilizing the fracture mechanics approach to calculate the fatigue life of welded joints in highway bridges. MacDougall et al. (2006) compared the impact of different vehicle types on fatigue life, specifically for short-span and medium-span bridges, using a LEFM model. Xiao et al. (2006) combined experimental data from the Kinuura Bridge with LEFM-based theoretical predictions, highlighting the significant reduction in fatigue strength of butt-welded joints due to the presence of $2-3\ mm$ lack of penetration zones.

These studies demonstrate the importance of fracture mechanics in understanding and evaluating fatigue-related issues in steel bridges. By incorporating fracture mechanics concepts and considering factors such as stress, vehicle characteristics, and weld quality, researchers have gained insights into fatigue crack development and the fatigue life of welded joints. The findings contribute to the enhancement of steel bridge design, maintenance procedures, and the development of reliable fatigue evaluation methodologies.

2.1.3 Strain-life (ϵ-N) approach

The strain-life approach, developed in the 1960s, primarily focuses on the fracture initiation phase of fatigue analysis. It is particularly suitable for materials experiencing plasticity, indicating behaviour beyond pure elasticity. The ϵ-N approach is highly relevant for LCF scenarios characterized by relatively short fatigue lives. Some research has been conducted to explore the application of the ϵ-N approach in evaluating the fatigue performance of steel bridges through LCF testing and theoretical calculations Ge et al. (2013); Sakano and Wahab (2001).

However, the use of the ϵ-N approach for assessing the fatigue life of steel bridges has received limited attention compared to other fatigue analysis techniques. This is mainly because HCF rather than LCF is the dominant factor contributing to fatigue issues in steel bridges. Nonetheless, certain studies have focused on ϵ-N fatigue data obtained from historic Portuguese metallic riveted bridges. De Jesus et al. (2011) examined the fracture propagation fatigue data of these bridges, employing probabilistic and deterministic models to correlate the ϵ-N fatigue data. Nevertheless, the application of the ϵ-N approach in fatigue assessment for steel bridges remains relatively underutilized compared to alternative techniques.

2.1.4 Field measurement data

Obtaining accurate load and resistance information is essential for fatigue assessment in the S-N approach for evaluating and predicting bridge fatigue damage. Even a slight change in the stress range when using live load stresses in cubic equations Sartor et al. (1999) might result in very different fatigue evaluation outcomes. Properly accounting for all factors in a typical analysis can pose challenges due to the inability of computational models and simulations to accurately capture the variations in stress range experienced by a structural element. Field measurement is required to gather accurate information that takes these variables into account.

Field measurement entails attaching sensors to bridge components in order to directly measure and record the stresses and stress distributions that the structural component really experiences. Given that it considers the conditions and variations found in real-world settings, this method offers the most straightforward and accurate basis for fatigue assessment. A comprehensive examination of fatigue analysis methods for bridge structures that rely on field-measured data. Specifically, it discusses the application of NDT, such as NDE and SHM techniques. Engineers can improve fatigue assessment and life prediction by using field-measured data to acquire more precise and reliable information about the real loads and stress that bridge structures experience Ye et al. (2014).

2.1.5 Fatigue life assessment using NDE techniques

Many existing structures need to be strengthened, repaired, or rebuilt due to rising traffic volumes, greater truck weights, and deteriorating bridge conditions in order to guarantee an adequate degree of safety when taking into account the present and future traffic conditions Zhao and Haldar (1996). NDE technology has emerged as a means to enhance the accuracy of bridge condition assessment, particularly in situations where financial constraints and the high costs associated with reconstruction are a concern Russo et al. (2000). When assessing the fatigue condition of bridges, it is common to employ load-controlled diagnostic testing under typical traffic loads as an evaluation technique. These techniques are frequently complemented by the utilization of sensors and data collection systems.

The benefit of using known loadings in load-controlled diagnostic testing is that bridge response can be roughly quantified and a thorough baseline model may be established. However, it takes longer to set up, requires traffic management while being tested, and only captures a moment in time. Monitoring through the use of NDT techniques offers advantages such as not requiring traffic control, quick setup, and the ability to record responses resulting from background traffic. This approach provides statistical data on actual responses over time, offering valuable insights into structural behaviour. However, it is important to note that NDE, as a short-term in-service monitoring technique, provides limited information for a comprehensive evaluation of bridge parameters. Additionally, it does not capture specific details related to truck loadings, which can be crucial for a thorough analysis Chajes et al. (2000).

NDE techniques have been used in a number of investigations on bridge fatigue assessments. These studies evaluated the fatigue life Hahin et al. (1993), condition, and remaining lifespan of bridges under real traffic loads using field strain data, portable computer-based strain gauge data gathering systems DeWolf et al. (2002), strain monitoring at important places, and field measurements. The identification of maintenance, repair, and replacement solutions for bridge infrastructure Chakraborty and DeWolf (2006) has been made possible by the application of NDE techniques. Numerous studies have reviewed diagnostic load testing, repair techniques, and strengthening schemes based on field measurements and laboratory tests to address the issue of distortion-induced fatigue Ermopoulos and Spyrakos (2006).

NDE techniques have been applied by researchers like Hahin et al. (1993), DeWolf et al. (2002), Chakraborty and DeWolf (2006), Ermopoulos and Spyrakos (2006), Moses et al. (1994), Spyrakos et al. (2004), and Alampalli and Lund (2006) to the field of fatigue evaluation of steel bridges, furthering our understanding and management of bridge infrastructure.

2.1.6 Fatigue life assessment using SHM techniques

SHM, being an advanced and continuous version of NDE testing, is becoming more widely recognized Pines and Aktan (2002); Casciati (2003) for its ability to maintain the structural integrity and safety of bridges throughout their whole lives. SHM provides advance notice of degradation or damage, allowing prompt repairs and avoiding catastrophic collapses. Due to their significant financial outlays, economic importance, creative design, and construction methods, computer, and sensor-based SHM systems have witnessed an increase in popularity when it comes to being integrated into bridges, particularly long-span bridges. Monitoring the structural performance and health of bridges while precisely predicting fatigue state and remaining lifespan is one of the important roles of SHM systems. On the other hand, there hasn't been much research on analyzing fatigue and assessing conditions based on long-term monitoring data. The relative novelty of SHM technology in civil engineering, the absence of agreed-upon definitions and design standards, and the high implementation costs have all hindered its widespread acceptance Ye et al. (2014); Chan et al. (2001).

Several research studies have concentrated on fatigue analysis and condition assessment based on SHM techniques. These research studies used SHM data from notable bridges such as the Tsing Ma Bridge Chan et al. (2001) and the Bronx-Whitestone Bridge Connor et al. (2003) to develop methodologies and strategies for fatigue life prediction. They have incorporated important factors such as wind effects and structural components to assess long-term fatigue damage caused by buffeting in suspension bridges, employing specific methodologies for fatigue damage assessment. Additionally, conventional daily stress spectrum methods have been employed to evaluate the fatigue life of bridges, including the Tsing Ma Bridge Radaj et al. (2006). These studies demonstrate the possibilities of using long-term SHM monitoring data for fatigue analysis and bridge condition evaluation.

2.2 RUL prediction using SHM techniques

The commonly used fatigue analysis methodologies for evaluating fatigue life and RUL of structures are discussed in the existing approaches Ye et al. (2012); Marques et al. (2018). Based on the presence or the absence of a crack in the civil structure, methodologies are classified into two specific categories as follows:

1. RUL prediction using the S-N approach (assuming crack attributes are either not available or visible)

2. RUL prediction using the fracture mechanics approach (when the crack is visible and its growth time history is available)

2.2.1 RUL prediction using the S-N approach

To ensure the safety of structures in hard-to-reach areas, a traditional method is to use the safe life design approach, which aims to prevent structural failure caused by fatigue. This approach operates under the assumption that there are no fatigue cracks in the structure during its expected lifespan for safe operation Kim et al. (2006). In the cases where the structure appears to be in good condition, fatigue life estimation is straightforward through the employment of a cumulative damage approach, which relies on the S-N curve for the component material. For monitoring structural health, stress history data is utilized from the SHM technique. Techniques such as rain flow analysis are employed to simplify complex stress history data into a sequence of simple cyclic stress data. Based on the outcomes of the rain flow analysis, a histogram of cyclic stress is generated to construct a fatigue damage spectrum. The cumulative damage level for each stress level is established by referencing the S-N curve. The individual contributions are consolidated by applying the cumulative damage approach. By following these steps (cf. Figure 2.1), the fatigue life of each structural element can be assessed in terms of fatigue damage, taking into account the complex and varying loading conditions experienced by civil structures.

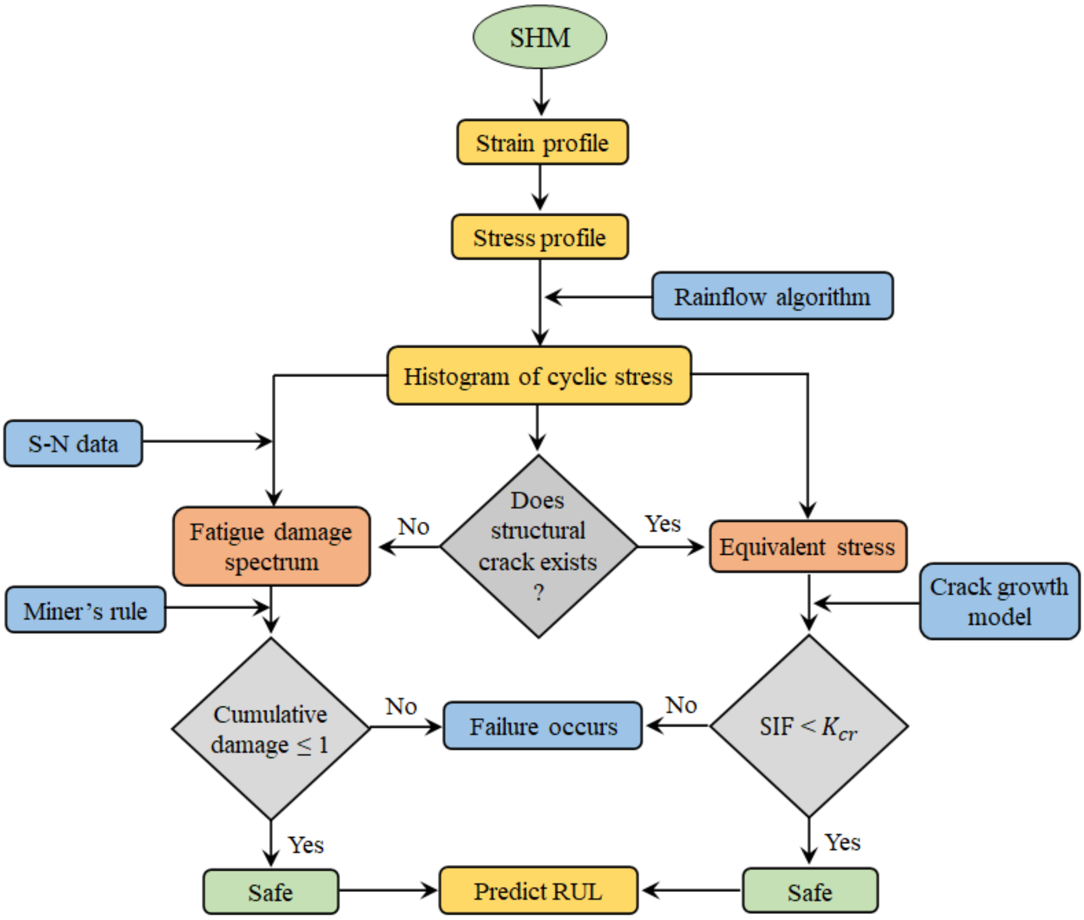

Figure 2.1: Generic procedure for estimating both the safe fatigue life and RUL using two different approaches.

Cumulative damage approach under random loading

Civil structures experience a range of complex and random load patterns, encompassing both substantial and minor loads. To determine the reliable fatigue life of such a component using S-N methods, the typical cumulative damage approach has been used.

Basquin and Coffin-Manson fatigue life models are considered empirical methods since they involve curve fitting two parameters based on SN data. On the other hand, Cumulative Damage Model (CDM) takes into account environmental and physical factors that affect fatigue behaviour. In this model, it is assumed that a component undergoes deformation and experiences "damage." This damage is a measurable quantity, and the CDM determines how much damage is needed for a component to fail under specific conditions Celli (2021). The equation provides a general form for the CDM approach.

$$\sum_{i=1}^{n} \frac{D_i}{D_{f,i}} = 1 \tag{2.1}$$

This approach assumes that the ratio of discrete damage events (D_i) to the total damage required to cause fracture for a specific load condition ($D_{f,i}$) is considered. When the sum of these ratios, calculated for a total of n events, reaches 1, it indicates the occurrence of failure or fatigue fracture.

One of the simplest and earliest widely used methods for fatigue analysis and prediction is commonly known as Miner's rule. Originally proposed by A. Palmgren but popularized by M. A. Miner, this approach considers a linear combination of overstress cycles (n_i) and the corresponding cycle life at the same overstress level (i), as described in Equation (2.2) Miner (1945); Metallurgy (1986).

$$\sum_{i=1}^{k} \frac{n_i}{N_i} = \frac{n_1}{N_1} + \frac{n_2}{N_2} + \cdots + \frac{n_k}{N_k} = 1 \tag{2.2}$$

Miner's rule operates under the assumption that all stress cycles N_i are referenced to the original, healthy curve. In other words, if a component is subjected to a stress cycle and becomes damaged, resulting in a shift in its S-N curve, Miner's rule still considers the original S-N curve as the reference point. This means that the rule does not account for the cumulative damage caused by each subsequent cycle or the fact that the component has undergone deterioration. Miner's rule treats each stress cycle independently and assumes that the order in which the loads are applied is irrelevant. It does not consider the accumulated damage resulting from previous cycles or the altered S-N curve due to the degradation of component Therefore, the method of calculating the total damage of an item based on Miner's rule does not take into account the deterioration or the sequential effects of cyclic loading.

2.2.2 RUL prediction using the fracture mechanics approach

Fatigue life prediction of a critical component of structural health management systems, particularly when dealing with cracks. In the cases of fatigue crack damage in metallic materials, Paris's Law Paris (1963) is commonly used to estimate the crack growth rate, as demonstrated in Equation (2.3):

$$\frac{da}{dN} = C(\Delta K)^m \tag{2.3}$$

where a represents the characteristic crack length, N denotes the number of fatigue loading cycles, da/dN is the rate of crack growth and m and C are the model parameters of Paris' law that are material-specific constants. Lastly, ΔK refers to the range of SIF. Even though the number of cycles is an integer, it is treated as a real number because the crack grows over a large number of cycles. The values of C and m are typically obtained through experimental methods. By plotting the growth rate against the SIF on a log-log scale, the slope of the line corresponds to m, and the y-intercept at $\Delta K = 1$ corresponds to C. To calculate the range of SIF, one can find the difference between the maximum and minimum SIFs (i.e., $\Delta K = K_{max}$ - K_{min}). Newman's approximation Newman Jr and Raju (1981) can be used to estimate the SIF range as:

$$\Delta K = \Delta S \, Y(a)\sqrt{\pi a} \tag{2.4}$$

The range of applied nominal stress, denoted by ΔS (i.e., stress located far from the crack tip), and the dimensionless geometry function $Y(a)$ (which relies on the geometry around the crack) are involved in the above equation. Equation (2.3) can be utilized to evaluate the fatigue life of a structure (cf. Figure 2.1). The differential Equation (2.3) can be solved to determine the crack length as:

$$a_{k+1} = a_k + C(\Delta K)^m \Delta N \tag{2.5}$$

However, instability arises in situations where the maximum SIF reaches a critical SIF value (K_{IC}) or when the crack size reaches a critical threshold (a_c). Using the SHM system, it is possible to detect the initial crack length a_k. Then Equation (2.5) can be used to predict the crack size a_{k+1} after ΔN cycles, starting from an initial crack size of a_k, assuming that the model parameters C and m are known.

In addition to these primary factors, there are various other variables that can influence fatigue, such as stress concentration, corrosion, temperature, overload, and more. Fatigue cracks typically initiate at the surface, making the condition of the loaded component surface critical to its fatigue life. Surface roughness plays a significant role as it directly affects the level and number of stress concentrations on the surface. Higher stress concentrations increase the likelihood of crack initiation, while smoother surfaces delay nucleation. Notches, scratches, and other stress risers decrease fatigue life. This study focuses on fatigue life predictions considering a limited number of factors, including random loading, stress concentration, and thermomechanical loading caused by temperature.

2.3 Crack modelling with eXtended Finite Element Method (XFEM)

Traditionally, standalone ABAQUS-XFEM modules are employed Baptista et al. (2018) to model crack and its propagation targeting fatigue life estimation for simple as well as complex structures. Unfortunately, the procedure lacks the flexibility to assign Paris law parameters and to control the critical parameters of crack propagation.

Focusing on the computational cost, the majority of the research works dealing with such problems employed a quasi-static approach provided by Dhondt (2014). In this approach, the SIF for the various crack opening modes must be calculated for an initial crack. In the current work, the quasi-static crack growth model is employed for crack propagation. Eventually, with this approach, the crack geometry can be recursively updated, and the process can be repeated for each time step. Shi et al. (2010) suggested that the domain does not need to be re-meshed in each iteration and thereby reducing the computational expense provided the mesh around the crack tip is fine enough to ensure precision in the calculated SIF.

To execute the quasi-static approach, the present study utilizes XFEM in the ABAQUS package to calculate the SIF. The approximation of the primary variable is further enriched with additional mathematical functions for the completeness and accuracy of the solution. The enrichment has been employed with a partition of unity characteristics. Displacement-based approximation with enriched function can be written as,

$$u(\mathbf{x}) = \sum_{i=1}^{n} N_i(\mathbf{x}) \left[u_i + H(\mathbf{x})a_i + \sum_{\alpha=1}^{4} F_\alpha(\mathbf{x}) b_i^\alpha \right] \tag{2.6}$$

where $N_i(\mathbf{x})$ and u_i are the nodal shape functions and nodal displacement vectors, respectively, connected with the continuous part of the finite element solution. a_i represents the nodal enriched degree of freedom (*dof*) and $H(\mathbf{x})$ represents the discontinuous jump function across the crack surfaces. b_i is the nodal-enriched *dof* vector with its associated elastic asymptotic crack-tip functions $F_\alpha(\mathbf{x})$. Here, the $H(\mathbf{x})$ function has a value +1/-1 for above or below the crack surface. This function is defined for those elements that are completely cut by the crack and able to capture strong discontinuity due to the crack surface. The tip enrichment function is defined for those elements which are partially cut by the crack and have a singularity in the stress field. For isotropic media, the crack tip enrichment functions are given in terms of polar coordinates (r,θ) with its origin at the crack tip as,

$$F_\alpha(\mathbf{x}) = \left[\sqrt{r} sin\frac{\theta}{2}, \sqrt{r} cos\frac{\theta}{2}, \sqrt{r} sin\theta sin\frac{\theta}{2}, \sqrt{r} sin\theta cos\frac{\theta}{2} \right] \tag{2.7}$$

The crack model is simulated to obtain SIF parameters which are subsequently used to model quasi-static fatigue crack growth. In general, crack growth direction (θ) is obtained by Maximum Tangential Stress (MTS) criterion which assumes that the crack may grow in a direction perpendicular to the maximum principal stress. Therefore, for each small crack increment, θ corresponding to the applied load can be obtained following MTS criteria given by Erdogan and Sih (1963). Consequently, the associated crack driving force (i.e., ΔK_{eq}) can also be calculated as,

$$\begin{aligned} \theta &= 2tan^{-1}\left[\frac{1}{4} \left(\frac{\Delta K_I}{\Delta K_{II}} \pm \sqrt{\left(\frac{\Delta K_I}{\Delta K_{II}} \right)^2 + 8} \right) \right] \\ \Delta K_{eq} &= \Delta K_I cos^3\frac{\theta}{2} - 3\Delta K_{II} sin\frac{\theta}{2} cos^2\frac{\theta}{2} \\ \Delta K_I &= [K_I]_{max} - [K_I]_{min} \\ \Delta K_{II} &= [K_{II}]_{max} - [K_{II}]_{min} \end{aligned} \tag{2.8}$$

with $[K_I]_{max}$ and $[K_{II}]_{max}$ are the SIFs in mode I and II with respect to maximum applied load under cyclic fatigue loading conditions. In the same way, $[K_I]_{min}$ and $[K_{II}]_{min}$ are the SIFs in mode I and II with respect to the minimum applied load. With this direction and driving force, the ABAQUS model is updated with this redefined crack font, and iterations are continued till the critical conditions, yielding a series of SIFs corresponding to various crack sizes.

ABAQUS software includes the capability to calculate the J-integral, which is a parameter used to determine the strain energy release rate or the work per unit fracture surface area in a material. The concept of J-integral was independently developed by Cheperanov (1967); Rice (1968). It represents an energetic contour path integral (denoted as J) that remains constant around a crack. The J-integral is widely accepted in fracture mechanics and provides insights into the energy release associated with crack growth. It serves as a measure of deformation intensity at a notch or crack tip, particularly for nonlinear materials, and can be correlated with SIF in linear materials. The relationship between the J-integral and ΔK_{eq} is expressed as follows:

$$J = \begin{cases} \frac{\Delta K_{eq}^2}{E} \quad (Plane \quad stress) \\ \frac{\Delta K_{eq}^2}{E}(1-\nu^2) \quad (Plane \quad strain) \end{cases} \tag{2.9}$$

where E represents the elastic modulus and ν denotes the Poisson's ratio of the material. Accurate numerical evaluation of J-integral holds great significance for practical applications of fracture mechanics in design calculations. ABAQUS/Standard includes a procedure for evaluating the J using the virtual crack extension/domain integral methods introduced by Parks (1977) and further developed by Shih et al. (1986).

2.4 Automated calculation of SIF

Automated calculation of SIF

Complex geometries often encountered in civil structures present a challenge because while SIFs for simpler geometries are available in the literature, the same is not true for complex geometries. Calculating SIFs for various crack sizes necessitates modeling the structure multiple times, adjusting the crack growth direction and size each time, which is a time-consuming process.

To simplify and expedite this process, an automated method for calculating SIFs (for different crack sizes) is employed, utilizing a combination of ABAQUS, Python, and MATLAB in this study.

This algorithm begins by creating an initial model with structural and crack details in ABAQUS and then translating this information into a Python script. Subsequently, this Python script is employed to update the model and generate a new Python script based on the modified crack length values. The initial model undergoes analysis, and the SIF calculations using K_I and K_{II} (referred to as ABAQUS-K) and those using J (referred to as ABAQUS-J) are transferred to MATLAB. The crack growth direction θ and the new crack length are computed using MATLAB and a new Python script is created (see Figure 2.2).

To automate this process, the initial Python script is used as a function file in MATLAB. It is updated based on the initial data, generating new Python scripts recursively. This enables the simulation of SIFs within the ABAQUS environment under specified conditions. This newly generated Python script is then utilized to run the ABAQUS model, calculating another new crack growth direction, determining another new crack length, and generating yet another new Python script.

This iterative process continues until the crack length reaches a critical value. By integrating ABAQUS, Python, and MATLAB, this approach automates the iterative modeling and analysis, streamlining the efficient computation of SIFs and facilitating crack growth simulations.

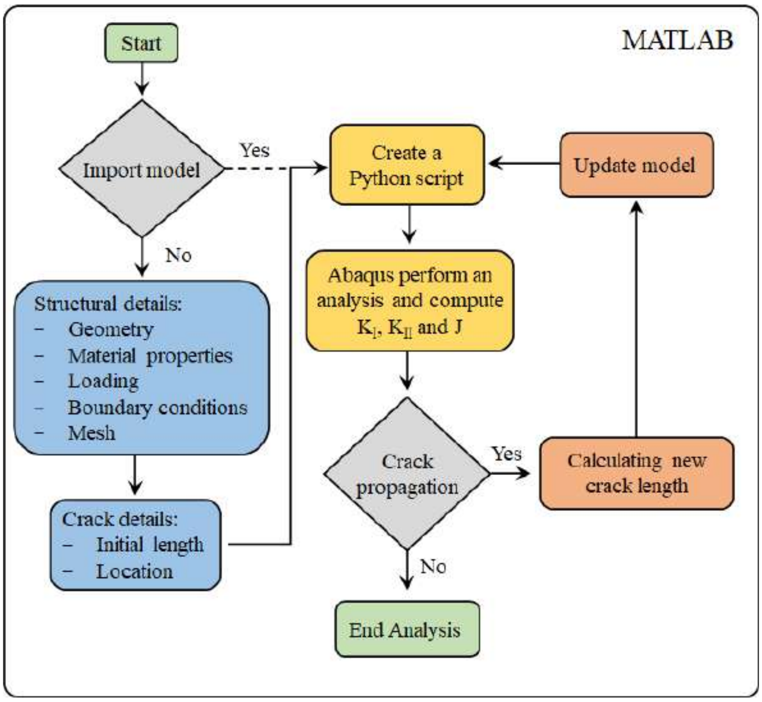

Figure 2.2: Flowchart of the algorithm to calculate SIF.

2.5 Numerical validation of the proposed SIF calculation

This study heavily relies on numerically simulated SIFs for simulating crack growth under different crack geometries and operational conditions. Eventually, it is essential to validate these SIF measures against corresponding benchmarks to ensure their reliability. To accomplish this, separate models of a finite homogeneous plate with edge and centre cracks are created. In the edge crack model, a square plate with a width (b) and height ($2h$) of 50 mm each is modelled, with a uniform thickness of 9 mm. A crack of length (a) 5 mm is positioned at the left edge of the plate. The elastic modulus is assumed to be $71,700$ MPa, and the Poisson's ratio is 0.33. The bottom edge of the plate is constrained only in the y-direction, and a tensile load of 36 kN is applied at the opposite edge.

Similarly, for the centre crack problem, a square plate with equal width ($2b$) and height ($2h$) of 50 mm is considered, with a centrally located crack of width ($2a$) of 5 mm. The other material properties remain the same as in the edge crack problem. A schematic diagram illustrating the boundary conditions is presented in Figure 2.3. SIFs are obtained using automated calculation of SIF technique 2.4 for crack sizes ranging from 5 mm to 40 mm, with a 2 mm increment.

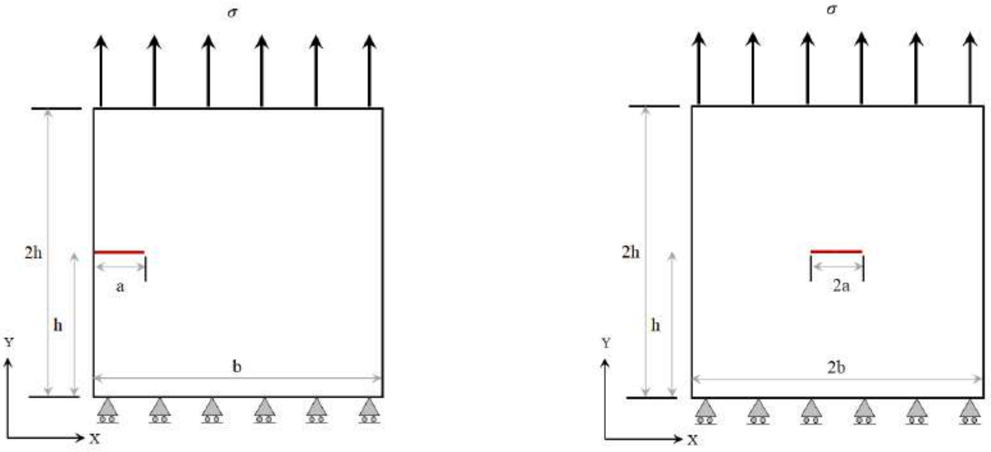

(a) Edge crack (b) centre crack

Figure 2.3: Crack domain for standard specimen under mechanical loading.

2.5.1 Mesh convergence study

To validate the accuracy of the proposed algorithm, mesh convergence studies were conducted to assess the finite element solutions. The simulation uses an 8-node linear brick element (C3D8R). An initial discrete finite element mesh size of 20 is being considered in relation to the width of the center crack specimen. Moreover, it was extended up to the point where the solution converges to an acceptable error level with a stable value, as shown in Figure 2.4. The optimal discrete finite element mesh size is 100 with the total number of elements and nodes as $1,80,000$ and $3,94,022$ respectively. In subsequent simulations, the same mesh size is used to calculate the SIFs.

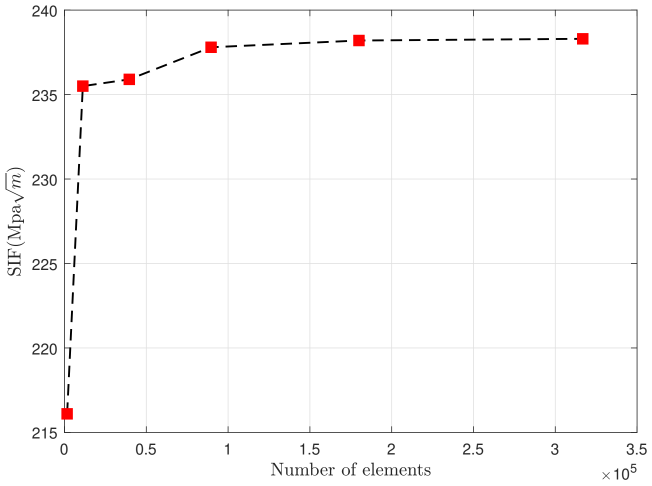

Figure 2.4: Mesh convergence test for centre crack under mechanical loading

2.5.2 Mechanical loading

The proposed algorithm is applied to calculate the SIFs for both edge and centre cracks under mechanical loading conditions. Considering the potential occurrence of mode-I failure, the numerically obtained SIFs are compared to the benchmark values provided by Tada et al. (2000). Figure 2.5 presents the comparison results for both edge and centre cracks. It is evident from the results that the simulated mode I SIFs (K_I in $MPa\sqrt{m}$) exhibit a strong agreement with the analytical values.

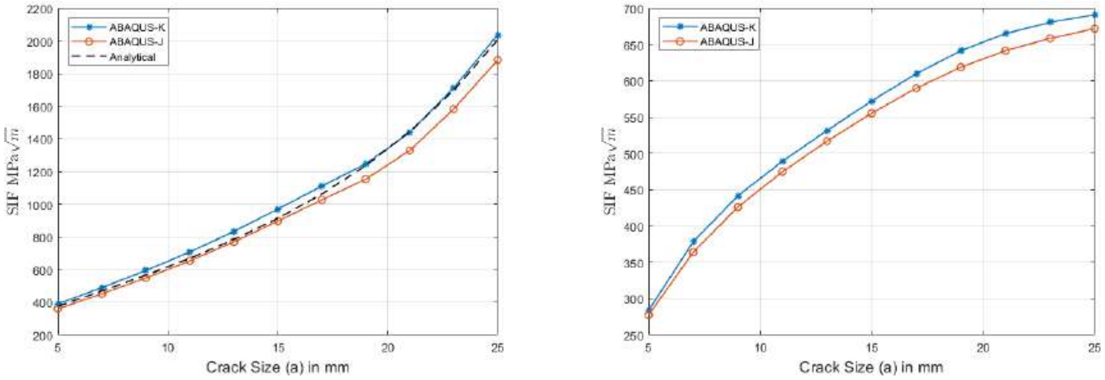

(a) Edge crack

(b) centre crack

Figure 2.5: SIF calculation for standard specimen under mechanical loading.

Furthermore, a comparative analysis is conducted between the SIF calculations using two methods: ABAQUS-K and ABAQUS-J. The comparison reveals that ABAQUS-K yields significantly closer results to the analytical values for both the edge and centre crack scenarios.

The same approach is further applied to a complex specimen with similar material properties subjected to mechanical loading, as illustrated in Figure 2.6. Since an analytical formulation is not available for this complex specimen, a comparison is only conducted between the ABAQUS-K and ABAQUS-J methods, revealing minor differences in their patterns Figure 2.7. Consequently, the proposed algorithm facilitates the automated calculation of SIFs for both standard and complex specimens.

2.5.3 Thermo-mechanical loading

The efficacy of the algorithm is validated for thermo-mechanical loading conditions. Using Section 2.4, SIFs specific to this loading type have been computed

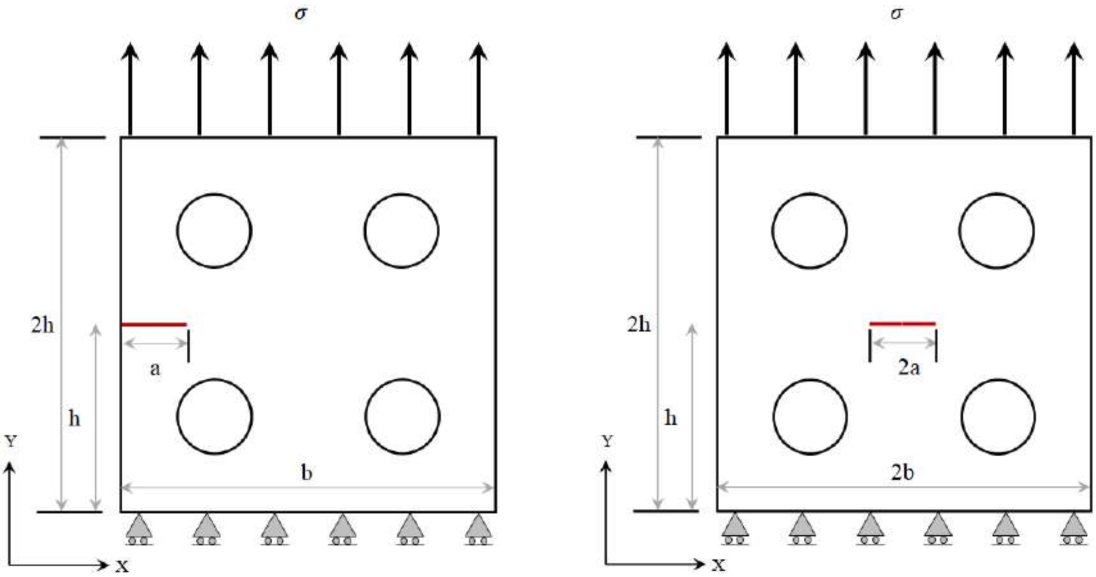

(a) Edge crack with holes. (b) centre crack with holes.

Figure 2.6: Crack domain for complex specimen under mechanical loading.

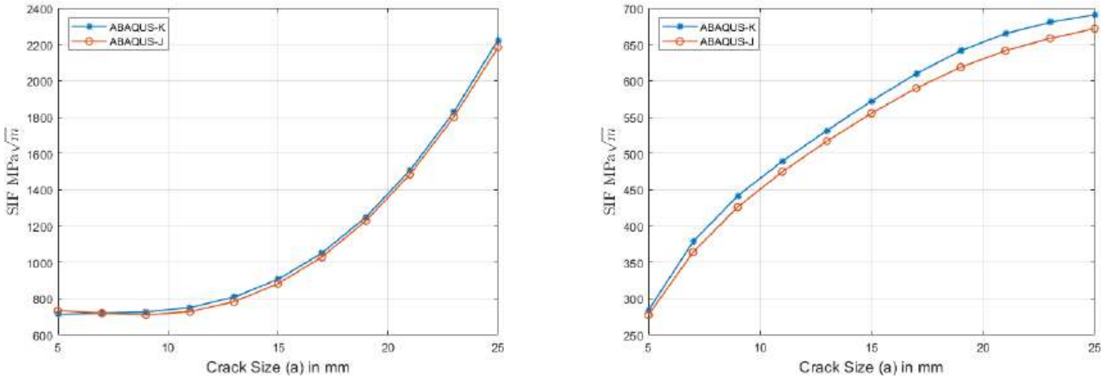

(a) Edge crack with holes. (b) centre crack with holes.

Figure 2.7: SIF calculation for complex specimen under mechanical loading.

as before. In this process, thermo-mechanical loading is created by superimposing the mechanical and thermal loading as presented in Figure 2.8. A similar finite plate, as in the earlier experiment, is considered with a similar boundary and loading condition with the initial crack length of 5 mm. The material properties are assumed to vary with temperature and the respective functional relationship is defined following the references Reddy and Chin (1998); Zhu et al. (2019).

Considering typical Indian tropical climatic conditions, the ambient temperature has been realistically assumed to lie in between 25 $°C$ to 50 $°C$. The initial temperature of the specimen is fixed at $T_1 = 50\ °C$, which is then reduced to $T_2 = 25\ °C$, resulting in a temperature difference of $\Delta T = T_2 - T_1$. This

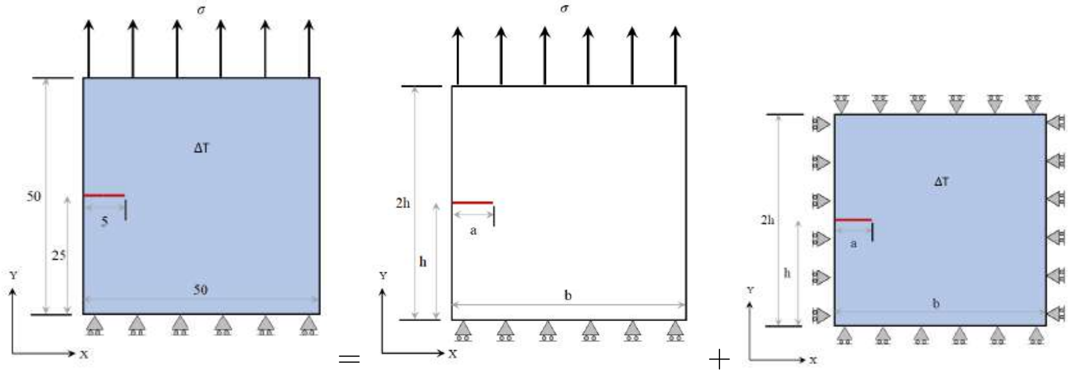

(a) Thermo-mechanical (b) Mechanical (c) Thermal

Figure 2.8: Superposition of SIF with mechanical and thermal loading to determine the thermo-mechanical loading.

temperature reduction induces tensile stress within the plate.

A similar process was performed to calculate SIFs under thermo-mechanical loading conditions, and the corresponding results are depicted in Figure 2.9. The results appeared to be similar to the earlier experiment demonstrating the fact that the proposed algorithm is equally efficient for both loading scenarios.

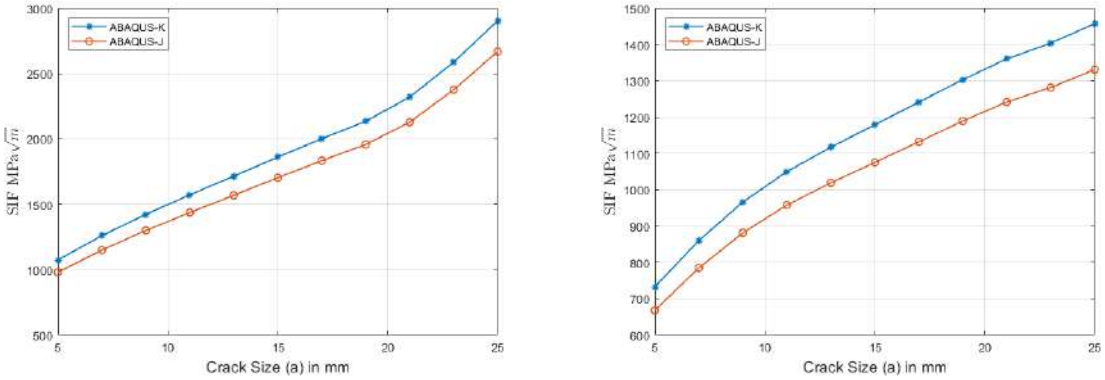

(a) Edge crack (b) centre crack

Figure 2.9: SIF calculation under thermo-mechanical loading.

2.6 Summary

Standard fatigue analysis methods have evolved over time to meet the requirements of designers and engineers, aiming for simplicity, affordability, and accuracy. Fatigue analysis in bridge structures commonly employs S-N, ϵ-N, and fracture mechanics approaches. Field measurement data obtained through sensors and non-destructive testing techniques play a crucial role in accurately assessing load and resistance factors for fatigue analysis. NDE and SHM techniques contribute to improved fatigue assessment and condition evaluation of bridges, providing valuable insights into structural behaviour and facilitating maintenance, repair, and replacement decisions. These methods collectively enhance the understanding and management of fatigue-related issues in bridges.

This chapter focuses on fatigue analysis methodologies using SHM techniques to evaluate the fatigue life and RUL of structures. Two approaches are discussed: RUL prediction using the S-N approach and RUL prediction using the fracture mechanics approach. In the S-N approach, the fatigue life of structural elements is assessed based on fatigue damage using stress history data obtained from SHM techniques. Rain flow analysis simplifies the complex stress history data, and a fatigue damage spectrum is constructed based on the analysis results. The cumulative damage approach consolidates individual contributions to estimate the fatigue life.

In the fracture mechanics approach, Paris's Law is used to estimate the crack growth rate based on the SIFs. The SHM system predicts the crack size and growth direction, considering known model parameters. Factors influencing fatigue life, such as loading patterns, stress levels, and material properties, are also discussed. Cumulative damage assessment and fatigue life prediction methods, such as the CDM and Miner's rule are presented. The chapter further explores crack modelling using the XFEM in ABAQUS and the automated calculation of SIFs using a combination of ABAQUS, Python, and MATLAB. The proposed algorithm allows for the iterative prediction of crack growth and fatigue life.

The framework is validated by comparing the numerical solutions with analytical results. Numerically simulated SIFs, validated against benchmark values, are used for estimating fatigue life. ABAQUS-XFEM is employed to obtain SIFs for edge and centre crack models with varying crack sizes. The calculated SIFs align well with analytical values. The algorithm is also applied to a complex specimen, demonstrating minor differences in SIFs obtained using ABAQUS-K and ABAQUS-J methods. The proposed framework enables the automatic calculation of SIFs for both standard and complex specimens, facilitating fatigue life determination under similar loading conditions. The algorithm's effectiveness is further confirmed for thermo-mechanical loading conditions, yielding similar results. Overall, the study showcases the reliability and efficiency of the proposed algorithm in calculating SIFs under various scenarios.

Chapter 3

Fatigue life prediction under constraints of limited data availability

This study first attempts to deal with structures in which fatigue crack is visible, measurable, and propagating under cyclic operational loading in order to predict its life. This chapter further addresses the challenges and limitations in fatigue damage estimation for civil infrastructures under the scarcity of data. To overcome these challenges, a novel SHM-based fatigue estimation approach is proposed for structural systems that are under monitoring yet sufficient data is not available to approach traditional RUL estimation methods. The proposed algorithm employs a Bayesian filtering framework to assess fatigue parameters in real-time, improving estimates as more data becomes available. The effectiveness of the proposed approach is evaluated through a series of experiments, including numerical and real-time laboratory experiments. The worst-case scenario possible for a real structure, identified from these experiments, is then imposed on a numerical bridge joint in order to validate the capability of the proposal in dealing with real-life problems.

3.1 Introduction

Simulating the propagation of fatigue cracks in structures is commonly approached using a well-established parameterized fatigue model, i.e. Paris model for which the model parameters depend on the material properties. Yet, for large civil infrastructures, neither it is pragmatic to expect the material to be of consistent quality all over the structure, nor component-wise material property estimation can be considered a practical breakthrough. Different production batches will inherently induce variation in the material properties. Fatigue and its consequence, on the other hand, is sensitive to the presence of small and unavoidable micro-structural irregularities caused during manufacturing Wang et al. (2016). In addition, the incoming service load is also not certain and constant throughout the service life of the structure which may induce randomness in the crack propagation process. These aspects eventually render the problem of material property or model parameter estimation complex. However, it can be holistically dealt with using a probabilistic approach to address uncertainty quantification.

In this context, this study concentrates on predicting fatigue life for steel bridges with welded joints. Under usual service loading, a critical part of a structural configuration such as joints, are typically subjected to cyclic stresses which might drive them to undergo fatigue failure Łagoda and Głowacka (2020) and therefore should ideally be monitored for their fatigue life Marques et al. (2018). Typically welded joints have complex geometries, sometimes with existing fatigue cracks. For damage prognosis of such structural components, the ambient variability in temperature induces a combined thermo-mechanical loading that may at times accelerate the fatigue process. Also, the associated uncertainties of unknown origin and magnitude inherent in the predictor model, material properties, and loading render the entire problem to be probabilistic. Moreover, the complex geometry, typical for civil engineering structures, makes the problem of predicting its remaining service life, a challenging task that has to be addressed in a systematic manner.

3.2 Challenges and limitations in fatigue life estimation for civil infrastructures

Several studies investigated probabilistic approaches for fatigue life prediction for various types of structures: offshore platforms Karamchandani et al. (1992) and aircraft Cavallini and Lazzeri (2007) are to name few. There exist several detection techniques for cracks and/or damages in the literature Li et al. (2015); Nanthakumar et al. (2016); Feng and Feng (2018) approaching the problem using nondestructive techniques, vibration-based approaches Sen et al. (2021); Aswal et al. (2021a), computer vision, machine learning Sharma and Sen (2021), etc. In this process, predicting the RUL (or fatigue life) has become one of the prime concerns Sun et al. (2014) taking the objective beyond crack detection. With fatigue life estimation-based approaches, the damage evaluation has typically been defined with Paris' law, and the associated parameters are estimated offline from the measured SHM data Kwon et al. (2012); Mohammadi et al. (1998).

In light of the uncertainties associated with fatigue estimation in civil infrastructures, it is more practical to employ probabilistic estimation approaches that enable real-time estimation while accounting for uncertainties related to parameters, models, and forces. By incorporating probabilistic methods, the proposed approach acknowledges the inherent variability and lack of complete information in the estimation process, allowing for more robust and reliable predictions of fatigue damage. This approach considers the uncertainties as a crucial aspect and provides a pragmatic solution to address them effectively during online real-time estimation.

3.2.1 Bayesian filtering-based approaches for RUL estimation

The relative robustness of sample-based filtering approaches like PF or EnKF for nonlinear system estimation has been explored extensively in the literature Lin et al. (2018); Chen et al. (2016); Compare and Zio (2014); Branco et al. (2009). Yet, their computational demand is most often perceived to be impractical for problems where either an economical or prompt solution is needed. For parameter estimation problems, EKF jointly estimates the parameters in parallel to the system states with a joint estimation approach termed the Joint-EKF or JEKF approach. Despite the extensive application for parameter estimators, concerns have been raised against JEKF since it lacks ergodicity and the analytical format Chen et al. (2003). Moreover, JEKF estimation has been reported to diverge with a larger state dimension Ljung (1979). Even after such shortcomings, JEKF has the potential for being the computationally cheapest nonlinear estimator for moderate-size and moderately nonlinear systems. Furthermore, UKF, even after being theoretically superior to EKF, is reported to not be capable of yielding good estimates for crack and parameters in practice Wang et al. (2016).

Eventually, EKF has been seen in numerous applications recently for fatigue prognosis problems. Singleton et al. (2014) employed EKF for bearing damage prognosis and RUL estimation. Material degradation-sensitive features are extracted from the vibration signals which are then fitted in order to avoid employing the full-scale degradation model. EKF has also been applied to estimate the prognostics of proton exchange membrane fuel cells in Bressel et al. (2016). In this attempt, with each new state of health estimation, the RUL is updated and further extrapolated to its threshold. A similar fatigue crack growth prognosis problem is solved using EKF in order to develop a straightforward method that is easy to implement while being computationally cheaper Wang et al. (2017); Robinson et al. (2018). Xu and Chen (2017) estimated the probability mass function of the RUL of lithium-ion batteries by extrapolating samples from the state-parameter distribution based on the EKF.

3.2.2 Challenges with limited data availability

A thorough examination of the existing literature reveals that the majority of approaches for estimating fatigue life in civil infrastructures are characterized as offline methods Kwon et al. (2012); Adasooriya and Siriwardane (2014); Mohammadi et al. (1998). Offline methods require the availability of complete measured data to determine the RUL of the structure or component. On the contrary, an online algorithm allows this flexibility to use data only when it is available. Further, with Bayesian filtering-based approaches, prior information (or belief) on the fatigue model parameters and their evolution can be used in the absence of measured data. Of course, the estimation accuracy should ideally be better post-drawing inference from measured data. Yet for such estimation problems, filtering approaches are preferred since they allow fusing prior beliefs with information embedded in measurement while dealing with real-life uncertainties. Finally, it can also be verified that most filtering-based RUL estimation approaches available in the literature deal with systems operated under a controlled environment, made of reliable materials, and subjected to sufficiently known stress cycles. Unfortunately, the same can never be expected for civil infrastructural systems and one needs to take required measures in order to employ such filtering approaches for RUL estimation for civil engineering structures.

3.2.3 Limitations of the Paris model

This chapter proposes an online model-based approach to predict (/estimate) the fatigue life from the available SHM data by employing EKF. Initially, a Paris law model is used to develop a numerical representation of the fatigue crack propagation through the associated model parameters, and the crack propagation is studied by considering the various uncertainties that dwell in reality. Nevertheless, not conforming to the idealization made with Paris law about the stress being tensile only, the typical bridge structures experience both tensile and compressive stress in their members and joints. However, the crack propagates only when the stress is tensile while under compressive stress, a crack closure effect generally takes place reversing the crack growth. In order to achieve an accurate estimate of the fatigue life of a bridge or its components, both effects need to be considered in the predictor model. The proposed method is therefore modified with updated Paris law that takes the crack closer effect into consideration.

An extensive numerical study is conducted on finite plates with different damage scenarios like centre cracks and edge cracks under mechanical and thermo-mechanical loading conditions. Estimation of updated Paris model parameters and fatigue crack prognosis with the proposed approach has been demonstrated on this test set. Further, an extensive numerical study is performed on a welded joint of a bridge based on the assumption of the worst operational scenario. A laboratory experiment is finally conducted on CT specimens to validate the proposed method.

3.3 The proposed approach to predict fatigue life

The proposed method comprises two steps: first, estimating the Paris model parameters based on the past crack growth history, and second, performing crack prognosis using the estimated model parameters. In this study, a Bayesian filtering-based prediction-correction approach is employed to estimate crack propagation and the associated model parameters in a joint state-parameter estimation framework using available SHM data. The selection of the appropriate SHM data type is crucial depending on the specific scenario. For structures with visible cracks, the estimation of RUL primarily relies on the prognosis of crack length based on the available crack growth history. This type of problem necessitates a deeper understanding of crack geometry, evolution, and fatigue crack propagation, rendering it more complex and requiring the use of computationally intensive numerical models.

In order to replicate the physical system and its fatigue crack propagation, a parameterized model is required. The selection of the model parameters depends on the specific objective of the study. In this particular approach, the objective is to perform damage prognosis using an updated Paris model incorporated into a state space predictor model. The parameters of the Paris model, namely c and m, are considered estimable parameters. The associated parametric uncertainty is assumed to be epistemic in nature, indicating that it is deterministic and time-invariant, but lacks sufficient knowledge. As more information is collected from the SHM data, specifically the crack growth history, the uncertainty is expected to be reduced. Therefore, the proposed approach aims to update and refine the estimations of the model parameters based on the available SHM data, gradually reducing the epistemic uncertainty associated with them.

In this joint estimation approach, the parameters and crack length are treated as the unobservable state (or state-parameter) vector that evolves over time according to a state (or process) equation or model. The predictor model is used to propagate the estimates of the crack length (a) in time, conditioned on the current estimate of the system parameters. A measurement equation (or mapping) is employed to observe these unobservable states through measurements. It is important to note that the actual value of the crack length cannot be directly observed and can only be measured with some measurement noise introduced by the sensors. The measurement model captures this mapping of the system states to the available measurements within a probabilistic framework, considering the measurement uncertainty. The subsequent correction step then refines the estimate by simultaneously correcting the parameters using the available data. The following section provides a detailed explanation of the crack propagation model used in the process equation, followed by the measurement model employed in this study.

3.3.1 Fatigue crack growth model

Traditionally, the fatigue crack growth follows a degradation model based on the Paris-Erdogan rule Paris (1963), as shown in Equation (2.1). However, this traditional Paris law is not applicable in cases where the stress intensity alternates between compression and tension, resulting in the occurrence of the crack closure effect. To address such scenarios, researchers have proposed alternative rules that account for the shortcomings of Paris Law by considering the effects of crack closure and stress ratio (R). These approaches modify the influence of the SIF, considering only the tensile part of the stress cycle. This yields a relationship that defines the fatigue crack growth rate (i.e., $\frac{da}{dN}$) as a function of the effective SIF range (ΔK_{eff}) and R. Based on experimental data on fatigue crack propagation, Kujawski and Ellyin (1987) proposed an approach to calculate ΔK_{eff} using the following expressions Ellyin (2012):

$$\begin{aligned} \Delta K^0_{eff}|_{R=0} &= \Delta K_{eq}\left[1-\frac{1}{2}\left(\frac{\Delta K_{th}}{\Delta K_{eq}}\right)^2\right] > \Delta K_{eq}-\Delta K_{th} \\ \Delta K_{eff}|_{R\neq 0} &= \frac{\Delta K^0_{eff}}{\left[1-\left(\frac{(1+R_\sigma)S_{max}}{2\sigma'_f}\right)\right]} \end{aligned} \tag{3.1}$$

where ΔK_{th} is the threshold SIF range, S_{max} is the maximum stress, and σ'_f is the fatigue strength coefficient. The calculation of ΔK_{eq} is performed using an automated calculation of SIFs, as described in Section 2.4. The numerically obtained data is then subjected to curve-fitting in order to establish a correlation between ΔK_{eq} and a using a polynomial equation. R_σ is the modified stress ratio at the crack tip region and is calculated by the following equation:

$$\begin{aligned} \overline{R}_\sigma &= 1-2\left[\frac{(1-R)^2}{4}\right]^{\frac{n'}{1+n'}} \\ R_\sigma &= \overline{R}_\sigma + \frac{log(\delta^*)-log(r_c)}{log(r_m)-log(r_c)} \end{aligned} \tag{3.2}$$

where $n^{'}$ is the cyclic exponent, δ^* is the material length parameter, r_c is the cyclic plastic zone and r_m is the monotonic plastic zone under the fatigue loading condition. Ellyin (2012) discussed that R_σ sharply decreases as the distance from the crack tip increases from the regions r_c to r_m.

Figure 3.1 reveals that the fatigue crack growth rule is applicable for a specific crack propagation region that is between the near-threshold crack propagation

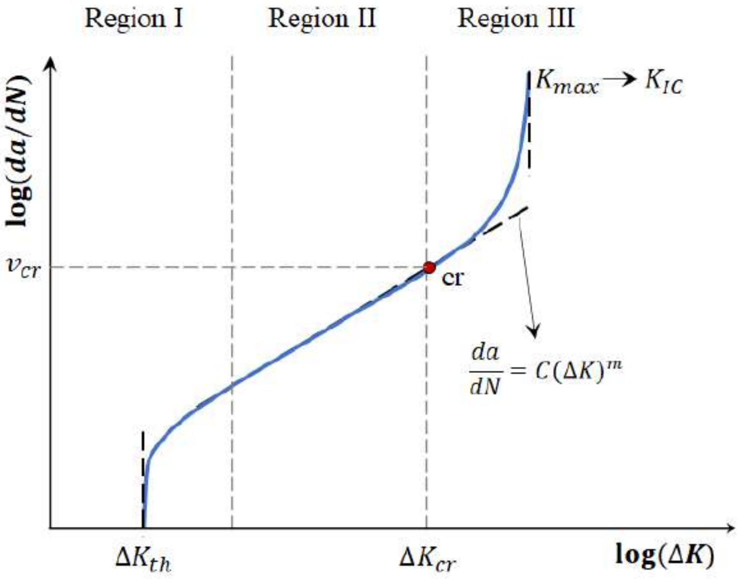

Figure 3.1: Typical fatigue crack growth curve.

region I and the near-unstable crack propagation region III.

$$\left(\frac{da}{dN}\right)_{cr} = C(\Delta K_{cr})^m = v_{cr} \tag{3.3}$$

Further, $\frac{da}{dN}$ can be established as a function of not only ΔK_{eq} but also of the condition of crack growth instability for the cases when maximum SIF (K_{max}) is approaching its critical value (K_{IC}) Forman et al. (1967) causing the crack propagation rate to be infinity. Eventually, the fast deviation from the linear part of Region II can be attributed to the sudden rise in the crack propagation rate. At the transition point between Region II and Region III, designated as cr in Figure 3.1, the following holds true, with $\Delta K_{cr} = \Delta K_{IC}$. Reasonably, ΔK_{cr} can be assumed to take the maximum value as K_{IC} due to the fact that fast fluctuation in $\frac{da}{dN}$ occurs on triggering crack instability, yielding the following rule,

$$\Delta K_{cr} = (1 - R)K_{IC} \tag{3.4}$$

As a result, incorporating Equation (3.4) into Equation (3.3), an approximate relationship in logarithmic form between the Paris constants can be established, assuming that the rise of the Paris instability corresponds to the Griffith-Irwin instability Carpinteri and Paggi (2007):

$$\log C = log(v_{CR}) + mlog\left[\frac{1}{(1 - R)K_{IC}}\right] \tag{3.5}$$

It should be noted here that the functional relationship between C and m involves additional parameters like R, v_{CR}, and K_{IC} which can either be estimated from the field test or can be safely assumed to be constant for each group of materials Radhakrishnan (1980).

3.3.2 System description

It has been already discussed that C and m, being assumed with epistemic uncertainty, must be estimated probabilistically using available measured SHM data (i.e., crack size variation over stress cycles). With a predictor-corrector environment for such estimation, there is an imperative requirement for a sufficiently accurate predictor model (as in Equation (3.1)). In this process, the associated model parameters like ΔK_{th}, R, σ'_f can be considered to be reliably estimated through field investigation or combined numerical-experimental analysis. Of course, ΔK_{eff} is a deduced variable depending on a as the unknown variable (i.e., $\Delta K_{eff} = \phi(a)$). The associated details are presented in the following.

Finally, the analytical formulation for crack propagation can be discretized in time. The uncertainty due to possible modeling inaccuracy can be represented with an SWGN process model $\mathcal{N}(0; Q^a)$. This leads to a state-space system model with a_k being one of the state variables as,

$$\begin{aligned} a_{k+1} &= a_k + C(\Delta K_{eff})^m \Delta N + \mathbf{v}_k^a \\ &= f(a_k, m_k, C_k) + \mathbf{v}_k^a \end{aligned} \tag{3.6}$$

$\mathbf{v}_k^a$ is a realization of the assumed SWGN model and $f(\bullet)$ provides the functional representation of the crack size propagation model between two consecutive steps. Clearly, the process equation boils down to three variables of interest, i.e. a (already assumed as a time-varying state) with C and m, which can be considered as parameters.

3.3.3 Joint state-parameter estimation

Joint estimation of states and parameters is a well-researched topic in the fields of stochastic inverse estimation problems. The same approach is employed in this chapter to probabilistically estimate the material parameter states C and

m while filtering out noises from the measured crack size to facilitate better estimation of response state a. Eventually, the parameter states are required to be appended in the state vector in order to jointly estimate the augmented state $\mathbf{X}_k$ using the available measurements. The propagation model for such unobservable states however needs them to be of similar scales which is not possible with the material parameter C in the state vector. The assumed state vector has therefore been defined with Θ as a negative logarithmic mapping of C as:

$$\mathbf{X}_k = [a_k \quad m_k \quad \Theta_k]^T \tag{3.7}$$

This ensures that the estimable parameter Θ_k is of comparable scales of a and m. The process equation specific to this problem can therefore be defined as:

$$\mathbf{X}_{k+1} = \left\{ \begin{array}{c} f_1(\mathbf{X}_k) \\ \\ m_k \\ \\ f_2(\mathbf{X}_k) \end{array} \right\} + \left\{ \begin{array}{c} \mathbf{v}_k^a \\ \\ \mathbf{v}_k^m \\ \\ \mathbf{v}_k^\Theta \end{array} \right\} = \mathcal{F}(\mathbf{X}_k) + \mathbf{v}_k \tag{3.8}$$

where $f_1(\mathbf{X}_k)$ and $f_2(\mathbf{X}_k)$ can be elaborated as: $f_1(\mathbf{X}_k) = a_k + C_k(\Delta K_{eff})^{m_k}\Delta N$ and $f_2(\mathbf{X_k}) = log(v_{cr}) + m_k log\left[\frac{1}{(1-R)K_{IC}}\right]$. The associated process noise (i.e. $[\mathbf{v}_k^a \ \mathbf{v}_k^m \ \mathbf{v}_k^\Theta]^T$) can be modeled as a realization from an SWGN process model of covariance $\mathbf{Q}_k = diag(Q_k^a, Q_k^m, Q_k^\Theta)$ where in $Q_k^a, Q_k^m, and Q_k^\Theta$ are the variances of the assumed SWGN noise associated to the states and parameters a, m and Θ respectively and operator $diag(\bullet)$ returns a diagonalized block matrix of its arguments.

It has been discussed in this chapter previously, that the true values of the crack size a_k can never be measured. The available data on the measured crack size is therefore only a mapping of true a_k perturbed by the associated measurement uncertainty due to the rough measuring environment and sensor limitations. The model predicted crack size a_{k+1} as given in Equation (3.8), is therefore mapped to measured crack size z_{k+1}. With a_{k+1} being functions of the other two state variables Θ_{k+1} and m_{k+1}, the measurement model can therefore be defined as:

$$z_{k+1} = \mathcal{H}(a_{k+1}, m_{k+1}, \Theta_{k+1}) + \mathbf{w}_{k+1} \tag{3.9}$$

Here $\mathbf{w}_{k+1}$ denotes the measurement noise realized from an SWGN measurement uncertainty model $\mathcal{N}(0; \mathbf{R}_{k+1})$, with $\mathbf{R}_{k+1}$ being the time-invariant measurement noise covariance.

3.3.4 JEKF-based joint estimation of states and parameters

It is evident from the system Equations 3.8 and 3.9 that the state evolution as well as the measurement mapping, are nonlinear, which calls for nonlinear filter variants to be employed for estimation. EKF is one of the efficient approaches for nonlinear system estimation that extends the applicability of KF for nonlinear systems (and hence the name Extended-KF) is therefore employed in this attempt. With the mentioned process and measurement equation, EKF is employed in this study for the estimation of the state a and the model parameters m_k and Θ_k. In order to estimate a nonlinear system, EKF linearizes the system locally by employing Taylor's first-order expansion. Subsequently, a KF-based estimation approach can be employed, as elaborated in the following. The notation $\mathbf{X}_{i|j}$ for estimated state variable $\mathbf{X}$ represents its estimate at time instant i, provided inference from observation up to and including the time instant j is embedded in the estimate. In the following, the initialization, prediction, and update phases with EKF are detailed.

To start with the estimation, a reasonable assumption must be made on the initial state estimate $\mathbf{X}_{0|0}$ along with the state error covariance ($\mathbf{P}_{0|0}$), denoting the amount of certainty in the initial state estimate. It is normal to presume a high value for the $\mathbf{P}_{0|0}$ in the absence of any prior knowledge of the initial state values. Besides, the time-invariant process and measurement noises, i.e., $\mathbf{Q}_k$ and $\mathbf{R}_{k+1}$ are to be assumed as well. While the selection of $\mathbf{R}_{k+1}$ is quite straightforward and can be established by directly measuring the statistics of inherent sensor noise, $\mathbf{Q}$ needs to be assumed based on the desired estimation accuracy and promptness. Ideally, the components of $\mathbf{Q}_k$ allow perturbation to their mean estimates and therefore should be chosen wisely.

For each time iteration, the prior mean estimate for the state, i.e, $\mathbf{X}_{k|k}$ is propagated in time through the process equation detailed in Equation (3.8), as,

$$\mathbf{X}_{k+1|k} = \mathcal{F}(\mathbf{X}_{k|k}) \tag{3.10}$$

Accordingly, the predicted state error covariance matrix can be estimated as:

$$\mathbf{P}_{k+1|k} = \mathbf{\Phi}_k \mathbf{P}_{k|k} \mathbf{\Phi}_k^T + \mathbf{Q}_k \tag{3.11}$$

Φ_k denotes the Jacobian matrix of the augmented system equation around the current state estimate $\mathbf{X}_{k|k}$, elaborated as:

$$\mathbf{\Phi}_k = \left[\frac{\partial \mathcal{F}}{\partial \mathbf{X}}\right]_{\mathbf{X}=\mathbf{X}_{k|k}} = \left.\begin{bmatrix} \frac{\partial f_1(a)}{\partial a} & \frac{\partial f_1(a)}{\partial m} & \frac{\partial f_1(a)}{\partial \Theta} \\ 0 & 1 & 0 \\ 0 & \frac{\partial f_2(a)}{\partial m} & \frac{\partial f_2(a)}{\partial \Theta} \end{bmatrix}\right|_{a=a_{k|k},\ m=m_{k|k},\ \Theta=\Theta_{k|k}} \tag{3.12}$$

With the propagated statistics, the Kalman gain $\mathbf{K}_{k+1}$ can then be calculated from the associated innovation covariance $\mathbf{S}_{k+1}$ matrix as,

$$\begin{aligned} \mathbf{S}_{k+1} &= \mathbf{H}_{k+1}\mathbf{P}_{k+1|k}\mathbf{H}_{k+1}^T + \mathbf{R}_{k+1} \\ \mathbf{K}_{k+1} &= \mathbf{P}_{k+1|k}\mathbf{H}_{k+1}^T\mathbf{S}_{k+1}^{-1} \end{aligned} \tag{3.13}$$

with $\mathbf{H}_{k+1}$ being the Jacobian of the measurement equation (cf. Equation (3.9)) around the propagated state estimate $\mathbf{X}_{k+1|k}$ as:

$$\mathbf{H}_{k+1} = \left[\frac{\partial \mathcal{H}}{\partial \mathbf{X}}\right]_{\mathbf{X}=\mathbf{X}_{k+1|k}} \tag{3.14}$$

Next, with the measurement model defined in Equation (3.9), the propagated state estimate is observed in terms of predicted measurement $\tilde{z}_{k+1}$ at $(k+1)^{th}$ time instant. Subsequently the innovation (ε_{k+1}) between predicted ($\tilde{z}_{k+1}$) and actual (z_{k+1}) measurement can be estimated as,

$$\begin{aligned} \varepsilon_{k+1} &= z_{k+1} - \tilde{z}_{k+1} \\ \tilde{z}_{k+1} &= \mathcal{H}(\mathbf{X}_{k+1|k}) \end{aligned} \tag{3.15}$$

Finally, the innovation, ε_{k+1}, is used as output feedback in order to correct the state mean and error covariance prediction as,

$$\begin{aligned} \mathbf{X}_{k+1|k+1} &= \mathbf{X}_{k+1|k} + \mathbf{K}_{k+1}\varepsilon_{k+1} \\ \mathbf{P}_{k+1|k+1} &= [\mathbf{I} - \mathbf{K}_{k+1}\mathbf{H}_{k+1}]\mathbf{P}_{k+1|k} \end{aligned} \tag{3.16}$$

The approach is elaborated in Algorithm 1 with a pseudo-code for the same.

Algorithm 1 JEKF-based joint estimation

```
**I. Estimating the state parameters**
***1. Initialization***:
When k = 0; $\mathbf{X}_{0|0}$, $\mathbf{P}_{0|0}$, $\mathbf{Q}_k$, $\mathbf{R}_{k+1}$    ▷ Initial values
***2. Prediction***:
for $k = 1, 2, \ldots, N_L - 1$ do    ▷ $N_L$ - available data out of total cycles $N_T$
    $\mathbf{X}_{k+1|k} = \mathcal{F}(\mathbf{X}_{k|k})$    ▷ State space function see Eq. (3.10)
    $\mathbf{P}_{k+1|k} = \mathbf{\Phi}_k \mathbf{P}_{k|k} \mathbf{\Phi}_k^T + \mathbf{Q}_k$    ▷ State error covariance see Eq. (3.11)
    $\mathbf{\Phi}_k = \left[\frac{\partial \mathcal{F}}{\partial \mathbf{X}}\right]_{\mathbf{X}=\mathbf{X}_{k|k}}$    ▷ Jacobian function - augmented, see Eq. (3.12)
    ***3. Update***:
    $\mathbf{S}_{k+1} = \mathbf{H}_{k+1} \mathbf{P}_{k+1|k} \mathbf{H}_{k+1}^T + \mathbf{R}_{k+1}$    ▷ Innovation covariance see Eq. (3.13a)
    $\mathbf{K}_{k+1} = \mathbf{P}_{k+1|k} \mathbf{H}_{k+1}^T \mathbf{S}_{k+1}^{-1}$    ▷ Kalman gain see Eq. (3.13b)
    $\mathbf{H}_{k+1} = \left[\frac{\partial \mathcal{H}}{\partial \mathbf{X}}\right]_{\mathbf{X}=\mathbf{X}_{k+1|k}}$    ▷ Jacobian function - measurement, see Eq. (3.14)
    $\varepsilon_{k+1} = z_{k+1} - \tilde{z}_{k+1}$    ▷ Innovation see Eq. (3.15)
    $\mathbf{X}_{k+1|k+1} = \hat{\mathbf{X}}_{k+1|k} + \mathbf{K}_{k+1} \varepsilon_{k+1}$    ▷ Updated mean see Eq. (3.16a)
    $\mathbf{P}_{k+1|k+1} = [\mathbf{I} - \mathbf{K}_{k+1} \mathbf{H}_{k+1}] \mathbf{P}_{k+1|k}$    ▷ Updated covariance see Eq. (3.16b)
end for
**II. State prognosis approach based on estimated parameters**
When k = $N_L$; $\begin{bmatrix} a_k & m_k & \Theta_k \end{bmatrix}^T = \mathcal{N}(\hat{\mathbf{X}}_{k|k}; \mathbf{P}_{k|k})$    ▷ Initial conditions
***Prognosis***:
for $k = N_L, \ldots, N_P$ do    ▷ $N_P$ Number of cycles in prognosis, for $a_{k+1} < a_c$
    $a_{k+1} = f(a_k, m_k, C_k)$    ▷ see Eq. (3.8)
end for
```

3.4 Validation Study

The proposed approach has undergone validation through three sets of experiments, including two numerical experiments and one real experiment, in order to demonstrate its effectiveness. The flow chart illustrating the proposed approach is presented in Figure 3.2. The first numerical experiment focuses on mechanical and thermo-mechanical loading applied to a finite plate, where the crack propagation is modeled using MATLAB. The proposed approach is then utilized to estimate the known system parameters and states based on the available crack propagation history data collected over loading cycles. The objective of this experiment is to verify whether the proposed algorithm can accurately drive the state and parameter estimates toward their assumed true values. Additionally, with the converged estimate, the prognosis of fatigue crack growth is conducted, and the accuracy and precision of the predictions are evaluated for various levels of measurement noise. These experiments aim to provide validation and assessment of the proposed approach, demonstrating its capability in estimating parameters, predicting fatigue crack growth, and assessing the impact of measurement noise on prediction accuracy.

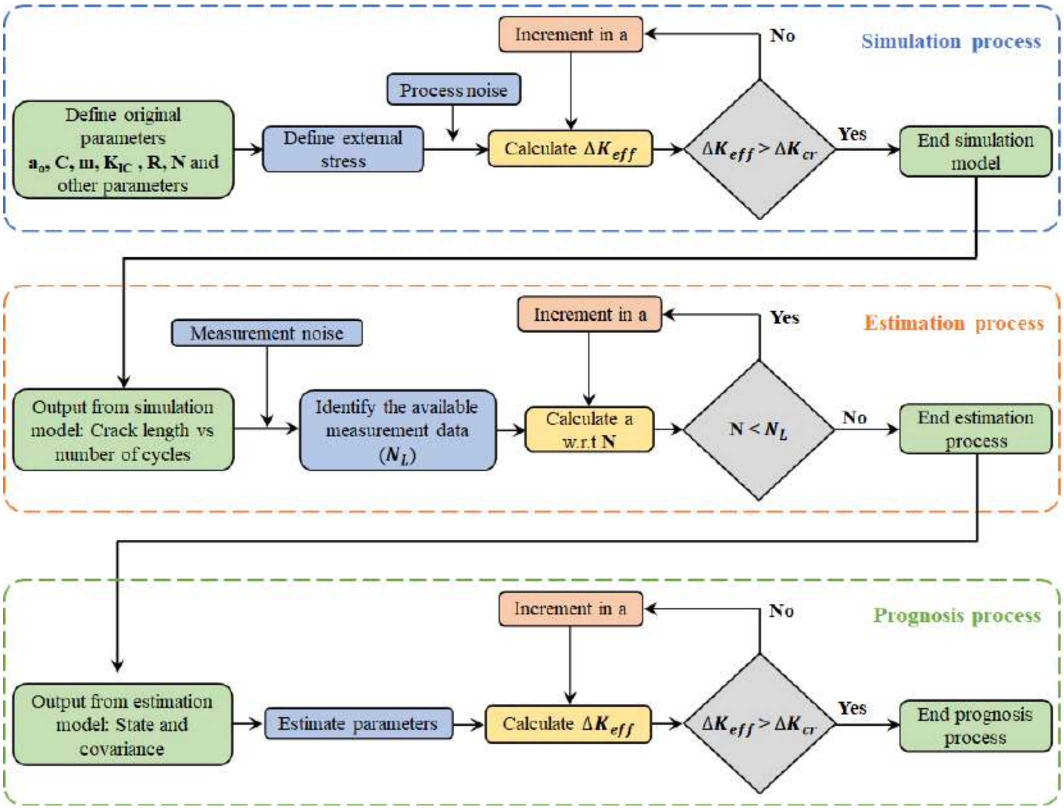

Figure 3.2: Flowchart of the proposed approach.

In the subsequent experiments, the proposed approach is applied to a real-life welded gusset joint in a bridge structure, which is subjected to fatigue loading. Joint is modeled using ABAQUS software to simulate the corresponding crack growth history. By utilizing similar data that depicts the crack growth over loading cycles, the proposed algorithm is employed to perform fatigue prognosis for the system, and the predicted results are compared with the actual crack growth. This experiment aims to demonstrate the potential and applicability of the algorithm for real-life infrastructures with complex geometries.

Additionally, a CT specimen is subjected to fatigue loading, and the crack propagation over the loading cycle is monitored. A portion of the monitored data is used for system estimation using the proposed approach, while the remaining data is utilized to cross-validate the accuracy and validity of the prognosis results. This experiment provides further evidence of the effectiveness and reliability of the proposed algorithm in estimating and predicting fatigue crack growth.

Each of these experiments is described in detail to provide a comprehensive understanding of the methodology employed and the outcomes obtained, highlighting the potential of the proposed algorithm in addressing fatigue prognosis challenges for real-life civil infrastructures.

3.4.1 Numerical validation

The fatigue life estimation of standard specimens with edge and center cracks is performed, employing identical material properties and boundary conditions as outlined in Section 2.5. The numerically obtained SIFs from ABAQUS-K are utilized to simulate the fatigue crack growth under a constant amplitude applied load. The crack growth time history data is simulated by using Equation (3.8).

State-parameters estimation and prediction

In the following analysis, the proposed approach is applied to estimate the system states and parameters based on the crack growth time history data. Different levels of information, ranging from 10% to 90% of the complete data, are utilized for both estimation and prediction. This allows for an assessment of the achievable estimation and prediction accuracy using the proposed approach in relation to the available data.

To ensure a realistic experiment, the simulated crack growth time history data is contaminated with noise using a SWGN noise process. The noise contamination levels are defined with a signal-to-noise ratio (snr) that represents the ratio between the powers of the signal to the added SWGN noise (typically defined as the ratio of the variances of the response and noise signals). Various snr levels, including 0%, 1%, 2%, 5%, and 10%, are examined in this study to evaluate the impact of different noise levels on the estimation and prediction accuracy.

In several studies focusing on probabilistic fatigue life estimation for bridges, crack length has been treated as a random variable to enable probabilistic estimation based on SHM data. Similarly, the Paris model parameters have also been modeled as Gaussian random variables in these studies Marques et al. (2018); Albrecht and Yazdani (1986). This probabilistic framework allows for a more comprehensive and robust estimation of crack length and model parameters, taking into account the inherent uncertainties associated with fatigue crack growth and SHM measurements.

In this study, similar to previous works Marques et al. (2018); Lin et al. (2018), crack length, and model parameters are treated as random variables and estimated using the available crack growth history. However, it is important to note that an uncertainty analysis should be conducted before categorizing a parameter as deterministic or stochastic Hamdia et al. (2017). In this study, the parametric uncertainty for the Paris model parameters is assumed to be epistemic, meaning that it is reducible through inference. On the other hand, other sources of uncertainty such as uncertain loading, modeling inaccuracies arising from uncertain parameters and assumptions, and sensor noises are assumed to be aleatoric and are subsequently examined in the presence of process and measurement noises.

Table 3.1 presents explicit details regarding the initial assumptions for the state and parameter, their characteristics and distributions, as well as fracture parameters of the assumed material. The initial state covariance $P_{0|0}$ is set to $diag(0, 0, 0)$, and the process noise covariance Q_k is set to $diag(1.43 \times 10^{-8}$, $m_{0|0} \times 10^{-3}$, $\Theta_{0|0} \times 10^{-5})$. The loading cycle steps (ΔN) are consistently chosen to be 10 cycles. It is assumed that when the effective stress intensity factor range ΔK_{eff} exceeds a predefined critical threshold ΔK_{cr}, the structure reaches a critical state, leading to crack growth into region III and eventual catastrophic failure.

Table 3.1: EKF parameters for finite plate experiment

Parameters	Type	Numerical values
a_o	True value	5 mm
m	True value	3.88
Θ	True value	34
$a_{0\|0}$	Initial estimate	$\mathcal{N}(5, 1)$
$m_{0\|0}$	Initial estimate	$\mathcal{N}(3, 2)$
$\Theta_{0\|0}$	Initial estimate	$\mathcal{N}(27.65, 14.44)$
ΔK_{th}	Deterministic	4 MPa$\sqrt{m}$
ΔK_{IC}	Deterministic	48 MPa$\sqrt{m}$
σ'_f	Deterministic	150 MPa
v_{cr}	Deterministic	2.5×10^{-3} mm/cycles

Subsequently, the estimation of states and parameters is conducted for various combinations of available information and noise contamination levels. Figure 3.3 illustrates the convergence of the statistical estimates, including the mean and variance, for the parameters (Θ and m) as the level of available information increases. This investigation is carried out considering different levels of available data with an snr of 5%.

The test structure in this case features an edge crack, and the response is simulated under cyclic mechanical loading with $P_{\max} = 36\ kN$ and $P_{\min} = 3.6\ kN$, along with a $R = 0.1$. The true values for the parameters are depicted with dashed lines. The inset figure demonstrates that the parameter estimation process has been prompt and accurate. It can also be observed from the estimation of the parameter distribution that the peak is gradually reaching the true value, while the distribution is becoming narrower, indicating increased precision.

The convergence of the parameter means toward their true values is relatively fast, even with only 10% of the available information. However, the precision of the estimation, represented by the parameter distribution, improves as more information becomes available. Eventually, with 90% of the information, the estimation uncertainty is significantly reduced, and both the accuracy and precision of the estimates fall within acceptable limits.

Next, the accuracy and precision of crack growth prediction are evaluated, and the corresponding results are presented in Figure 3.4a. It is observed that as the level of available information increases, the likelihood of accurately predicting the actual crack growth within the prediction band also increases. Therefore, while parameter estimates may be sufficiently accurate with 10%, 20%, or 50% of the available information, the prognostic results with those estimates may not be very accurate. This indicates that the accuracy of fatigue crack prognosis is dependent on the level of information available.

Furthermore, the sensitivity of the proposed algorithm to noise contamination is investigated. In this analysis, the number of cycles required for ΔK_{eff} to reach the critical condition is compared to its true value, and the deviations are presented in Figure 3.4b. The true curve is simulated using the true values of the Paris law parameters through traditional crack propagation methods. The mean crack length estimate is presented, along with the 95% confidence band. It is observed that the accuracy of the estimation is significantly affected by the level of noise contamination. However, with noise-free data, the estimation is found to be perfect regardless of the level of available information. For noisy

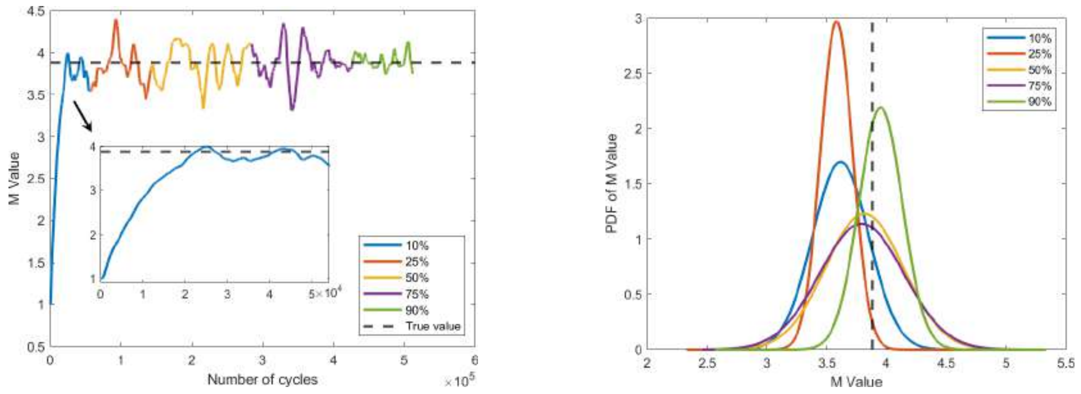

(a) Mean estimation for m.

(b) Parameter distribution for m.

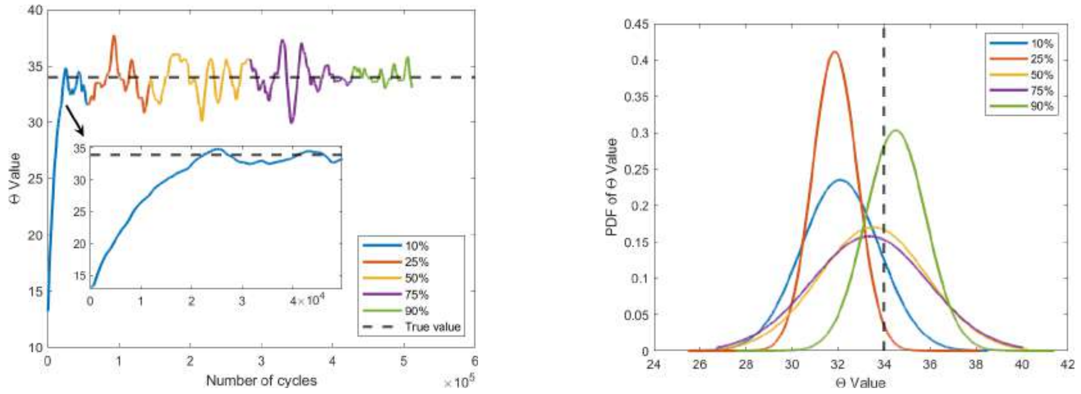

(c) Mean estimation for Θ.

(d) Parameter distribution for Θ.

Figure 3.3: Convergence of estimated parameters m (above) and Θ (below).

data, it is observed that the noise effect can be reduced by employing recursive estimation with more information.

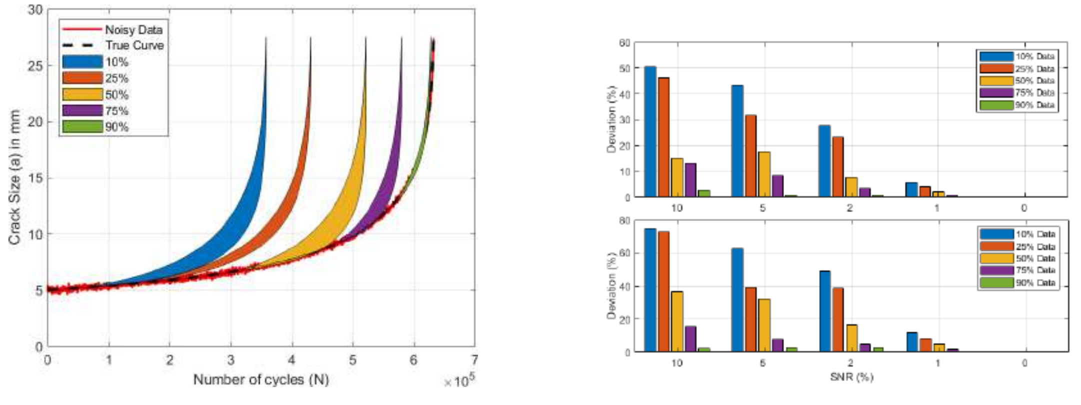

(a) Estimation and prognosis of crack growth with different levels of available data with 5 % *snr*.

(b) The relative error in predicting the number of cycles with various noise levels for edge and center crack.

Figure 3.4: Deviation in estimation and prognosis under mechanical loading.

Similar experiments are also conducted for the center crack case, and it is found that the estimation sensitivity is similar for both the edge crack and center crack scenarios.

3.4.2 Experimental validation

Finally, the proposed algorithm is tested using crack growth time history data obtained from a real laboratory-level experiment on a CT specimen, as conducted by Kumar et al. (2021). In this experiment, the fatigue crack growth rates were monitored, and the parameters Θ and m were estimated as C_0 and m_0 using the complete test data, following the guidelines provided in ASTM E647 Standard (2015). The same dataset is then utilized with the proposed online algorithm, and the Paris model parameters are estimated in real-time. These estimated parameters are subsequently compared to their corresponding earlier estimates.

The CT specimen used in this experiment is made of 12.5 mm thick aluminum alloy (AA 5754) and features a V-notch with a length of 12 mm, created using an electric discharge machine according to the test specifications. The geometry of the test specimen is depicted in Figure 3.5a. To control the crack propagation direction during the fatigue test, a sharp crack of 1 mm is machined as a pre-crack at the notch tip of the specimen by applying a fatigue load of 4 kN at a frequency of 10 Hz. The crack growth at each load step is measured using a crack opening displacement (COD) gauge attached to the specimen. The experimental setup is illustrated in Figure 3.5b. Further details regarding the experimental procedure can be found in the work of Kumar et al. (2021).

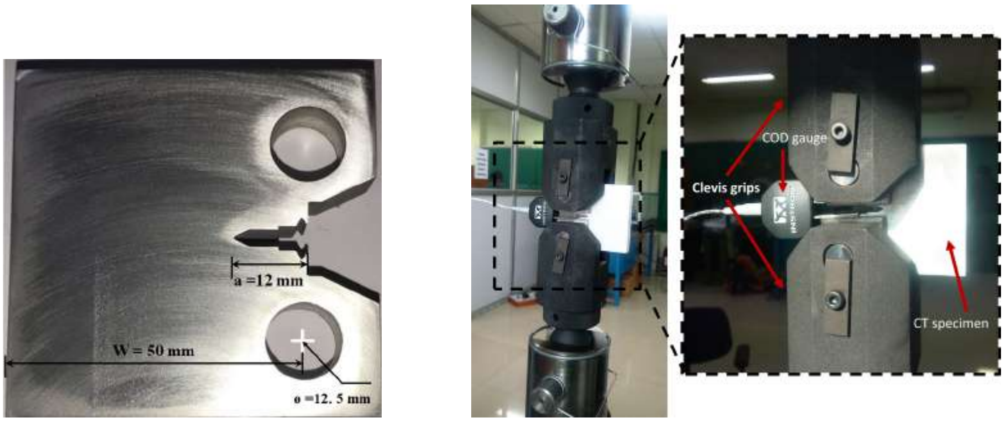

(a) The geometry of the CT specimen.

(b) The experimental setup with a closed view of the specimen in hold with COD gauges.

Figure 3.5: Fatigue crack growth test setup.

The validation study in this experiment focuses on a CT specimen subjected to tensile loading. The test is conducted under a constant fatigue load with a frequency of 5 Hz, a $\Delta P = 4\ kN$, and $R = 0.2$. The experiment continues until the crack reaches its critical length of 41.25 mm. Figure 3.6a presents the experimental fatigue crack growth curves for the CT specimen. A linear relationship in the form of a sigmoidal curve is observed between $\frac{da}{dN}$ and ΔK when plotted on a log-log scale. The range of crack growth rate $[10^{-4} - 10^{-2}]$ $mm/cycle$ is identified as Zone II of fatigue cracking, as evident from Figure 3.6b.

Traditional approaches for offline estimation of Paris model parameters are adopted in the following in which the C and m are obtained through fitting all the observations by a least-square regression approach. The other parameters required for prediction (i.e. a_c, v_{cr}, K_{IC}, N) are also obtained and are shown in Table 3.2. The values of Q_k, R_{k+1} are 19.08 and 0.77 respectively.

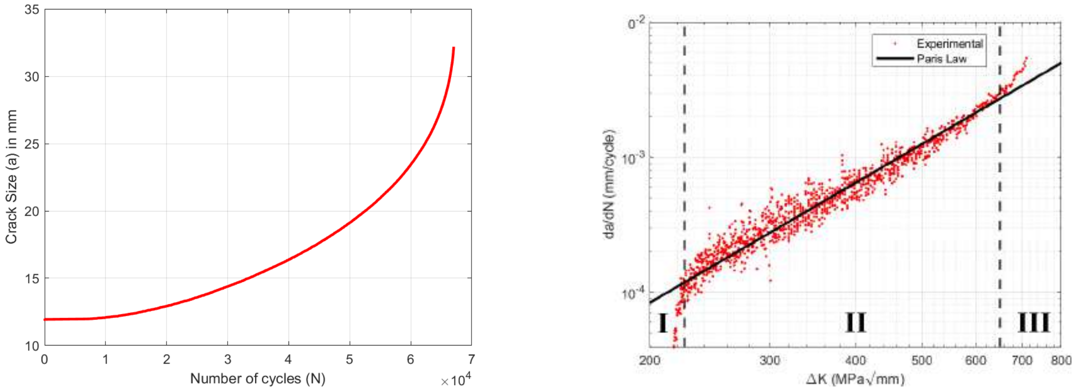

(a) Fatigue crack growth curve.

(b) Sigmoidal curve.

Figure 3.6: Experimental results of CT specimen.

Table 3.2: Parameters calculated from experimental and assumed data

Paris model parameters		a_c	K_{IC}	v_{cr}	N
C_0	m_0	(mm)	(Mpa $\sqrt{m}$)	(mm/cycles)	
1.35×10^{-11}	2.95	32.19	28	2.58×10^{-3}	67033

Similar to the numerical experiments, the proposed algorithm is employed for fatigue damage prognosis of the CT specimen using the measured crack growth time history. Figures 3.7 and 3.8 demonstrate the accuracy and promptness in estimating the Paris model parameters (C and m) compared to the corresponding C_0 and m_0 obtained using the complete data. The prognosis is attempted with different levels of available measurement data, and the accuracy and precision of the prediction can be observed from Figure 3.8b. It is evident that the estimates of C and m do not perfectly match the values of C_0 and m_0 even with assimilating 90% of the measured data. However, despite this discrepancy, the estimates yield better prognosis results (Figure 3.8a) compared to using C_0 and m_0. This highlights the practicality of the proposed approach, which incorporates past beliefs and assimilates new data based on its likelihood, avoiding overfitting that can occur with deterministic approaches.

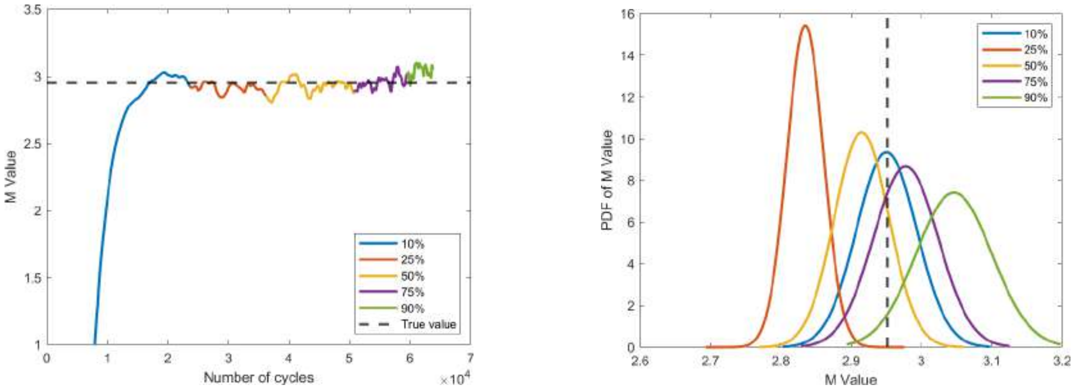

(a) The mean estimate for m.

(b) Parameter distribution for m.

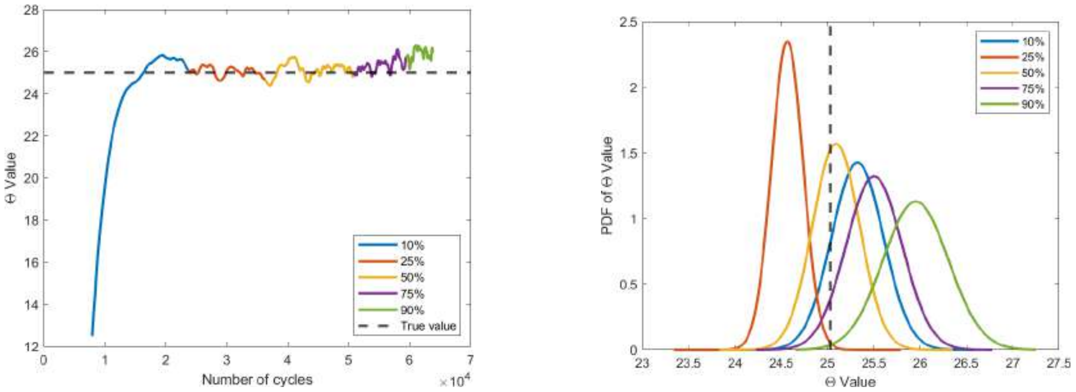

(c) The mean estimate for Θ.

(d) Parameter distribution for Θ.

Figure 3.7: Convergence of estimated parameters m (above) and Θ (below) at different levels of experimental data of a CT specimen.

Furthermore, the investigation includes the estimation of the remaining fatigue life (N) using both Deterministic (Det) and Bayesian filter (Bay) approaches with the measured crack growth time history. The results are compared to the true values, demonstrating that the Bayesian filter approach is more accurate than the deterministic approach. As the level of available information increases, crack growth is more likely to be predicted within the prediction band. This clearly establishes the efficiency of the proposed approach in the context of damage prognosis.

It is important to note that in practical scenarios, the loading conditions are assumed to be known in advance for calculating the SIF. The geometry

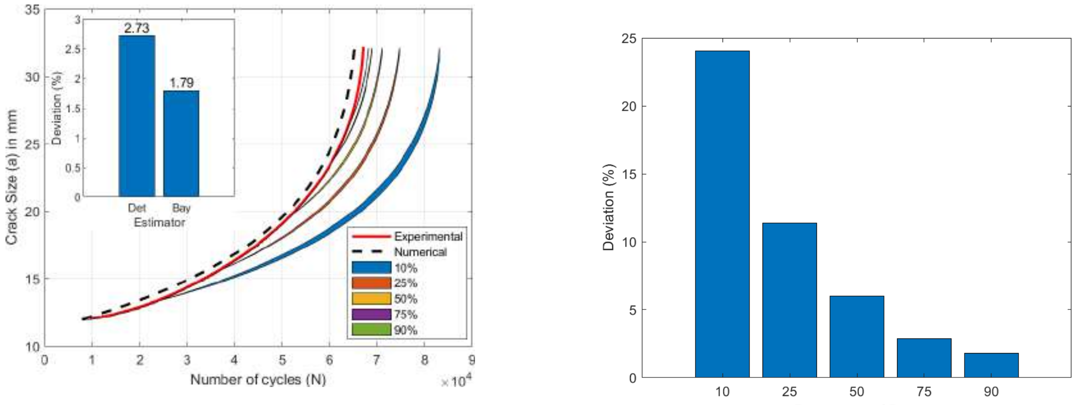

(a) Estimation and prognosis of crack growth with different levels of available data with 1% *snr*.

(b) The relative error in predicting the number of cycles.

Figure 3.8: Estimation and prognosis for CT specimens based on experimental data.

function is considered based on the guidelines provided in the handbook Tada et al. (2000). These assumptions are made to simplify the calculation of SIF while maintaining accuracy and practicality in real-world applications.

The idea of this experiment is to mimic real field testing in which the location of the crack is known. Accordingly, the alternating stresses that are coming onto the cracked domain can be estimated by analyzing the structure globally. The SIF can further be made available through a rigorous numerical analysis involving the geometry function of the cracked domain. Finally, through monitoring the crack over time using instruments like a crack meter, the crack growth history can be recorded from which Paris model parameters can be estimated online using the proposed filtering-based approach. Eventually, the estimate gets better with each measurement set made available and as such does not demand the complete measurement at once, allowing ever-evolving estimates that ensure better accuracy in RUL estimation than traditional offline approaches.

3.4.3 Thermo-mechanical loading

In a similar fashion to the previous experiment discussed in Section 2.5, the same finite plate with consistent boundary conditions, temperature range, and loading conditions are utilized. The initial crack length of 5 *mm* is maintained for consistency as well. The estimation approach described in Algorithm 1 is employed to investigate crack growth under thermo-mechanical loading, and the corresponding results are presented in Figure 3.9 and 3.10. These results demonstrate similarities to the earlier experiment, providing further confirmation of the effectiveness of the proposed algorithm in accurately predicting fatigue life for both loading scenarios.

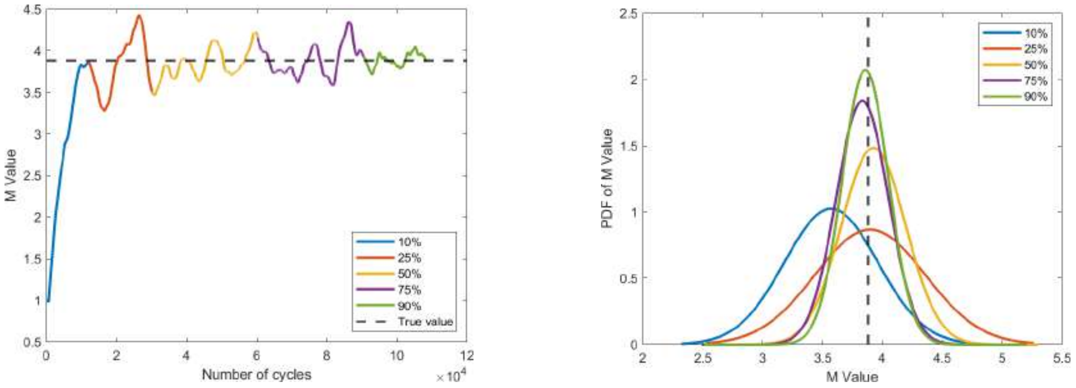

(a) The mean estimate for m.

(b) Parameter distribution for m.

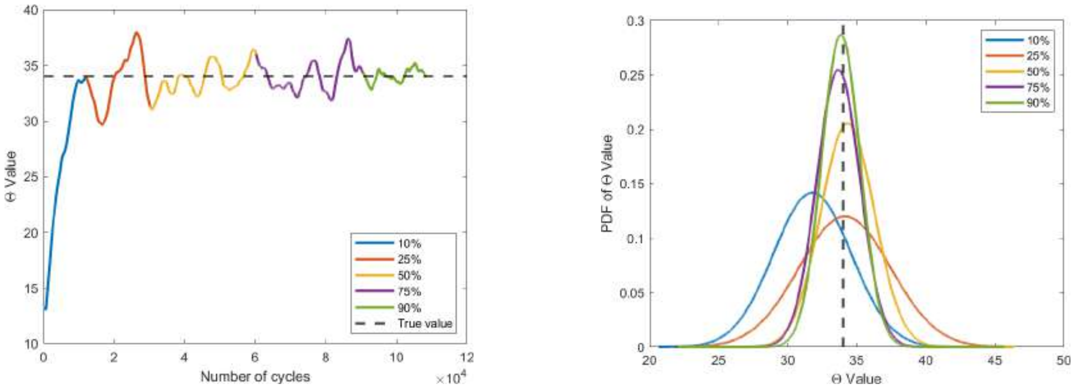

(c) The mean estimate for Θ.

(d) Parameter distribution for Θ.

Figure 3.9: Convergence of estimated parameters m (above) and Θ (below) under harmonic thermo-mechanical loading.

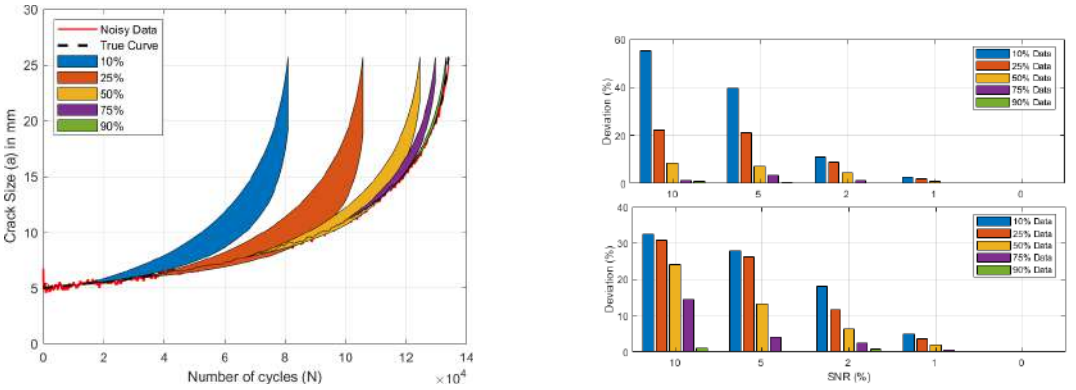

(a) Estimation and prognosis of crack growth with different levels of available data with 5 % *snr*.

(b) Relative error in predicting the number of cycles with various noise levels for edge and centre crack.

Figure 3.10: Deviation in estimation and prognosis under thermo-mechanical loading.

In order to identify the worst-case scenario for both loading types and crack positions, all possible combinations are tested under similar external loading and material properties. Table 3.3 provides a comparison of the number of loading cycles required for the specimen to fail under mechanical and thermo-mechanical loading conditions for both edge and center crack positions. It is evident from the table that an edge crack renders the structure more vulnerable to fatigue-induced failure compared to a center crack. Additionally, it is observed that thermo-mechanical loading substantially accelerates the rate of fatigue damage. This observation motivated us to further conduct experiments with bridge joints, focusing on an edge crack subjected to thermo-mechanical loading as it represents a critical scenario.

Table 3.3: Comparing the number of cycles in different scenarios

Loading	Mechanical		Thermo-mechanical	
Location	Center	Edge	Center	Edge
Number of cycles	7319430	631750	897660	134030

3.4.4 Bridge joint

Fatigue cracks typically initiate in areas with significant geometric variations such as bends or notches Haghani et al. (2012). In the case of bridge structures, the gusset plate within welded joints emerges as a pivotal component susceptible to fatigue crack initiation, which can eventually lead to overall structural failure. It is important to note that in this study, perfect welding conditions are assumed for all joints, and as such, the welding itself is not prone to fatigue damage.

The following numerical experiment focuses on validating the proposed approach for a real-life civil infrastructure, specifically a bridge structure adapted from Yin et al. (2017). The corresponding geometric details of the bridge structure are presented in Figure 3.11a. This experiment aims to assess the effectiveness of the proposed approach in estimating fatigue crack growth and predicting the remaining useful life of the bridge structure, considering its complex geometry and realistic conditions.

The calculation of SIFs for structures with simple geometries is extensively discussed in the literature Tada et al. (2000). However, connections in real-life bridge structures often exhibit complex geometries, requiring special attention when determining the corresponding geometrical function and calculating the associated SIFs. It is crucial to develop structure-specific geometrical functions

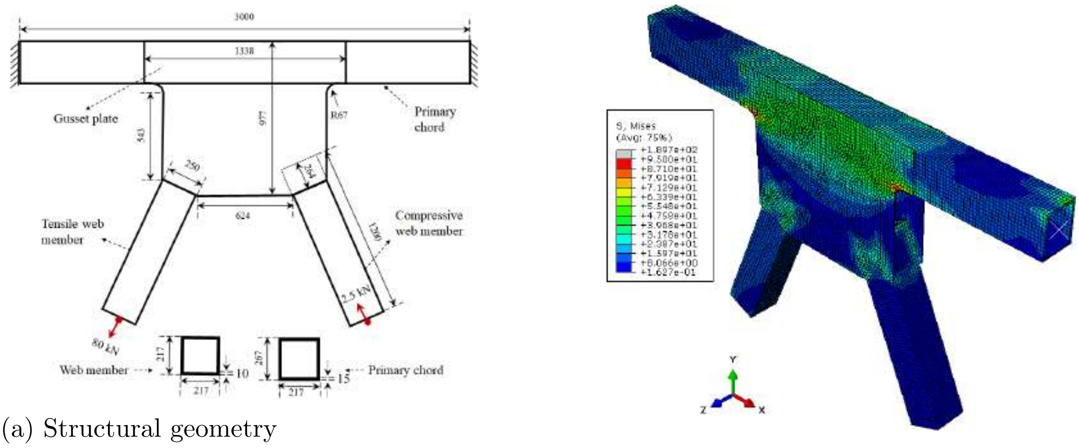

(a) Structural geometry
all units are in millimeters.

(b) von Mises stress field.

Figure 3.11: Numerical model of the bridge joint.

to accurately assess the SIFs in such cases. To address this challenge, XFEM models are employed, where simulated cracks of different lengths are incorporated. Numerical computations are then carried out to determine the SIFs under various loading conditions. In order to optimize the structure-specific geometrical function, a higher-order polynomial fitting approach is utilized. This ensures that the geometrical function accurately captures the complexities of the bridge structure and enables precise computation of the SIFs.

With Bayesian filtering-based approaches for fatigue damage prognosis, this study adopts the predictor model-based estimation approach for a bridge structure with fatigue damage which relies on a high-fidelity numerical model, such as XFEM models, for accurate estimation. However, it is important to consider the computational cost and accuracy of the overall process, which is dependent on the model dimension. Clearly, simulating the entire bridge structure for fatigue damage is not only computationally expensive but also not practical. As a measure, a simplified model of the bridge is firstly simulated under usual service loading conditions, and member force time histories are obtained. From this investigation, the joint with maximum stress can easily be isolated, for which further fatigue modeling is performed.

To determine the geometry function of the welded joint with complex geometry, an uncracked numerical model (Figure 3.11b) representing only the joint is created as a substructure. The interface boundaries of the model are subjected to member forces obtained from the simulation of the simplified bridge model. The structure is fixed at the centroid of the main chord on both sides and constrained using rigid body mechanisms. The bottom ends of the web members are also constrained using rigid body mechanisms. The model incorporates solid elements and three-dimensional (3D) surface-to-surface contact pairs with perfect bonding to capture the effects of contact between the gusset plate and the main chord, as well as the contact between the web and the gusset plate. The numerical model consists of $45,144$ elements and $83,064$ nodes. The thermal properties of the material are adopted based on the work of Reddy and Chin (1998) and are presented in Table 3.4. The bridge structure is simulated under a thermo-mechanical loading condition, where the base temperature is reduced from $50°C$ to $25°C$ to induce thermal stresses. This loading condition allows for assessing the response of the joint to both mechanical and thermal effects, providing insights into the fatigue behavior of the welded joint in a realistic operating environment.

Table 3.4: Material properties of steel at different temperatures

Temperature ($°C$)	Elastic modulus (MPa)	Poisson's ratio	Thermal expansion coefficient ($1/°C$)
25	206×10^3	0.296	12×10^{-6}
50	205×10^3	0.301	12.105×10^{-6}

Consequently, the zone of stress concentration in the joint, located near the bend of the gusset plate (Figure 3.11b), is identified. It is reasonable to assume, without any loss of generality, that a potential fatigue crack would likely initiate from this high-stress zone. The SIF can be calculated using the algorithm described in Section 2.4. By utilizing the previously obtained geometry function, the SIF under a specific real variable amplitude loading can be determined, taking into account factors such as fracture mode, crack shape, and specimen geometry Imam et al. (2007); Guyer and Laman (2012); Albuquerque et al. (2015).

To further reduce computational costs, the high-stressed zone identified previously is modeled separately and simulated with an edge crack under the equivalent thermo-mechanical loading obtained from the previous model. The high-stressed zone is represented as a plate, and an equivalent load of $22.25\ kN$ is applied with a $R = 0.1$. The boundary interface is maintained as the boundary condition for the simulation. An initial crack length of $10\ mm$ is assumed in the plate, and the simulation continues until the crack reaches its critical length of $41.25\ mm$ ($K_{IC} = 100\ MPa\sqrt(m)$ Carpinteri and Paggi (2007)).

The initial values for the crack length and Paris model parameters used in the simulation are taken from the works of Coppe et al. (2012) and Carpinteri and Paggi (2007). A detailed description of the preliminary assumptions regarding the state and parameters of the material is discussed in Section 3.4.1. Their characteristics and distribution, as well as the assumed fracture parameters, are presented in Table 3.5. The initial state covariance $P_{0|0}$ is $diag(0, 0, 0)$ and process noise covariance Q is $diag(1.43 \times 10^{-8}, m_{0|0} \times 10^{-3}, \Theta_{0|0} \times 10^{-5})$ are considered.

The proposed algorithm is then employed to estimate the fatigue life based on the crack growth history simulated from this numerical model. The simulated crack growth history is subsequently contaminated with 1% *snr* SWGN, as in previous experiments. This contamination allows for assessment of the performance of the algorithm in the presence of measurement noise.

Table 3.5: EKF parameters for bridge joint experiment

Parameters	Type	Numerical values
a_o	True value	10 mm
m	True value	3.4
Θ	True value	30.55
$a_{0\|0}$	Initial estimate	$\mathcal{N}(10, 1)$
$m_{0\|0}$	Initial estimate	$\mathcal{N}(3, 2)$
$\Theta_{0\|0}$	Initial estimate	$\mathcal{N}(43.27, 11.46)$
ΔK_{th}	Deterministic	7 MPa$\sqrt{m}$
ΔK_{IC}	Deterministic	100 MPa$\sqrt{m}$
σ'_f	Deterministic	450 MPa
v_{cr}	Deterministic	3×10^{-2} mm/cycles

The crack growth history is further employed with the proposed approach to simultaneously estimate the crack size while estimating the pertinent Paris model parameters. The results of both parameter estimation are given in Figures 3.12 in which convergence of mean estimate along with the associated estimation uncertainty is presented. It can be verified that the estimates are not only prompt but also precise. Further, the crack size estimation and prognosis and their sensitivity towards data size and noise contamination are presented in Figure 3.13a and 3.13 from which it can be perceived that the proposed method can practically perform the crack prognosis well ahead in time being within practical levels of noise contamination.

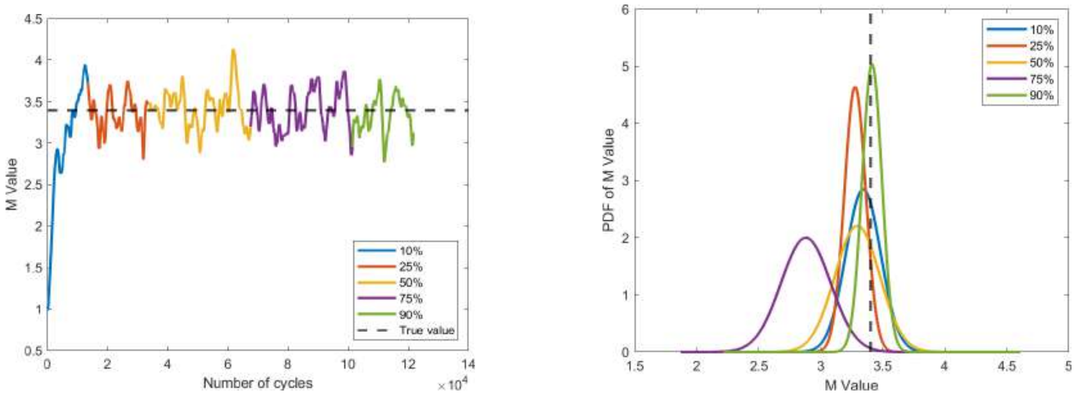

(a) The mean estimate for m.

(b) Parameter distribution for m.

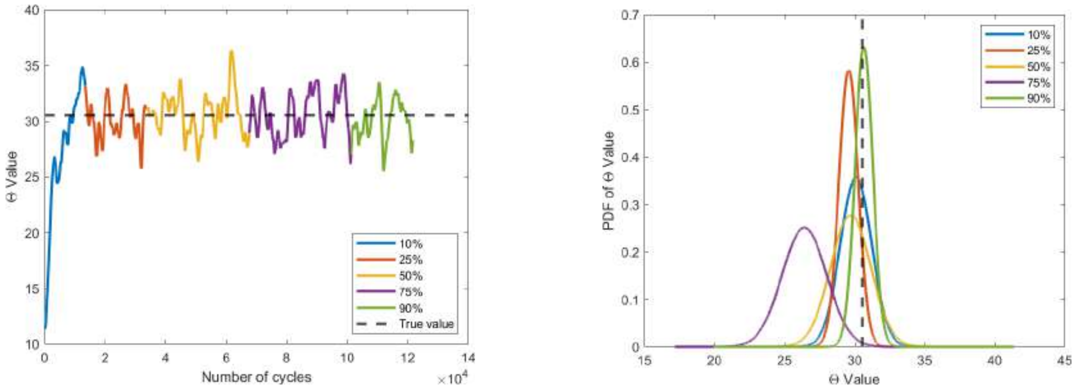

(c) Mean estimate for Θ.

(d) Parameter distribution for Θ.

Figure 3.12: Convergence of estimated parameters m (above) and Θ (below) for the case of equivalent gusset plate under harmonic thermo-mechanical loading.

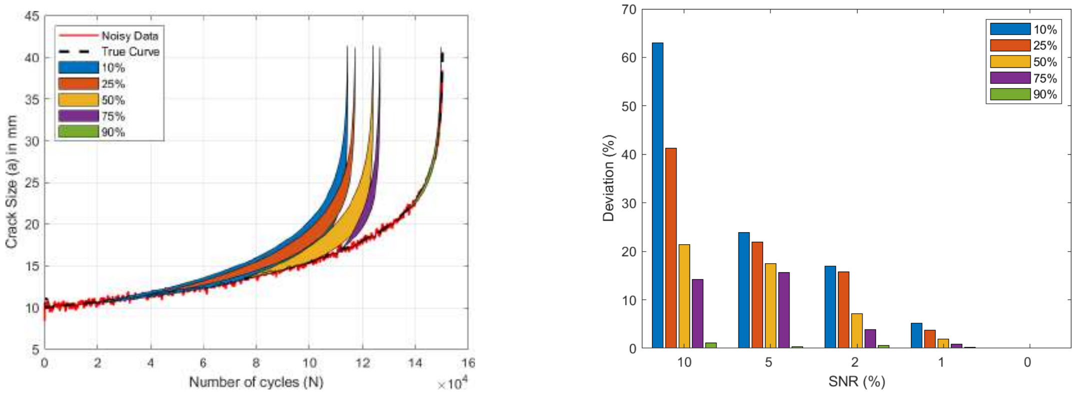

(a) Estimation and prognosis of crack growth with different levels of available data with 5% *snr*.

(b) Relative error in predicting the number of cycles with various noise levels for edge crack.

Figure 3.13: Estimation and prognosis of equivalent gusset plate under harmonic thermo-mechanical loading.

3.5 Summary

In this chapter, an online model-based prognosis algorithm powered by a Bayesian filtering-based estimation approach has been proposed focusing on predicting the service life of civil infrastructural components vulnerable to fatigue failure. The approach takes its basis on defining the crack growth with an updated Paris law model and subsequently estimating the associated parameters under the unavoidable measurement and process uncertainty. The adoption of the updated Paris law model helps incorporate the crack closure effects into the estimation, while the consideration of uncertainty in estimation renders the proposed approach more pragmatic and suitable to be used for real-life applications. The proposed algorithm consists of two sequential steps: 1. State-parameter estimation using the JEKF filter, and 2. Prediction of crack growth based on the estimated parameters.

The following was experienced:

- Application of stochastic inverse estimation technique using EKF-based filtering approach for fatigue life estimation helped to deal with process uncertainty (model inaccuracy) in simultaneity with the measurement uncertainty.

- Unlike traditional offline approaches, which demand a sufficiently long crack growth history in order to conclude on the RUL, the present study takes an online approach that ensures smooth convergence towards the actual RUL gradually using the available data. It has been observed that, even with 10% of the available information, the mean estimates of the parameters reach at least in the vicinity of the respective true values. The estimation is further improved with the availability of the data.

- Being a recursive data assimilation-based approach, the estimation accuracy is observed to be largely affected by noise contamination levels.

- The edge crack makes the structure more vulnerable to fatigue failure than the center crack. In addition, it is also found that thermo-mechanical loading advances fatigue damage dramatically. Accordingly, a combination of edge crack with thermo-mechanical loading is considered the worst operational scenario for investigating the proposed approach for the RUL estimation in the bridge joints.

- The present approach provided not only the mean estimates of the parameters or RUL but also the confidence interval around those estimates. This makes the approach more practical and suitable for real-life application.
- Taking the basis of the experimental and numerical case studies, the proposed approach is perceived to be more efficient in the context of damage prognosis in comparison with deterministic approaches. Also, the proposed approach is experienced to be quite accurate under practical loading conditions and robust against moderate-level noise contamination.

Eventually, it can be concluded that the proposed approach is a good candidate to estimate the RUL of civil infrastructure under fatigue loading with sufficient accuracy and promptness. Future work will involve the use of the proposed algorithm on real bridge structures for their RUL estimation.

Chapter 4

Component-wise fatigue estimation using substructure monitoring approach

In the previous chapter, we explored the application of fracture mechanics in predicting the fatigue life of different structures. This approach was primarily employed to examine joints, as they are prone to fatigue damage at critical locations. For precise life prediction, it is imperative to accurately estimate the boundary force acting on the bridge joint, which relies on ambient or vehicle loading. However, when dealing with large civil structures, the process of fatigue life prediction becomes computationally intensive and can lead to false alarms. To tackle these challenges, we propose a substructure technique that allows for monitoring specific subdomains of interest. Consequently, the induced boundary force resulting from real-time loading can be estimated for these selected subdomains. This technique has undergone rigorous validation through numerical and experimental investigations, with a focus on several key aspects. In this chapter, our primary objective is to validate the effectiveness of the substructure technique and assess the current condition of the subdomain system.

4.1 Introduction

In the real world, evaluating civil structures like buildings, and bridges often requires mathematical models consisting of many dofs and unknown parameters. However, measuring and identifying the entire structure simultaneously is a challenging task. While advanced SHM techniques have been developed to address uncertainties and nonlinearity, they face difficulties when dealing with large structures due to the increased dimensionality of the prediction models. This higher dimensionality not only leads to computational challenges but also increases the likelihood of false positive alarms. For the model-assisted estimation approach, consequent high-resolution monitoring of the real structure requires extensive instrumentation. With limited measurement channels (usual for any SHM application), employment of high dimensional models affects the observability Maes et al. (2021). This eventually renders the SHM algorithm to be inefficient and unreliable.

An effective way of monitoring large structures is to monitor one subdomain at a time instead of monitoring the entire structure at once. Numerically decoupling a structure into smaller substructures for efficient analysis of the structure is known as substructuring. Large complex structures can be economically monitored with the help of the substructuring techniques Koh et al. (1991) as it reduces the required resources as well as the need for measurement data from inaccessible locations. With the aim of model reduction de Klerk et al. (2008), substructuring can be done in the physical (mass, stiffness, etc.), frequency (Fourier transform), or modal (eigenvalue decomposition) domain. Nevertheless, the substructures have been predominantly defined in the modal domain Hou et al. (2013); Zhang and Jankowski (2017); Huang et al. (2021) with a few exceptions Koh and Shankar (2003) where they are defined in the time domain. Numerical substructuring does not physically isolate a subdomain from the rest, but only fragments the entire domain numerically into smaller manageable domains. Eventually, these fragmented subdomains individually should conform to the force equilibrium or displacement continuity. The interaction among them is generally incorporated in terms of the interface forces between the substructures Tee et al. (2003). These interface forces can later be estimated during the re-coupling of the component substructures in order to realize the original entire structure de Klerk et al. (2008).

Nonetheless, the external force inputs are hardly known/measured in real-life problems, either explicitly or statistically. Such forces can however be estimated as additional states Hou et al. (2011); Souid et al. (2009); Tatsis et al. (2021) which will eventually increase the state dimension and consequently, the complexity and efficiency of the state estimation. Moreover, health state assessment for a structure is also sensitive to changes in internal forces (prestress) as well as boundary conditions Mendler et al. (2022). Boundary forces, present on the substructural boundary dofs, have also been directly measured Weng et al. (2020) as well as estimated by modeling them as modulated filtered white noise Yuen and Huang (2018) or by constructing a relationship between the interface forces and the measured responses Yang et al. (2021). Forward genetic algorithms have been utilized to directly use the interface measurement data (sensor output) to account for the interface interaction instead of estimating interface force Koh and Shankar (2003); Trinh and Koh (2012).

4.2 Pilot study

Here, the proposed method by Koh and Shankar (2003); Trinh and Koh (2012), termed the simple substructure technique, is employed as a pilot study to identify substructural damage using a Bayesian filter. The objective is to identify the magnitude of challenges encountered in the process of subdomain monitoring and devise suitable breakthroughs to avert them.

4.2.1 State space formulation for the simple substructure system

As stated in the last chapter, with Bayesian filter-based SHM algorithms, it is necessary to represent the system (here the dynamics of the physical structure) in the form of a state-space model. The Governing Differential Equation (GDE) of the linear time-varying beam system can be defined with time-invariant mass $\mathbf{M}$, time-varying stiffness $\mathbf{K}(\mathrm{t})$, damping $\mathbf{C}(t)$ matrices and external force $\mathbf{f}(\mathrm{t})$ as,

$$\mathbf{M}\ddot{\mathbf{q}}(t) + \mathbf{C}(t)\dot{\mathbf{q}}(t) + \mathbf{K}(t)\mathbf{q}(t) = \mathbf{f}(t) \tag{4.1}$$

where $q(t)$,$\dot{q}(t)$, and $\ddot{q}(t)$ are the displacement, velocity, and acceleration response at the nodes. This definition is consistent with any mechanical system and can be employed through a selection of corresponding mass, stiffness, and damping properties of the system under consideration. Here in this pilot study, a simple substructure technique is demonstrated on a numerical beam which is further idealized (through proper calibration) as a lumped mass system as represented in Figure 4.1.

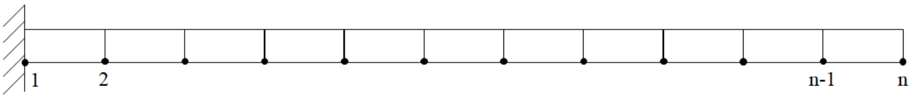

a) Cantilever beam model

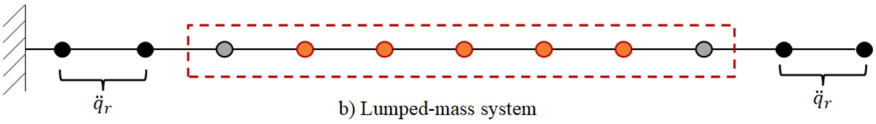

b) Lumped-mass system

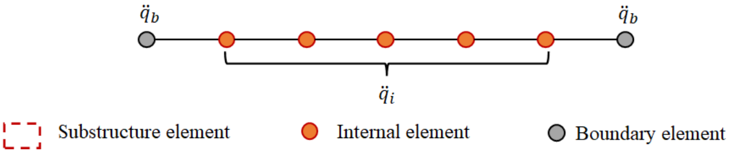

c) Substructure model

Figure 4.1: Cantilever beam model with substructure

The complete structural domain is further divided into a zone of consideration as the "*selected substructure*" while considering the rest as the "*rest of the domain*" connected through the *boundary*. With the subscripts i, r, and b, the domain is categorized as *internal*, *rest*, and *boundary*. With this, the dynamic equation of the complete beam structure is expressed as,

$$\begin{bmatrix} \mathbf{M}_{rr} & \mathbf{M}_{rb} & 0 \\ \mathbf{M}_{br} & \mathbf{M}_{bb} & \mathbf{M}_{bi} \\ 0 & \mathbf{M}_{ib} & \mathbf{M}_{ii} \end{bmatrix} \begin{Bmatrix} \ddot{\mathbf{q}}_r \\ \ddot{\mathbf{q}}_b \\ \ddot{\mathbf{q}}_i \end{Bmatrix} + \begin{bmatrix} \mathbf{C}_{rr} & \mathbf{C}_{rb} & 0 \\ \mathbf{C}_{br} & \mathbf{C}_{bb} & \mathbf{C}_{bi} \\ 0 & \mathbf{C}_{ib} & \mathbf{C}_{ii} \end{bmatrix} \begin{Bmatrix} \dot{\mathbf{q}}_r \\ \dot{\mathbf{q}}_b \\ \dot{\mathbf{q}}_i \end{Bmatrix} + \begin{bmatrix} \mathbf{K}_{rr} & \mathbf{K}_{rb} & 0 \\ \mathbf{K}_{br} & \mathbf{K}_{bb} & \mathbf{K}_{bi} \\ 0 & \mathbf{K}_{ib} & \mathbf{K}_{ii} \end{bmatrix} \begin{Bmatrix} \mathbf{q}_r \\ \mathbf{q}_b \\ \mathbf{q}_i \end{Bmatrix} = \begin{Bmatrix} \mathbf{f}_r \\ \mathbf{f}_b \\ \mathbf{f}_i \end{Bmatrix} \tag{4.2}$$

From Equation (4.2), the dynamics for the substructured domain can further be isolated. The superscript s denotes the relevance of the internal element to the structure as,

$$\mathbf{M}_{ii}^{s}\ddot{\mathbf{q}}_i^{s} + \mathbf{C}_{ii}^{s}\dot{\mathbf{q}}_i^{s} + \mathbf{K}_{ii}^{s}\mathbf{q}_i^{s} = \mathbf{f}_i^{s} - \mathbf{M}_{ib}^{s}\ddot{\mathbf{q}}_b^{s} - \mathbf{C}_{ib}^{s}\dot{\mathbf{q}}_b^{s} - \mathbf{K}_{ib}^{s}\mathbf{q}_b^{s} \tag{4.3}$$

with the right side of Equation (4.3) inclusively considered as the external force or disturbance acting on the substructure. The same when represented in state space, can be defined as,

$$\dot{\mathbf{x}}^{s}(t) = \mathbf{A}^{s}(t)\,\mathbf{x}^{s}(t) + \mathbf{B}^{s}(t)\,\mathbf{u}^{s}(t) + \mathbf{E}^{s}(t)\,\ddot{\mathbf{q}}_b^{s}(t) + \mathcal{G}^{s}(t)\,\dot{\mathbf{x}}_b^{s}(t) + \mathbf{v}^{s}(t) \tag{4.4}$$

where, $\mathbf{x}^s(t) = \begin{Bmatrix} \mathbf{q}_i^s \\ \dot{\mathbf{q}_i}^s \end{Bmatrix}$, $\dot{\mathbf{x}}_b^s(t) = \begin{Bmatrix} \mathbf{q}_b^s \\ \dot{\mathbf{q}_b}^s \end{Bmatrix}$, $\mathbf{A}^s(t) = \begin{bmatrix} \mathbf{0}_{n_i} & \mathbf{I}_{n_i} \\ -\mathbf{M}_{ii}^{s\ -1}\mathbf{K}_{ii}^s & -\mathbf{M}_{ii}^{s\ -1}\mathbf{C}_{ii}^s \end{bmatrix}$, $\mathbf{B}^s(t) = \begin{bmatrix} \mathbf{0}_{n_i} \\ \mathbf{M}_{ii}^{s\ -1} \end{bmatrix}$, $\mathbf{E}^s(t) = \begin{bmatrix} \mathbf{0}_{n_i} \\ -\mathbf{M}_{ii}^{s\ -1}\mathbf{M}_{ib}^s \end{bmatrix}$, $\mathcal{G}^s(t) = \begin{bmatrix} \mathbf{0}_{n_b} & \mathbf{0}_{n_b} \\ -\mathbf{M}_{ii}^{s\ -1}\mathbf{K}_{ib}^s & -\mathbf{M}_{ii}^{s\ -1}\mathbf{C}_{ib}^s \end{bmatrix}$, and, $\mathbf{u}^s(t) = \mathbf{f}_i^s$. The additional term $\mathbf{v}^s(t)$ represents process uncertainty originating from the model inaccuracies and unmodelled inputs. Similarly, the measurement equation can be presented as:

$$\mathbf{y}^s(t) = \mathbf{H}^s(t)\mathbf{x}^s(t) + \mathbf{D}^s(t)\mathbf{u}^s(t) + \mathbf{L}^s(t)\ddot{\mathbf{q}}_b^s(t) + \ \mathcal{S}^s(t)\,\dot{\mathbf{x}}_b^s(t) + \mathbf{w}^s(t) \qquad (4.5)$$

here, $\mathbf{H}^s(t) = \begin{bmatrix} -\mathbf{M}_{ii}^{s\ -1}\mathbf{K}_{ii}^s & -\mathbf{M}_{ii}^{s\ -1}\mathbf{C}_{ii}^s \end{bmatrix}$, $\mathbf{L}^s(t) = -\mathbf{M}_{ii}^{s\ -1}\mathbf{M}_{ib}^s$, $\mathbf{D}^s(t) = \mathbf{M}_{ii}^{s\ -1}$, $\mathcal{S}^s(t) = \begin{bmatrix} -\mathbf{M}_{ii}^{s\ -1}\mathbf{K}_{ib}^s & -\mathbf{M}_{ii}^{s\ -1}\mathbf{C}_{ib}^s \end{bmatrix}$, and $\mathbf{w}^s(t)$ denoting measurement noise. Equations (4.4) and (4.5) can also be represented in discrete time since responses are typically discretely sampled in reality.

$$\begin{aligned} \mathbf{x}_k^s &= \mathbf{A}_k^s\mathbf{x}_{k-1}^s + \mathbf{B}_k^s\mathbf{u}_k^s + \mathbf{E}_k^s\ddot{\mathbf{q}}_{b,k}^s + \mathcal{G}_k^s\dot{\mathbf{x}}_{b,k}^s + \mathbf{v}_k^s \\ \mathbf{y}_k^s &= \mathbf{H}_k^s\mathbf{x}_k^s + \mathbf{D}_k^s\mathbf{u}_k^s + \mathbf{L}_k^s\ddot{\mathbf{q}}_{b,k}^s + \mathcal{S}_k^s\dot{\mathbf{x}}_{b,k}^s + \mathbf{w}_k^s \end{aligned} \qquad (4.6)$$

In order to compute the external force, all accelerations, velocities, and displacements at the interface *dof*s ideally have to be measured Koh et al. (1991). It is usually preferred to measure accelerations (by accelerometers) instead of velocities and displacements. According to Trinh and Koh (2012), acceleration measurement can be directly used to compute the interface force vector directly in order to improve the accuracy of damage identification results. Based on measured interface acceleration, the following equations are used to embed a simple numerical integration scheme to determine interface velocity and displacement:

$$\begin{aligned} \dot{\mathbf{q}}_{b,k+1}^s &= \dot{\mathbf{q}}_{b,k}^s + \frac{\Delta t}{2}\left(\ddot{\mathbf{q}}_{b,k}^s + \ddot{\mathbf{q}}_{b,k+1}^s\right) \\ \mathbf{q}_{b,k+1}^s &= \mathbf{q}_{b,k}^s + \frac{\Delta t}{2}\left(\dot{\mathbf{q}}_{b,k}^s + \dot{\mathbf{q}}_{b,k+1}^s\right) \end{aligned} \qquad (4.7)$$

4.2.2 State and parameter estimation with interacting particle ensemble Kalman filter

For estimating the substructure, the health of the structure is parameterized with p_s number of location-based health indices (**HI**s), which are estimated using IPEnKF Sen et al. (2021); Aswal et al. (2021b) algorithm. IPEnKF is an interactive filtering framework wherein two filters, namely Particle and Ensemble Kalman filter interact in order to estimate the system states and parameters conditioned to each other. A detailed discussion on this algorithm can be found in Aswal et al. (2021b). The same has also been schematically detailed in Figure 4.2 for quick reference. An elaborated discussion is avoided for the sake of brevity.

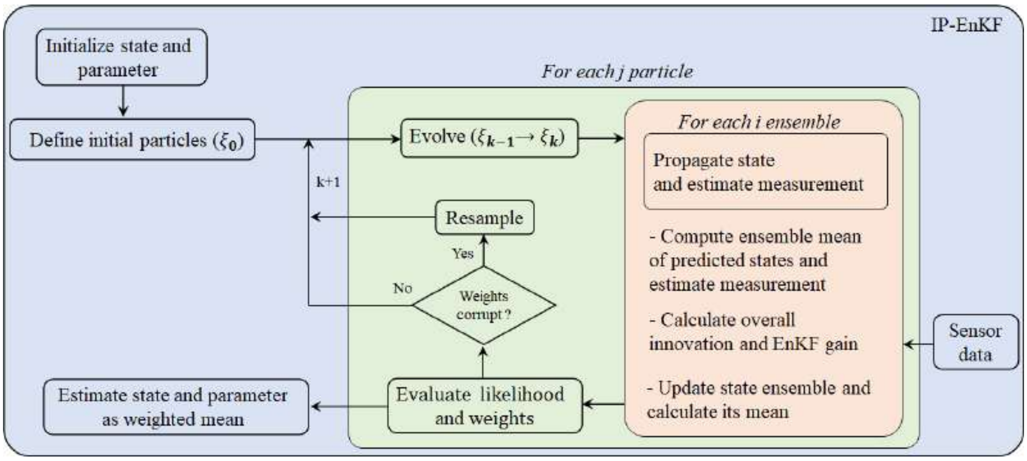

Figure 4.2: Flowchart of IPEnKF algorithm.

The state-space formulation for simple substructure systems has been described in Section 4.2.1. Further, the states and parameters are estimated from the formulated equations with the help of a set of ensembles and particles ($\boldsymbol{\xi}$) respectively. **HI** is defined as the reduction in the flexural rigidity of the element, $(EI)_k^d = \xi.(EI)_k^0$, from its initial health state, $(EI)_k^0$ and is estimated through the PF. This allows monitoring health corresponding p_s locations of the structure rendering the monitoring resolution depending on p_s. The state ($\mathbf{x}_k$) estimation is further approached through EnKF which is nestled within the PF. The current health estimates are employed to define the current state/system or measurement/output matrices, and thereby both filters interact with each other leading to state estimates conditional to the health estimates.

PF employs a crude sample-based uncertainty propagation approach wherein the prior estimates are propagated through the state evolution equation using

N_p independent particles ($\boldsymbol{\xi}_{p_s \times 1}$), each of which can be considered as a realization of the multivariate random variable **HI**. Accordingly, at k^{th} time step, the prior parameter estimates (and associated uncertainties) are propagated through a state evolution equation with PF using a set of parameter particles $\boldsymbol{\xi} = [\xi_{k-1}^1, \xi_{k-1}^2, \cdots, \xi_{k-1}^{N_p}]_{p_s \times N_p}$. During time evolution, each of the particles (ξ_{k-1}^j) evolve through random perturbations around their current position. A Gaussian blurring is performed on ξ_{k-1}^j with a shift $\delta\xi_k = (1-\alpha)\bar{\xi}_{k-1}$ and a spread of σ_k^{ξ}[1]. The turbulence in the particle estimation is controlled with the help of α by re-centering the particles towards their mean ($\bar{\xi}_{k-1}$), given by the following,

$$\xi_k^j = \alpha \xi_{k-1}^j + \mathcal{N}(\delta\xi_k, \sigma_k^{\xi}) \tag{4.8}$$

Eventually, the particles evolved based on their likelihood against the current time-step measurement. Thus, the particle evolution becomes independent of the initial distribution assumed for $\boldsymbol{\xi}$. Embedded EnKF for state estimation is then applied to the propagated particles in order to estimate the likelihood.

For each j^{th} particle, EnKF propagates N_e state ensembles through the system model (cf. Equation (4.16)) conditioned on the current parameter estimate (ξ_k^j from Equation (4.8)). The predicted value of the states ($\mathbf{x}_{k|k-1}^{i,j}$) and transformed measurement ($\mathbf{z}_{k|k-1}^{i,j}$) corresponding to j^{th} particle and i^{th} ensemble is given by,

$$\begin{aligned} \mathbf{x}_{k|k-1}^{i,j} &= \mathbf{A}_k^{i,j}\mathbf{x}_{k-1|k-1}^{i,j} + \mathbf{B}_k^{i,j}\mathbf{u}_k^{i,j} + \mathbf{E}_k^{i,j}\ddot{\mathbf{q}}_{b,k}^{i,j} + \mathcal{G}_k^{i,j}\dot{\mathbf{x}}_{b,k}^{i,j} + \mathbf{v}_k^{i,j} \\ \mathbf{y}_{k|k-1}^{i,j} &= \mathbf{H}_k^{i,j}\mathbf{x}_{k|k-1}^{i,j} + \mathbf{D}_k^{i,j}\mathbf{u}_k^{i,j} + \mathbf{L}_k^{i,j}\ddot{\mathbf{q}}_{b,k}^{i,j} + \mathcal{S}_k^{i,j}\dot{\mathbf{x}}_{b,k}^{i,j} + \mathbf{w}_k^{i,j} \end{aligned} \tag{4.9}$$

It should be noted that, from here on, superscript s is dropped for better readability. Further, innovation for i^{th} ensemble is calculated as the departure of predicted transformed measurement from the output transformed measurement sensor data $\varepsilon_k^{i,j} = \mathbf{y}_k - \mathbf{y}_{k|k-1}^{i,j}$. The overall innovation is computed as $\varepsilon_k^j = \frac{1}{N_e}\sum_{i=1}^{N_e} \varepsilon_k^{i,j}$. The predicted state and transformed measurement error covariance, $C_k^{j,xz}$, and the transformed measurement error covariance ($\mathbf{S}_k^j$) is given by,

$$\begin{aligned} C_k^{j,xz} &= \frac{1}{N_e - 1}\sum_{i=1}^{N_e}\left(\mathbf{x}_{k|k-1}^{j} - \mathbf{x}_{k|k-1}^{i,j}\right)\left(\mathbf{y}_{k|k-1}^{j} - \mathbf{y}_{k|k-1}^{i,j}\right)^T \\ \mathbf{S}_k^j &= \frac{1}{N_e - 1}\sum_{i=1}^{N_e}\left(\mathbf{y}_{k|k-1}^{j} - \mathbf{y}_{k|k-1}^{i,j}\right)\left(\mathbf{y}_{k|k-1}^{j} - \mathbf{y}_{k|k-1}^{i,j}\right)^T + \mathbf{R} \end{aligned} \tag{4.10}$$

---

[1] $A + B\mathbb{N}(\mu, \sigma)$ means $A + Bz$ where z follows $\mathbb{N}(\mu, \sigma)$

where, $\mathbf{x}^j_{k|k-1}$ and $\mathbf{z}^j_{k|k-1}$ are the respective ensemble mean of the predicted states and transformed measurement, respectively. From the covariances obtained from Equation (4.10), EnKF gain is obtained as, $\mathbb{G}^j_k = C^{j,xz}_k(\mathbf{S}^j_k)^{-1}$. Based on the innovation mean, $\varepsilon^{i,j}_k$, and the EnKF gain, $\mathbb{G}^j_k$, the state ensembles are updated as follows,

$$\mathbf{x}^{i,j}_{k|k} = \mathbf{x}^{i,j}_{k|k-1} + \mathbb{G}^j_k \varepsilon^{i,j}_k \tag{4.11}$$

Further, the likelihood, $\mathcal{L}(\xi^j_k)$, of each particle is also calculated, as $\mathcal{L}(\xi^j_k) = \frac{1}{(2\pi)^n\sqrt{|\mathbf{S}^j_k|}} e^{-0.5{\varepsilon^j_k}^T {\mathbf{S}^j_k}^{-1} \varepsilon^j_k}$. For each j^{th} particle, the normalized weight is computed as follows,

$$w(\xi^j_k) = \frac{w(\xi^j_{k-1})\mathcal{L}(\xi^j_k)}{\sum_{j=1}^{N_p} w(\xi^j_{k-1})\mathcal{L}(\xi^j_k)} \tag{4.12}$$

Finally, particle approximations for states and parameters are estimated as follows,

$$\mathbf{x}_{k|k} = \sum_{j=1}^{N_p} w(\xi^j_k)\mathbf{x}^j_{k|k} \quad \text{and} \quad \boldsymbol{\xi}_{k|k} = \sum_{j=1}^{N_p} w(\xi^j_k)\xi^j_k \tag{4.13}$$

The proposed approach has been provided as a pseudo-code (cf. Algorithm 2) for the SHM of substructure systems.

4.2.3 Numerical Experiment - cantilever beam

The validation of the simple substructure is carried out using a numerical model of a prismatic cantilever beam with specific geometric properties. The beam has a span = 0.75 m, a width (w) = 0.025 m, and a depth (d) = 0.006 m. The material properties include a mass density (ρ)= 7850 kg/m^3 and an elastic modulus (E) = 208 GPa. The beam is divided into 11 equal parts (cf. Figure 4.3), and the length of each element is (l_e)=0.0682 m. In this study, a lumped mass assumption is employed to replicate the continuous system for the sake of simplicity. The mass and stiffness of each element are calculated as $33\rho w d l_e/140$, and $3EI_e/l_e^3$ following the reference of Reddy (1999). Here, I_e $=wd^3/12$ represents the moment of inertia of the beam section.

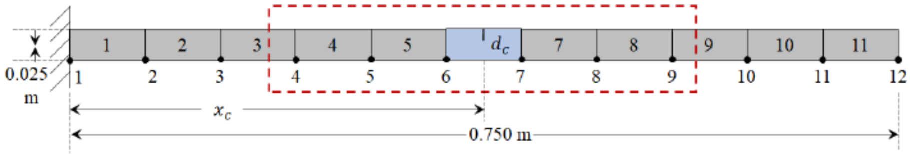

Figure 4.3: Schematic diagram of a cantilever beam model with its substructure

Algorithm 2 Proposed SHM algorithm for simple substructures.

```
procedure IPEnKF($\mathbf{y}_k, \mathbf{Q}, \mathbf{R}$)
    Initialize particles $\{\xi_0^j\}$, and state estimates $\{\mathbf{x}_{0|0}^{i,j}\}$
    for <each $k^{th}$ measurement $\mathbf{y}_k$> do
        procedure IP-EnKF($\{\xi_{k-1}^j\}, \{\mathbf{x}_{k-1|k-1}^{i,j}\}$)
            for <each particle $\xi_k^j$> do
                Evolve $\{\xi_{k-1}^j\} \rightarrow \{\xi_k^j\}$                ▷ as per Eq. (4.8)
                procedure EnKF($\xi_k^j, \{\mathbf{x}_{k-1|k-1}^{i,j}\}, \mathbf{y}_k$)      ▷ For each $j^{th}$ particle
                    for <each ensemble $\mathbf{x}_{k-1|k-1}^{i,j}$> do
                        Prediction: Propagate state to $\mathbf{x}_{k|k-1}^{i,j}$       ▷ Eq. (4.9)
                        Estimate measurement, $\mathbf{z}_{k|k-1}^{i,j}$                ▷ Eq. (4.9)
                    end for
                    Calculate $\mathbf{x}_{k|k-1}^j$ and $\mathbf{y}_{k|k-1}^j$             ▷ as per Sec 4.2.2
                    Evaluate overall innovation ($\varepsilon_k^j$)             ▷ as per Sec 4.2.2
                    Compute covariances $C_k^{j,xz}$ and $\mathbf{S}_k^j$ and $\mathbb{G}_k^j$   ▷ as per Sec 4.2.2
                    Correction: Correct predicted state estimate      ▷ Eq. (4.11)
                end procedure
                Calculate the ensemble mean of the corrected state, i.e., $\mathbf{x}_{k|k}^j$
            end for
        end procedure
        procedure Particle re-sampling($\{\xi_k^j\}$)
            For each $\xi_k^j$, calculate $w(\xi_k^j)$                      ▷ Eq. (4.12)
            Update: $\mathbf{x}_{k|k}$, $\boldsymbol{\xi}_{k|k}$, as their weighted mean        ▷ Eq. (4.13)
        end procedure
    end for
end procedure
```

The proposed algorithm is validated using a damaged beam that contains a crack. In order to simulate the effects of a crack present in the substructure element, an exponential function for stiffness reduction, denoted as $EI(x)$, is employed. Here, x represents the position along the rectangular beam element, and this function accounts for the variations in stiffness as employed in this chapter Christides and Barr (1984).

$$EI(x) = \frac{EI}{1 + C\exp^{((-2\beta|x-l_c|)/d_c)}} \tag{4.14}$$

where $C = (I_e - I_c)/I_c$ for $I_c = w(d - d_c)^3/12$. The constant β, estimated from experiments as in Christides and Barr (1984), is found to be 0.6667. To simulate the crack in the third element of the substructure, specific crack attributes are considered. The crack depth (d_c) is set to 0.0045 m, and its position (l_c) is located at a distance of 0.375 m from the fixed end Khatir et al. (2018).

The beam is subjected to an SWGN $\mathcal{N}(0, 1e^{-5}N)$ force applied to each node of the structure for a time window of 1 s, with a sampling frequency of 1000 Hz. Acceleration responses are recorded at each node of the substructure element. To simulate real-life scenarios, the dynamic response measurements collected at the nodes are contaminated with SWGN of snr of 1%. The initial distribution of the parameters followed a normal distribution $\mathcal{N}(1, 0.02)$, with the parameter α set to 0.98 (refer to Equation (4.7)). In the numerical experiment, 2000 particles are used for the PF, and 500 ensembles are utilized for EnKF.

In Figure 4.4, the convergence of parameters to their true values is shown for both undamaged and damaged elements. Additionally, Figure 4.5 compares the estimated and measured acceleration of an internal *dof*. The results indicate that the simple substructure algorithm, assuming the availability of acceleration response, accurately and precisely estimates the measurement response and parameters for damaged cases, even under a noise severity of 1% *snr*. This algorithm offers computational efficiency by monitoring only a specific subdomain of interest while providing prompt estimation. The performance evaluation on a numerical cantilever beam demonstrates that the simple substructure algorithm is accurate, precise, and efficient.

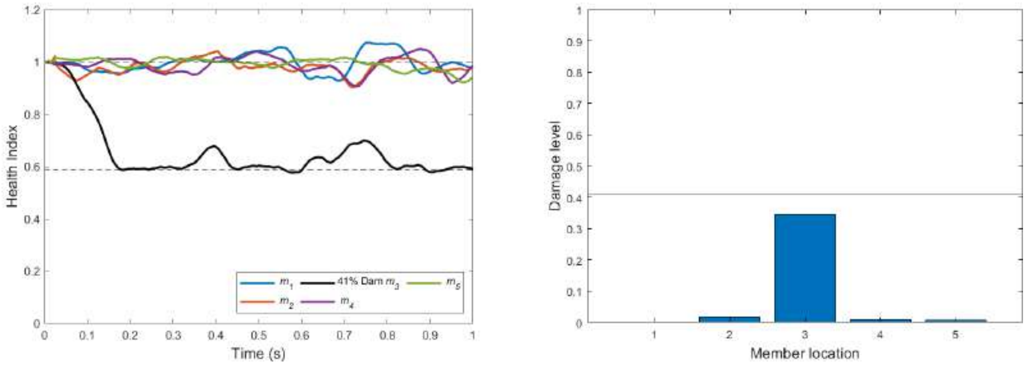

(a) Identifying damage by time domain.

(b) Identifying damage by mean calculation.

Figure 4.4: Estimated parameter of a substructure beam element for damage case (*dashed lines represent respective actual values*).

4.2.4 Challenges with simple substructure techniques

The simple substructure-based monitoring approach described in this work requires extensive monitoring of all the interfaces, which are typically inaccessible in real structures. Additionally, this approach creates interdependencies among all the substructure models. To address these limitations and develop a

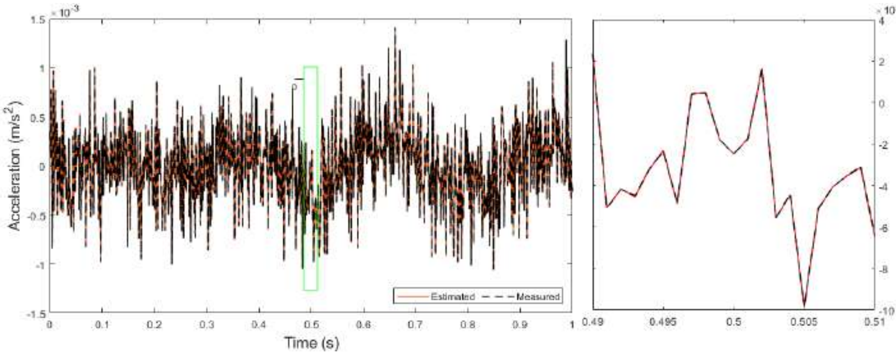

Figure 4.5: Recreating the internal response from the estimated states.

component-wise monitoring algorithm, Yuen and Katafygiotis (2006) introduced a probabilistic frequency domain approach. They employed Bayesian inference to monitor only a specific subdomain of interest.

In their study, the monitored substructures were categorized as either stable (supported subdomain with defined Dirichlet boundary conditions and no rigid motion) or unstable (unsupported subdomain with interface forces and subjected to rigid motion). The proposed approach was numerically investigated in a multi-story building to estimate parameters using recorded substructure responses under specific driving forces, such as a single-channel base excitation and a force generated by a vibrating machine. However, while both stable and unstable substructure types are discussed, the numerical experimentation focused solely on stable substructures, overlooking the importance of modeling the rigid motion of unstable substructures. Furthermore, due to its definition in the frequency domain, the approach is not an online algorithm that can be implemented in real-time.

4.3 Proposed substructure techniques

The present study proposes a novel computationally efficient online structural health assessment approach that bypasses the requirement of the interface force quantities and is also applicable for stand-alone stable as well as unstable substructures. The numerical and experimental studies have been performed on unstable substructures where substructural boundaries are set as unknown/free. The proposed approach utilizes output injection methodology Zhang and Zhang (2018); Sen et al. (2021) in order to be robust to variations in the interface force/acceleration with the help of known measurement data of the internal nodes of the particular substructure. This makes targeted health monitoring of the substructure possible, without the need of monitoring the other substructures. An interacting filtering strategy combining PF and EnKF (IPEnKF), for the estimation of health parameters and states respectively, has been utilized in this attempt. Complexity in system estimation depends majorly on observability issues (generally originating from lack of instrumentation) rather than the physical size or geometric complexity of the system. Accordingly, both numerical and experimental validations of the proposed algorithm have been undertaken on a minimally instrumented simply supported beam. Further, noise sensitivity, limiting damage severity, and required sensor density to assess the scalability of the algorithm have also been investigated for the proposed approach. The need for information on boundary conditions for SHM of a structure can also be bypassed with the proposed algorithm, which has been demonstrated later in this chapter with numerical and experimental studies.

4.3.1 Improvisation in dynamics of simple substructure

The isolated dynamics of the simple substructure described by Equation (4.3) undergo additional modifications. The motion of the internal *dof*s, i.e., $\mathbf{q}_i^s(t)$, can further be represented as a summation of a quasi-static ($\mathbf{q}_i^{s,d}$) and a relative ($\mathbf{q}_i^{s,r}$) component Koh and Shankar (2003), wherein the quasi-static component ($\mathbf{q}_i^{s,d}$) provides a rigid body motion to the subdomain Ω^{s_i} and relative component ($\mathbf{q}_i^{s,r}$) enables relative (/flexible) motion. Thereby, the overall response can be defined as:

$$\mathbf{q}_i^s = \mathbf{q}_i^{s,r} + \mathbf{q}_i^{s,d} \tag{4.15}$$

$\mathbf{q}_i^{s,d}$ can further be obtained by forcing all the force components and time-derivative terms in Equation (4.3) to zero while assuming the boundary to be free, as

$$\mathbf{q}_i^{s,d} = -{\mathbf{K}_{ii}^s}^{-1}\mathbf{K}_{ib}^s\mathbf{q}_b^s = \eta^s\mathbf{q}_b^s \tag{4.16}$$

with η^s acting as a transmissibility term correlating boundary to internal responses. Further, substituting $\mathbf{q}_i^s(t)$ in Equation (4.3), the following can be obtained,

$$\begin{aligned}\mathbf{M}_{ii}^s(\ddot{\mathbf{q}}_i^{s,r} + \ddot{\mathbf{q}}_i^{s,d}) + &\mathbf{C}_{ii}^s(\dot{\mathbf{q}}_i^{s,r} + \dot{\mathbf{q}}_i^{s,d}) + \mathbf{K}_{ii}^s(\mathbf{q}_i^{s,r} + \mathbf{q}_i^{s,d}) \\ &= \mathbf{f}_i^s - \mathbf{M}_{ib}^s\ddot{\mathbf{q}}_b^s - \mathbf{C}_{ib}^s\dot{\mathbf{q}}_b^s - \mathbf{K}_{ib}^s\mathbf{q}_b^s\end{aligned} \tag{4.17}$$

Next, the relative dynamics of the substructure can be isolated from the above equation by considering all terms pertinent to the rigid dynamics of the substructure as an external force and subsequently addressing them jointly with external and resisting forces (right side of Equation (4.17)).

$$\begin{aligned}&\mathbf{M}_{ii}^{s}\ddot{\mathbf{q}}_{i}^{s,r}+\mathbf{C}_{ii}^{s}\dot{\mathbf{q}}_{i}^{s,r}+\mathbf{K}_{ii}^{s}\mathbf{q}_{i}^{s,r}\\&=\mathbf{f}_{i}^{s}\;-\mathbf{M}_{ib}^{s}\ddot{\mathbf{q}}_{b}^{s}-\mathbf{C}_{ib}^{s}\dot{\mathbf{q}}_{b}^{s}-\mathbf{K}_{ib}^{s}\mathbf{q}_{b}^{s}-\mathbf{M}_{ii}^{s}\ddot{\mathbf{q}}_{i}^{s,d}-\mathbf{C}_{ii}^{s}\dot{\mathbf{q}}_{i}^{s,d}-\mathbf{K}_{ii}^{s}\mathbf{q}_{i}^{s,d}\end{aligned} \tag{4.18}$$

Because of the general nature of a typical linearly damped mechanical system, its system matrices are banded and sparse leading to very feeble interaction between two distant nodes. With internal and boundary nodes segregated, the insignificant off-diagonal terms associated with cross-coupling between these distant node sets, i.e., internal and boundary nodes, therefore, can be ignored without affecting the generality. Moreover, the impact of the ignored part of damping will surely be overshadowed by the noise which is more significant, as verified later on. Thus, the minuscule damping can be ignored in the modeling and can still be accounted for in the model by including it in the modeling error process. Thereby, the insignificant amount of damping force, i.e. $(\mathbf{C}_{ii}^{s}\dot{\mathbf{q}}_{i}^{s,d}+\mathbf{C}_{ib}^{s}\dot{\mathbf{q}}_{b})$ has been considered under the process uncertainty (discussed later) and removed from the dynamics from now on.

$$\mathbf{M}_{ii}^{s}\ddot{\mathbf{q}}_{i}^{s,r}+\mathbf{C}_{ii}^{s}\dot{\mathbf{q}}_{i}^{s,r}+\mathbf{K}_{ii}^{s}\mathbf{q}_{i}^{s,r}=\mathbf{f}_{i}^{s}\;-\mathbf{M}_{ib}^{s}\ddot{\mathbf{q}}_{b}^{s}-\mathbf{K}_{ib}^{s}\mathbf{q}_{b}^{s}-\mathbf{M}_{ii}^{s}\ddot{\mathbf{q}}_{i}^{s,d}-\mathbf{K}_{ii}^{s}\mathbf{q}_{i}^{s,d} \tag{4.19}$$

Using Equation (4.16), $\mathbf{q}_{i}^{s,d}$ can be substituted with $\mathbf{q}_{b}^{s}$ as,

$$\mathbf{M}_{ii}^{s}\ddot{\mathbf{q}}_{i}^{s,r}+\mathbf{C}_{ii}^{s}\dot{\mathbf{q}}_{i}^{s,r}+\mathbf{K}_{ii}^{s}\mathbf{q}_{i}^{s,r}=\mathbf{f}_{i}^{s}\;-\mathbf{M}_{ib}^{s}\ddot{\mathbf{q}}_{b}^{s}-\mathbf{K}_{ib}^{s}\mathbf{q}_{b}^{s}-\mathbf{M}_{ii}^{s}\eta^{s}\ddot{\mathbf{q}}_{b}^{s}+\mathbf{K}_{ii}^{s}\mathbf{K}_{ii}^{s\,-1}\mathbf{K}_{ib}^{s}\mathbf{q}_{b}^{s} \tag{4.20}$$

and, further can be simplified as,

$$\mathbf{M}_{ii}^{s}\ddot{\mathbf{q}}_{i}^{s,r}+\mathbf{C}_{ii}^{s}\dot{\mathbf{q}}_{i}^{s,r}+\mathbf{K}_{ii}^{s}\mathbf{q}_{i}^{s,r}=\mathbf{f}_{i}^{s}-(\mathbf{M}_{ib}^{s}+\mathbf{M}_{ii}^{s}\eta^{s})\ddot{\mathbf{q}}_{b}^{s} \tag{4.21}$$

4.3.2 State-space formulation of substructure

Finally, the system dynamics defined in physical space can be cast in the corresponding state-space, considering only the boundary acceleration response as,

$$\dot{\mathbf{x}}^{s}\left(t\right)=\mathbf{A}^{s}\left(t\right)\mathbf{x}^{s}\left(t\right)+\mathbf{B}^{s}\left(t\right)\mathbf{u}^{s}(t)+\;\mathbf{E}^{s}\left(t\right)\ddot{\mathbf{q}}_{b}^{s}(t)+\mathbf{v}^{s}\left(t\right) \tag{4.22}$$

where, $\mathbf{x}^s(t) = \begin{Bmatrix} \mathbf{q}_i^{s,r} \\ \dot{\mathbf{q}}_i^{s,r} \end{Bmatrix}$, $\mathbf{E}^s(t) = \begin{bmatrix} \mathbf{0}_{n_i} \\ -(\mathbf{M}_{ii}^{s\ -1}\mathbf{M}_{ib}^s + \eta^s) \end{bmatrix}$ and other terms are same as in Equation (4.4). The additional term $\mathbf{v}^s(t)$ represents process uncertainty (due to modeling inaccuracies, unmodelled input, damping, etc.), which is modeled as an SWGN of constant covariance $\mathbf{Q}^v$. The measurable acceleration responses $\ddot{\mathbf{q}}_i^s$ correspond to total acceleration due to pseudo-static ($\ddot{\mathbf{q}}_b^{s,d}$) and relative ($\ddot{\mathbf{q}}_b^{s,r}$) response components combined as $\mathbf{y}^s(t)$.

$$\begin{aligned} \mathbf{y}^s(t) &= S\{\ddot{\mathbf{q}}_i^{s,r}(t) + \eta^s\ddot{\mathbf{q}}_b^s(t)\} \\ &= S\{\mathbf{H}^s(t)\mathbf{x}^s(t) + \mathbf{D}^s(t)\mathbf{u}^s(t) + \mathbf{L}^s(t)\ddot{\mathbf{q}}_b^s(t) + \mathbf{w}^s(t)\} \end{aligned} \tag{4.23}$$

where $\mathbf{H}^s(t), \mathbf{D}^s(t)$, and $\mathbf{L}^s(t)$ are given in Equation (4.5) and $\mathbf{w}^s(t)$ denotes measurement uncertainty, described as SWGN of known statistics, $\mathbf{R}$, as $\mathbf{w}^s(t) \sim \mathcal{N}(0, \mathbf{R})$. S represents the Boolean selection matrix defining the measured *dof*s. Since in reality, responses are discretely sampled, Equations (4.22) and (4.23) are presented in discrete time with continuous variables reproduced with their corresponding discrete-time entities.

$$\begin{aligned} &\text{Process model} &: \quad &\mathbf{x}_k^s = \mathbf{A}_k^s\mathbf{x}_{k-1}^s + \mathbf{B}_k^s\mathbf{u}_k^s + \mathbf{E}_k^s\ddot{\mathbf{q}}_{b,k}^s + \mathbf{v}_k^s \\ &\text{Measurement model} &: \quad &\mathbf{y}_k^s = \mathbf{H}_k^s\mathbf{x}_k^s + \mathbf{D}_k^s\mathbf{u}_k^s + \mathbf{L}_k^s\ddot{\mathbf{q}}_{b,k}^s + \mathbf{w}_k^s \end{aligned} \tag{4.24}$$

Selection matrix S has been dropped from the formulation assuming its impact has been adopted in the discrete-time matrices.

4.3.3 Interface robustness

With the aforementioned substructure system definition, the approach toward achieving interface robustness is discussed next. Developed with the intent to reject the impact of noise of unknown statistics from the state evolution, the output injection technique Zhang and Zhang (2018) has been exploited for eliminating the requirement of the interface measurements in this approach. By suitably injecting a part of the measured output ($\mathbf{y}_k^s$) into the state transition model, the imperative requirement of interface measurement can be alleviated. Owing to the measurement equation (cf. Equation (4.24)), the following holds true for an arbitrary bounded matrix $\mathbf{G}_k^s \in \mathbb{R}$.

$$\mathbf{0} = \mathbf{G}_k^s \left(\mathbf{y}_k^s - \mathbf{H}_k^s\mathbf{x}_k^s - \mathbf{D}_k^s\mathbf{u}_k^s - \mathbf{L}_k^s\ddot{\mathbf{q}}_{b,k}^s - \mathbf{w}_k^s\right) \tag{4.25}$$

Adding Equation (4.25) to Equation (4.24) and further setting $\mathcal{L}_k = \mathbf{I} - \mathbf{G}_k\mathbf{H}_k$, process model equation (cf. Equation (4.24)) can be modified as,

$$\begin{aligned}\mathbf{x}_k^s =& \mathbf{A}_k^s\mathbf{x}_{k-1}^s + \mathbf{B}_k^s\mathbf{u}_k^s + \mathbf{E}_k^s\ddot{\mathbf{q}}_{b,k}^s + \mathbf{v}_k^s + \mathbf{G}_k^s \left(\mathbf{y}_k^s - \mathbf{H}_k^s\mathbf{x}_k^s - \mathbf{D}_k^s\mathbf{u}_k^s - \mathbf{L}_k^s\ddot{\mathbf{q}}_{b,k}^s - \mathbf{w}_k^s\right)\\ =& \widetilde{A}_k^s\mathbf{x}_{k-1}^s + \widetilde{B}_k^s\mathbf{u}_k^s + \widetilde{E}_k^s\ddot{\mathbf{q}}_{b,k}^s + \mathbf{G}_k^s\mathbf{y}_k^s + \widetilde{\mathbf{v}}_k^s\end{aligned} \tag{4.26}$$

with $\widetilde{A}_k^s = \mathcal{L}_k^s\mathbf{A}_k^s, \widetilde{B}_k^s = \mathcal{L}_k^s\mathbf{B}_k^s - \mathbf{G}_k^s\mathbf{D}_k^s, \widetilde{E}_k^s = \mathcal{L}_k^s\mathbf{E}_k^s - \mathbf{G}_k^s\mathbf{L}_k^s$, and $\widetilde{\mathbf{v}}_k^s = \mathcal{L}_k^s\mathbf{v}_k^s - \mathbf{G}_k^s\mathbf{w}_k^s$. If $\mathbf{G}_k^s$ is chosen such that $\mathbf{G}_k^s = \mathbf{E}_k^s(\mathbf{H}_k^s\mathbf{E}_k^s + \mathbf{L}_k^s)^\dagger$ with † denoting Moore-Penrose Pseudo-inverse operation, $\widetilde{E}_k^s$ renders to a null matrix. Equation (4.26) is then transformed to Equation (4.27), with no dependency on the boundary measurements, $\ddot{\mathbf{q}}_{b,k}^s$, as,

$$\mathbf{x}_k^s = \widetilde{A}_k^s\mathbf{x}_{k-1}^s + \widetilde{B}_k^s\mathbf{u}_k^s + \mathbf{G}_k^s\mathbf{y}_k^s + \widetilde{\mathbf{v}}_k^s \tag{4.27}$$

with, Equation (4.27) showing the dependence of $\mathbf{x}_k^s$ on known states ($\mathbf{x}_{k-1}^s$), and internal *dof* measured response, $\mathbf{y}_k^s$, only. Thus, with the proposed approach, states of substructure s can be estimated without measuring the interface response.

However, the measurement equation, as in Equation (4.24), is dependent on the unknown interface response. To alleviate this, the measurement equation has been transformed through pre-multiplying with a suitably chosen matrix $\mathbf{T}_k^s$ such that $\mathbf{T}_k^s\mathbf{L}_k^s = 0$. This leads to the following transformed measurement equation,

$$\mathbf{z}_k^s = \widetilde{H}_k^s\mathbf{x}_k^s + \widetilde{D}_k^s\mathbf{u}_k^s + \widetilde{w}_k^s \tag{4.28}$$

wherein, $\mathbf{z}_k^s = \mathbf{T}_k^s\mathbf{y}_k^s$, $\widetilde{H}_k = \mathbf{T}_k^s\mathbf{H}_k^s$, $\widetilde{D}_k = \mathbf{T}_k^s\mathbf{D}_k^s$ and $\widetilde{w}_k^s = \mathbf{T}_k^s\mathbf{R}$. Eventually, this needs the estimate for the transformation matrix $\mathbf{T}_k^s$ which is the left null space of $\mathbf{L}_k^s$. Taking into account an unknown and unmeasured perturbation in the measurement equation is a novelty compared to past output injection approaches.

4.4 Numerical experiment

The proposed approach has been validated with numerical experiments to establish its efficacy. In this study, the numerical experiment is carried out using a finite element model of a prismatic simply supported beam with geometric properties: span $= 3\ m$, area $= 0.013 \times 0.013\ m^2$, and material properties: mass density $(\rho) = 7850\ kg/m^3$ and elastic modulus $(E) = 200\ GPa$. The numerical model of the beam is divided into 10 equal parts as elements, with each element being modeled as a two-noded Euler-Bernoulli beam with two dofs at each node (vertical and rotational). In the following, the usual simulation strategy adopted in this study has been detailed. The states and parameters are estimated using the formulated equations, employing an IPEnKF Kuncham et al. (2023), as discussed in Section 4.2.2.

The model is simulated under an SWGN forcing $(\mathcal{N}(0, 1e^{-3}N))$ exerted on each dof (both vertical and rotational) of the structure for a time window of 60 s. Assuming the numerical beam is instrumented at its fifth element/substructure, i.e., M_5, the element is further discretized into six more elements. This leads to the introduction of five internal nodes within element M_5. The simulation recorded the responses at these internal nodes (cf. Figure 4.6) at a sampling frequency of 50 Hz (i.e. $dt = 0.02\ s$). To mimic real-life scenarios, recorded response measurements are further contaminated with SWGN of snr of 1%.

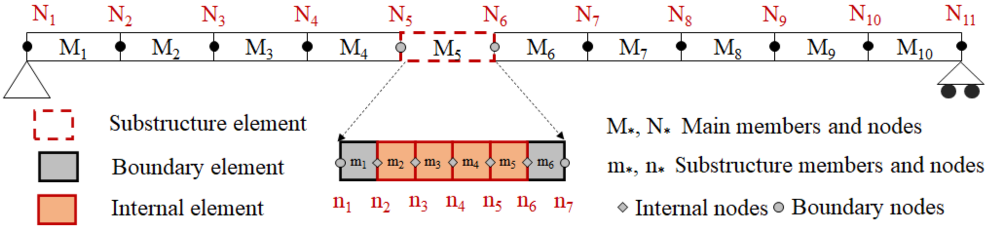

Figure 4.6: Schematic diagram of a simply supported beam model with its substructure.

For simulating damage scenarios, damage in the beam is introduced by reducing the bending stiffness (EI) of the constituent element/s. The numerical validation has been performed under several operational conditions: reduced instrumentation, plausible damage, noise severities, estimation for a longer time, etc. For each of the cases, the reduction of EI, noise snr levels, damage location and severity, sensor number, and simulation time have been altered accordingly while keeping the sampling frequency fixed at 50 Hz. All simulation conditions adopted in this study are detailed in Table 4.1.

Table 4.1: Numerical simulations with different scenarios.

Objective	Scenario name	N_{s_i}	$\mathbf{HI}_{act}$ (internal)	D_l	snr (%)
SS boundary are fixed	S1-BC	10	0.6	m_3	1
SS measurement as SWGN	S2-SWGN	10	0.6	m_3	1
SS boundary are known	S3-BM	10	0.6	m_3	1
Proposed SS with robustness	S4-ROBUST	10	0.6	m_3	1
Damage quantification	S5-DQ	10	1	m_3	1
		10	0.8	m_3	1
		10	0.6	m_3	1
		10	0.2	m_3	1
Damage location away from the SS	S6-DL	10	1	M_2 & M_9	1
		10	1	M_4 & M_6	1
		10	0.2	m_5 & M_6	1
Double damage	S7-DD	10	0.6 in m_3 & 0.4 in m_4		1
No. of interior sensors	S8-NIS	8	0.6	m_3	1
		6	0.6	m_3	1
Noise sensitivity test	S9-NST	10	0.6	m_3	2
		10	0.6	m_3	5
		10	0.6	m_3	10
Stability check	S10-SC	10	0.6	m_3	1

Here SS represent substructure, N_{s_i} denotes the number of interior sensors and D_l denotes location of damage induced.

The proposed approach has ignored the terms in the damping matrix corresponding to cross-coupling between the internal and boundary dofs assuming them to be insignificant to cause any impact on the estimation. In this study, a comparison is therefore drawn between two scenarios: one with and the other without considering those damping terms. The comparison is presented in Figure 4.7 wherein it can be verified that the neglected damping terms are in fact very small and therefore should not affect the estimation if neglected. Figure 4.7b presents the relative error between the presence and absence of damping which corresponds to an *snr* ratio of 0.006%, much smaller compared to the minimum level of sensor noise assumed, i.e. 1%.

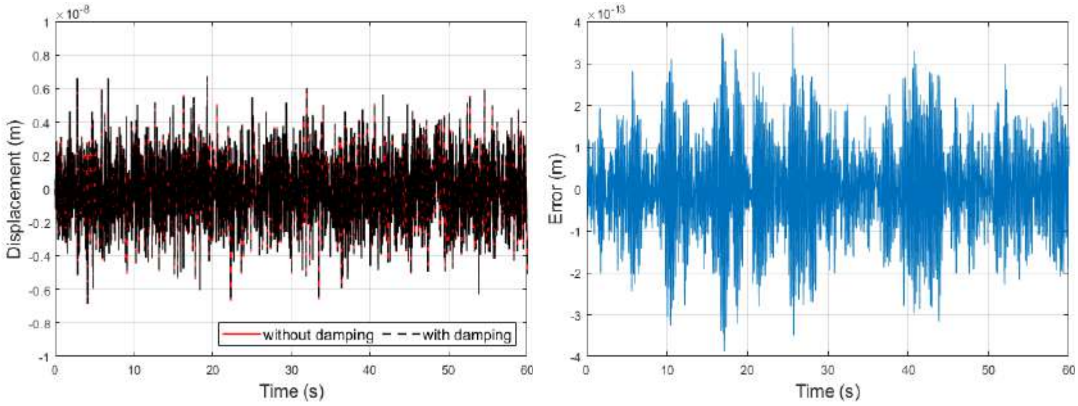

(a) Comparison of displacement. (b) Error b/w estimated and measured states.

Figure 4.7: Comparison of states corresponding to the presence and absence of damping.

Initially, the value of the parameters (health indices) is assumed to be unknown for both the undamaged and damaged cases. For system estimation purposes, the initial distribution of the parameter is assumed to have a mean of 1 (corresponding to a 100% healthy state) with a 2% variance, i.e., $\mathcal{N}(1, 0.02)$. Meanwhile, the tuning parameter, α is set to 0.99 (cf. Equation (4.8)) based on previous experience with IPEnKF Sen et al. (2021). The response recorded from the substructure under consideration (in this case M_5) is used along with the substructured predictor model. For the PF simulation, 2000 particles are used while the EnKF is simulated with 100 ensembles.

4.4.1 Justification of the proposed algorithm

Prior to the validation of the proposed algorithm, the need for this approach has to be established. For this, the same system response has been processed with four different estimation approaches: 1. The substructured (M_5) model is assumed with fixed end nodes (boundaries), 2. M_5 is assumed with SWGN boundary forces, 3. M_5 is estimated by supplying the actual boundary forces as if they have been measured and finally, 4. M_5 is estimated with the proposed algorithm. For all the cases the simulated measurement response is run through the same IPEnKF strategy, but the substructure support FEM model is different according to the mentioned cases. The comparative study is presented in Figure 4.8, wherein it can be verified that while with the first two assumptions (cf. Figures 4.8a and 4.8b), the estimation of the health indices is not possible, the third assumption yielded prompt and smooth estimation (cf. Figure 4.8c). However, for the fourth experiment which avoids the boundary estimation (cf. Figure 4.8d), the results are found to be similar to the case when the actual boundary measurements are supplied (case 3). This illustrates that the proposed method has successfully alleviated the requirement of boundary response measurement without sacrificing the estimation accuracy.

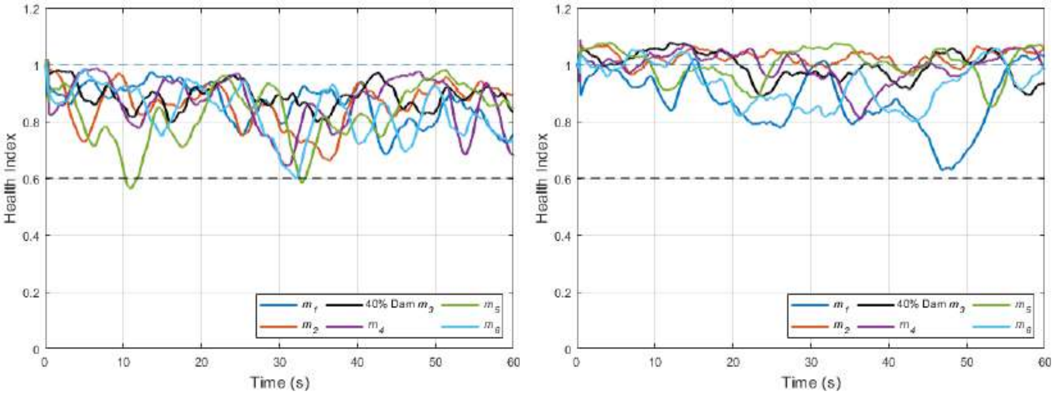

(a) Estimation assuming fixed boundary conditions (S1-BC).

(b) Estimation assuming SWGN forcing on the boundary (S2-SWGN).

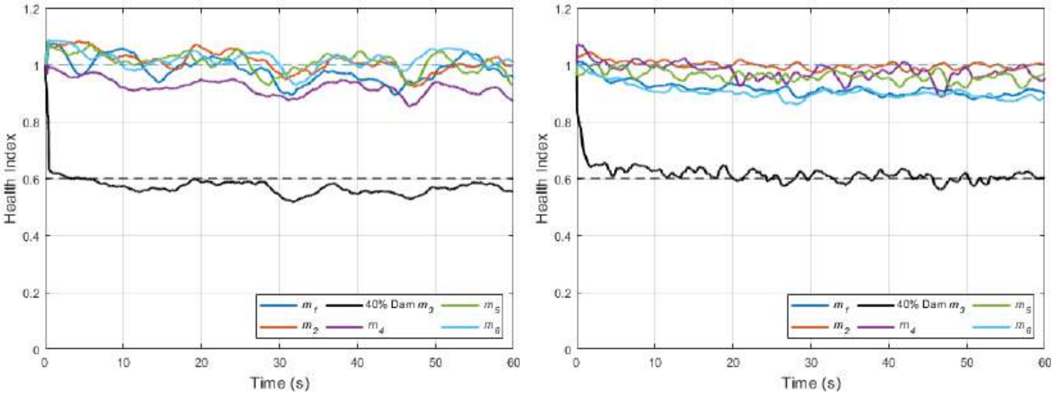

(c) Estimation with boundary forces as known (S3-BM).

(d) Estimation with the proposed method (S4-ROBUST).

Figure 4.8: Estimation of health indices under different conditions (*dashed lines represent respective actual values*).

The predicted measurements obtained from the estimated states with the proposed approach are further compared with their actual values obtained during simulation. Figure 4.9a presents the comparison between the true states and their estimation with the proposed approach. Figure 4.9b depicts the relative difference between the measured and estimated acceleration which corresponds to an *snr* of 0.9%. Considering that uncorrelated uncertainties originating from multiple sources are additive, a significant modeling error would result in an increase of the observed uncertainty above the expected level, i.e. the 1% noise level. Since the estimated *snr* is at 0.9%, similar to the noise level, it is deduced that the modeling error can be considered negligible since it does not impact significantly the response estimation and the proposed approach.

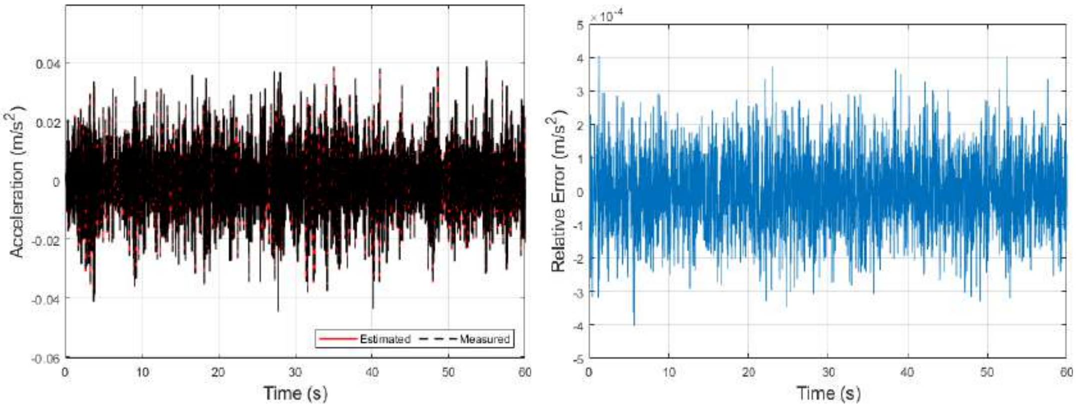

(a) Comparison of acceleration.

(b) Error b/w estimated and measured.

Figure 4.9: Comparison of reconstructed internal response to the actual measurement response.

4.4.2 Sensitivity to damage severity

Further, the sensitivity of the proposed algorithm for different levels of damage severity is investigated. For this, four different damage levels are experimented with, i.e. 20%, 40%, 60%, and 80% along with the undamaged condition. Accordingly, the element elasticity of one element of the numerical beam is reduced by the corresponding percentage to simulate damage. It has been perceived that the proposed approach is equally efficient for all the mentioned damage levels while the estimation has been observed to be smoother (less fluctuating) for higher damage levels, cf. Figure 4.10. Alongside, the undamaged condition has also been detected precisely with no instances of false alarms.

4.4.3 False alarm sensitivity

Next, the false alarm sensitivity of the algorithm is investigated. In this attempt, two aspects have been emphasized: 1. health deterioration owing to

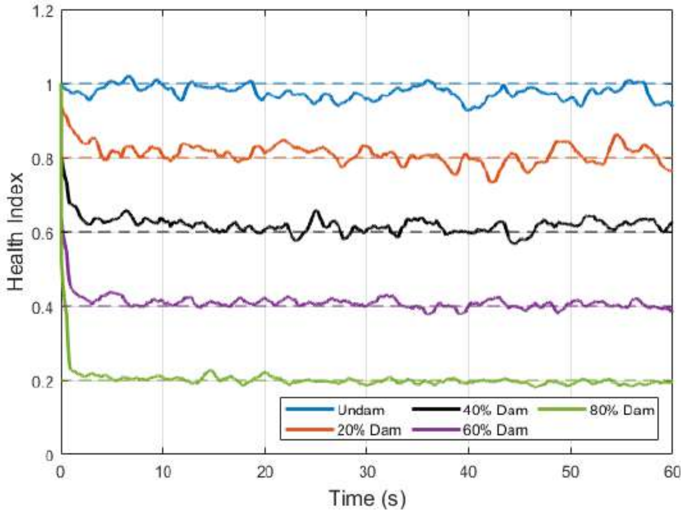

Figure 4.10: Detection of various damage levels (S5-DQ) in the element m_3 with the proposed approach (*dashed lines represent respective actual values*).

incurred damage/s in the substructure should be detected with precision (this also refers to identifying healthy states causing no false positive alarm and multi-damage scenario causing no false negative alarm) and 2. damage in other parts of the structure should not get confused with damage in the monitored substructure and consequent raising of any false positive alarm. Moreover, the required sensor density to ensure such robustness against false alarms is required to be investigated.

Accordingly, two experiments are firstly performed in which adjacent and distant elements of the monitored substructure are damaged while keeping the domain of concern undamaged. The first experiment assumes damage in the vicinity of the monitored substructure (M_5), i.e., M_4 and M_6 while the second experiment assumes damage in locations (M_2 and M_9) away from the concerned substructure M_5. The results are presented in Figure 4.11. It can be verified that for both cases, the proposed approach identified the health indices of the monitored substructure M_5 and was not confused by the presence of damage elsewhere in the structure. A separate case study (cf. Table 4.1) is also undertaken wherein two adjacent elements are damaged: one within the monitored substructure (m_5) while the other outside (M_6) is the monitored domain. The proposed approach is observed to detect damage in the monitored element without being deterred by the damage in the adjacent element.

The capability of the proposed algorithm to assess health under multiple damages within the substructure has also been envisaged in order to establish that

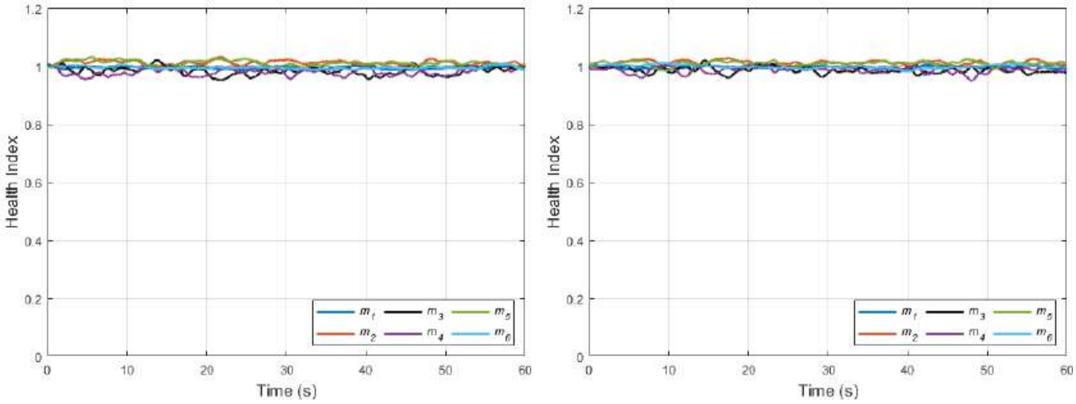

(a) With 40% damage in M_4 and M_6. (b) With 40% damage in M_2 and M_9.

Figure 4.11: False alarm sensitivity (S6-DL) with near and far damage locations (*dashed lines represent respective actual values*).

the proposed method can identify the location and severity of damage distinctly without suppression or false detection of damage elsewhere within the monitored substructure. The estimation results are presented in Figure 4.12a which establishes that the proposed approach performs efficiently even with multiple damage scenarios without failure.

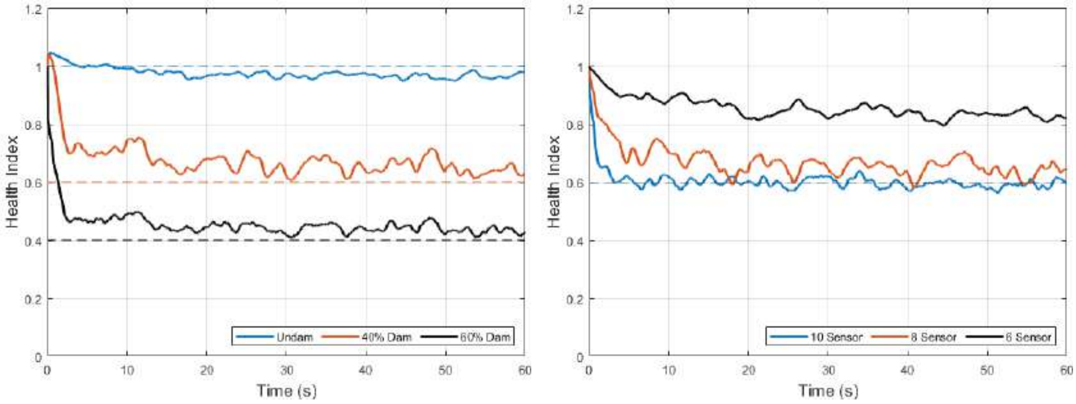

(a) Health assessment under multiple damage scenario (S7-DD). (b) Sensitivity to instrumentation density (S8-NIS).

Figure 4.12: Performance of the proposed algorithm under different operating scenarios (*dashed lines represent respective actual values*).

Moreover, a separate experiment is also performed under different instrumentation densities: a number of 6, 8, and 10 of measurement channels are therefore employed for the estimation (cf. Figure 4.12b). It should be noted that since a total of four channels of boundary measurements are being rejected in this numerical experimentation, the employment of a minimum of five channels of measurement becomes imperative. Accordingly, the minimum number of channels for the experiment is selected to be 6. However, it has been observed that mere 6 channels render the problem to be very ill-posed leading to missed detection while 8 and 10 channels have successfully estimated the location and severity of stiffness deterioration.

4.4.4 Noise severity

The noise severity has been investigated under four different noise levels, i.e., 1%, 2%, 5%, and 10% *snr*. As expected, it has been observed (cf. Figure 4.13a) that while the proposed algorithm has been successful in identifying deteriorating health under the mentioned noise severity levels, higher noises are perceived to cause more fluctuations in the estimation. Further, the stability of the algorithm has been tested by subjecting it to longer time series data, and the pertinent results are presented in Figure 4.13b. The insets in the right figure present the evolution of HIs corresponding to one damaged and one undamaged element. The health estimation has been observed to be non-divergent and smooth even for prolonged usage, with no evidence of error accumulation or instability. The temporal variation of particles (health indices) corresponding to both damaged and undamaged elements has been plotted with a 95% confidence interval for a better understanding of the Bayesian filtering-based approach.

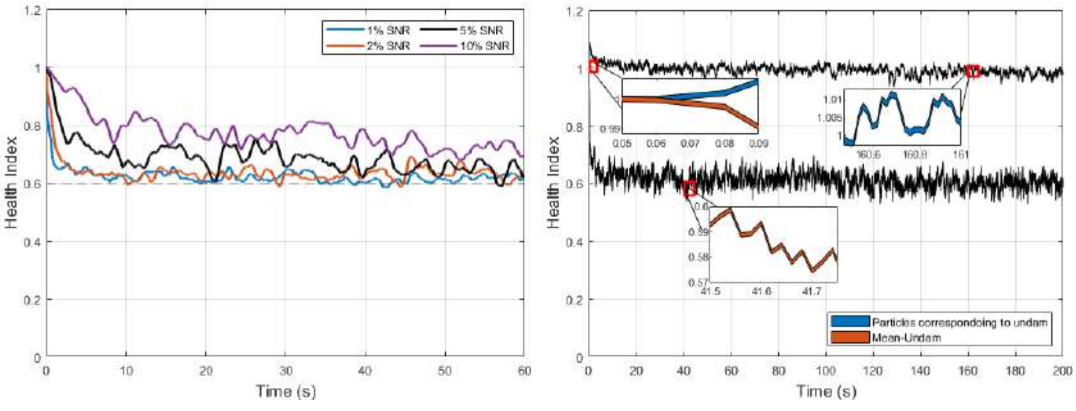

(a) Sensitivity to noise severity (S9-NST). (*The dashed line represents the actual* ***HI***)

(b) Check for the stability of the algorithm (S10-SC).

Figure 4.13: Noise sensitivity and stability performance of the proposed algorithm.

The performance of the proposed approach in terms of estimated **HI** and corresponding error has been summarized in Table 4.1 for the case studies undertaken. The estimation means over the last 100 iterations for **HI**s along with their respective root mean square error (RMSE) are presented in Table 4.2.

Table 4.2: Summarised performance of the proposed method under different scenarios.

Scenario name	$\mathbf{HI}_{act}$ (internal)	Damage assessment	$\mathbf{HI}_{est}$ (mean) (internal)	Error (RMSE)
S1-BC	0.6	×	–	
S2-SWGN	0.6	×	–	
S3-BM	0.6	✓	0.57	0.06
S4-ROBUST	0.6	✓	0.61	0.02
S5-DQ	1	✓	0.97	0.04
	0.8	✓	0.82	0.03
	0.4	✓	0.40	0.02
	0.2	✓	0.20	0.01
S6-DL	1	✓	0.98	0.02
	1	✓	0.99	0.02
	0.2	✓	0.29	0.14
S7-DD	0.6 - m_3 & 0.4 - m_4	✓	0.63 & 0.43	0.04 & 0.03
S8-NIS	0.6	✓	0.65	0.05
	0.6	✓	0.82	0.22
S9-NST	0.6	✓	0.62	0.03
	0.6	✓	0.64	0.05
	0.6	✓	0.72	0.12
S10-SC	0.6	✓	0.61	0.02

4.5 Experimental validation - fixed beam

A laboratory experiment has been conducted on a fixed-fixed steel beam of a rectangular cross-section to evaluate the performance of the proposed algorithm on real-life structures. The relevant geometric properties as adopted are: span = 1.5 m, area = 261.45 mm^2, with depth 8.3 mm and a very rough estimate of the initial material properties: mass density (ρ) = 7850 kg/m^3 and elastic modulus (E) = 190 GPa. The beam is held in place by clamping both ends, which is then numerically replicated by assuming fixed-fixed boundary conditions. The proposed model-based health assessment approach replicates the real beam numerically with a 2D Euler-Bernoulli beam. The experimental beam and its numerical replica (or model) are firstly discretized into three equal parts as component substructures ($M_1,\ M_2,\ M_3$). The second substructure, i.e., M_2, is opted for independent health monitoring and is accordingly discretized into five elements. This leads to the introduction of four internal nodes within substructure M_2. The experimental details and schematic for the substructured domain are presented in Figure 4.14a and Figure 4.14b.

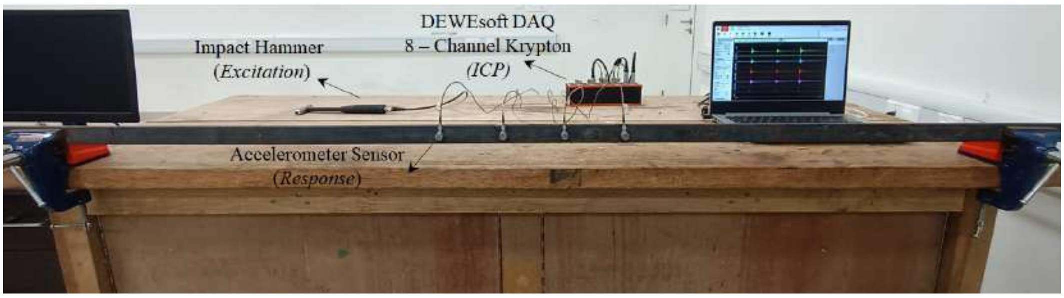

(a) Experimental setup.

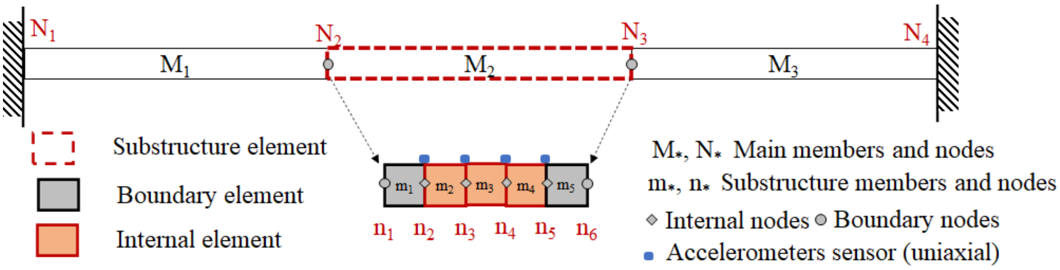

(b) Schematic numerical model of the real beam.

Figure 4.14: Experimental setup - fixed-fixed beam.

4.5.1 Bench-marking the undamaged beam

It is always advisable to calibrate the basic material properties of the numerical FEM support model with respect to the real structure. Further, it accounts for the non-homogeneous nature of the material property (Elastic Modulus) of the structure. Accordingly, the undamaged beam is excited with an impact load, and the obtained acceleration, sampled at 500 Hz, is used to estimate its frequencies. In this attempt, the material density has been found to be quite consistent with no need for any substantial calibration. However, the estimated frequencies obtained from frequency domain decomposition (FDD) of the recorded response obtained from the beam do not match with the numerically obtained frequencies where the material elasticity is assumed to be uniform throughout the length of the beam. The material elasticity is perturbed to approximately match (within acceptable limits) the numerical frequencies with the ones obtained experimentally (cf. Table 4.3), and the calibrated uniform elasticity throughout the beam length is estimated as 150 GPa.

Table 4.3: Comparison between frequencies obtained experimentally and numerically.

Data		Experimental value	Calibrated numerical	Relative error (%)
Frequency (Hz)	ω_1	16.36	16.43	0.43
	ω_2	46.02	45.71	0.67

The numerical model of the experimental setup is further benchmarked to accommodate the non-homogeneous nature of elasticity in real-life structures. This has been undertaken through the proposed health assessment algorithm. Eventually, this entails the re-calibration of the modulus of elasticity for each of the elements. For this, the substructure M_2 is instrumented with four uniaxial accelerometers placed at four equidistant internal nodes fetching structural vibration response only in the vertical dofs at a sampling frequency of 500 Hz. 100 ensembles and 2000 particles have been selected for IPEnKF with $\alpha = 0.99$ (cf. Equation (4.8)). Each element elasticity is initiated at 150 GPa which was obtained through the aforementioned calibration approach. The system health is estimated by assuming prior estimates for all the **HI**s as 1 with a standard deviation of 0.02 and subsequently, the algorithm is allowed to update them drawing inference from the time domain response data collected from the known healthy state of the test structure.

This kind of material property calibration can be considered as health indices benchmarking of a structure with an unknown health state. The **HI** estimation results are presented in Figure 4.15a where it is observed that the **HI**s converged to different values (mostly above 1). The model-predicted measurements are also compared to the actual measurements obtained from the sensors in order to validate the quality of the updated model. Since the experimental beam structure did not have any visible damage, the change in the **HI**s has been attributed to an incorrect presumption of elasticity. Accordingly, the element elasticity of the concerned substructure has been updated (cf. Table 4.4). This updated model has further been adopted as the undamaged benchmark for the experimental beam.

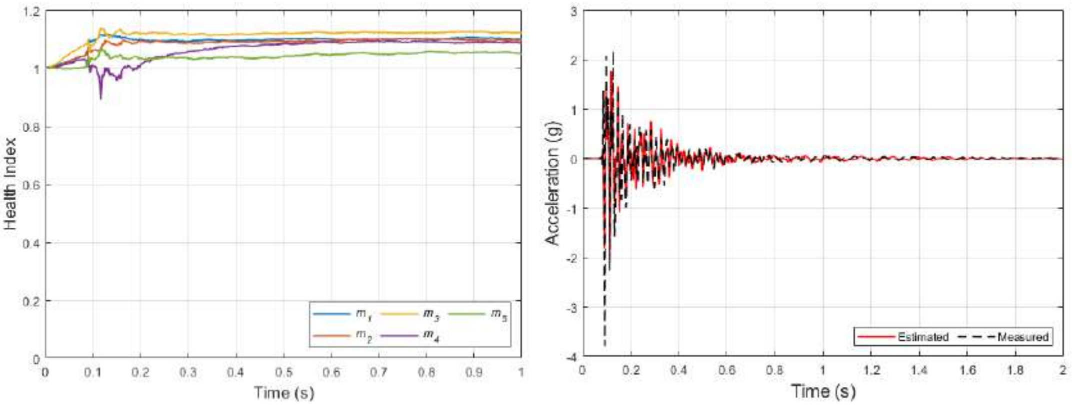

(a) Benchmarking of **HI**s for the undamaged structure.

(b) Sensor v/s numerical model predicted measurements.

Figure 4.15: Evaluation of substructure health indices and measurement data comparison for undamaged beam.

Table 4.4: Initial, and benchmarked element elastic moduli.

Elastic modulus (E)	Substructure members				
	m_1	m_2	m_3	m_4	m_5
Initial (GPa)			150.0		
Calibrated (GPa)	165.7	165.4	168.9	164.2	158.3

4.5.2 Performance of the proposed algorithm

In the following, the damage has been induced in the third element (m_3) of the second substructure (M_2). The experiment is intended to replicate the local deterioration of the structural material leading to a loss in thickness (e.g. due to spalling and scaling in concrete, corrosion and rusting in steel, etc.). For this, some material from the beam has been scrapped along its depth, reducing the depth of substructure element m_2 down to 7.26 mm (average value over the element length), which can roughly be attributed to 33.08% loss in the element stiffness (**HI** $= 0.67$). The damage in the m_3 element is shown in Figure 4.16. The damaged beam has been sampled with four uni-axial accelerometers patched at four internal nodes of the substructure at a constant sampling frequency of 500 Hz for 2 s with the rest of the hyper-parameters (required for the algorithm) being the same as mentioned in Section 4.5.1.

The proposed approach is then employed to estimate the **HI**s corresponding to each of the elements of M_2 substructure without measuring the responses at the substructural boundary nodes (n_1 and n_6, cf. Figure 4.14b). In accor-

Figure 4.16: Experimental setup - damaged structure.

dance with Section 4.4.1, the assumption of SWGN forcing on the boundaries of substructure, M_2, yields an incorrect estimation of the health indices of the substructural elements, cf. Figure 4.17a. The health estimation results, presented in Figure 4.17b, illustrate that the algorithm is capable of estimation and localization of damage without any false alarms. The estimate of the elasticity of substructural element m_3 approximately converges to 0.65 which closely matches its expectation. Further, the **HI** estimation is perceived to be very prompt, with the location of the weakened part getting detected within 0.3 s of its occurrence. The health indicators corresponding to the other non-damaged elements have also been observed to fluctuate below 1 corresponding to non-significant damage (around 10%) which can, however, be ignored from a practical viewpoint and is related to the inherent uncertainty of the statistical algorithm.

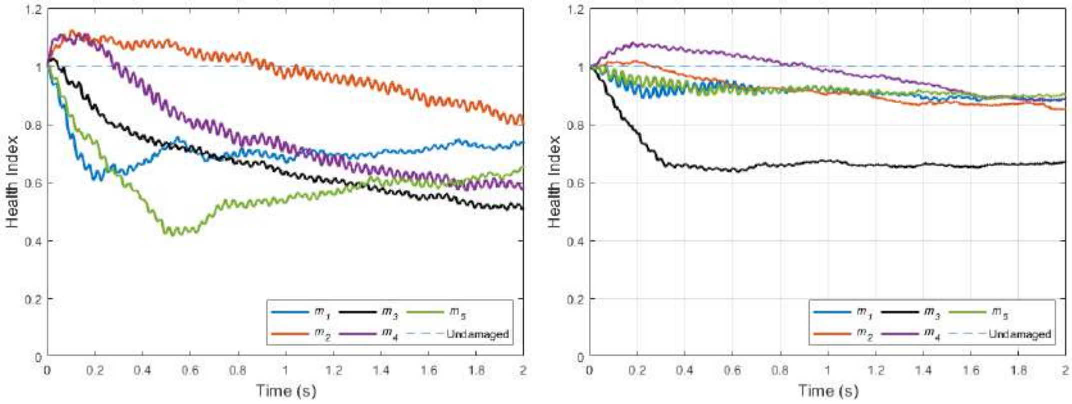

(a) Health estimation with the assumption of SWGN forcing acting on the boundary.

(b) Health estimation with the proposed approach.

Figure 4.17: Health estimation in the concerned substructure - M_2.

4.5.3 Robustness to boundary conditions

Apart from the application of the proposed algorithm for substructure monitoring, a supplementary contribution of the proposed approach is its capability to alleviate the requirement of exact boundary information. Typically structures are idealized with boundaries like free, fixed, or hinged while reality seldom conforms to this idealization. Typically, these boundary fixities have been experienced to behave like a semi-rigid joint wherein the boundary forces or displacements keep on changing during the operation of the structure. Such complex behavior can either be modeled in detail, rendering the predictor model to be complex and computationally inefficient for a recursive estimation platform, or ignored making the algorithm vulnerable to inaccurate and sometimes false estimation (false alarms). However, if the monitoring efficiency can be made independent of such boundary forces, such complications can be averted. With the proposed algorithm, the same can be achieved, detailed next.

To demonstrate this, the experimental focus is shifted from the previously considered substructure to the entire structure. The beam is now simply divided into 5 main elements and 4 uni-axial accelerometers are positioned at the internal nodes as depicted in Figure 4.18a. The actual clamped fixed boundaries of the beam are considered as the mentioned boundary dofs in the support FEM model of the proposed approach, cf. Figure 4.18b with their forces and displacements to be completely unknown to the investigator. Eventually, the model of the test structure considers a free-free beam kept in equilibrium with unknown boundary forces. Keeping all the experimental and algorithm hyper-parameters same as before (cf. Section 4.5.1), the measurement data is analyzed with the proposed algorithm in order to arrive at the health indices of the discretized elements. Figure 4.19a shows that the algorithm has promptly detected the instance of health deterioration in the element m_3 as expected, establishing the robustness of the algorithm against the boundary information.

The traditional approach is also applied to the entire structure, which considers the boundary to be fixed, and the results are compared (cf. Figure 4.19b). It can however be observed that with a presumption of fixity in the boundary, the estimated health is more severe compared to the estimation provided by the proposed approach. Since, through numerical experiments, it has already been established that with the boundary condition properly known, the proposed approach matches the actual result, it can be concluded that the presumption of the proper fixity was not exactly in the true sense. This obviously signifies the importance of the boundary robustness of the proposed algorithm even for problems wherein the boundary behavior is presumed to be known while the reality does not conform to the presumption. Eventually, with the proposed method, uncertainty caused by boundary conditions is eliminated, making it more accurate than the traditional approach.

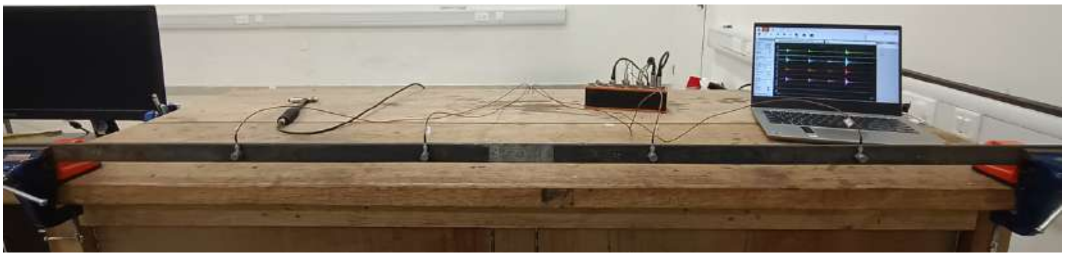

(a) Experimental setup.

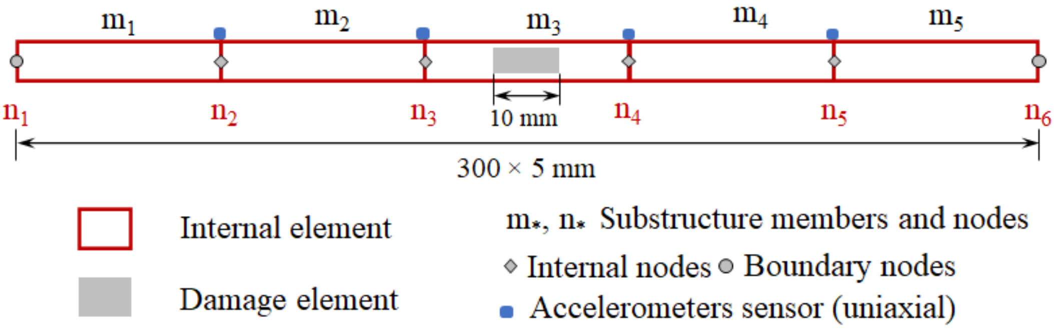

(b) Schematic numerical model of the real beam.

Figure 4.18: Experimental setup - entire structure.

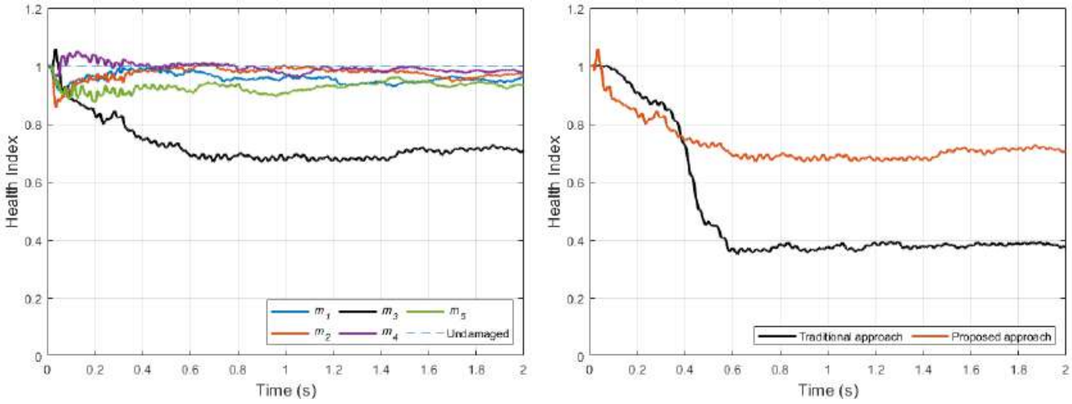

(a) Robustness of the proposed algorithm to boundary conditions.

(b) Comparison of traditional and proposed approaches.

Figure 4.19: Comparison between health estimation of the entire structure using traditional (known boundary conditions) and proposed (unknown boundary conditions) SHM methods.

4.6 Summary

The conventional process of monitoring health for fatigue life assessment typically involves deploying sensors across the entire structural domain to capture responses. However, applying the traditional approach to high-dimensional structures poses challenges due to computational demands and the need for dense instrumentation.

To address these challenges, substructuring has emerged as an effective approach for monitoring large structures. This technique involves dividing the structure into smaller subdomains, enabling more efficient and targeted analysis. Domain-wise monitoring is particularly relevant for fatigue monitoring as not the entire structure is equally susceptible to fatigue damage. In this context, a simple substructure technique is utilized as a preliminary study to assess its suitability for substructure-based monitoring approaches. A numerical experiment is conducted on a cantilever beam to demonstrate the accuracy and precision of the algorithm in estimating acceleration response and parameters for damaged cases. However, it is important to acknowledge the limitations of the simple substructure technique, such as the extensive monitoring required for all interfaces and the interdependence of substructure models.

In this study, a novel Bayesian filter-based approach is introduced to address the challenge of unavailable boundary measurements. An output injection method is employed, making the approach stand-alone, computationally efficient, and prompt in estimation. This approach also enables the utilization of a reduced number of sensors, reducing overall monitoring costs. The proposed approach combines two efficient filtering strategies, the PF and EnKF, enabling parallelization of the estimation algorithm. The interface-independent estimation approach allows complete parallelization and component-wise estimation, making it suitable for distributed health monitoring systems. The effectiveness of the proposed algorithm is validated through numerical and real experiments, confirming its accuracy, precision, and efficiency in promptly detecting, localizing, and quantifying health deterioration.

Overall, the aim of this chapter was to develop a component-wise monitoring approach that can offer computational and instrumentation benefits. Once established as efficient, this framework can be further utilized for fatigue life estimation in large structural domains.

Chapter 5

RUL prediction based on crack growth model

In the previous chapter, a method for estimating the health of individual components within structures is discussed, aiming to reduce computational requirements and instrumentation demands. This chapter builds upon that by integrating the Bayesian filtering-based approach discussed earlier into real-life civil structures that exhibit visible cracks. Additionally, it addresses the challenge of estimating the required boundary force, which may not be known or easily determined. The main focus of this chapter is the integration of substructure estimation with online fatigue life estimation. To accomplish this, we have enhanced the existing substructure technique to estimate the boundary force under vehicle loading conditions. This involves modeling the interaction between the vehicle and the structure within the dynamic simulation of the relevant bridge segment. The effectiveness of this updated substructure technique has been verified through both numerical simulations and experimental investigations. Finally, the proposed technique is applied to estimate the fatigue life of a structure experiencing visible crack growth.

5.1 Introduction

To accurately determine the RUL of a structure that has visible cracks, it is crucial to identify the critical areas where the cracks are located. This task can be achieved using a health assessment algorithm based on Bayesian filtering, as discussed earlier in the preceding chapter. Once the cracked zone is isolated, it becomes possible to monitor the growth of the cracks and assess the remaining lifespan of the structure. However, this monitoring process often requires the entire structure to be monitored, which can be burdensome, requiring extensive instrumentation and the use of expensive predictive models.

Alternatively, as described in Chapter 3, a simpler approach can be employed. This approach involves analyzing only the cracked zone, assuming external forces acting on its boundaries. However, this approximation may not provide a comprehensive solution for the entire structure. The ideal solution would involve isolating the cracked zone as a subdomain and accurately estimating the boundary forces, enabling a precise estimation of the RUL.

Chapter 4 introduced a practical technique known as substructure monitoring, which is referenced by Kuncham et al. (2023). This technique involves the numerical isolation of a relevant subdomain from the main structure and considering a specific set of boundary forces. By estimating the statistical properties of these forces within the identified subdomains, a Bayesian framework can be applied to predict the RUL of the entire bridge. This methodology focuses on the critical subdomains, allowing for more efficient and accurate RUL estimations. It facilitates targeted analysis of the areas that are most prone to fatigue, ensuring that maintenance and structural integrity efforts are directed where they are most needed.

In this chapter, the research focuses on estimating the RUL of the fatigue-prone domain in a bridge that exhibits visible cracks. The aim is to establish the correlation between the history of crack growth and fatigue loading and/or frequency. To achieve this goal, a computationally efficient approach for estimating forces at the substructure boundary is proposed. These forces are simulated by solving the coupled dynamics of the vehicle, structure, and their interactions. The methodology incorporates the output injection technique to enhance robustness. The reconstructed forces are then utilized in the IPEnKF algorithm for RUL estimation. To validate the proposed algorithm, numerical experiments are conducted on a simply supported bridge structure subjected to a half-car model with four degrees of freedom. This framework offers a practical solution for estimating the RUL of the fatigue-prone domain by considering the interplay between fatigue loading, boundary forces, and the remaining lifespan of the bridge.

Subsequently, a real-time experiment is performed on the Chandra bridge, situated in Sissu near Atal Tunnel, Himachal Pradesh. The proposed methodology is validated through this experiment, and the RUL of the bridge is predicted by considering various assumed crack growth scenarios.

5.2 Bridge-vehicle interaction

The dynamic equations of the half-car model vehicle Duan and Yang (2013) can be defined with mass $\mathbf{M}_v$, stiffness $\mathbf{K}_v$, damping $\mathbf{C}_v$ matrices, and exciting force of vibration $\mathbf{F}_v$ as

$$\mathbf{M}_v\ddot{\mathbf{y}}_v + \mathbf{C}_v\dot{\mathbf{y}}_v + \mathbf{K}_v\mathbf{y}_v = \mathbf{F}_v \tag{5.1}$$

$$\mathbf{C}_v = \begin{bmatrix} c_{s1}+c_{s2} & c_{s1}a_1 - c_{s2}a_2 & -c_{s1} & -c_{s2} \\ c_{s1}a_1 - c_{s2}a_2 & c_{s1}{a_1}^2 + c_{s2}{a_2}^2 & -c_{s1}a_1 & c_{s2}a_2 \\ -c_{s1} & -c_{s1}a_1 & c_{s1}+c_{t1} & 0 \\ -c_{s2} & c_{s2}a_2 & 0 & c_{s2}+c_{t2} \end{bmatrix},$$

$$\mathbf{K}_v = \begin{bmatrix} k_{s1}+k_{s2} & k_{s1}a_1 - k_{s2}a_2 & -k_{s1} & -k_{s2} \\ k_{s1}a_1 - k_{s2}a_2 & k_{s1}{a_1}^2 + k_{s2}{a_2}^2 & -k_{s1}a_1 & k_{s2}a_2 \\ -k_{s1} & -k_{s1}a_1 & k_{s1}+k_{t1} & 0 \\ -k_{s2} & k_{s2}a_2 & 0 & k_{s2}+k_{t2} \end{bmatrix},$$

$$\mathbf{M}_v = \begin{bmatrix} m_s & 0 & 0 & 0 \\ 0 & J & 0 & 0 \\ 0 & 0 & m_{t1} & 0 \\ 0 & 0 & 0 & m_{t2} \end{bmatrix}, \mathbf{F}_v = \begin{Bmatrix} 0 \\ 0 \\ k_{t1}y_{c1} + c_{t1}\dot{y}_{c1} \\ k_{t2}y_{c2} + c_{t2}\dot{y}_{c2} \end{Bmatrix}, \mathbf{y}_v = \begin{Bmatrix} y_s & \theta & y_{t1} & y_{t2} \end{Bmatrix}^T$$

where m_s is the mass of the body and frame of the vehicle (c.f Figure 5.1), m_{t1}, m_{t2} are the mass of the axle between the front and back wheel-set and the tires, $k_{s1}, k_{s2}, c_{s1}, c_{s2}$ are the stiffness and damping between wheel-set and body of the vehicle, $k_{t1}, k_{t2}, c_{t1}, c_{t2}$ are the stiffness and damping between of the tires, a_1, a_2 are the distances from the center of gravity to the back/front wheel set, y_{c1}, y_{c2} are the displacement on the point which the bridge contacts with the front and back wheel-set in the vertical, $\dot{y}_{c1}, \dot{y}_{c2}$ are the velocity at the point which the bridge contacts with the front and back wheel-set.

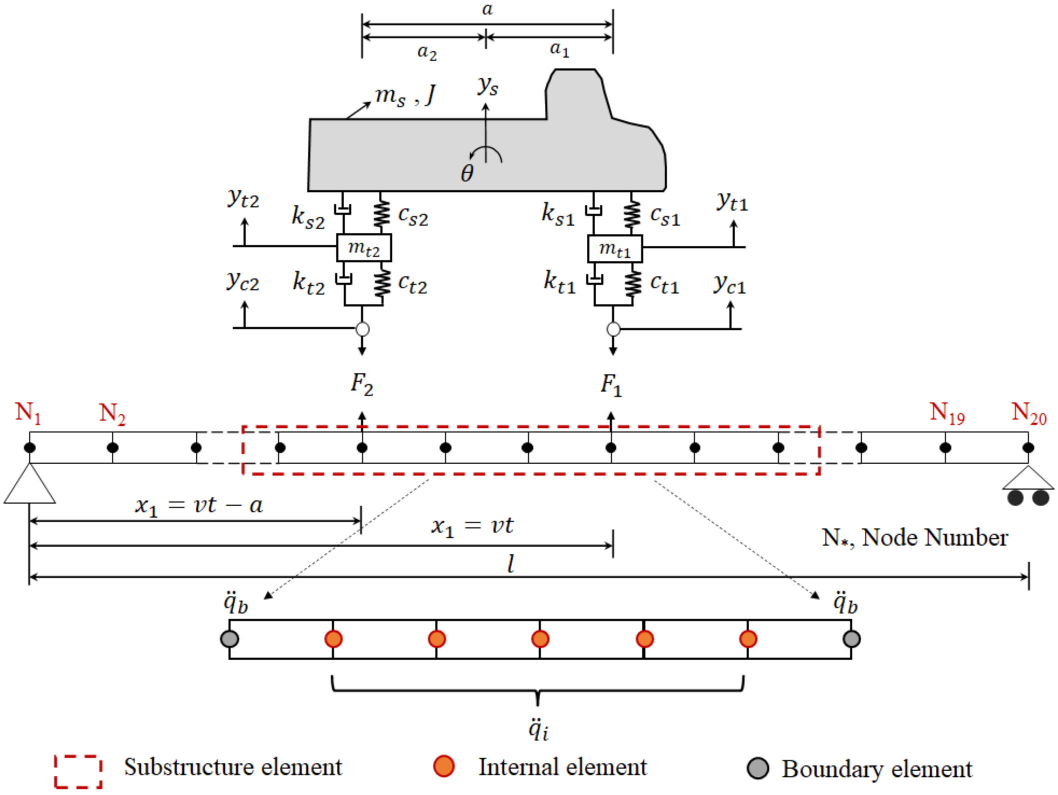

Figure 5.1: Schematic diagram of a bridge-vehicle interaction with substructure.

The modal equation for the bridge under half car model can be expressed as,

$$\ddot{\eta}_n + 2\zeta_n\omega_n\dot{\eta}_n + \omega_n^2\eta_n = -F_1(t)\phi_{1n}\delta_1 - F_2(t)\phi_{2n}\delta_2 \tag{5.2}$$

$$\phi_{1n} = \sqrt{\frac{2}{\rho l}}sin\frac{n\pi vt}{l}, \phi_{2n} = \sqrt{\frac{2}{\rho l}}sin\frac{n\pi(vt-a)}{l},$$

$$\delta_1(t) = \begin{cases} 1, 0 \leq t \leq \frac{l}{v} \\ 0, else \end{cases}, \delta_2(t) = \begin{cases} 1, \frac{a}{v} \leq t \leq \frac{l+a}{v} \\ 0, else \end{cases}$$

Here, $2\zeta_n\omega_n = \frac{\mu}{\rho}$, $\omega_n^2 = \frac{EI}{\rho}(\frac{n\pi}{l})^4$, E is Young's modulus of the bridge, I is the moment of inertia of the cross-section, ρ is the mass of the bridge per unit length, μ is the damping coefficient per unit length (l), F is the vehicle-bridge coupled force on the bridge, η is modal coordinates of the bridge, n is the number of modes considered for the vibration analysis and v is the velocity of the vehicle.

Based on the compatibility condition, the vehicle-bridge coupled function has been computed as,

$$\begin{aligned}\frac{a_2\phi_{1n}\delta_1 + a_1\phi_{2n}\delta_2}{a} m_s\ddot{y}_s + \frac{\phi_{1n}\delta_1 - \phi_{2n}\delta_2}{a} J\ddot{\theta} + \phi_{1n}\delta_1 m_{t1}\ddot{y}_{t1} + \phi_{2n}\delta_2 m_{t2}\ddot{y}_{t2} + \\ \ddot{\eta}_n + 2\zeta_n\omega_n\dot{\eta}_n + \omega_n^2\eta_n = -[\phi_{1n}W_1\delta_1 + \phi_{2n}W_2\delta_2]\end{aligned} \tag{5.3}$$

where W_i is the static load acting on the wheel due to the vehicle weight. $W_1 = (m_s\frac{a_2}{a} + m_{t1})g$, $W_2 = (m_s\frac{a_1}{a} + m_{t2})g$ and g is the acceleration due to gravity. Further converting Equation 5.3 to the standard dynamic equation of the coupled vehicle-bridge can express as follows

$$\mathbf{M}(t)\ddot{\mathbf{U}}(t) + \mathbf{C}(t)\dot{\mathbf{U}}(t) + \mathbf{K}(t)\mathbf{U}(t) = \mathbf{Q}(t) \tag{5.4}$$

Here, mass $\mathbf{M}(t)$, stiffness $\mathbf{K}(t)$, damping $\mathbf{C}(t)$ matrices for the coupled system with degrees of freedom as $\mathbf{U} = \{y_s \quad \theta \quad y_{t1} \quad y_{t2} \quad \eta_1 \quad \eta_2 \quad \cdots \quad \eta_n\}^T$ and $\mathbf{Q}(t)$ is the force on the coupled system. For detailed derivation and corresponding matrices, the reader may follow Duan and Yang (2013). Using the mode shape matrix of the bridge structure, modal domain response $\mathbf{U}$ can further be converted to time domain response denoted as $\mathbf{q}$. Accordingly, $\ddot{\mathbf{q}}$, i.e. bridge acceleration responses, are collected as measurements from where inference can be drawn during RUL estimation. Eventually, by analyzing the responses, the fatigue-prone area can be identified which can further be isolated as a substructure in order to estimate the forces acting on its boundaries.

5.3 State space formulation for boundary force estimation

Substructure technique (for detailed derivation refer to Section 4.3.2) is used to derive the state space formation of a vehicle-bridge structure (cf. Equation (5.4)) as,

$$\begin{aligned}&\text{Process model} &&: \quad \mathbf{x}_k^s = \mathbf{A}_k^s\mathbf{x}_{k-1}^s + \mathbf{B}_k^s\mathbf{u}_k^s + \mathbf{E}_k^s\ddot{\mathbf{q}}_{b,k}^s + \mathbf{v}_k^s \\ &\text{Measurement model} &&: \quad \mathbf{y}_k^s = \mathbf{H}_k^s\mathbf{x}_k^s + \mathbf{D}_k^s\mathbf{u}_k^s + \mathbf{L}_k^s\ddot{\mathbf{q}}_{b,k}^s + \mathbf{w}_k^s\end{aligned} \tag{5.5}$$

In the context of Section 4.3.2, the matrices $\mathbf{x}^s(t), \mathbf{A}^s, \mathbf{B}^s$, and $\mathbf{E}^s$ remain unchanged, while only $\mathbf{u}^s(t) = \mathbf{F}_{bv}^{int}$ is modified to account for the vehicle-bridge interaction. $\mathbf{F}_{bv}^{int}$ denotes the force acting on the internal nodes of the substructure element while $\ddot{\mathbf{q}}_b^s$ is the force acting on its boundaries. In order to eliminate the interface forces from the state equation, the output injection technique Zhang and Zhang (2018) is used and the process model and measurement model are modified (for detailed derivation refer to Section 4.3.3) as,

$$\mathbf{x}_k^s = \widetilde{A}_k^s \mathbf{x}_{k-1}^s + \widetilde{B}_k^s \mathbf{u}_k^s + \mathbf{G}_k^s \mathbf{y}_k^s + \widetilde{\mathbf{v}}_k^s \tag{5.6}$$

Hence, the Bayesian filtering approaches utilized in Chapter 4 can be employed to estimate the interface response without direct measurements. In this study, to account for real-life complexity, the stiffness parameters of the bridge have been assumed to be unknown and are therefore estimated simultaneously with the system states $\mathbf{x}_k^s$. This requires the application of the above-mentioned IP-EnKF algorithm, which decouples the estimation of states and parameters, utilizing separate filters for each. Subsequently, with the system states estimated, drawing inferences from measurements, the boundary acceleration can be reconstructed as follows:

$$\ddot{\mathbf{q}}_{b,k}^s = [\ \widetilde{E}_k^s\ ]^{-1} [\ \mathbf{x}_k^s - (\widetilde{A}_k^s \mathbf{x}_{k-1}^s + \widetilde{B}_k^s \mathbf{u}_k^s + \mathbf{G}_k^s \mathbf{y}_k^s + \widetilde{\mathbf{v}}_k^s)\ ] \tag{5.7}$$

The boundary force is then estimated by applying the inertial force as,

$$\mathbf{f}_{b,k}{}^s = \mathbf{M}_{bb} \ddot{\mathbf{q}}_{b,k}^s \tag{5.8}$$

A pseudo-code of the proposal is presented in Algorithm 3.

5.4 Numerical study

To validate the proposed algorithm, dynamic analysis has been performed on a simply supported box-girder bridge subjected to a half-car moving vehicle at a constant speed (V) of 20 *kmph*. Details of the bridge and vehicle model are given in Table 5.1. The bridge span of length $l = 60\ m$ is divided into 20 equal parts as elements which are further defined with a two-node 4 *dof*s Euler Bernoulli beam model. Following, the fatigue-prone zone in the bridge span is identified and the proposed algorithm is employed considering this domain as the monitored substructure (cf. Figure 5.1). The assumed parameters for the numerical simulation are given in Table 5.1.

Algorithm 3 Proposed boundary force estimation algorithm for substructures

```
procedure IP-EnKF($\mathbf{y}_k, \mathbf{Q}, \mathbf{R}$)
    Initialize particles $\{\xi_0^j\}$, and state estimates $\{\mathbf{x}_{0|0}^{i,j}\}$    ▷ Initial values
    for <each $k^{th}$ measurement $\mathbf{y}_k$> do
        procedure IP-EnKF($\{\xi_{k-1}^j\}, \{\mathbf{x}_{k-1|k-1}^{i,j}\}$)    ▷ Initiating EnKF
            for <each particle $\xi_k^j$> do    ▷ Initiating PF
                Evolve $\{\xi_{k-1}^j\} \rightarrow \{\xi_k^j\}$    ▷ Equation (4.8)
                procedure EnKF($\xi_k^j, \{\mathbf{x}_{k-1|k-1}^{i,j}\}, \mathbf{y}_k$)    ▷ For each $j^{th}$ particle
                    for <each ensemble $\mathbf{x}_{k-1|k-1}^{i,j}$> do
                        Prediction: Propagate state to $\mathbf{x}_{k|k-1}^{i,j}$    ▷ Equation (5.5)
                        Boundary measurement, $\ddot{\mathbf{q}}_{b,k|k-1}^{i,j}$    ▷ Equation (5.7)
                        Estimate measurement, $\mathbf{y}_{k|k-1}^{i,j}$    ▷ Equation (5.5)
                    end for
                    Mean calculation:
                    $\mathbf{x}_{k|k-1}^j$, $\mathbf{y}_{i,k|k-1}^j$    ▷ as per Section 4.2.2
                    Propagated boundary measurement, $\ddot{\mathbf{q}}_{b,k|k-1}^j = \frac{1}{N_e}\sum_{i=1}^{N_e} \ddot{\mathbf{q}}_{b,k|k-1}^{i,j}$
                    Overall innovation $\varepsilon_k^j$    ▷ as per Section 4.2.2
                    Estimated boundary force $\ddot{\mathbf{F}}_{b,k|k-1}^j$    ▷ Equation (5.8)
                    Covariance calculation: $C_k^{j,xy}$    ▷ Equation (4.10)
                    Correction:    ▷ as per Section 4.2.2
                    Innovation error: $\mathbf{S}_k^j$ & EnKF gain $\mathbf{g}_k^j$
                    Update predicted state estimate $\mathbf{x}_{k|k}^{i,j}$
                end procedure
                Calculate the ensemble mean of the corrected state, i.e., $\mathbf{x}_{k|k}^j$
            end for
        end procedure
        procedure Particle re-sampling($\{\xi_k^j\}$)    ▷ For each $\xi_k^j$
            Evaluate $w(\xi_k^j)$.    ▷ Equation (4.12)
            Update: State $\mathbf{x}_{k|k}$ and Parameter estimates $\boldsymbol{\theta}_{k|k}$    ▷ Equation (4.13)
        end procedure
    end for
end procedure
```

The bridge structure is excited under the aforementioned vehicle loading, and acceleration responses are sampled from the chosen substructure nodes (internal *dof*s only) at a sampling frequency of 50 Hz for 20 s under its undamaged state. The simulated signal is further contaminated with SWGN having a *snr* of 1% in order to emulate real-life situations. The initial distribution of the parameters is assumed to be $\mathcal{N}(1.3, 0.01)$, and α is set to 0.98. Numerical experiments were conducted using 2000 filter particles for PF and 100 ensembles for EnKF.

The proposed algorithm is validated under undamaged conditions wherein the location-based undamaged health parameters (normalized elasticity of each

Table 5.1: Bridge and vehicle parameters for the numerical study

Parameters of the bridge					
$EI\ (N-m^2)$	$2.12\ \times 10^{1}1$	$\rho\ (kg/m)$	$3.03\ \times 10^{4}$	μ	0.02
Parameters of the vehicle					
$m_s\ (kg)$	38500	$J\ (kgm^2)$	$2.446\ \times 10^{6}$	$m_{t1}(kg)$	4330
$m_{t2}(kg)$	4330	$k_{s1}(N/m)$	$2.535\ \times 10^{6}$	$k_{s2}(N/m)$	$2.535\ \times 10^{6}$
$k_{t1}(N/m)$	$4.28\ \times 10^{6}$	$k_{t2}\ (N/m)$	$4.28\ \times 10^{6}$	c_{s1} (N/sm)	$1.96\ \times 10^{5}$
$c_{s2}(N/sm)$	$1.96\ \times 10^{5}$	$c_{t1}(N/sm)$	$9.8\ \times 10^{4}$	$c_{t2}(N/sm)$	$9.8\ \times 10^{4}$
$a_1(m)$	4.2	$a_2(m)$	4.2	$V(kmph)$	20

substructure element) are considered to be unknown. The mean of the initial estimate is considered to be 1.3 which is further estimated to check if it converges to its true value, i.e. 1. In Figure 5.2a, the smooth convergence of all five substructure element elasticity (normalized) to their true values can be verified. The comparison between estimated and actual (simulated) acceleration of an internal *dof* is presented in Figure 5.2b. Similarly, estimated, and actual boundary force (simulated) is compared in Figure 5.3. In both cases, close matching can be observed throughout the signal length which can also be verified from the scatter plots presented in additional. The proposed algorithm has undergone rigorous validation through numerical experiments, which have conclusively demonstrated its precision and accuracy in estimating boundary forces.

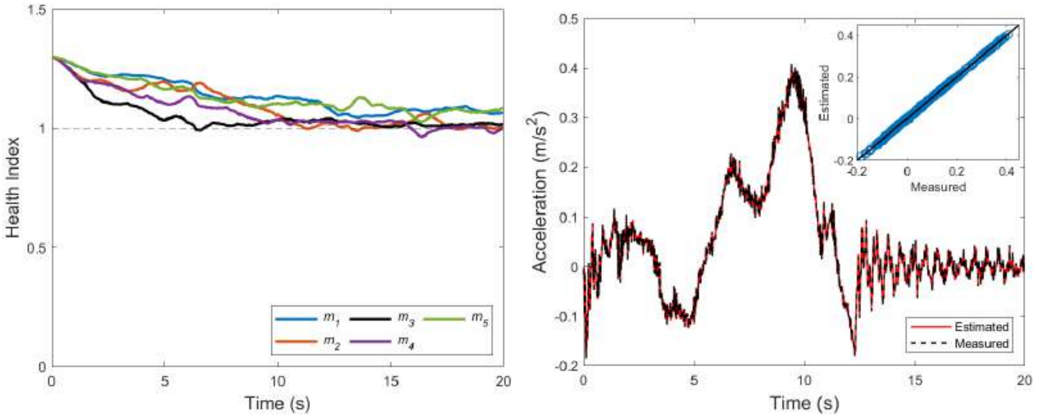

(a) Estimation of health indices (*dashed lines represent respective actual values.*)

(b) Comparison of internal response recreated from the estimated states.

Figure 5.2: Performance of the proposed algorithm under vehicle loading.

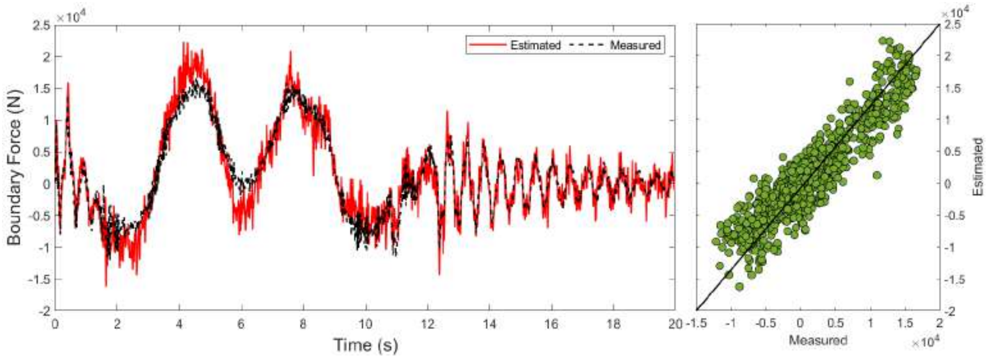

Figure 5.3: Comparison of boundary force recreating from the estimated states to the actual excitation.

5.5 Experimental study on a real bridge

To accurately predict the RUL of a structure considering crack growth, it is crucial to estimate the boundary forces of a real bridge structure using the proposed method. In order to achieve this, a comprehensive series of field experiments were conducted on an actual truss bridge known as the “Chandra bridge” (cf. Figure 5.4. The Chandra Bridge is a highway bridge situated over the Chandra River, which is a tributary of the Chenab River. It is located just after the North portal of the Atal Tunnel in Himachal Pradesh, India. The bridge is designed and constructed by the Border Roads Organisation (BRO) in 2020. It is a warren-type truss bridge with vertical members, measuring 100 m in length, 12 m in width, 10 m in height, and featuring a main span of 60 m. Equipped with two lanes, the bridge has a daily capacity of approximately 4500 vehicles.

Figure 5.4: Chandra bridge, near Atal tunnel, Teling, Himachal Pradesh, India.

The truss section of the bridge is supported by a pin at one end and roller support at the other. The bearings were thoroughly examined, and due to the bridge being recently erected, no issues related to locked bearings were identified. On both sides of the river, the truss section is approached by two separate concrete girders, which are detached from the truss using a construction joint of adequate width. Consequently, these two structural components can be distinctly regarded as separate entities, as they do not impact each other's performance. Subsequently, the instrumentation strategy and response sampling methodology employed for the bridge will be presented and detailed.

5.5.1 Sensors installation and data acquisition for bridge monitoring

Wireless accelerometers and strain sensors were employed to conduct experiments intended at monitoring the condition of the bridge. The wireless triaxial accelerometers (G-LINK-200-8G) selected for this purpose are suitable for low-frequency applications within the range of $0 - 200\ Hz$. This frequency range is typical for structural monitoring, considering that most structures have dominant frequencies well below 200 Hz.

The wireless accelerometers were strategically placed at the nodes of the mid-span deck, and their responses were sampled using a base station (WSDA 2000, Lord Micro-strain). Vertical vibrations were specifically measured after an initial inspection revealed that vibrations in other directions were not as significant compared to vertical vibrations. The positions of the sensors are indicated in the schematic presented in Figure 5.5. Acceleration time history signals were recorded from nine wireless sensors located at the web joints (at deck level) of the bridge. The selection of sensor locations, both for the actual measurements and later for numerical replication, is based on the understanding that vehicular loads primarily redistribute through the web joints to other truss members.

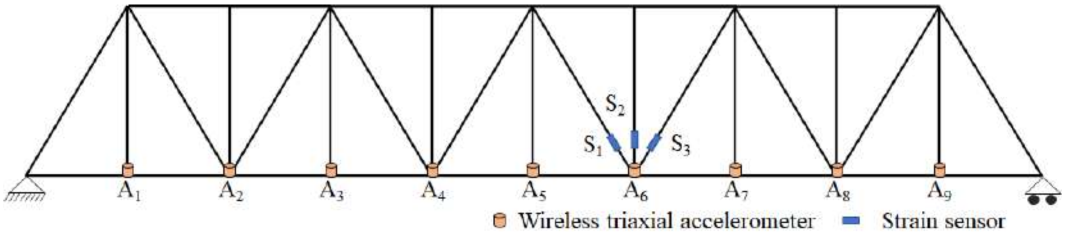

Figure 5.5: Schematic diagram illustrates the placement of sensors on the truss bridge.

Considering that the first three dominant modes of the bridge are expected to have frequencies below 64 Hz, the sampling frequency for all accelerometers is set at 128 Hz. Additionally, strain measurements were recorded from various locations on the structure to determine the nominal strain levels under regular service loading. This information is subsequently used to calculate fatigue cycles using rain-flow counting methods. The strain gauges, specifically Type ICP Piezoelectric (Model no:740B02, PCB), is positioned at one of the web joints. The sixth node (A_6) is identified for strain sampling, and three strain gauges were attached to record axial strain profiles in three directions of the adjoining members. The dynamic strain data were sampled using a Dewesoft Krypton-STG data acquisition system, with the response recorded for the same duration and sampling frequency as the accelerometers. Acceleration and strain profiles recorded under vehicle loading are shown in Figure 5.6.

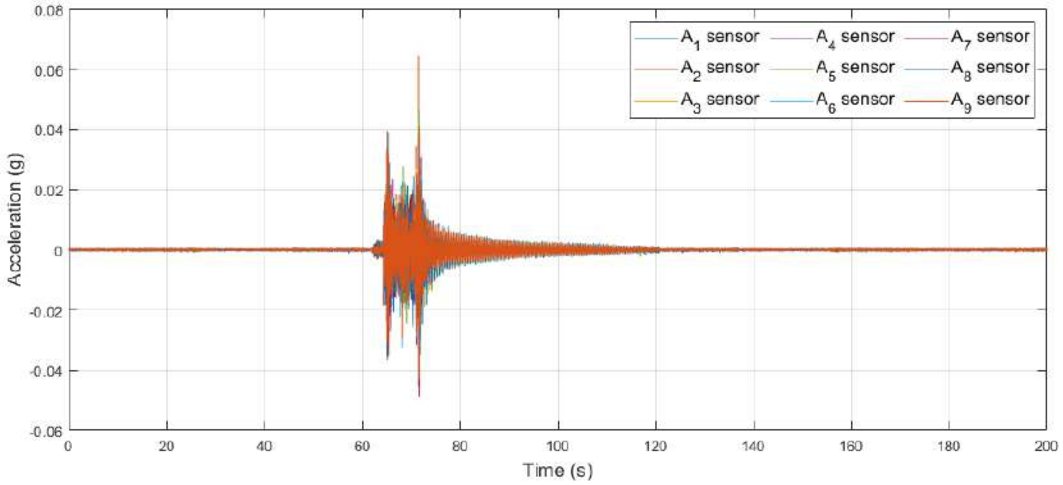

(a) Acceleration profile.

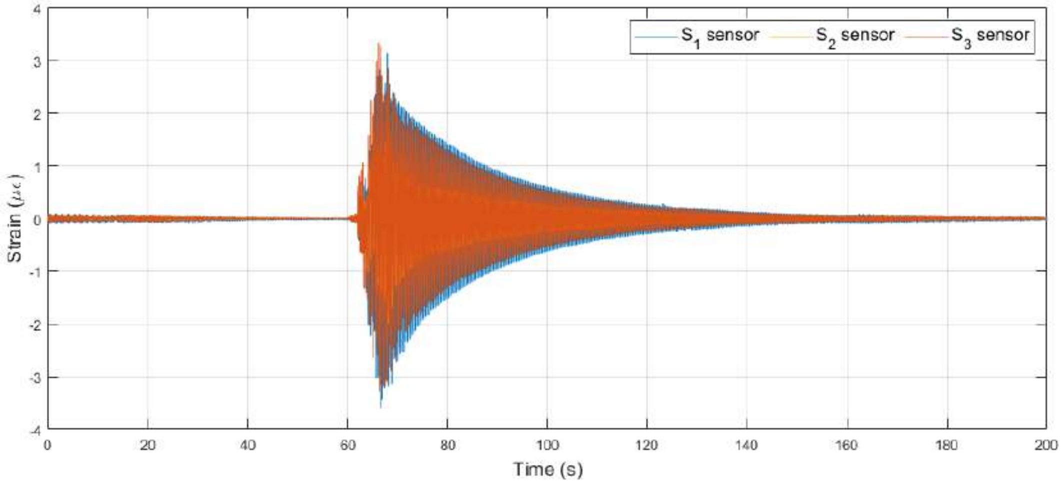

(b) Strain profile.

Figure 5.6: Structural responses are recorded through sensors.

5.6 Numerical replica of Chandra bridge

The truss segment of the Chandra bridge is modelled using the commercial finite element modelling software CSi-Bridge. A 3D FE model is created to replicate the middle span of the bridge, which supports the truss segment. A schematic of the model is shown in Figure 5.7. The members are modelled as truss elements, and their geometries are adapted according to the specifications provided in Sharma and Sen (2023). The boundary constraints observed in the actual bridge, such as pin support at one end and roller support at the other end, are replicated in the model. The concrete deck is modelled using shell elements with a membrane thickness of 0.3 m. The floor system, consisting of the concrete deck and longitudinal stringers, is modelled as a series of beam elements connected to a node at the mid-span of each floor beam. In CSi-Bridge, a body constraint ensures that all constrained joints move together as a three-dimensional rigid body, meaning that they cannot displace relative to each other. The initial assumptions for various model parameters are provided in Table 5.2. Ultimately, this preliminary model needs to be calibrated to accurately represent the real structure as its DT.

Table 5.2: Parameters calculated from experimental and assumed data

Parameters	Elastic modulus (GPa)	Poisson's ratio	Mass Density (Kg/m^3)
Steel	210	0.3	7850
Concrete	33.5	0.2	2500

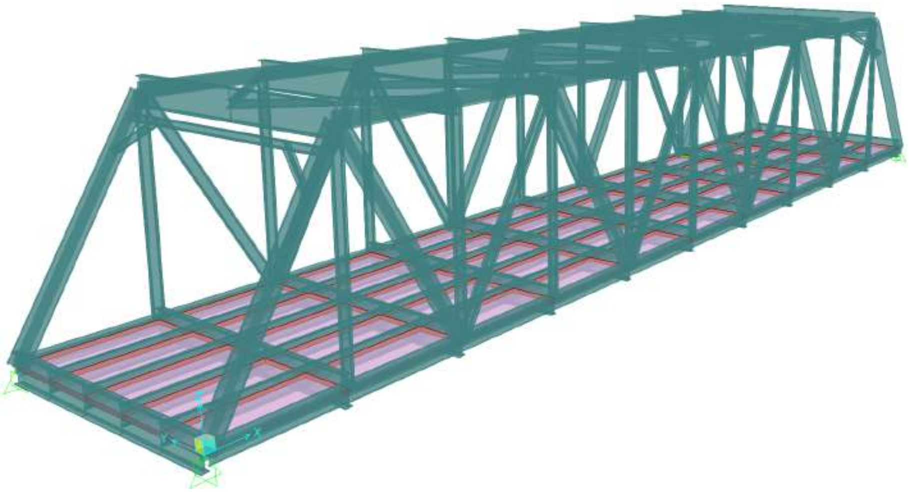

Figure 5.7: Development of a 3D model of the Chandra bridge using CSi bridge FEM software.

5.6.1 Calibration of the DT model of Chandra bridge

The material elasticities of steel and concrete are believed to be the key parameters influencing the frequencies of the real bridge. Consequently, a calibration study is conducted to identify an optimal set of elasticities that minimize discrepancies in the natural frequencies and acceleration profiles. To assess the acceleration profiles, the numerical model is simulated with a vehicle model, and its response is compared to the actual recorded response from the real bridge. The selected recorded response predominantly corresponds to vehicle loading conditions.

An optimization procedure is employed, with the elasticity of steel and concrete as the control parameters, to minimize errors in the first three simulated frequencies and acceleration profiles. The optimized Young's Modulus for steel is determined to be 195 GPa, while Young's Modulus for concrete is calibrated to 32.8 GPa.

Through this calibration study, it is ensured that both the real bridge and its numerical model exhibit similar dynamic properties and produce comparable vibrational responses. Table 5.3 presents a sample comparison between the estimated frequencies from the real structure and the corresponding model-predicted values. To map the acceleration profile, a commercial vehicle (cf. Table 5.4) according to IRC 3:1983 (Type 3) standards is considered to simulate the acceleration in the DT model. The acceleration signal recorded from the real structure and the numerical model are compared in Figure 5.8, and the error found is of the order 9.91% *snr*. These results confirm that the updated model replicates the actual modal properties and time domain responses with sufficient accuracy and precision. Based on this, the final calibrated model is considered a DT of the real structure, enabling the identification of critical elements of the bridge structure under vehicle loading.

Table 5.3: Comparison between frequencies obtained experimentally and numerically.

Data		Experimental value	Calibrated numerical	Relative error (%)
Frequency (Hz)	ω_1	2.563	2.568	0.20
	ω_2	5.125	5.170	0.88
	ω_3	6.719	6.905	2.77

Table 5.4: Parameters of commercial vehicle.

Weight	No. of axles	Speed of truck	Axle width	Front axle	Rear axle
21 Ton	3	11.1 m/s	2.5	Single tyre	Dual tyre

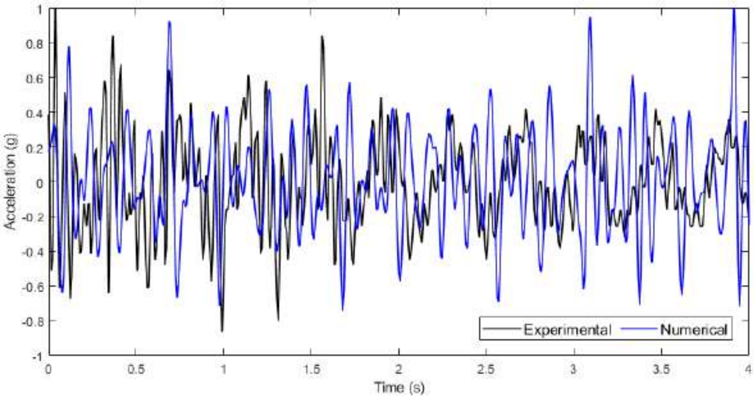

Figure 5.8: Comparison of experimental and numerical acceleration profile.

5.6.2 Estimation of boundary forces of selected elements

To assess and forecast the fatigue life of the Chandra bridge under crack growth conditions, special emphasis is placed on one of the floor beams where a crack has been assumed. In Chapter 3, we delve into the simulation of crack growth, which requires utilizing material properties, section properties, and boundary forces. Achieving precise calculations for crack growth becomes challenging due to the presence of the crack, making it difficult to monitor the current state of the constituent material properties of the cracked member. However, an alternate arrangement can be made by considering the material properties of the adjacent element to the substructure. This is justified by the likelihood of similar weathering effects and operational loading experienced by the two adjacent members, leading to similar material degradation. Hence, the adjacent element is treated as the substructure, and its responses are sampled to estimate the current state of material properties.

To apply the proposed approach, the selected element is defined by five internal nodes and two boundary nodes. In accordance with real-life conditions, acceleration responses under vehicle load are sampled from the internal nodes at a sampling frequency of 128 Hz. Additionally, the responses are contaminated with SWGN at an snr of 1% to replicate realistic scenarios. Subsequently, the proposed algorithm is utilized to estimate the boundary forces based on the current health condition, using the internal acceleration responses.

The proposed approach utilizes location-based **HI**s as the health parameters, which range from [0; 1]. For system estimation, following the algorithm described in Algorithm 3, the initial distribution of the **HI**s is assumed as $\mathcal{N}(1, 0.01)$. This is done to benchmark the current health of the bridge, with the parameter α set to 0.99 (cf. Equation (4.8)). PF simulations are conducted with 1000 particles, while EnKF simulations are performed with 50 ensembles.

The proposed algorithm is validated using a benchmarked model, where the location-based undamaged health parameters are unknown. The initial estimate is set to a mean value of 1, which is then estimated to check for convergence to its true value. Figure 5.9a shows the smooth convergence of all five substructure element elasticities (normalized) to their true values. The comparison between the estimated and actual (simulated) acceleration of an internal *dof* is presented in Figure 5.9b.

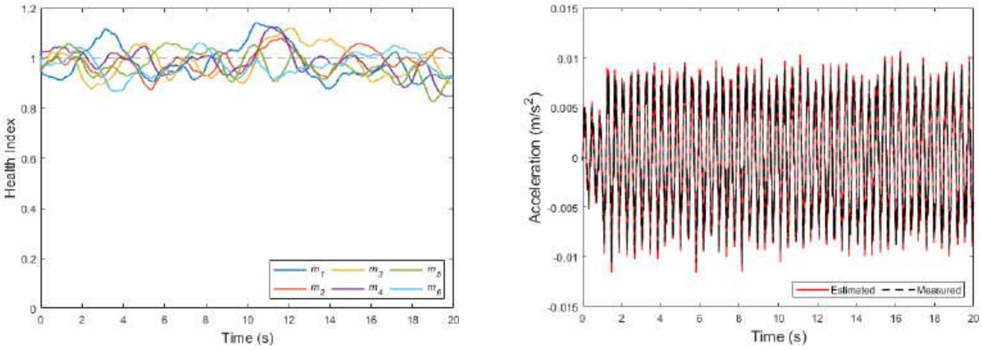

(a) Estimation of health indices (*dashed lines represent respective actual values.*) (b) Comparison of internal response recreated from the estimated states.

Figure 5.9: Performance of the proposed algorithm on the benchmarked model under vehicle loading.

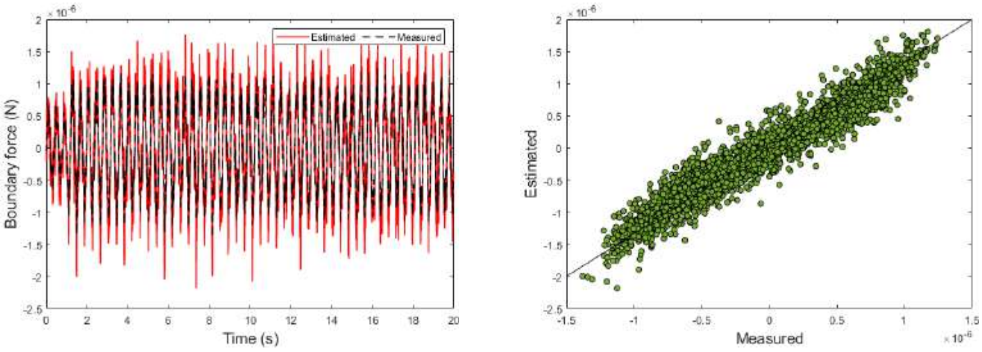

(a) Time series data of measured and estimated boundary force. (b) Correlation plot of measured and estimated boundary force.

Figure 5.10: Comparison of boundary force of a benchmarked model.

Similarly, the estimated and actual boundary forces (simulated) are compared in Figure 5.10a. A close match can be observed throughout the signal length, as also evident from the correlation plot presented in Figure 5.10b. The proposed algorithm has undergone rigorous validation using a benchmarked model, which conclusively demonstrates its precision and accuracy in estimating boundary forces.

5.6.3 Updated fatigue crack growth model

Chapter 3 presented a crack growth model for the bridge joint under constant amplitude load in tension and compression. However, in reality, the load is not constant and accordingly, fatigue stress history needs to be estimated for prognosis purposes. To determine the number of stress cycles, the rain flow counting algorithm is used to convert the boundary forces into equivalent stress levels. This information is then applied to the selected location to determine the actual crack growth condition under vehicle loading. To implement this technique, the selected member is assumed to have an initial crack length of 0.1 m. The algorithm used in *Chapter* 2 is utilized to calculate the SIFs of the selected section. However, previously it only considered Mode-I dominance. To accurately simulate the crack propagation rate in the selected member, the contribution of Mode-II and Mode-III is also taken into account by substituting ΔK with an effective stress intensity factor range ΔK_{eq} Silva et al. (2017), given as Milne et al. (1988); Wang et al. (2020b):

$$\Delta K_{eq} = \sqrt{\Delta K_I^2 + \Delta K_{II}^2 + \beta \Delta K_{III}^2/(1-\upsilon)} \tag{5.9}$$

where K_I, K_{II}, and K_{III} are the stress intensity factors for Mode-I, Mode-II, and Mode-III scenarios, respectively. υ represents the Poisson's ratio of the steel structure, and β is usually assumed to be 1.0 Zhao et al. (2022). Equation (5.9) can be used to estimate the equivalent stress intensity factor ΔK_{eq}.

With this direction and driving force, the ABAQUS-Python script is updated to incorporate the redefined crack front, and iterations are continued until the critical conditions are reached (corresponding to $K_{IC} = 158MPa\sqrt{m}$ Djoković et al. (2015)), resulting in a series of SIFs corresponding to various crack sizes. The numerically obtained data is then curve-fitted to establish a correlation between ΔK_{eq} and a using a polynomial equation.

The Paris model parameters used for the simulation are obtained from the works of Zhao et al. (2022). In *Chapter* 3, *Section*3.4.1, a detailed discussion is provided regarding the preliminary assumptions made about the state and parameters of the assumed material. The characteristics and distribution of these parameters, as well as the assumed fracture parameters, are presented in Table 5.5.

Table 5.5: EKF parameters of a critical element of the Chandra bridge.

Parameters	Type	Numerical values
a_o	True value	0.1 m
m	True value	3
Θ	True value	24.73
$a_{0\|0}$	Initial estimate	$\mathcal{N}(0.1, 0.05)$
$m_{0\|0}$	Initial estimate	$\mathcal{N}(1, 0.01)$
$\Theta_{0\|0}$	Initial estimate	$\mathcal{N}(14.82, 0.1)$
ΔK_{th}	Deterministic	2 MPa$\sqrt{m}$
ΔK_{IC}	Deterministic	158 MPa$\sqrt{m}$
σ'_f	Deterministic	450 MPa
v_{cr}	Deterministic	5.25×10^{-5} mm/cycles

The proposed filtering algorithm is then employed to estimate the fatigue life based on the crack growth history simulated from this numerical model. The simulated crack growth history is further contaminated with 1% *snr*, as mentioned previously.

With the proposed approach, the crack size is simultaneously estimated while estimating the relevant Paris model parameters. The results of both the parameter estimation and crack size estimation are presented in Figures 5.11. These results demonstrate the convergence of the mean estimate along with the associated estimation uncertainty. It is evident from the results that the estimates are both prompt and precise.

Furthermore, the crack size estimation and prognosis, as well as their sensitivity to data size under 1% noise contamination, are presented in Figures 5.12a and 5.12b. These figures illustrate that the proposed method can effectively perform crack prognosis well in advance.

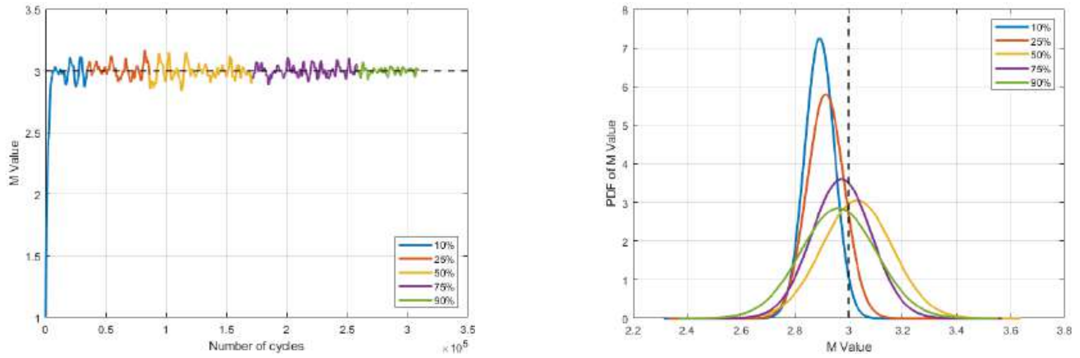

(a) The mean estimate for m.

(b) Parameter distribution for m.

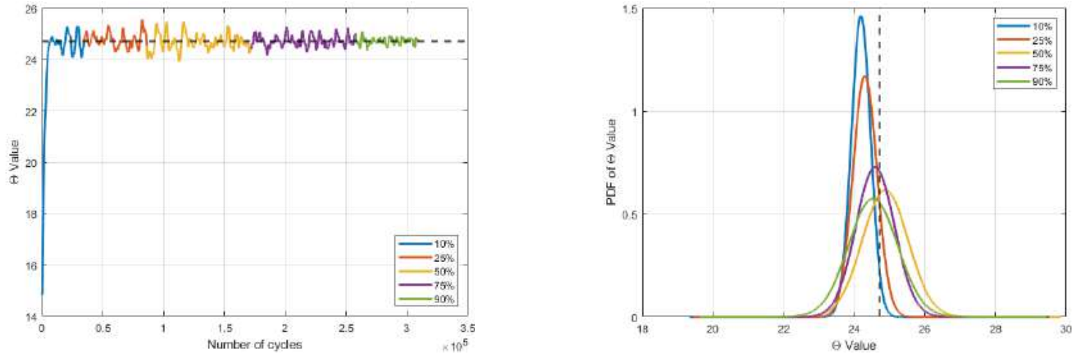

(c) Mean estimate for Θ.

(d) Parameter distribution for Θ.

Figure 5.11: Convergence of estimated parameters m (above) and Θ (below) for the case of critical element of the Chandra bridge.

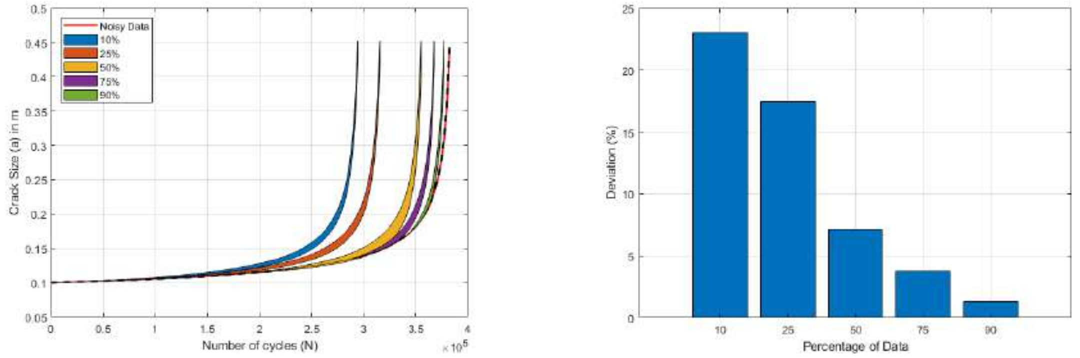

(a) Estimation and prognosis of crack growth with different levels of data.

(b) The relative error in predicting the number of cycles.

Figure 5.12: Estimation and prognosis of critical element of the Chandra bridge.

5.6.4 RUL prediction under different loading scenarios

The RUL prediction of a critical member in the bridge structure is estimated based on the life index (LI) calculated from the crack growth model. The LI is determined using the equation:

$$LI = 1 - a_{cu}/a_{cr} \tag{5.10}$$

where a_{cu} represents the current crack length and a_{cr} is the critical crack length. $a_{cr} = 0.45\ m$, is calculated based on the K_{IC} of the material. The value of LI approaching zero, indicates the imminent failure of the structure. The number of cycles obtained from the above approach is converted into a time period based on the number of cycles experienced by the structure per year.

The dashed line in Figure 5.13 represents the true value calculated based on the simulation of the crack growth model till its failure. In this case, the RUL of the structure is estimated using the crack growth model with 50% of the available data and under assumed traffic loading conditions. With the initial crack size assumed, the actual RUL of the critical structural member is obtained as 8.5 $years$, while the proposed algorithm estimated it to be 7.9 $years$, sufficiently close to its real value. The estimated RUL is also lower than the actual value, indicating a conservative estimation by the proposed algorithm.

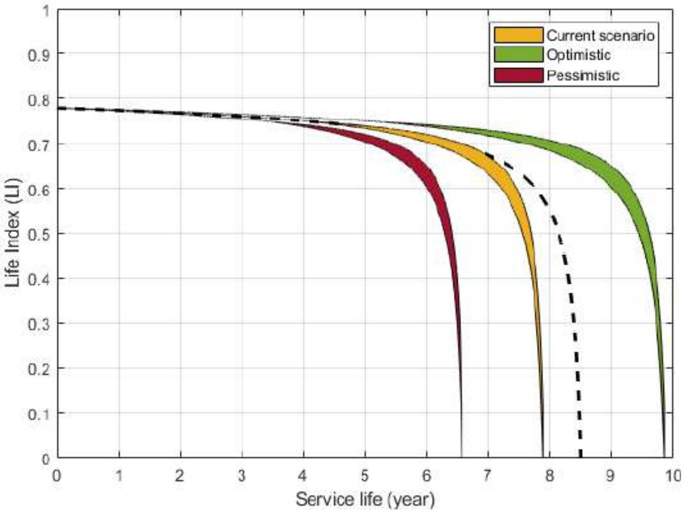

Figure 5.13: Service life of a critical element of the Chandra bridge.

Moreover, two distinct scenarios are examined: an optimistic one where traffic loading is reduced by 20%, and a pessimistic one where traffic loading is increased by 20%. The findings reveal a substantial impact on the RUL due to changes in loading conditions. Specifically, under the optimistic and pessimistic scenarios, the algorithm estimated the RUL to be 9.86 $years$ and 6.57 $years$, respectively. These values are not the mean value; instead, they are converging to a deterministic value. This underscores the significance of traffic modulation in controlling the RUL of the considered bridge when dealing with crack presence in real-world situations. Furthermore, for the present case, the implementation of the optimistic scenario, which reduces operational loading, has been numerically demonstrated to extend the service life of the structure.

5.7 Summary

This chapter is dedicated to the integration of a substructure monitoring-based SHM approach for fatigue life assessment, particularly for large civil structures with visible cracks. The primary objective is to achieve precise estimates of fatigue life while considering crack growth, which relies on accurately estimating the boundary force in the substructure model. To achieve this, an improved substructure technique capable of estimating the boundary force under vehicle loading conditions has been developed and validated through numerical simulations and experimental investigations.

The proposed approach utilizes information about the current structural health and boundary forces to estimate the fatigue life of a bridge experiencing visible crack growth. By establishing a connection between traffic loading and forces exerted on the structure through appropriate modelling of the vehicle-structure interaction, a comprehensive and accurate approach for estimating fatigue life in real-life scenarios is provided. The effectiveness of the proposed algorithm is validated through numerical experiments, showing precision and accuracy in estimating boundary forces.

To further validate the approach, field experiments were conducted on a truss bridge located in Himachal Pradesh, India. Wireless accelerometers and strain sensors were employed to monitor the bridge's condition, and the collected data is thoroughly analyzed. A DT model is implemented using CSibridge software to analyze the Chandra bridge, with the floor beam identified as the critical element based on Miner's rule. The filtering-based method is then used to estimate the RUL of the bridge, taking into account the crack growth in the critical element. To improve the model's accuracy, the crack growth model is updated to incorporate the consideration of Mode III SIF.

The results demonstrated close agreement between the estimated and actual RUL, showcasing the effectiveness of the proposed algorithm. Moreover, this chapter explores the influence of different loading conditions on fatigue life estimation and proposes implementing a suitable reduction in operational load to prolong the service life of the structure. Overall, the proposed approach provides a comprehensive framework for accurately predicting fatigue life in real-life scenarios.

Chapter 6

RUL prediction for bridges using substructure technique in crack-free conditions

In the field of predicting the RUL of large civil structures, existing methods typically treat the entire structure as a whole and assume a constancy in structural health at any stage of monitoring. This aspect of disregarding the current health status, especially for aging structures may lead to a non-conservative estimate for RUL. To overcome this limitation, a novel component-wise monitoring approach is introduced for estimating the fatigue life of civil structures, building upon the substructure monitoring approach described in the previous chapter. This approach incorporates an IP-EnKF algorithm, which accounts for the current health status of the structure. The RUL is further estimated taking the basis of the current health status. The input force is modeled using a vehicle structure model which further helped in assessing vehicle-wise impact on the fatigue life of a bridge. The proposed approach is validated through numerical experiments on a replicated box girder bridge under vehicle-bridge interaction. A case study further demonstrates its applicability, focusing on a real bridge in Himachal Pradesh, India.

6.1 Introduction

Bridge structures are susceptible to cyclic loads that can lead to fatigue-induced weakening and eventual structural failure Karamchandani et al. (1992), even without a visible crack. In cases where a visible and measurable fatigue crack exists, a fatigue crack model can be applied to predict crack growth, and appropriate filtering-based SHM solutions have already been detailed in an earlier section. However, this chapter specifically focuses on scenarios where cracks are not visible, and fatigue damage progressively deteriorates the structural integrity under normal operating conditions involving repetitive cyclic loads. In such cases, there are no measurable cracks available to assess the fatigue in the material, which poses a significant challenge for the filtering-based algorithms proposed earlier. Consequently, this chapter addresses the estimation of RUL for bridge infrastructures in crack-free conditions. A comprehensive discussion of the relevant literature in this context is therefore warranted.

Further, fatigue, as a localized weakening process, offers the opportunity to monitor specific subdomains instead of the entire structural domain efficiently Marques et al. (2018). Consequently, it becomes possible to identify and monitor a fatigue-critical subdomain independently, allowing for the estimation of the RUL of the entire bridge. This approach enables a more rigorous investigation of the subdomain of interest while reducing expenses associated with instrumentation and computation. Such methodologies are commonly referred to as substructure estimation, where the specific subdomain of interest is isolated numerically from the main structure and complemented with a set of boundary forces Tee et al. (2003). A substructure-based localized estimation approach has been detailed in the previous chapter. The same will be taken as a basis in this chapter in order to devise algorithms for localized fatigue estimation.

6.1.1 RUL estimation conditioned on current health

Traditionally, the estimation of RUL involves measuring stresses in the fatigue critical domain of the operational structure and extrapolating them for damage prognosis, assuming constant structural health Zhou et al. (2013); Leander et al. (2010). However, the concept of the fatigue critical domain is likely to change when damage occurs or operational loading conditions are altered. There are situations where the service life or loading of a structure may need to be extended beyond the prescribed limits to avoid the cost of replacement. Such extensions can invalidate the RUL estimate since they do not account for the structural health deterioration resulting from ageing. As RUL estimates heavily rely on the current health and operating condition of the structure, the value needs to be re-estimated whenever the structure undergoes changes in its health or loading conditions.

In the context of bridge infrastructures, data-based inverse fatigue life prediction approaches conditioned on the current health state of structures using SHM techniques have become crucial for ensuring operational safety Kuncham et al. (2022). While data-driven black box models are efficient, they do not provide insights into the underlying failure mechanisms Feng et al. (2021). Therefore, model-based RUL prediction is more appreciated in this regard as it enables a better understanding of fatigue damage prognosis and allows infrastructure owners to make informed decisions regarding future operations, including allowable traffic load, speed, frequency, and maintenance schedules. Recursive estimation of RUL, conditioned on the current estimated health, can be achieved through a model-based inverse estimation approach that draws inferences from structural responses and utilizes a high-fidelity support model that accurately replicates reality. In this regard, the incorporation of vehicle-bridge interaction is imperative to account for vehicle-load-induced fatigue in the support model.

6.1.2 Limited research on reinforced concrete structures

Previous studies on fatigue life estimation have primarily focused on steel bridges due to their gradual crack propagation characteristics resulting from their ductile nature. In contrast, reinforced concrete (RC) bridges, which are more commonly found, have not received sufficient attention in the literature. While cracks are the more dominant fatigue feature showcased by the typical truss bridges, for concrete bridges fatigue damage-induced material deterioration is more common. Existing fatigue evaluation studies on RC bridges have predominantly concentrated on localized or mesoscale fatigue estimation Wang et al. (2020a).

The limited attention given to RC bridges stems from various factors, including the high execution costs, potential traffic disruptions during assessments, and the challenges associated with conducting fatigue estimation across the entire structural domain. However, a few studies have examined full-scale RC structures, albeit not in abundance. In an effort to enhance the prediction accuracy of RUL for RC bridges, researchers have explored the integration of fracture mechanics knowledge Rocha and Brühwiler (2012). Additionally, comprehensive fatigue analysis studies involving dynamic testing on bridges in northern Sweden have been reported by Elfgren et al.Elfgren et al. (2007). The impact of track irregularities and damping on fatigue damage in RC deck slabs was investigated by Malveiro et al.Malveiro et al. (2018) in the context of a railway bridge.

6.1.3 Challenges with substructure interface boundaries

Estimating the structural health and fatigue life of a bridge subdomain simultaneously and conditionally, without prior information on its health, poses a significant challenge. Additionally, obtaining boundary forces at the boundary $dofs$ is necessary for fatigue estimation but challenging, whether through measurement or estimation. Compounding the problem is the need to perform this estimation under unknown and uncertain operational loading conditions, using sensor responses that are contaminated with noise. To achieve optimal risk-based monitoring and maintenance of bridges, it is crucial to frame this problem in the probabilistic domain, accounting for uncertainties in loading and measurement. This study tackles the estimation of the subdomain using a Bayesian filtering-based approach Sen et al. (2021), with the employment of an output injection approach Zhang and Zhang (2018) to ensure robustness. The same framework has already been validated in the previous chapter from an SHM perspective, and this study integrates it with fatigue life estimation.

Within the Bayesian approach, fatigue estimation can be formulated as a joint state-parameter estimation problem. This involves estimating the structural responses as states for RUL estimation while conditioning on the parameters, which represent the structural health indices. The derived health state is then used for renewed fatigue life estimation, incorporating updated information on the constitutive relationship into the stress/strain calculation during the RUL estimation process. For practicality, it is advantageous to employ an interacting filtering environment, following the algorithm detailed in the previous chapter. The PF-EnKF interacting framework is thus utilized, where the PF estimates the parameters (resulting in updated constitutive relationships), while the state estimation can be handled using the EnKF to address modelling and measurement uncertainties Hommels et al. (2009). Vehicle-bridge interaction is further included in the modelling approach to directly connect vehicle-induced vibration to fatigue life deterioration.

6.1.4 Proposed approach for RUL prediction

A Bayesian model-based approach for RUL estimation can be employed under any arbitrary vehicle-induced loading scenario, but the central idea of connecting the RUL to the individual vehicle loading or frequency will surely be missed. This study, therefore, includes vehicle-structure interaction in the support model in order to bring in the direct connection between traffic loading and its impact on structural fatigue. The objective of the research is therefore to monitor only a fatigue-critical subdomain of a bridge structure and relate that to the traffic loading and/or frequency. The proposed algorithm has been validated numerically on an RC box girder bridge structure excited by traffic loading prior to employing it on a real bridge.

The following section details the vehicle-bridge interaction model that maps the vehicle load to the corresponding structural response. Following, the system identification and fatigue estimation approach proposed is discussed in detail.

6.2 Coupled vehicle-bridge vibration system

Simulating the dynamic interactions between bridges and vehicles has majorly been attempted in two ways. First, there is the uncoupled iteration method Fafard et al. (1997), which solves each system independently and performs iterative calculations at each time iteration in order to equilibrate the forces between the deck and tires. The alternative method involves solving the fully-coupled super-system and obtaining the solution implicitly. Moreover, there are two different ways of modelling vehicle dynamics. The first approach, termed the moving load model, uses influence lines and dynamic amplification factors to model vehicle dynamics. However, such a static model fails to account for the dynamics of vehicle-bridge interaction Wang et al. (2020a). Alternatively, vehicle models can be simulated by using a moving spring-mass-damper (MSMD) which is well-suited for modelling complex vehicle models. For moving vehicles, the load position changes with time, and the surface irregularities on the deck and the deck vibration jointly oscillate the vehicle suspension Duan and Yang (2013). Hence, MSMD-coupled systems are employed to determine actual fatigue stresses on bridge structures Liu et al. (2013).

Based on the FEM-based approach developed by Gao et al. (2014), this study adopts a simulation method that systematically incorporates the dynamics of bridge-vehicle interaction. The coupled equation of the vehicle-bridge vibration system is further improvised and transformed to the state space equation of a Bayesian filter for estimating fatigue life. The proposed approach is described in detail as follows.

6.2.1 Vehicle model

A three-dimensional setup demonstrating the coupled vehicle-structure dynamics is schematically presented in Figure 6.1 detailing all the notations used herein. The governing differential equation for vehicle dynamics Gao et al. (2014) can be presented as,

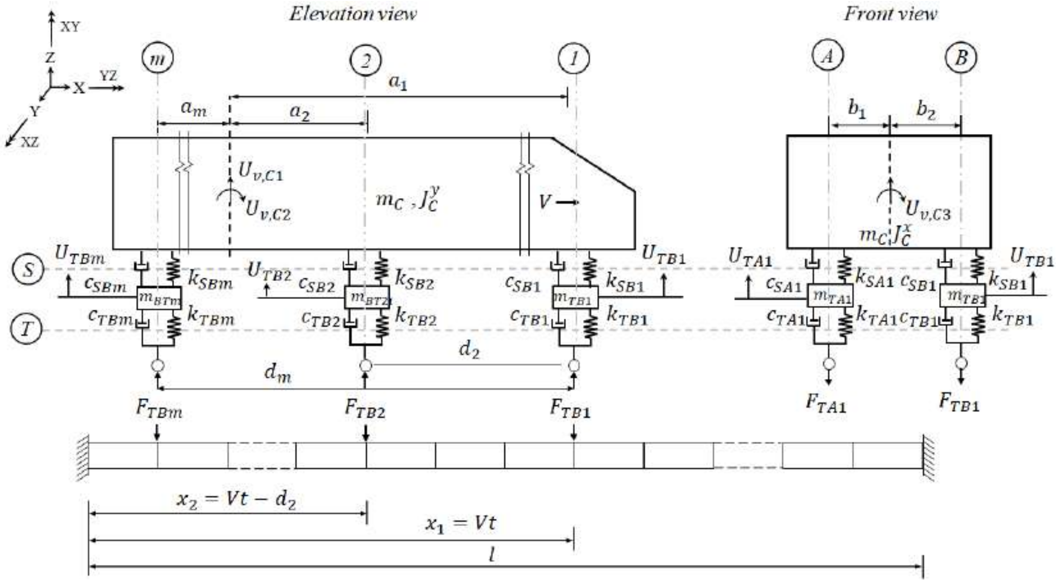

Figure 6.1: Schematic plot of the bridge-vehicle interaction *Left side shows the vehicle's front view.*

$$\mathbf{M}_v\ddot{\mathbf{U}}_v + \mathbf{C}_v\dot{\mathbf{U}}_v + \mathbf{K}_v\mathbf{U}_v = \mathbf{F}_g - \mathcal{F}_v(x,t) \tag{6.1}$$

here, $\mathbf{M}_v$, $\mathbf{C}_v$, and $\mathbf{K}_v$ are mass, damping, and stiffness matrices of the vehicle respectively. $\mathbf{U}_v$, $\dot{\mathbf{U}}_v$, and $\ddot{\mathbf{U}}_v$ are the displacement, velocity, and acceleration responses of the vehicle. $\mathcal{F}_v$ and $\mathbf{F}_g$ correspond to interaction force vectors applied on the vehicle and force vector caused by the effect of the gravitation respectively. $\mathcal{F}_v$'s dependence on the position of the vehicle on the bridge is defined through the arguments x (position) and t (time). Assuming there are m_a axles, the vehicle is accordingly defined with $2m_a + 3$ dofs (2 vertical dofs (left and right) per axle along with 3 additional *dof*s due to vertical (U_{C1}), pitching (U_{C2}) and swung (U_{C3}) motions of the carriage (C)).

Accordingly, $\mathbf{M}_v = \begin{bmatrix} \mathbf{M}_{v,C} & 0 \\ 0 & \mathbf{M}_{v,T} \end{bmatrix} = diag\{m_C, J_C^y, J_C^x, m_{A1}, m_{B1}, \cdots, m_{Bm}\}$,

$$\mathbf{U}_v = \left\{ \mathbf{U}_C \mathbf{U}_T \right\}^T = \{U_{v,C1}, U_{v,C2}, U_{v,C3}, U_{v,A1}, U_{v,B1}, \cdots, U_{v,Bm}\}^T,$$

$$\mathbf{C}_v = \begin{bmatrix} \mathbf{C}_{v11} & \mathbf{C}_{v12} \\ \mathbf{C}_{v21} & \mathbf{C}_{v22} \end{bmatrix}, \ \mathbf{C}_{v12} = \begin{bmatrix} -c_{SA1} & -c_{SB1} & \cdots & -c_{SBm} \\ -a_1 c_{SA1} & -a_1 c_{SB1} & \cdots & -a_m c_{SBm} \\ b_1 c_{SA1} & b_2 c_{SB1} & \cdots & b_m c_{SBm} \end{bmatrix},$$

$$\mathbf{C}_{v11} = \begin{bmatrix} \sum_{q=1}^{m}(c_{SAq} + c_{SBq}) & \sum_{q=1}^{m} a_q(c_{SAq} + c_{SBq}) & -\sum_{q=1}^{m}(b_1 c_{SAq} + b_2 c_{SBq}) \\ \sum_{q=1}^{m} a_i(c_{SAq} + c_{SBq}) & \sum_{q=1}^{m} a_q^2(c_{SAq} + c_{SBq}) & -\sum_{q=1}^{m}(b_1 a_q c_{SAq} + b_2 a_q c_{SBq}) \\ -\sum_{q=1}^{m}(b_1 c_{SAq} + b_2 c_{SBq}) & -\sum_{q=1}^{m}(b_1 a_q c_{SAq} + b_2 a_q c_{SBq}) & \sum_{q=1}^{m}(b_1^2 c_{SAq} + b_2^2 c_{SBq}) \end{bmatrix},$$

$$\mathbf{C}_{v22} = \begin{bmatrix} c_{SA1} + c_{TA1} & 0 & \cdots & 0 \\ 0 & c_{SB1} + c_{TB1} & \cdots & 0 \\ \vdots & \vdots & \ddots & \vdots \\ 0 & 0 & \cdots & c_{SBm} + c_{TBm} \end{bmatrix}, \text{ and } \mathbf{C}_{v21} = \mathbf{C}_{v12}{}^T.$$

Note that $\mathbf{K}_v$ is exactly the same as $\mathbf{C}_v$, only substituting the symbol c for the symbol K. a_q and b_q denote, respectively, the distance from the wheel to the centre in longitudinal and transverse directions.

The subscripts A/B and $C/S/T$ denote the association of the variable with wheel axis (A (left) or B (right)) and levels (Carriage (C), suspension (S) or tire level (T)) respectively. The symbols $m,\ k,\ c,\ J$ denote mass, stiffness, damping, and polar moment of inertia in general for the single *dof* subsystems defined in

Figure 6.1. $\mathcal{F}_v = \{\mathbf{F}_C, \mathbf{F}_T\}^T = \{\mathbf{0}_{n_C}, \mathbf{F}_T\}^T$ with $\mathbf{F}_T$ listing the interaction forces at the tyre levels and $\mathbf{F}_T = \{k_{Tpq}\Delta_{pq} + c_{Tpq}\dot{\Delta}_{pq}\}$ for all $p \in [A,\ B]$, $q \in [1, \cdots, m_a]$. Δ_{pq} and $\dot{\Delta}_{pq}$ (for detailed derivation refer Gao et al. (2014)) are the relative displacement and velocity at tire levels at the point of contact between the bridge and the wheel (p^{th} side in q^{th} axle). n_C is the number of dofs of the vehicle carriage.

6.2.2 Bridge model

The dynamics of the bridge deck (cf. Figure 6.1) is defined with its mass ($\mathbf{M}_d$), damping ($\mathbf{C}_d$), stiffness ($\mathbf{K}_d$) matrices and the corresponding interaction force ($\mathbf{F}_d(x,t)$).

$$\mathbf{M}_d\ddot{\mathbf{U}}_d + \mathbf{C}_d\dot{\mathbf{U}}_d + \mathbf{K}_d\mathbf{U}_d = \mathbf{F}_d\delta(x - Vt) \tag{6.2}$$

where $\mathbf{U}_d$, $\dot{\mathbf{U}}_d$, and $\ddot{\mathbf{U}}_d$ are the displacement, velocity, and acceleration response of the bridge deck in the physical domain. V represents speed of the moving vehicle, and δ is the Dirac function having the following characteristics:

$$\int_{t_{en}}^{t_{ex}} \mathbf{F}_d(x,t)\delta(x - Vt)dx = \begin{cases} 0, (t < t_{en}) \\ \mathbf{F}_d(x,t), (t_{en} \leq t \leq t_{ex}) \\ 0, (t > t_{ex}) \end{cases} \tag{6.3}$$

The function $\mathbf{F}_d(x,t)$ is continuous in the closed interval of $t \in [t_{en}, t_{ex}]$, where t_{en}, t_{ex} are the entering and exiting time of the vehicle respectively Duan and Yang (2013). Assuming the Rayleigh model for damping, Equation (6.2) can be transformed to the modal domain as:

$$\mathbb{M}_d\ddot{\mathbb{U}}_d(t) + \mathbb{C}_d\dot{\mathbb{U}}_d(t) + \mathbb{K}_d\mathbb{U}_d(t) = \mathbf{\Phi}^T\mathbf{F}_d(x,t)\delta(x - Vt) \tag{6.4}$$

here $\mathbb{M}_d = \mathbf{I}$, $\mathbb{C}_d = diag([2\xi_1\omega_1 \ldots 2\xi_n\omega_n])$, $\mathbb{K}_d = diag([\omega_1^2 \ldots \omega_n^2])$, and $\mathbb{U}_d = \mathbf{\Phi}^T\mathbf{U}_d$, where $\mathbb{M}_d$, $\mathbb{C}_d$, $\mathbb{K}_d$ and $\mathbb{U}_d$ are modal mass, damping, stiffness, and displacement matrices respectively. $\mathbf{\Phi}$ represents the mass normalized mode shape vectors. ω_n, ξ_n represents the modal frequency and damping ratio for the n^{th} mode shape.

6.2.3 Vehicle-bridge interaction

The interaction force for the pq^{th} wheel (detailed earlier) is given by,

$$\mathcal{F}_v(x,t) = -\mathbf{F}_d(x,t) = k_{Tpq}\Delta_{pq} + c_{Tpq}\dot{\Delta}_{pq} \tag{6.5}$$

The relative displacement at an arbitrary interaction point for a wheel at p^{th} side of q^{th} axle can further be elaborated as $\Delta_{pq} = \mathbf{U}_{d,pq}(t) - \mathbf{U}_{v,pq}(x,t) + \mathbf{r}_{pq}(x)$, and accordingly, $\dot{\Delta}_{pq} = \mathbf{U}'_{d,pq}V + \dot{\mathbf{U}}_{d,pq} - \dot{\mathbf{U}}_{v,pq} + \mathbf{r}'_{pq}V$, where $\mathbf{U}$ denotes displacement (in physical domain) and subscript b/v denotes its association with bridge or vehicle respectively. p, q denotes the position of the interaction point and $\mathbf{r}$ denotes the road surface roughness at the location mentioned through its subscript (see Section 6.2.4 for more detail).

Accordingly, the coupled equations of the vehicle-bridge system can be obtained by the combination of the vehicle Equation (6.1) and bridge Equation (6.4) as follows,

$$\begin{bmatrix} \mathbf{M}_v & \mathbf{0} \\ \mathbf{0} & \mathbb{M}_d \end{bmatrix} \begin{Bmatrix} \ddot{\mathbf{U}}_v \\ \ddot{\mathbb{U}}_d \end{Bmatrix} + \begin{bmatrix} \mathbf{C}_v & \mathbf{C}_{dv1} \\ \mathbf{C}_{dv1}^T & \mathbb{C}_d + \mathbb{C}_{dv} \end{bmatrix} \begin{Bmatrix} \dot{\mathbf{U}}_v \\ \dot{\mathbb{U}}_d \end{Bmatrix} + \begin{bmatrix} \mathbf{K}_v & \mathbf{K}_{dv1} \\ \mathbf{K}_{dv2} & \mathbb{K}_d + \mathbb{K}_{dv} \end{bmatrix} \begin{Bmatrix} \mathbf{U}_v \\ \mathbb{U}_d \end{Bmatrix} = \begin{Bmatrix} \mathbf{F}_v \\ \mathbb{F}_d \end{Bmatrix} \tag{6.6}$$

here, $\mathbf{C}_{dv1} = \begin{bmatrix} \mathbf{0}_{nc} \\ \mathbf{C}_{dT} \end{bmatrix}$, $\mathbf{C}_{dT} = \begin{bmatrix} \delta_1\phi_1^{(1)}c_{TA1} & \delta_1\phi_2^{(1)}c_{TA1} & \cdots & \delta_1\phi_n^{(1)}c_{TA1} \\ \delta_1\phi_1^{(2)}c_{TB1} & \delta_1\phi_2^{(2)}c_{TB1} & \cdots & \delta_1\phi_n^{(2)}c_{TB1} \\ \vdots & \vdots & \ddots & \vdots \\ \delta_m\phi_1^{(m)}c_{TBm} & \delta_m\phi_2^{(m)}c_{TBm} & \cdots & \delta_m\phi_n^{(m)}c_{TBm} \end{bmatrix}$,

$\mathbf{K}_{dv1} = \begin{bmatrix} \mathbf{0}_{nc} \\ \mathbf{K}_{dT1} \end{bmatrix}$, $\mathbf{K}_{dT1} = -\begin{bmatrix} \delta_1\phi_1^{(1)}k_{TA1} & \delta_1\phi_1^{(2)}k_{TB1} & \cdots & \delta_m\phi_1^{(m)}k_{TBm} \\ \delta_1\phi_2^{(1)}k_{TA1} & \delta_1\phi_2^{(2)}k_{TB1} & \cdots & \delta_m\phi_2^{(m)}k_{TBm} \\ \vdots & \vdots & \ddots & \vdots \\ \delta_1\phi_n^{(1)}k_{TA1} & \delta_1\phi_n^{(2)}k_{TB1} & \cdots & \delta_m\phi_n^{(m)}k_{TBm} \end{bmatrix}$,

$\mathbf{K}_{dv2} = \begin{bmatrix} \mathbf{0}_{nc} & \mathbf{K}_{dT2} \end{bmatrix}$,

$$\mathbf{K}_{dT2} = \begin{bmatrix} \delta_1\phi_1^{(1)}k_{TA1} + V\delta_1\phi_1^{'(1)}c_{TA1} & \delta_1\phi_1^{(2)}k_{TB1} + V\delta_1\phi_2^{'(1)}c_{TA1} & \cdots & \delta_m\phi_1^{(m)}k_{TBm} + V\delta_1\phi_n^{'(1)}c_{TA1} \\ \delta_1\phi_2^{(1)}k_{TA1} + V\delta_1\phi_1^{'(2)}c_{TB1} & \delta_1\phi_2^{(2)}k_{TB1} + V\delta_1\phi_2^{'(2)}c_{TB1} & \cdots & \delta_m\phi_2^{(m)}k_{TBm} + V\delta_1\phi_n^{'(2)}c_{TB1} \\ \vdots & \vdots & \ddots & \vdots \\ \delta_1\phi_n^{(1)}k_{TA1} + V\delta_m\phi_1^{'(n)}c_{TBm} & \delta_1\phi_n^{(2)}k_{TB1} + V\delta_m\phi_2^{'(n)}c_{TBm} & \cdots & \delta_m\phi_n^{(m)}k_{TBm} + V\delta_m\phi_n^{'(m)}c_{TBm} \end{bmatrix},$$

$$\mathbb{C}_d + \mathbf{C}_{dv} = \begin{bmatrix} \mathbb{C}_1 + \sum_{i=1}^n \delta_q\phi_1^{(i)}c_{Tpq}\phi_1^{(i)} & \sum_{i=1}^n \delta_q\phi_1^{(i)}c_{Tpq}\phi_2^{(i)} & \cdots & \sum_{i=1}^n \delta_q\phi_1^{(i)}c_{Tpq}\phi_n^{(i)} \\ \sum_{i=1}^n \delta_q\phi_2^{(i)}c_{Tpq}\phi_1^{(i)} & \mathbb{C}_2 + \sum_{i=1}^n \delta_q\phi_2^{(i)}c_{Tpq}\phi_2^{(i)} & \cdots & \sum_{i=1}^n \delta_q\phi_2^{(i)}c_{Tpq}\phi_n^{(i)} \\ \vdots & \vdots & \ddots & \vdots \\ \sum_{i=1}^n \delta_q\phi_n^{(i)}c_{Tpq}\phi_1^{(i)} & \sum_{i=1}^n \delta_q\phi_n^{(i)}c_{Tpq}\phi_2^{(i)} & \cdots & \mathbb{C}_n + \sum_{i=1}^n \delta_q\phi_n^{(i)}c_{Tpq}\phi_n^{(i)} \end{bmatrix},$$

$$\mathbb{C}_d + \mathbf{K}_{bv} = \begin{bmatrix} \mathbb{K}_1 + \sum_{i=1}^n \delta_q\phi_1^{(i)}\big(k_{Tpq}\phi_1^{(i)} + Vc_{Tpq}\phi_1^{'(i)}\big) & \cdots & \sum_{i=1}^n \delta_q\phi_1^{(i)}\big(k_{Tpq}\phi_n^{(i)} + Vc_{Tpq}\phi_n^{'(i)}\big) \\ \vdots & \ddots & \vdots \\ \sum_{i=1}^n \delta_q\phi_n^{(i)}\big(k_{Tpq}\phi_1^{(i)} + Vc_{Tpq}\phi_1^{'(i)}\big) & \cdots & \mathbb{K}_n + \sum_{i=1}^n \delta_q\phi_n^{(i)}\big(k_{Tpq}\phi_n^{(i)} + Vc_{Tpq}\phi_n^{'(i)}\big) \end{bmatrix},$$

$$\mathbf{F}_v = \begin{bmatrix} \mathbf{0}_{nc} \\ \delta_1(k_{TA1}r_{A1} + Vc_{TA1}r^{'}_{A1}) \\ \vdots \\ \delta_m(k_{TBm}r_{Bm} + Vc_{TBm}r^{'}_{Bm})] \end{bmatrix},$$

$$\mathbb{F}_d = \begin{bmatrix} -\sum_{i=1}^{n}\delta_i\phi_1^{(i)}\left[(\mathbf{M}_{v,Ci} + \mathbf{M}_{v,Tpq})g + k_{Tpq}r_{pq} + Vc_{Tpq}r^{'}_{pq}\right] \\ -\sum_{i=1}^{n}\delta_i\phi_2^{(i)}\left[(\mathbf{M}_{v,Ci} + \mathbf{M}_{v,Tpq})g + k_{Tpq}r_{pq} + Vc_{Tpq}r^{'}_{pq}\right] \\ \vdots \\ -\sum_{i=1}^{n}\delta_i\phi_n^{(i)}\left[(\mathbf{M}_{v,Ci} + \mathbf{M}_{v,Tpq})g + k_{Tpq}r_{pq} + Vc_{Tpq}r^{'}_{pq}\right] \end{bmatrix}$$

Subsequently, the $\mathbb{U}_d$ is transformed into $\mathbf{U}_d$ utilizing $\mathbf{\Phi}$. The stress time history is then computed based on $\mathbf{U}_d$, utilizing the strain-displacement and stress-strain relationships. Here, $r(x)$ is the road surface roughness, x is the position in the longitudinal direction of the bridge.

6.2.4 Road surface roughness

A periodically modulated random process can be used to describe the randomness of the bridge surface roughness. In this case, it is defined by its power spectral density function (PSD) Henchi et al. (1998); Dodds and Robson (1973), which is given by

$$S_r(\gamma) = A_r\gamma^{-2} \quad \gamma_L < \gamma < \gamma_U \tag{6.7}$$

where, $S_r(\gamma)$ is the PSD, A_r is the roughness coefficient and its values are considered from Gao et al. (2014) and γ, γ_L,γ_U is the spatial frequency, lower and upper limit. In this model, bridge surface roughness is assumed to be a stationary Gaussian random process. Thus, it can be generated using an inverse Fourier transform, to generate a random number θ_i distributed uniformly between 0 to 2π. The road profile in its discrete form is given by Henchi et al. (1998); Gao et al. (2014)

$$r(x) = \sum_{i=1}^{N}\left(4A_r\left(\gamma_L + (i-0.5)\Delta\gamma\right)^{-2}\Delta\gamma\right)^{0.5} cos(2\pi\gamma_i x - \theta_i) \tag{6.8}$$

where $\Delta\gamma = \frac{\gamma_U - \gamma_L}{N}$, N is the sampling number.

6.3 The robust state-space formulation for substructure system

The previous section details the procedure to map the individual vehicle loading to the corresponding structural response which will be useful for estimating the contribution of an individual vehicle to the fatigue damage provided the system health is estimated properly. This chapter, however, attempts health estimation only for the fatigue critical subdomain while being robust to any external (vehicle loading) or boundary forces with Bayesian filters. Accordingly, this mandates a state space model only for the concerned fatigue-prone subdomain, discussed next.

The bridge dynamics of the entire structural domain Ω given in Equation (6.2) have been simplified for better representation by removing the subscripts and associating the time-varying nature of the system matrices $\mathbf{M}$, $\mathbf{C}$, and $\mathbf{K}$ to enable system identification.

$$\mathbf{M}(t)\ddot{\mathbf{U}}\left(t\right) + \mathbf{C}\left(t\right)\dot{\mathbf{U}}\left(t\right) + \mathbf{K}\left(t\right)\mathbf{U}\left(t\right) = \mathbf{F}\left(t\right) \tag{6.9}$$

This study focuses only on subdomain Ω^s of the entire Ω which is further estimated using filter-based estimation approaches. As per the previous chapter, the state-space formulation of the substructure system is formulated as,

$$\begin{aligned} &\text{Process model} &:\quad &\mathbf{x}_k^s = \mathbf{A}_k^s\mathbf{x}_{k-1}^s + \mathbf{B}_k^s\mathbf{f}_k^s + \mathbf{E}_k^s\ddot{\mathbf{U}}_{b,k}^s + \mathbf{v}_k^s \\ &\text{Measurement model} &:\quad &\mathbf{y}_k^s = \mathbf{H}_k^s\mathbf{x}_k^s + \mathbf{D}_k^s\mathbf{f}_k^s + \mathbf{L}_k^s\ddot{\mathbf{U}}_{b,k}^s + \mathbf{w}_k^s \end{aligned} \tag{6.10}$$

In the context of Section 4.3.2, the matrices $\mathbf{A}^s, \mathbf{B}^s$, $\mathbf{E}^s$, $\mathbf{H}_k^s$, $\mathbf{D}_k^s$, and $\mathbf{L}_k^s$ remain unchanged, while only $\mathbf{x}_k^s = [\mathbf{U}_k{}^{s,r} \quad \dot{\mathbf{U}}_k^{s,r}]^T$, and $\mathbf{f}_k^s = \mathbf{F}(t)$ is modified to account for the vehicle-bridge interaction acting on the internal nodes of Ω^s. $\ddot{\mathbf{U}}_b^s$ is the acceleration acting on its boundaries inducing inertia force to the substructure. In order to eliminate the interface forces from the state equation, the output injection technique Zhang and Zhang (2018) is used and the process and measurement model are modified (for detail derivation refer to Section 4.3.3) as,

$$\begin{aligned} &\text{Process model} &:\quad &\mathbf{x}_k^s = \widetilde{A}_k^s\mathbf{x}_{k-1}^s + \widetilde{B}_k^s\mathbf{f}_k^s + \mathbf{G}_k^s\mathbf{y}_k^s + \widetilde{\mathbf{v}}_k^s \\ &\text{Measurement model} &:\quad &\mathbf{z}_k^s = \widetilde{H}_k^s\mathbf{x}_k^s + \widetilde{D}_k^s\mathbf{f}_k^s + \widetilde{w}_k^s \end{aligned} \tag{6.11}$$

The estimation of states and parameters is conducted by using the formulated equations by employing an IPEnKF, as described in Chapter 4, Section 4.2.2.

6.4 Fatigue evaluation model

Finally, in order to quantify the level of fatigue damage already incurred by the structure, a damage index needs to be adopted. In the context of concrete bridges, the Palmgren–Miner rule Miner (1945) and S–N curve are typically been used in the literature taking basis on Eurocode 2. With the Palmgren–Miner rule, the fatigue damage accumulation index (FDI) D can be defined as Equation (2.2). D denotes the level of fatigue-induced damage already incurred by the structure at its critical section with its highest value as 1 denoting complete failure Kwon et al. (2019). n_i is the number of stress cycles of the i^{th} fixed stress range the structure has been subjected to and N_i denotes the number of stress cycles at that given stress range needed for failure. Here, the entire stress range is assumed to be subdivided into m_s numbers of stress ranges. In order to prevent fatigue, condition $D \leq 1$ ideally should be satisfied. Accordingly, the remaining fatigue life can be defined as the departure of D from unity. n_i can further be determined using the rain-flow counting algorithm Downing and Socie (1982) obtained by analyzing the stress history while N_i can be obtained from the S-N curve of the material.

6.4.1 Fatigue evaluation of reinforcement

The fatigue failure of RC structures is majorly dependent on the steel reinforcement compared to concrete which is why an in-depth analysis of concrete fatigue can safely be circumvented in estimating the fatigue damage of the RC structure Elfgren (2015). Based on the verification conditions detailed in Wang et al. (2020a), the fatigue evaluation of reinforcement can be defined as follows:

$$\begin{aligned} &\text{If} \quad \frac{\Delta\sigma_{N^*}}{\gamma_S} \leq \gamma_F \Delta\sigma_i^s \leq \frac{\Delta\sigma_{N^*}}{\gamma_S}; \quad N_i = N^* \left(\frac{\frac{\Delta\sigma_{N^*}}{\gamma_S}}{\gamma_F \Delta\sigma_i^s} \right)^{k1}; \\ &\text{else} \quad \frac{\Delta\sigma_{N^*}}{\gamma_S} > \gamma_F \Delta\sigma_i^s \leq \frac{\Delta\sigma_{N^*}}{\gamma_S}; \quad N_i = N^* \left(\frac{\frac{\Delta\sigma_{N^*}}{\gamma_S}}{\gamma_F \Delta\sigma_i^s} \right)^{k2} \end{aligned} \tag{6.12}$$

here, N^* is the characteristic fatigue strength which can be obtained as the number of stress cycles required for failure $\Delta\sigma_{N^*}$ which generally depends on the type of reinforcement. N_i denotes the number of stress cycles for the i^{th} stress range needed for failure $\Delta\sigma_i^s$. γ_S and γ_F are the partial safety factors for the reinforcement and fatigue respectively with their recommended values as 1.15 and 1.0. k_1 and k_2 signify the slopes (first and second) of the S-N curve, respectively. Euro-code-2 specifies the values for $\Delta\sigma_{N^*}$, N^*, k_1, and k_2 as 162.5 MPa, 1×10^6, 5, and 9 respectively.

The following Figure 6.2 illustrates the proposed SHM-based fatigue life assessment method. The proposed approach is validated on a numerical RC bridge structure prior to applying it to a real bridge structure.

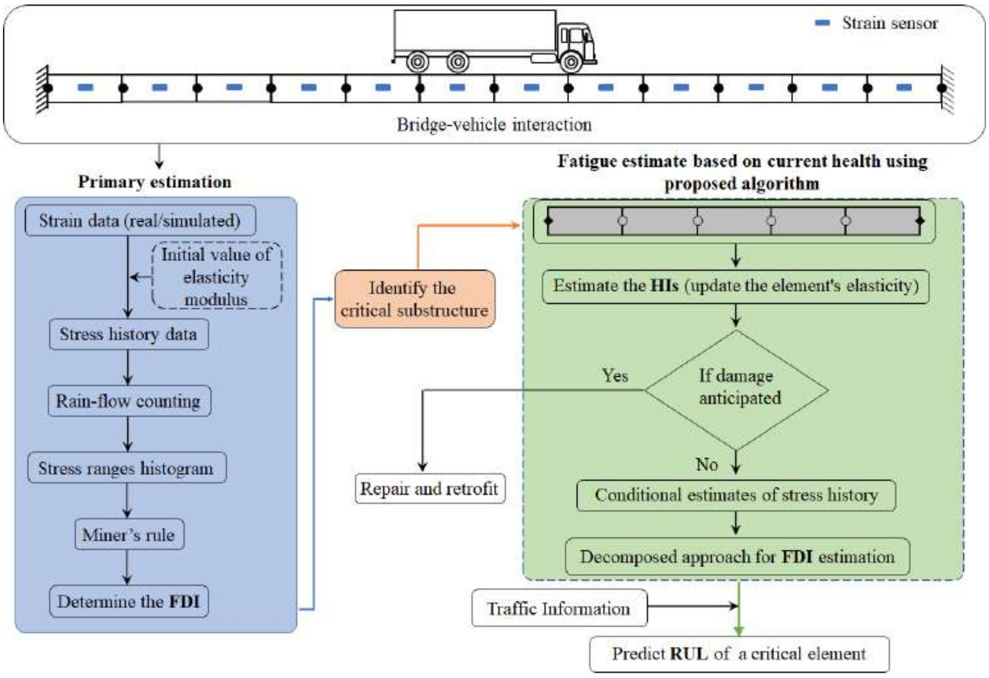

Figure 6.2: Flowchart of SHM-based fatigue life assessment method.

6.5 Numerical experiment

In this study, the numerical experiment is carried out using a 3D FEM of an RC box girder bridge (c.f Figure 6.3) with geometric properties: span = 31 m, area = 6.46 m^2, and material properties: mass density (ρ) = 2500 kg/m^3 and elastic modulus (E) = 40.6 GPa. Each element of the bridge is represented as a two-noded 3D Euler-Bernoulli beam with six dofs at each node (3 vertical and 3 rotational).

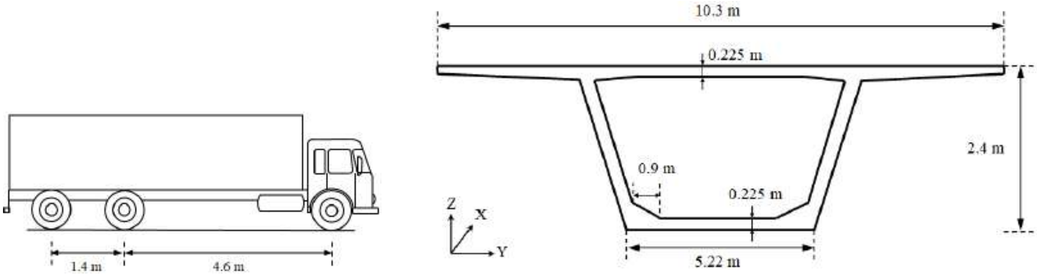

(a) Three-axle loading truck (b) Cross section of a box girder

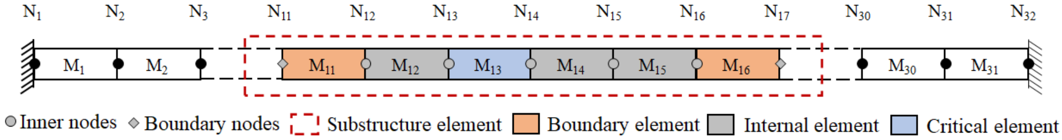

(c) Bridge model with its substructure

Figure 6.3: Schematic diagram of a box girder bridge model with its substructure used in numerical verification.

6.5.1 Identification of fatigue critical elements using primary estimation

In order to identify critical elements in the bridge, it is excited using simulated vehicle force, and accordingly, strain responses are sampled from each element. To simulate vehicle force, a three-axle truck is selected with its mechanical properties Gao et al. (2014) listed in Table 6.1. Subsequently, the vehicle structure interaction approach detailed previously is employed to simulate the bridge response under this loading. Next, critical elements of the bridge are identified using the stress history data. In this process, the stress history is first converted to the corresponding stress range vs cycles diagram using the rain-flow counting technique. Using the Miner rule, **FDI** is further calculated for all the elements (cf. Figure 6.2). Accordingly, the 13^{th} element is perceived to be critical as shown in Figure 6.4.

6.5.2 Local parameter estimation based on the substructure technique

In the process of identifying the critical element, it is typical to assume a standard value for the elastic modulus for mapping stress from the measured strain. Nevertheless, this assumption is still crude in the sense that over prolonged usage, the material properties are supposed to deteriorate. Eventually, this calls

Table 6.1: Mechanical properties of the three-axle vehicle model

Property	Value
Mass of truck body	31800 kg
Mass of front wheel	400 kg
Mass of middle/rear wheel	600 kg
Pitching moment of inertia	40000 kg m^2
Rolling moment of inertia	10000 kg m^2
Upper stiffness (front axle)	1200 kN m^{-1}
Upper stiffness (middle/rear axle)	2400 kN m^{-1}
Upper damping (front axle)	5 kN s m^{-1}
Upper damping (middle/rear axle)	10 kN s m^{-1}
Lower stiffness (front axle)	2400 kN m^{-1}
Lower stiffness (middle/rear axle)	4800 kN m^{-1}
Lower damping (front axle)	6 kN s m^{-1}
Lower damping (middle/rear axle)	12 kN s m^{-1}
Distance (front axle to center)	4.6 m
Distance (middle axle to center)	0.36 m
Distance (rear axle to center)	1.4 m
Wheelbase	1.8 m
Truck speed	10 km/h

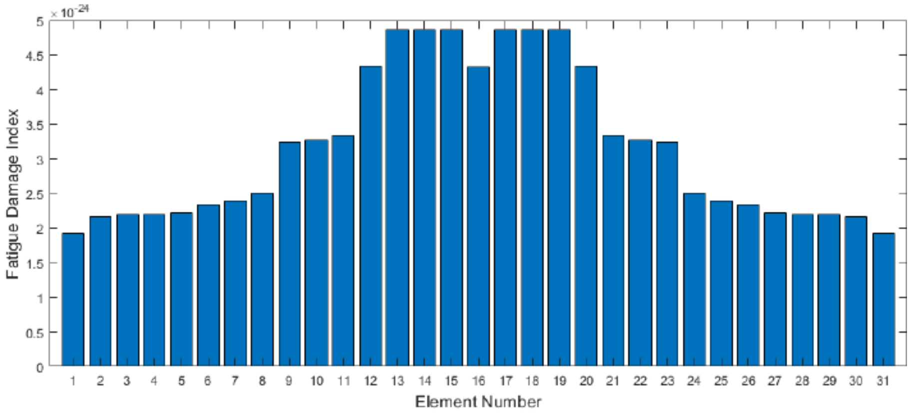

Figure 6.4: FDI for all structural elements under vehicle force.

for updated information on material properties which can be approached via the methodology proposed in this study. Surely, updating material properties will inevitably affect the stress mapping and selection of the S–N curve required for the fatigue analyses. This will also update the structural health by identifying any damages incurred by the bridge, which will require updating the support model as well. Yet this update will ensure a more precise estimation of **FDI** and/or RUL.

Eventually, following the approach proposed in this study, the bridge is monitored only for its fatigue critical zone in an attempt to estimate the **FDI** and RUL for the entire bridge. Supported by the initial numerical analysis, the 11^{th} to 16^{th} elements are accordingly adopted as the substructure under consideration. The adopted substructure is further defined by five internal nodes and two boundary nodes. Replicating the actual scenario, strain response under vehicle load is sampled from the internal nodes at a sampling frequency of 50 Hz (i.e. $dt = 0.02\ s$) and further added with SWGN of 1% *snr* to mimic real-life situations. Next, the proposed algorithm is employed for estimating stress histories conditioned on the current health while being completely unaware of the external loading or boundary forces.

The proposed approach adopts location-based **HI**s as the health parameters that take a value within a range of [0; 1]. This value for an arbitrary i^{th} element is further used to scale the standardized element elasticity E_0 in order to realize element elasticity E_i as $E_i = \mathbf{HI}_i E_0$. For system estimation as per the algorithm detailed in 2, the initial distribution of the parameter **HI**s are assumed as $\mathcal{N}(1.7, 0.01)$ for bench-marking the current health of the bridge with α set to 0.99 (cf. Equation (6.11)). 1000 particles and 50 ensembles are adopted for PF and EnKF simulations respectively.

Figure 6.5a demonstrates that the proposed approach has successfully estimated the stress histories while being conditioned on precise estimates for the **HI**s. This clearly demonstrates the capability of the proposal to avoid unnecessary instrumentation of the entire bridge especially when the fatigue critical zone is already identified. The proposal also investigates cases when damage is present in the structure. The pertinent case study deals with a system wherein one element within the fatigue critical zone is weakened (by 50%) through its elasticity and the proposed algorithm has precisely identified the location and severity (cf. Figure 6.5b). Figure 6.6, the estimated stress histories for substructure elements are compared against their true values (simulated from the full-scale model) and the results seem promising. In Figure 6.7, the actual measurements obtained through simulation are further compared with those predicted from the estimated states which can be found to be matching closely. Estimated **FDI** taking basis on the estimated state history is also found to be very close (relative error $< 6\%$) to the same obtained from the full-scale model simulation.

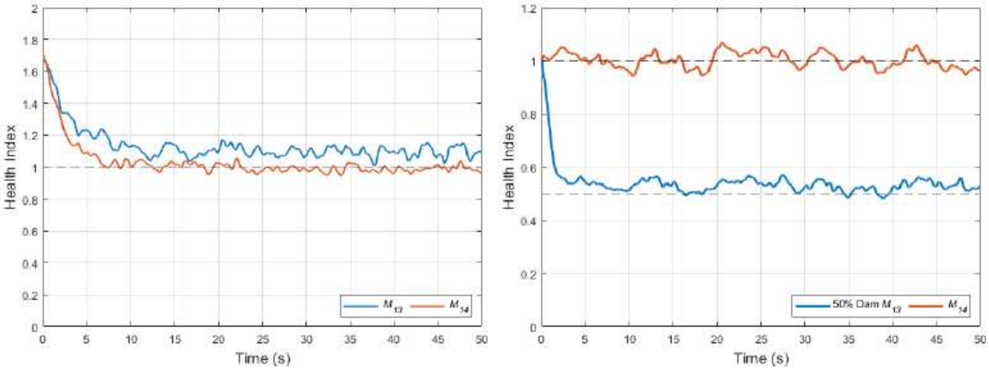

(a) Benchmarking of **HI**s for the undamaged structure (b) Health estimation for the damaged structure

Figure 6.5: Evaluation of substructure health indices for benchmarking and damaged beam (*dashed lines represent respective actual values*).

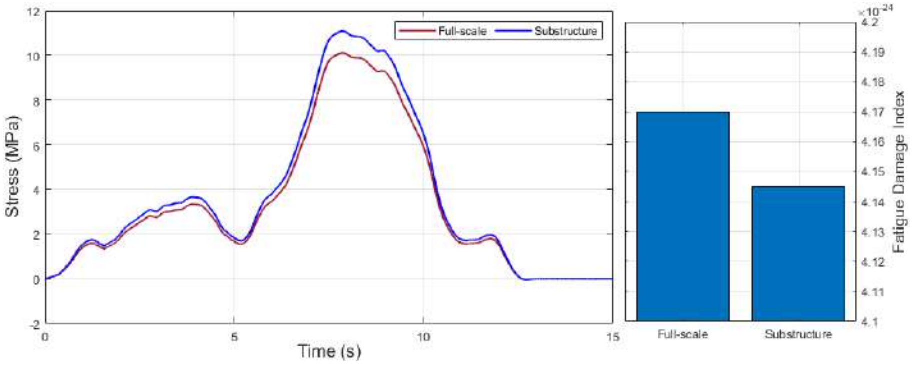

Figure 6.6: Comparison between estimated and actual vehicle-induced stress histories for the critical (13^{th}) element

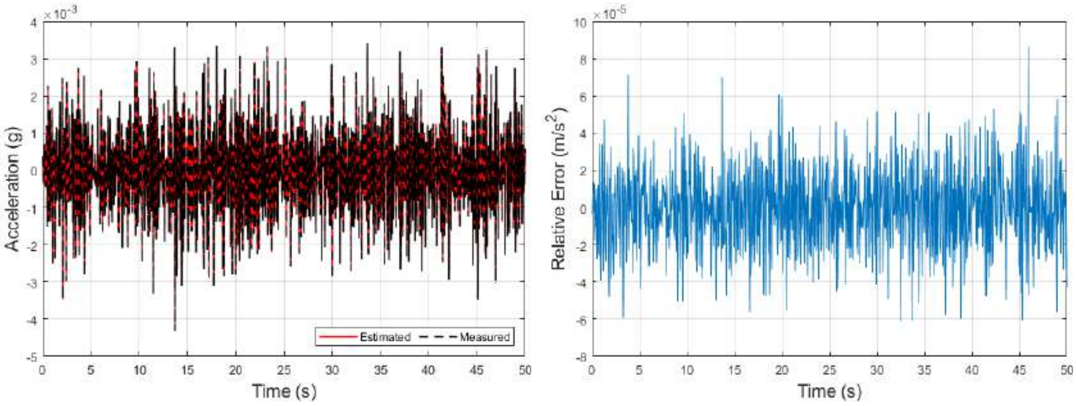

(a) Comparison of acceleration (b) Error b/w estimated and measured

Figure 6.7: Reconstruction of internal responses from estimated states and actual measurement responses.

6.6 Influence of vehicle parameters on FDI

In the previous investigation, it has been observed that under no knowledge of forces and bridge health, substructure stress histories, are conditioned on the current health estimate, and subsequently the **FDI** can be estimated using the proposed methodology. The further objective would be to perform prognosis studies to estimate the RUL of the structure under current and future loading status and road roughness. Of course, it is evident that RUL can be directly estimated if future stress history can be made available. However, this will eventually make the involvement of a numerical model mandatory to map the vehicle-induced loads to the corresponding stress in the critical member. This section attempts to assess the impact of each vehicle loading on the overall **FDI**. This way, the accumulated impact of a sequence of vehicles over a prolonged time can be decomposed into individual vehicle impacts so that **FDI** can be assessed directly from the vehicle loading history instead of the stress history. In achieving this objective, a parametric analysis must be undertaken under different vehicle parameters, like axle types, speed, the weight of vehicles, and also for different surface roughness of the road.

A numerical investigation for five different surface roughness: very good, good, average, poor, and very poor based on the roughness coefficient, has been undertaken (cf. Figure 6.8a). Nevertheless, the influence of roughness has been found not to be significant (except for very poor conditions) for **FDI**. Similarly, speed is varied (10, 25, 50, 75, 100 km/h) for a particular vehicle type under the same surface roughness and has been observed to be significantly affecting the **FDI**s (cf. Figure 6.8c). The impacts of axle types such as 2A-Car(2-axle car), 2A-Van(2-axle van), 2A-Truck(2-axle truck), 3A-Truck(3-axle truck), 4A-Truck(4-axle truck) are detailed in cf. Figure 6.8d and varying vehicular weight of 3A-Truck are detailed in Figure 6.8b on **FDI**s are also perceived to be major. Nevertheless, since axle type itself induces the impact of weight indirectly, consideration of vehicular weight separately for **FDI** calculation is avoided.

Finally, further investigation is taken up with vehicle type and speed varying simultaneously, and the **FDI**s for each of the cases are presented in Figure 6.9. With these individual **FDI** estimates, the cumulative impact of a sequence of vehicles on the **FDI** can be directly estimated without approaching costly model simulation for stress mapping. Of course, this inherently assumes that the bridge's health remains unchanged throughout this traffic loading. A change when anticipated or detected would, however, be estimated by the proposed monitoring approach and subsequently, the correlation between **FDI** and vehicle properties should be updated.

In the following, a real bridge is investigated with the proposed approach with traffic considered to be the only loading.

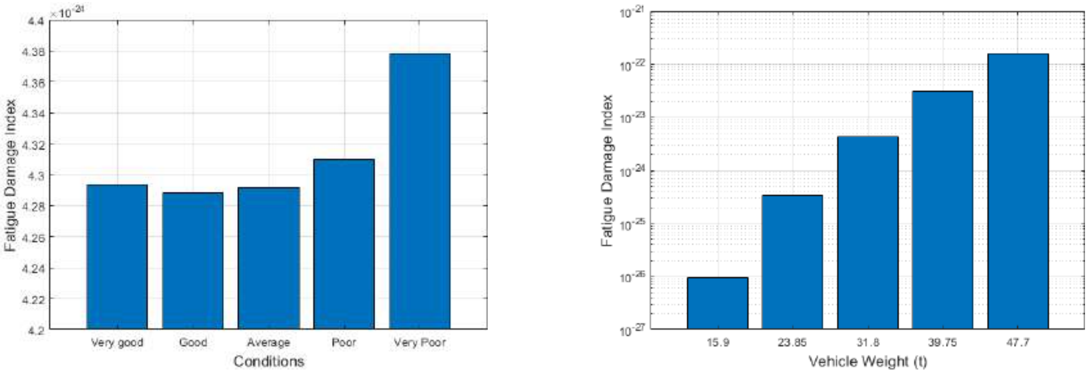

(a) Surface roughness (b) Vehicle weight

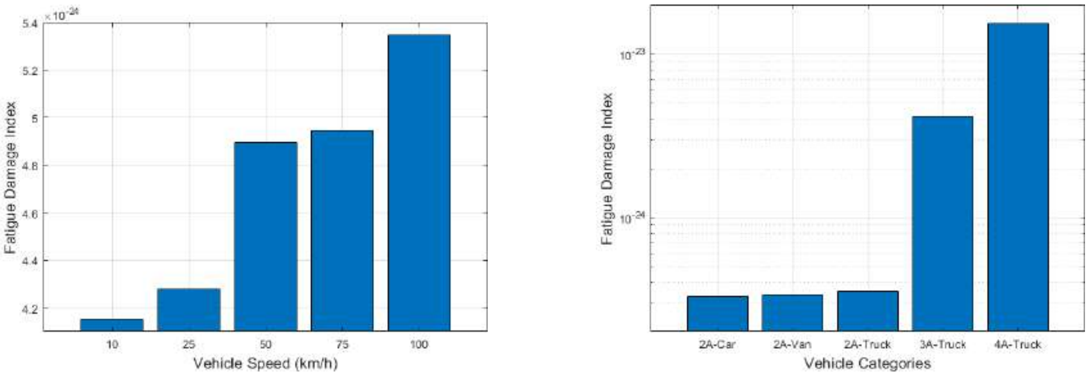

(c) Vehicle speed (d) Vehicle categories

Figure 6.8: **FDI** of a critical (13^{th}) element under different categories.

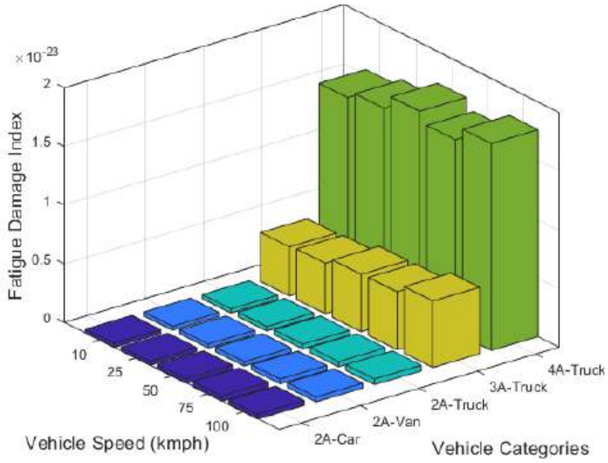

Figure 6.9: **FDI** of a critical (13^{th}) element with different vehicle speed and categories.

6.7 Experimental study

Real-time experiments are conducted on a reinforced concrete box girder bridge, locally called as “Kamand bridge” (cf. Figure 6.10) built over the river Uhl, a part of the river Beas watershed. The bridge is 72 m long, 4.3 m wide, whereas the main span is 41.35 m with a single lane capable. The average daily traffic data for this bridge is approximately 3000 vehicles, which is determined manually and categorized based on the type and speed of the vehicle in the Table 6.2

Figure 6.10: Kamand Bridge, Kamand village near Mandi town, Himachal Pradesh, India.

Table 6.2: Traffic classification according to vehicle type and speed

Vehicle	vehicle speed in km/h					Total by
type	10	25	50	75	100	vehicle type
2A- Car	404	1029	282	96	2	1813
2A-Van	92	224	36	14	0	366
2A-Truck	181	482	46	0	0	709
3A-Truck	78	52	1	0	0	131
4A-Truck	0	2	0	0	0	2
Total number of vehicles						3021

The health state of the bridge structure is benchmarked using wireless triaxial accelerometers as shown in Figure 6.11. Supported by the preliminary inspections that revealed that responses only in the vertical directions are insignificant, only vertical vibrations are measured. In total, 11 equidistant sensors are placed on the deck of the bridge with their positions schematically detailed in Figure 6.11. The acceleration history is recorded under moving vehicles with a sampling frequency of 64 Hz since the major dominant modes of the bridge are estimated to be lying within the bandwidth of $[0-32]$ Hz. .

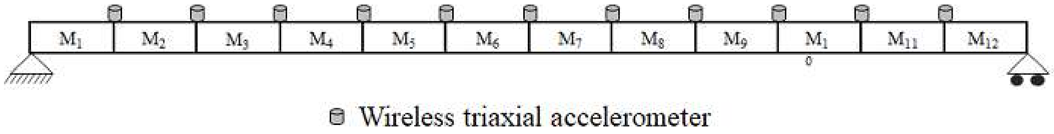

(a) Sensor locations over the main span

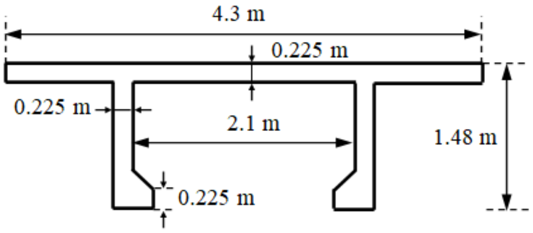

(b) Cross-section

Figure 6.11: Schematic representation of the bridge structure.

To implement the proposed approach on the real bridge, an accurate numerical replica (Digital Twin or DT) of the structure is prepared using the FEM approach with geometric details given in Figure 6.11. The actual boundary constraints, as found in the field, are modelled in the DT with pin and roller support at two of its ends.

6.7.1 Calibration of the digital twin model of Kamand bridge

Calibration of the DT model with respect to the real structure is undertaken in the modal domain. The modal analysis is performed and modes are compared against the same estimated using FDD of the measured response. For this, the material elasticity is, however, assumed to be uniform throughout the bridge, and subsequently tuned manually to match, within acceptable limits, the estimated frequencies to the same obtained from the measured response. The comparison between these is presented in Table 6.3. The calibrated model is further assessed to be sufficiently replicating the real structure. Further fine-tuning is subsequently approached via the proposed approach detailed in this chapter.

Table 6.3: Comparison between frequencies obtained experimentally and numerically.

Data		Experimental value	Calibrated numerical	Relative error (%)
Frequency (Hz)	ω_1	3.25	3.26	0.31
	ω_2	11.90	11.02	7.40

6.7.2 Proposed fatigue life assessment approach

As in reality, elasticity varies spatially, the numerical model of the bridge is required to be bench-marked assuming independent elasticity values for all its elements using the proposed algorithm. Similar to section 6.5.1, the DT model is examined under a simulated three-axle loading truck to determine the critical element [1]. Following, the stresses and subsequently the **FDI**s are calculated for each of the elements (as detailed in Figure 6.12) from which the 9^{th} element is identified as critical. Accordingly, the 7^{th} to 12^{th} elements are grouped under a single substructure which is required to be instrumented and monitored. Again, as detailed in section 6.5.2, 50 ensembles and 1000 particles are used for the proposed IPEnKF-based system estimation approach with $\alpha = 0.99$. Assuming a Gaussian distribution of $\mathcal{N}(1, 0.01)$ for the **HI**s of the elements within isolated substructures, the proposed algorithm is allowed to draw inferences from the measured data in order to estimate the stress histories in the monitored subdomain conditioned on its current health.

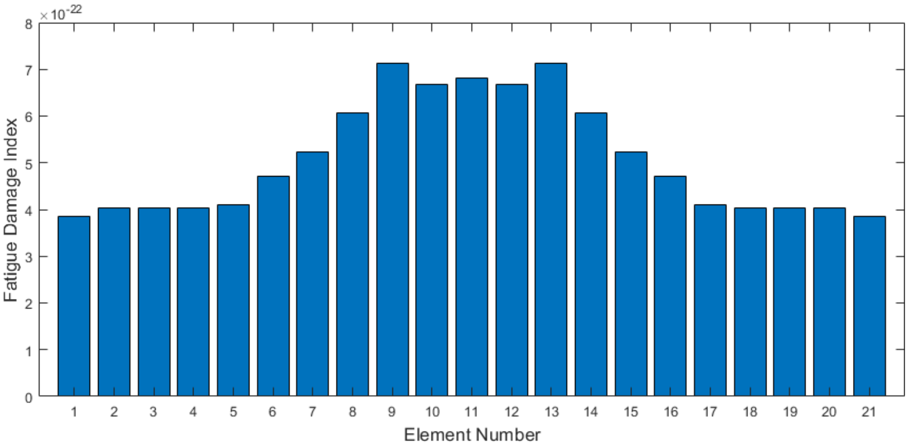

Figure 6.12: FDI for all structural elements of the DT model of the Kamand bridge under vehicle force.

---

[1] The same can also be obtained experimentally by abundantly instrumenting the entire structure, which, however, has been avoided in this study.

In order to validate the quality of the updated model, the predicted measurements are further compared against the actual measurements in Figure 6.13. Figure 6.14a demonstrates the convergence of the **HI**s to different values around 1, signifying the variation in the elasticity of the in-situ concrete. Finally, the **FDI** estimates are refined with the updated elasticity values which are then employed for the RUL estimation of the bridge under the assumption of constancy in the structural health (cf. Figure 6.14b). Typical traffic loads, as surveyed, have been taken into consideration for this RUL estimation only to demonstrate the capability of the proposed approach. The same can be undertaken for altered (or more detailed) loading scenarios (e.g. combined traffic, wind, etc.) depending on the need.

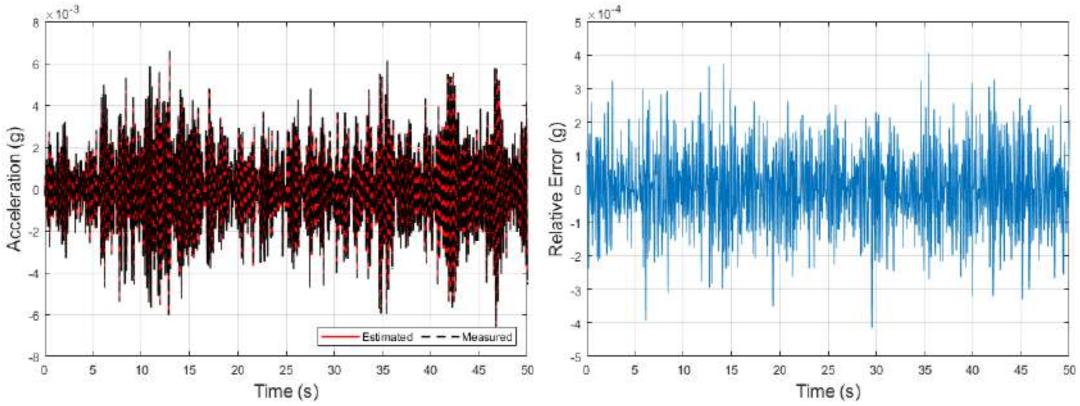

(a) Comparison of acceleration

(b) Error b/w estimated and measured

Figure 6.13: Reconstruction of internal responses from estimated states and actual measurement responses.

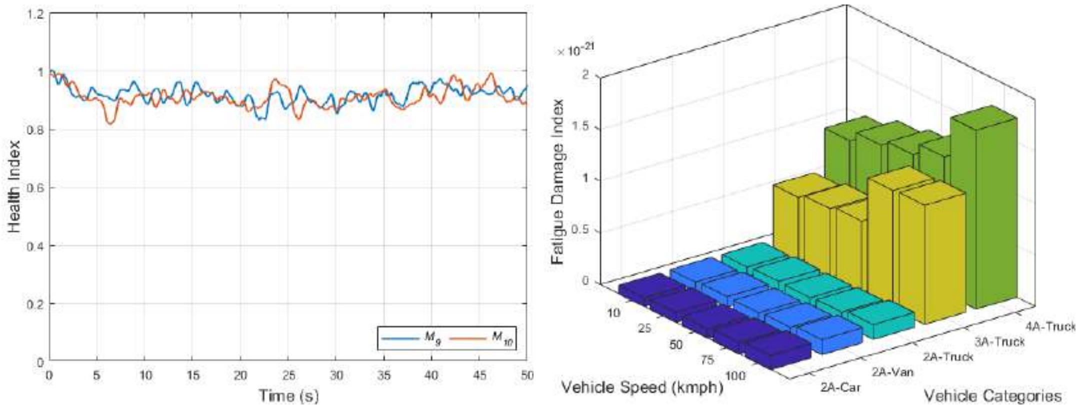

(a)

(b)

Figure 6.14: Evaluation of substructure **HI** and **FDI** of a digital twin model: a) Benchmarking of **HI**s; b) **FDI** of a critical (9^{th}) element.

In the context of the monitored bridge, which typically experiences low-magnitude traffic (refer to Table **??**), the **FDI**s for its critical location are derived through direct simulation involving a daily train of 3021 vehicles. Remarkably, the analysis of resulting stress history leads to an **FDI** value that deviates by only 4.6% (relative error) from the estimate obtained without a computationally intensive simulation, as outlined in this chapter. This impressive level of accuracy supports the conclusion that the decomposed approach for **FDI** estimation is not only highly reliable but also cost-effective.

An uncertainty analysis is also undertaken to establish a range of predicted **FDI** values, utilizing a probabilistic measure for traffic following a Gaussian distribution $\mathcal{N}(3021, 475)$ for the next 650 years (cf. Figure 6.15). The coefficient of variation in the vehicle numbers is assumed to be 15% and is used for the validation of the proposed approach within a Gaussian distribution framework. In addition, the estimation of a critical element's service life involves factoring in the annual traffic growth rate based on $IRC\ 108-1996$, which is determined by the bridge's location and subsequently calculating the yearly increase in traffic load. Interestingly, the proposed approach consistently produces predictions that align perfectly within a 95 percentile confidence interval. These findings further underscore the approach's robustness and its potential for dependable fatigue damage estimation even in long-term projections.

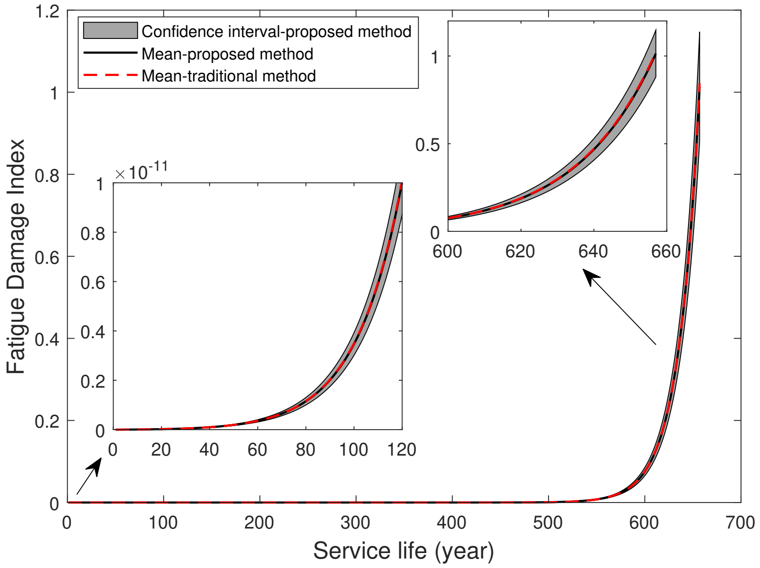

Figure 6.15: Service life of a critical element
The first subplot of the graph illustrates the projected service life of the Kamand bridge for the next 120 *years. During this period, the FDI remains at a low level. Moving on to the next subplot of the graph, the FDI gradually increases with respect to service time and reaches its highest point of* 1 *at the* 656 *year mark. Utilizing a conventional methodology, the anticipated service life of the Tsing Ma Bridge is predicated as a* 718 *years Ye et al. (2012)*

The **RUL** of the Kamand bridge is estimated approximately 650 *years*, a duration that might appear noteworthy. A similar study using conventional methodology is conducted on the Tsing Ma bridge, utilizing measured strain data, revealing a predicted fatigue life of 718 *years* Ye et al. (2012). This could be partly due to the possibility that the current traffic volume on the bridge is comparatively lower than the maximum allowable traffic volume required for the structure. It is important to note that the precision of **RUL** is intrinsically linked to the accessibility of a sufficient quantity of daily strain data for the critical element Ye et al. (2012).

6.8 Summary

The traditional method of fatigue life estimation for structures requires monitoring the entire structural domain regardless of its location-based fatigue proneness. The precise estimation employing high-dimensional models and dense instrumentation is however redundant for cases when information regarding fatigue critical location is available. Targeting such cases, a novel substructure-estimation-based approach powered by a Bayesian filtering algorithm is demonstrated here that concentrates the monitoring effort only for the fatigue-critical location. Isolating a subdomain from the entire structural domain needs a precise estimation of boundary forces, which is circumvented in this proposal through an output injection technique. Further, the proposal also addresses the idealistic assumption of the constancy of the health state throughout the service life of the bridge and provides a means to conditionally estimate the fatigue life with respect to the current health state. The approach is validated against a numerical model and found to be sufficiently accurate leading to an inexpensive yet generalized and robust approach to fatigue life estimation.

Nevertheless, precise RUL estimation demands a full-scale numerical model to be simulated under operational conditions (load, structural health, etc.). This cost-intensive simulation procedure is bypassed by defining a decomposed estimation approach for fatigue damage accumulation index (**FDI**)s wherein traffic properties can be employed directly to arrive at the **FDI** without the numerical simulation. The proposal is numerically validated before employing life prediction for a real bridge. The overall performance is perceived to be convincing and promising for fatigue life estimation for high-dimensional infrastructures.

Chapter 7

Conclusion

This dissertation focused on the assessment of fatigue life for bridge infrastructures. The inspiration for this study came from the remarkable longevity of Victoria Bridge in Mandi, Himachal Pradesh, which has served for 143 years. The goal was to understand the factors affecting the service life of structures and develop accurate prediction methods to safeguard their integrity.

The research proposed a probabilistic framework for fatigue life estimation using SHM techniques. Two approaches, stress life, and fracture mechanics, were discussed. The stress-life approach utilized stress history data obtained from SHM to assess fatigue damage and predict life. The fracture mechanics approach employed Paris's Law to estimate crack growth based on stress intensity factors. The effectiveness of the proposed framework for calculating SIFs was validated through numerical simulations and comparisons with analytical results. The results demonstrated the reliability and efficiency of the algorithm in calculating SIFs.

Chapter 3 presents an online Bayesian model-assisted filtering-based prognosis algorithm for predicting the service life of civil infrastructural components susceptible to fatigue failure. The algorithm incorporates an updated Paris law model to account for crack closure effects. The study demonstrates that the algorithm can effectively estimate the crack growth of the components, even with limited data availability. It provides mean estimates of parameters and crack growth, along with confidence intervals, making it practical for real-life applications. The proposed approach shows excellent performance with thermo-mechanical loading and makes it a suitable method for estimating the RUL of civil infrastructure subjected to fatigue-loaded.

Chapter 4 introduces a substructuring-based monitoring approach for assessing the fatigue life of large structures. The simple substructure technique with boundary forces known demonstrates its accuracy and precision in estimating response parameters for damaged cases. However, it acknowledges limitations such as extensive monitoring and interdependence of substructure models. To overcome the challenge of unavailable boundary measurements, a novel Bayesian filter-based approach is proposed. This approach proves to be stand-alone, computationally efficient, and prompt in estimation. The combination of Particle Filter and Ensemble Kalman Filter enables parallelization and interface-independent estimation, making it suitable for distributed health monitoring systems. The effectiveness of the proposed algorithm is validated through numerical and real experiments, confirming its accuracy, precision, and efficiency in detecting and quantifying health deterioration. In summary, this research provides a framework for efficient component-wise monitoring and its potential application in fatigue life estimation for large structural domains.

Chapter 5 presents a comprehensive approach for estimating the fatigue life of large civil structures with visible cracks. By integrating various techniques, including the updated substructure model and an algorithm for accurate estimation of boundary forces, the RUL estimation is achieved. The approach is validated through numerical simulations, experimental investigations, and field experiments on the Chandra bridge, demonstrating its precision and accuracy. Moreover, the application of the proposed approach with different loading conditions demonstrates the reliability of the fatigue life predictions. Overall, this research provides valuable insights and a practical framework for ensuring structural integrity and prolonging the service life of civil structures in real-life scenarios.

Chapter 6 presents a substructure-estimation-based approach that offers a practical solution for estimating fatigue life for structures with no visible crack by targeting critical fatigue locations instead of monitoring the entire structural domain. The proposed approach, powered by a Bayesian filtering algorithm, efficiently concentrates monitoring efforts on the fatigue-critical location, reducing the need for dense instrumentation. By addressing the idealistic (as well as non-realistic) assumption of a constant health state, the approach provides conditional fatigue life estimation based on the current health status. The numerical validation and subsequent application to a real bridge demonstrate the accuracy and cost-effectiveness of the proposed approach for fatigue life estimation in high-dimensional infrastructures.

Overall, this dissertation addresses a few of the major problems in the field of fatigue life estimation for bridge infrastructures. The developed methodologies and techniques provide valuable tools for engineers and researchers to assess the integrity and predict the RUL of structures.

7.1 Limitations of the work

Despite the attempts to address the challenges of SHM-based fatigue life assessment, such as limited data, large structures, and estimation of vehicle-induced forces on structural dynamics, there are still limitations with the proposed algorithms. These limitations are discussed below:

- While the algorithms have been primarily developed for bridge infrastructure, rigorous validation on actual bridge structures with fatigue damage is necessary to ensure their accuracy and reliability.
- Although the approaches have been developed and validated using numerical and real experiments, obtaining crack growth data from real structures was challenging due to practical constraints. Further, such opportunities of monitoring a crack present in a member of a bridge are rare. As an alternative, a replica of the real structure was created, and crack growth data was artificially induced through ABAQUS-XFEM.
- Currently, the algorithms incorporate only stationary white Gaussian noise to mimic real-time uncertainty in sensor data. To enhance realism, future work should consider the inclusion of non-stationary coloured Gaussian noise, which more closely represents the variability in real-world conditions.
- The estimation of RUL currently focuses on bridge-vehicle interaction. However, for more accurate life estimation, it is important to consider additional factors such as wind-induced vibration or vortex-induced vibration, which can significantly impact structural fatigue.
- The calculation of SIF currently considers only axial loading. For more accurate life estimation, it is recommended to incorporate loading in all translational and rotational directions of the structure, providing a more comprehensive understanding of crack propagation and fatigue life.

- To improve the realism of crack modelling, future studies should consider the inclusion of surface crack conditions, as these are commonly observed in practical scenarios.
- Previous studies calculated worst-case scenarios by applying thermomechanical loading conditions. To further enhance the calculation of RUL, it is suggested to apply these scenarios to real-time bridge structures, allowing for more accurate predictions under realistic operating conditions.

By addressing these limitations and incorporating the suggested improvements, future research can advance the field of SHM-based fatigue life assessment and provide more accurate predictions for the RUL of engineering structures.

7.2 Future work

Based on the accomplishments and remaining limitations of this study, the future scope is outlined as follows:

- **Real-time application:** The worst-case scenario determination based on thermo-mechanical loading conditions can be applied to real-time bridge structures, allowing for accurate and timely estimation of RUL under realistic operating conditions.
- **Further validation:** Rigorous validation of the developed methodology on bridge infrastructure is essential to ensure its applicability and robustness in real-world scenarios.
- **Comprehensive SIF:** The calculation of SIF can be further developed to consider loading conditions in all translational and rotational directions of the structure, thereby providing a more comprehensive understanding of crack propagation and fatigue life estimation. Furthermore, probabilistic XFEM will be considered for incorporating system uncertainties to provide a probabilistic SIF estimate.
- **Realistic crack modelling :** Future studies can focus on incorporating surface crack conditions to enhance the accuracy and realism of crack modelling, reflecting the diverse range of crack types observed in practical scenarios.

- **Expansion of RUL estimation:** The estimation of the RUL based on bridge-vehicle interaction can be expanded to include additional factors, such as wind-induced vibration or vortex-induced vibration, which can significantly impact the structural integrity of the system. Furthermore, stress induced by ambient conditions has to be considered as a random variable

- **Retrofitting strategies:** To enhance the RUL of structures, retrofitting techniques such as applying patches on the crack surface can be explored. These strategies can help restrict crack growth and extend the structural integrity of damaged/ageing systems.

- **Implementation of strain/stress reduction techniques:** Incorporating strain/stress reduction techniques, such as tuned mass dampers, can provide an alternative approach to enhance the RUL of structures by reducing applied stress levels and mitigating fatigue damage.

- **Application to other engineering structures:** The algorithm developed in this study shows potential for application in various engineering domains, including civil, mechanical, aerospace, military, and offshore structures. Further investigations can be conducted to assess its effectiveness and adaptability in these areas.

By addressing these aspects in future research, this study can contribute to further advancements in the field of fatigue life prediction and structural integrity assessment in engineering structures.

Bibliography

Adasooriya, N. and Siriwardane, S. (2014). Remaining fatigue life estimation of corroded bridge members. *Fatigue & Fracture of Engineering Materials & Structures*, 37(6):603–622.

Agerskov, H. and Nielsen, J. A. (1999). Fatigue in steel highway bridges under random loading. *Journal of Structural Engineering*, 125(2):152–162.

Aktan, A. E., Helmicki, A. J., and Hunt, V. J. (1998). Issues in health monitoring for intelligent infrastructure. *Smart Materials and Structures*, 7(5):674.

Al-Emrani, M. (2005). Fatigue performance of stringer-to-floor-beam connections in riveted railway bridges. *Journal of Bridge Engineering*, 10(2):179–185.

Al-Rubaie, K. (2008). A general model for stress-life fatigue prediction. *Materialwissenschaft und Werkstofftechnik: Entwicklung, Fertigung, Prüfung, Eigenschaften und Anwendungen technischer Werkstoffe*, 39(6):400–406.

Alampalli, S. and Lund, R. (2006). Estimating fatigue life of bridge components using measured strains. *Journal of Bridge Engineering*, 11(6):725–736.

Albrecht, P. and Yazdani, N. (1986). Risk analysis of extending bridge service life. *Report No. FHWA/MD*, 84(01).

Albuquerque, C., Silva, A. L., de Jesus, A. M., and Calçada, R. (2015). An efficient methodology for fatigue damage assessment of bridge details using modal superposition of stress intensity factors. *International Journal of Fatigue*, 81:61–77.

Anderson, T. L. (2017). *Fracture mechanics: fundamentals and applications.* CRC press.

API, R. (2005). Recommended practice for planning, designing, and constructing fixed offshore platforms-working stress design. api rp 2a-wsd.

Aswal, N., Kuncham, E., Sen, S., and Mevel, L. (2021a). Robust interacting particle-kalman filter based structural damage estimation using dynamic strain measurements under non-stationary excitation-an experimental study. In *SHMII-10 2021–10th International Conference on Structural Health Monitoring of Intelligent Infrastructure.*

Aswal, N., Sen, S., and Mevel, L. (2021b). Estimation of local failure in tensegrity using interacting particle-ensemble kalman filter. *Mechanical Systems and Signal Processing*, 160:107824.

Aygül, M., Bokesjö, M., Heshmati, M., and Al-Emrani, M. (2013). A comparative study of different fatigue failure assessments of welded bridge details. *International Journal of Fatigue*, 49:62–72.

Baptista, R., Santos, T., Marques, J., Guedes, M., and Infante, V. (2018). Fatigue behavior and microstructural characterization of a high strength steel for welded railway rails. *International journal of fatigue*, 117:1–8.

Barth, A. S. and Bowman, M. D. (2001). Fatigue behavior of welded diaphragm-to-beam connections. *Journal of Structural Engineering*, 127(10):1145–1152.

Bathias, C. (1999). There is no infinite fatigue life in metallic materials. *Fatigue & fracture of engineering materials & structures (Print)*, 22(7):559–565.

Board, N. T. S. and Board, U. S. N. T. S. (2008). *Collapse of I-35W Highway Bridge, Minneapolis, Minnesota, August 1, 2007*. Createspace Independent Pub.

Branco, R., Antunes, F., Ferreira, J. M., and Silva, J. (2009). Determination of paris law constants with a reverse engineering technique. *Engineering Failure Analysis*, 16(2):631–638.

Bressel, M., Hilairet, M., Hissel, D., and Bouamama, B. O. (2016). Extended kalman filter for prognostic of proton exchange membrane fuel cell. *Applied Energy*, 164:220–227.

Burhan, I. and Kim, H. S. (2018). Sn curve models for composite materials characterisation: An evaluative review. *Journal of Composites Science*, 2(3):38.

Callister, W. D., Rethwisch, D. G., et al. (2007). *Materials science and engineering: an introduction*, volume 7. John wiley & sons New York.

Carpinteri, A. and Paggi, M. (2007). Are the paris' law parameters dependent on each other? *Frattura ed Integrità Strutturale*, 1(2):10–16.

Casciati, F. (2003). An overview of structural health monitoring expertise within the european union. *Structural health monitoring and intelligent infrastructure*, pages 31–37.

Cavallini, G. and Lazzeri, R. (2007). A probabilistic approach to fatigue risk assessment in aerospace components. *Engineering fracture mechanics*, 74(18):2964–2970.

Celli, D. (2021). *Stochastic Energy-Based Fatigue Life Prediction Framework Utilizing Bayesian Statistical Inference*. The Ohio State University.

Chajes, M. J., Shenton III, H. W., and O'Shea, D. (2000). Bridge-condition assessment and load rating using nondestructive evaluation methods. *Transportation Research Record*, 1696(1):83–91.

Chakraborty, S. and DeWolf, J. T. (2006). Development and implementation of a continuous strain monitoring system on a multi-girder composite steel bridge. *Journal of Bridge Engineering*, 11(6):753–762.

Chan, T., Zhou, T., Li, Z., and Guo, L. (2005). Hot spot stress approach for tsing ma bridge fatigue evaluation under traffic using finite element method. *Structural Engineering and Mechanics*, 19(3):261–280.

Chan, T. H., Guo, L., and Li, Z. (2003). Finite element modelling for fatigue stress analysis of large suspension bridges. *Journal of Sound and Vibration*, 261(3):443–464.

Chan, T. H., Li, Z., and Ko, J. M. (2001). Fatigue analysis and life prediction of bridges with structural health monitoring data—part ii: Application. *International Journal of Fatigue*, 23(1):55–64.

Chen, H.-P. (2018). *Structural health monitoring of large civil engineering structures.* John Wiley & Sons.

Chen, J., Yuan, S., Qiu, L., Cai, J., and Yang, W. (2016). Research on a lamb wave and particle filter-based on-line crack propagation prognosis method. *Sensors*, 16(3):320.

Chen, Z. et al. (2003). Bayesian filtering: From kalman filters to particle filters, and beyond. *Statistics*, 182(1):1–69.

Cheperanov, G. (1967). Crack propagation in continuous media. *USSR J. Appl. Math. and Mech. Translation*, 31:504.

Christian, L. (1999). Mechanical vibration & shock: Fatigue damage.

Christides, S. and Barr, A. (1984). One-dimensional theory of cracked bernoulli-euler beams. *International Journal of Mechanical Sciences*, 26(11-12):639–648.

Collins, J. A. (1993). *Failure of materials in mechanical design: analysis, prediction, prevention.* John Wiley & Sons.

Committee, A. W. S. S. W., Society, A. W., and Institute, A. N. S. (1994). *Structural Welding Code–steel.* Amer Welding Society.

Compare, M. and Zio, E. (2014). Predictive maintenance by risk sensitive particle filtering. *IEEE Transactions on Reliability*, 63(1):134–143.

Connor, R. J. (2004). Influence of cutout geometry on stresses at welded rib-to-diaphragm connections in steel orthotropic bridge decks. *Transportation research record*, 1892(1):78–87.

Connor, R. J. and Fisher, J. W. (2006). Identifying effective and ineffective retrofits for distortion fatigue cracking in steel bridges using field instrumentation. *Journal of Bridge Engineering*, 11(6):745–752.

Connor, R. J., Richards, S. O., and Fisher, J. W. (2003). Long-term remote monitoring of prototype orthotropic deck panels on the bronx-whitestone bridge for fatigue evaluation. *Recent Developments in Bridge Engineering*, pages 257–268.

Coppe, A., Pais, M. J., Haftka, R. T., and Kim, N. H. (2012). Using a simple crack growth model in predicting remaining useful life. *Journal of Aircraft*, 49(6):1965–1973.

David, S. (2017). 10 years after bridge collapse, america is still crumbling.

De Jesus, A. M., da Silva, A. L., Figueiredo, M. V., Correia, J. A., Ribeiro, A. S., and Fernandes, A. A. (2011). Strain-life and crack propagation fatigue data from several portuguese old metallic riveted bridges. *Engineering Failure Analysis*, 18(1):148–163.

de Klerk, D., Rixen, D. J., and Voormeeren, S. (2008). General framework for dynamic substructuring: history, review and classification of techniques. *AIAA journal*, 46(5):1169–1181.

DeWolf, J. T., Lauzon, R. G., and Culmo, M. P. (2002). Monitoring bridge performance. *Structural Health Monitoring*, 1(2):129–138.

Dhondt, G. (2014). Application of the finite element method to mixed-mode cyclic crack propagation calculations in specimens. *International journal of fatigue*, 58:2–11.

Djoković, J. M., Nikolić, R. R., and Bujnak, J. (2015). Working life of the i-beam with a crack. *Procedia Engineering*, 111:142–148.

Dodds, C. and Robson, J. (1973). The description of road surface roughness. *Journal of sound and vibration*, 31(2):175–183.

Downing, S. D. and Socie, D. (1982). Simple rainflow counting algorithms. *International journal of fatigue*, 4(1):31–40.

Duan, R. and Yang, J. (2013). Modelling and simulation of a bridge interacting with a moving vehicle system.

Elfgren, L. (2015). *Fatigue Capacity of Concrete Structures: Assessment of Railway Bridges*. Luleå tekniska universitet.

Elfgren, L., Enochsson, O., Puurula, A., Thun, H., Paulsson, B., and Täljsten, B. (2007). Testing to failure of a reinforced concrete railway trough bridge in örnsköldsvik, sweden. In *Sustainable Bridges-Assessment for Future Traffic Demands and Longer Lives: 10/10/2007-11/10/2007*, pages 445–460. Dolnoslaskie Wydawnictwo Edukacyjne.

Ellyin, F. (2012). *Fatigue damage, crack growth and life prediction.* Springer Science & Business Media.

Erdogan, F. and Sih, G. (1963). On the crack extension in plates under plane loading and transverse shear. *Journal of Fluids Engineering.*

Ermopoulos, J. and Spyrakos, C. C. (2006). Validated analysis and strengthening of a 19th century railway bridge. *Engineering Structures*, 28(5):783–792.

Evensen, G. (2003). The ensemble kalman filter: Theoretical formulation and practical implementation. *Ocean dynamics*, 53:343–367.

Fafard, M., Bennur, M., and Savard, M. (1997). A general multi-axle vehicle model to study the bridge-vehicle interaction. *Engineering Computations.*

Farrar, C. R. and Lieven, N. A. (2007). Damage prognosis: the future of structural health monitoring. *Philosophical Transactions of the Royal Society A: Mathematical, Physical and Engineering Sciences*, 365(1851):623–632.

Farrar, C. R. and Worden, K. (2007). An introduction to structural health monitoring. *Philosophical Transactions of the Royal Society A: Mathematical, Physical and Engineering Sciences*, 365(1851):303–315.

Fatemi, A., Fuchs, H. O., Stephens, R. I., and Stephens, R. R. (2001). Metal fatigue in engineering. *A wiley-interscience Publication.*

Feng, D. and Feng, M. Q. (2018). Computer vision for shm of civil infrastructure: From dynamic response measurement to damage detection–a review. *Engineering Structures*, 156:105–117.

Feng, S., Xu, Y., Han, X., Li, Z., and Incecik, A. (2021). A phase field and deep-learning based approach for accurate prediction of structural residual useful life. *Computer Methods in Applied Mechanics and Engineering*, 383:113885.

File, D. (1998). Consider direction of loading when sizing fillet welds. *Welding innovation*, 15(2).

Fisher, J. (1984). Fatigue and fracture in steel bridges case studies, john willy & sons.

Forman, R. G., Kearney, V., and Engle, R. (1967). Numerical analysis of crack propagation in cyclic-loaded structures. *Journal of Fluids Engineering.*

Fricke, W. (2003). Fatigue analysis of welded joints: state of development. *Marine structures*, 16(3):185–200.

Gao, Q., Wang, Z., Guo, B., and Chen, C. (2014). Dynamic responses of simply supported girder bridges to moving vehicular loads based on mathematical methods. *Mathematical Problems in Engineering.*

Ge, H., Kang, L., and Tsumura, Y. (2013). Extremely low-cycle fatigue tests of thick-walled steel bridge piers. *Journal of Bridge Engineering*, 18(9):858–870.

Gonzalez, A., Schorr, M., Valdez, B., and Mungaray, A. (2020). Bridges: structures and materials, ancient and modern. *Infrastructure Management and Construction*.

González-Velázquez, J. L. (2020). *Mechanical behavior and fracture of engineering materials*. Springer.

Gordon, N. J., Salmond, D. J., and Smith, A. F. (1993). Novel approach to nonlinear/non-gaussian bayesian state estimation. In *IEE proceedings F (radar and signal processing)*, volume 140, pages 107–113. IET.

Gurney, T. R. (1979). *Fatigue of welded structures*. CUP Archive.

Guyer, R. C. and Laman, J. A. (2012). Distortion-induced stress investigation of double angle stringer-to-floorbeam connections in railroad bridges. *Engineering structures*, 38:104–112.

Haghani, R., Al-Emrani, M., and Heshmati, M. (2012). Fatigue-prone details in steel bridges. *Buildings*, 2(4):456–476.

Hahin, C., South, J., Mohammadi, J., and Polepeddi, R. (1993). Accurate and rapid determination of fatigue damage in steel bridges. *Journal of Structural Engineering*, 119(1):150–168.

Hamdia, K. M., Silani, M., Zhuang, X., He, P., and Rabczuk, T. (2017). Stochastic analysis of the fracture toughness of polymeric nanoparticle composites using polynomial chaos expansions. *International Journal of Fracture*, 206(2):215–227.

Henchi, K., Fafard, M., Talbot, M., and Dhatt, G. (1998). An efficient algorithm for dynamic analysis of bridges under moving vehicles using a coupled modal and physical components approach. *Journal of sound and Vibration*, 212(4):663–683.

Hernandez-Duque, G., Schorr, M., Carpio, J., and Martinez, L. (1995). Preservation of the infrastructure in the gulf of mexico. *Corrosion Reviews*, 13(2-4):65–80.

Hobbacher, A. et al. (2016). *Recommendations for fatigue design of welded joints and components*, volume 47. Springer.

Hommels, A., Murakami, A., and Nishimura, S.-I. (2009). A comparison of the ensemble kalman filter with the unscented kalman filter: application to the construction of a road embankment. *Geotechniek*, 13(1):52.

Hou, J., Jankowski, Ł., and Ou, J. (2011). A substructure isolation method for local structural health monitoring. *Structural Control and Health Monitoring*, 18(6):601–618.

Hou, J., Jankowski, Ł., and Ou, J. (2013). An online substructure identification method for local structural health monitoring. *Smart materials and structures*, 22(9):095017.

Huang, M., Cheng, X., and Lei, Y. (2021). Structural damage identification based on substructure method and improved whale optimization algorithm. *Journal of Civil Structural Health Monitoring*, 11(2):351–380.

IIW, A. (2000). Fatigue design procedures for welded hollow section joints, iiw doc. xiii-1804-99, iiw doc. xv-1035-99. In *Recommendations for IIW subcommission XV-E*. Abington Publishing Cambridge, UK.

Imam, B. M., Righiniotis, T. D., and Chryssanthopoulos, M. K. (2007). Numerical modelling of riveted railway bridge connections for fatigue evaluation. *Engineering Structures*, 29(11):3071–3081.

John, B. (2019). Design errors draw blame in collapse of fiu pedestrian bridge that killed.

Julia, P. (2019). A deadly tsunami of molasses in boston's north end.

Julier, S. J., Uhlmann, J. K., and Durrant-Whyte, H. F. (1995). A new approach for filtering nonlinear systems. In *Proceedings of 1995 American Control Conference-ACC'95*, volume 3, pages 1628–1632. IEEE.

Kaczinski, M. R., Stokes, F. E., Lugger, P., and Fisher, J. W. (1997). Williamsburg bridge orthotropic deck fatigue test. *ATLSS Rep. No. 97*, 4.

Kalman, R. E. (1960). A new approach to linear filtering and prediction problems. *Journal of Fluids Engineering*.

Karamchandani, A., Dalane, J., and Bjerager, P. (1992). Systems reliability approach to fatigue of structures. *Journal of Structural Engineering*, 118(3):684–700.

Karlsson, R., Schon, T., and Gustafsson, F. (2005). Complexity analysis of the marginalized particle filter. *IEEE Transactions on Signal Processing*, 53(11):4408–4411.

Karunananda, K., Ohga, M., Dissanayake, R., Siriwardane, S., and Chun, P.-j. (2012). New combined high and low-cycle fatigue model to estimate life of steel bridges considering interaction of high and low amplitudes loadings. *Advances in Structural Engineering*, 15(2):287–302.

Khatir, S., Dekemele, K., Loccufier, M., Khatir, T., and Wahab, M. A. (2018). Crack identification method in beam-like structures using changes in experimentally measured frequencies and particle swarm optimization. *Comptes Rendus Mécanique*, 346(2):110–120.

Kim, Y. and Hwang, W. (2019). High-cycle, low-cycle, extremely low-cycle fatigue and monotonic fracture behaviors of low-carbon steel and its welded joint. *Materials*, 12(24):4111.

Kim, Y., Sheehy, S., and Lenhardt, D. (2006). *A survey of aircraft structural-life management programs in the US Navy, the Canadian forces, and the US Air Force*, volume 370. Rand Corporation.

Koh, C. and Shankar, K. (2003). Substructural identification method without interface measurement. *Journal of engineering mechanics*, 129(7):769–776.

Koh, C. G., See, L. M., and Balendra, T. (1991). Estimation of structural parameters in time domain: a substructure approach. *Earthquake Engineering & Structural Dynamics*, 20(8):787–801.

Kujawski, D. and Ellyin, F. (1987). A fatigue crack growth model with load ratio effects. *Engineering Fracture Mechanics*, 28(4):367–378.

Kumar, P., Pathak, H., and Singh, A. (2021). Fatigue crack growth behavior of thermo-mechanically processed aa 5754: Experiment and extended finite element method simulation. *Mechanics of Advanced Materials and Structures*, 28(1):88–101.

Kuncham, E., Aswal, N., Sen, S., and Mevel, L. (2023). Bayesian monitoring of substructures under unknown interface assumption. *Mechanical Systems and Signal Processing*, 193:110269.

Kuncham, E., Sen, S., Kumar, P., and Pathak, H. (2022). An online model-based fatigue life prediction approach using extended kalman filter. *Theoretical and Applied Fracture Mechanics*, 117:103143.

Kwon, K., Frangopol, D. M., and Kim, S. (2019). Fatigue performance assessment and service life prediction of high-speed ship structures based on probabilistic lifetime sea loads. In *Structures and Infrastructure Systems*, pages 185–198. Routledge.

Kwon, K., Frangopol, D. M., and Soliman, M. (2012). Probabilistic fatigue life estimation of steel bridges by using a bilinear s-n approach. *Journal of Bridge Engineering*, 17(1):58–70.

Łagoda, T. and Głowacka, K. (2020). Fatigue life prediction of welded joints from nominal system to fracture mechanics. *International Journal of Fatigue*, 137:105647.

Leander, J., Andersson, A., and Karoumi, R. (2010). Monitoring and enhanced fatigue evaluation of a steel railway bridge. *Engineering Structures*, 32(3):854–863.

Li, D., Ho, S.-C. M., Song, G., Ren, L., and Li, H. (2015). A review of damage detection methods for wind turbine blades. *Smart Materials and Structures*, 24(3):033001.

Lichtenstein, A. G. (1993). The silver bridge collapse recounted. *Journal of performance of constructed facilities*, 7(4):249–261.

Lin, L., Luo, B., and Zhong, S. (2018). Multi-objective decision-making model based on cbm for an aircraft fleet with reliability constraint. *International Journal of Production Research*, 56(14):4831–4848.

Liu, K., Zhou, H., Shi, G., Wang, Y., Shi, Y., and De Roeck, G. (2013). Fatigue assessment of a composite railway bridge for high speed trains. part ii: Conditions for which a dynamic analysis is needed. *Journal of Constructional Steel Research*, 82:246–254.

Ljung, L. (1979). Asymptotic behavior of the extended kalman filter as a parameter estimator for linear systems. *IEEE Transactions on Automatic Control*, 24(1):36–50.

MacDougall, C., Green, M. F., and Shillinglaw, S. (2006). Fatigue damage of steel bridges due to dynamic vehicle loads. *Journal of Bridge Engineering*, 11(3):320–328.

Maes, K., Chatzis, M., Vandebril, R., and Lombaert, G. (2021). Observability of modally reduced order models with unknown parameters. *Mechanical Systems and Signal Processing*, 146:106993.

Malveiro, J., Sousa, C., Ribeiro, D., and Calçada, R. (2018). Impact of track irregularities and damping on the fatigue damage of a railway bridge deck slab. *Structure and Infrastructure Engineering*, 14(9):1257–1268.

Marques, F., Correia, J. A., de Jesus, A. M., Cunha, A., Caetano, E., and Fernandes, A. A. (2018). Fatigue analysis of a railway bridge based on fracture mechanics and local modelling of riveted connections. *Engineering Failure Analysis*, 94:121–144.

Matt, R. (2017). The deadliest bridge disaster in us history was caused by a tiny crack just three millimeters deep.

Mendler, A., Döhler, M., and Hille, F. (2022). Detecting changes in boundary conditions based on sensitivity-based statistical tests. In *International Symposium Non-Destructive Testing in Civil Engineering (NDT-CE) in Zurich, Switzerland.*

Metallurgy, M. (1986). Ge dieter.

Milne, I., Ainsworth, R., Dowling, A., and Stewart, A. (1988). Assessment of the integrity of structures containing defects. *International Journal of Pressure Vessels and Piping*, 32(1-4):3–104.

Miner, M. A. (1945). Cumulative damage in fatigue. *Journal of Applied Mechanics.*

Mohammadi, J., Guralnick, S. A., and Polepeddi, R. (1998). Bridge fatigue life estimation from field data. *Practice Periodical on Structural Design and Construction*, 3(3):128–133.

Mohammed, M. K. (2015). *Multi-scale response of sustainable self-compacting concrete (SCC) to carbonation and chloride penetration.* PhD thesis, University of Nottingham.

Moses, F., Lebet, J. P., and Bez, R. (1994). Applications of field testing to bridge evaluation. *Journal of Structural Engineering*, 120(6):1745–1762.

Murakami, Y. and Miller, K. (2005). What is fatigue damage? a view point from the observation of low cycle fatigue process. *International Journal of Fatigue*, 27(8):991–1005.

Nanthakumar, S., Lahmer, T., Zhuang, X., Zi, G., and Rabczuk, T. (2016). Detection of material interfaces using a regularized level set method in piezoelectric structures. *Inverse Problems in Science and Engineering*, 24(1):153–176.

Newman Jr, J. and Raju, I. (1981). An empirical stress-intensity factor equation for the surface crack. *Engineering fracture mechanics*, 15(1-2):185–192.

on Bridges, T. O. S. (1990). *Guide Specifications for Fatigue Evaluation of Existing Steel Bridges, 1990.* American Association of State Highway and Transportation Officials.

Paris, Paul a3nd Erdogan, F. (1963). A critical analysis of crack propagation laws. *Journal of Basic Engineering.*

Parks, D. (1977). The virtual crack extension method for nonlinear material behavior. *Computer methods in applied mechanics and engineering*, 12(3):353–364.

Patricia, M. (2014). Long island span closes: A bridge to somewhere?

Pilar, W. (2021). Ntsb says united engine failure caused by metal fatigue.

Pilkey, W. and Pilkey, D. (1997). Petersons stress concentration factors, john wiley & sons. *New York.*

Pines, D. and Aktan, A. E. (2002). Status of structural health monitoring of long-span bridges in the united states. *Progress in Structural Engineering and materials*, 4(4):372–380.

Pipinato, A. and Brühwiler, E. (2022). Fatigue and fracture. In *Innovative Bridge Design Handbook*, pages 61–100. Elsevier.

Poutiainen, I., Tanskanen, P., and Marquis, G. (2004). Finite element methods for structural hot spot stress determination—a comparison of procedures. *International journal of fatigue*, 26(11):1147–1157.

Pyttel, B., Schwerdt, D., and Berger, C. (2011). Very high cycle fatigue–is there a fatigue limit? *International Journal of fatigue*, 33(1):49–58.

Radaj, D. (1990). *Design and analysis of fatigue resistant welded structures.* Woodhead Publishing.

Radaj, D. (1996). Review of fatigue strength assessment of nonwelded and welded structures based on local parameters. *International Journal of Fatigue*, 18(3):153–170.

Radaj, D., Sonsino, C. M., and Fricke, W. (2006). *Fatigue assessment of welded joints by local approaches*. Woodhead publishing.

Radhakrishnan, V. (1980). Quantifying the parameters in fatigue crack propagation. *Engineering Fracture Mechanics*, 13(1):129–141.

Reddy, J. (1999). On the dynamic behaviour of the timoshenko beam finite elements. *Sadhana*, 24:175–198.

Reddy, J. and Chin, C. (1998). Thermomechanical analysis of functionally graded cylinders and plates. *Journal of thermal Stresses*, 21(6):593–626.

Rice, J. R. (1968). A path independent integral and the approximate analysis of strain concentration by notches and cracks. *Journal of Applied Mechanics*, 35(2).

Rob, H. (2021). Mississippi river bridge — broken beam went unnoticed for at least two years.

Robinson, E. I., Marzat, J., and Raïssi, T. (2018). Filtering and uncertainty propagation methods for model-based prognosis of fatigue crack growth in unidirectional fiber-reinforced composites. *ASCE-ASME Journal of Risk and Uncertainty in Engineering Systems, Part A: Civil Engineering*, 4(4):04018040.

Rocha, M. and Brühwiler, E. (2012). Prediction of fatigue life of reinforced concrete bridges using fracture mechanics. *Proceedings bridge maintenance, safety, management, resilience and sustainability*, 1(CONF):3755–3761.

Rösler, J., Harders, H., and Bäker, M. (2007). *Mechanical behaviour of engineering materials: metals, ceramics, polymers, and composites*. Springer Science & Business Media.

Ross, R. (2016). Integrated vehicle health management in aerospace structures. In *Structural Health Monitoring (SHM) in Aerospace Structures*, pages 3–31. Elsevier.

Russo, F. M., Wipf, T. J., and Klaiber, F. W. (2000). Diagnostic load tests of a prestressed concrete bridge damaged by overheight vehicle impact. *Transportation Research Record*, 1696(1):103–110.

Saha, B., Goebel, K., Poll, S., and Christophersen, J. (2007). A bayesian framework for remaining useful life estimation. In *AAAI Fall Symposium: Artificial Intelligence for Prognostics*, pages 97–102.

Sakano, M. and Wahab, M. A. (2001). Extremely low cycle (elc) fatigue cracking behaviour in steel bridge rigid frame piers. *Journal of Materials Processing Technology*, 118(1-3):36–39.

Sartor, R. R., Culmo, M. P., and DeWolf, J. T. (1999). Short-term strain monitoring of bridge structures. *Journal of Bridge Engineering*, 4(3):157–164.

Sen, S., Aswal, N., Zhang, Q., and Mevel, L. (2021). Structural health monitoring with non-linear sensor measurements robust to unknown non-stationary input forcing. *Mechanical Systems and Signal Processing*, 152:107472.

Sen, S. and Bhattacharya, B. (2016). Progressive damage identification using dual extended Kalman filter. *Acta Mechanica*, 227(8):2099–2109.

Sen, S. and Bhattacharya, B. (2017). Online structural damage identification technique using constrained dual extended Kalman filter. *Structural Control and Health Monitoring*, 24(9):e1961.

Sharma, A., Oh, M. C., and Ahn, B. (2020). Recent advances in very high cycle fatigue behavior of metals and alloys—a review. *Metals*, 10(9):1200.

Sharma, S. and Sen, S. (2021). Bridge damage detection in presence of varying temperature using two-step neural network approach. *Journal of Bridge Engineering*, 26(6):04021027.

Sharma, S. and Sen, S. (2023). Real-time structural damage assessment using lstm networks: regression and classification approaches. *Neural Computing and Applications*, 35(1):557–572.

Shi, J., Chopp, D., Lua, J., Sukumar, N., and Belytschko, T. (2010). Abaqus implementation of extended finite element method using a level set representation for three-dimensional fatigue crack growth and life predictions. *Engineering Fracture Mechanics*, 77(14):2840–2863.

Shih, C., Moran, B., and Nakamura, T. (1986). Energy release rate along a three-dimensional crack front in a thermally stressed body. *International Journal of fracture*, 30:79–102.

Silva, A., De Jesus, A., Xavier, J., Correia, J., and Fernandes, A. (2017). Combined analytical-numerical methodologies for the evaluation of mixed-mode (i+ ii) fatigue crack growth rates in structural steels. *Engineering Fracture Mechanics*, 185:124–138.

Singleton, R. K., Strangas, E. G., and Aviyente, S. (2014). Extended kalman filtering for remaining-useful-life estimation of bearings. *IEEE Transactions on Industrial Electronics*, 62(3):1781–1790.

Sonsino, C. M. (2007). Course of sn-curves especially in the high-cycle fatigue regime with regard to component design and safety. *International Journal of Fatigue*, 29(12):2246–2258.

Sonsino, C. M., Fricke, W., De Bruyne, F., Hoppe, A., Ahmadi, A., and Zhang, G. (2012). Notch stress concepts for the fatigue assessment of welded joints–background and applications. *International Journal of Fatigue*, 34(1):2–16.

Souid, A., Delaplace, A., Ragueneau, F., and Desmorat, R. (2009). Pseudo-dynamic testing and nonlinear substructuring of damaging structures under earthquake loading. *Engineering structures*, 31(5):1102–1110.

Spyrakos, C. C., Raftoyiannis, I. G., and Ermopoulos, J. C. (2004). Condition assessment and retrofit of a historic steel-truss railway bridge. *Journal of Constructional Steel Research*, 60(8):1213–1225.

Standard, A. (2015). E647-15e1. 2015. *Standard test method for measurement of fatigue crack growth rates. ASTM International, West Conshohocken, PA.*

Standard, B. (1980). Bs 5400: Steel, concrete and composite bridges-part 10. *Code of practice for fatigue.*

Stephens, R. I., Fatemi, A., Stephens, R. R., and Fuchs, H. O. (2000). *Metal fatigue in engineering*. John Wiley & Sons.

Sun, J., Zuo, H., Wang, W., and Pecht, M. G. (2014). Prognostics uncertainty reduction by fusing on-line monitoring data based on a state-space-based degradation model. *Mechanical Systems and Signal Processing*, 45(2):396–407.

Tada, H., Paris, P., and Irwin, G. (2000). The analysis of cracks handbook. *New York: ASME Press*, 2:1.

Tatsis, K. E., Dertimanis, V. K., Papadimitriou, C., Lourens, E., and Chatzi, E. N. (2021). A general substructure-based framework for input-state estimation using limited output measurements. *Mechanical Systems and Signal Processing*, 150:107223.

Tee, K.-F., Koh, C.-G., and Quek, S.-T. (2003). System identification and damage estimation via substructural approach. *Computational Structural Engineering: An International Journal*, 3(1):1–7.

Trinh, T. N. and Koh, C. G. (2012). An improved substructural identification strategy for large structural systems. *Structural Control and Health Monitoring*, 19(8):686–700.

Tsakopoulos, P. and Fisher, J. (2002). " fatigue resistance investigation for the orthotropic deck on the bronx whitestone bridge final report" atlss report no. 02-05. *Department of Civil and Environmental Engineering, Lehigh University, Bethlehem PA.*

van Delft, D. (1981). A two dimensional analyses of stress at the vicinity of weld toes of tubular structures. In *Stevin Report 6-81-8*. Delft University of Technology Delft, The Netherlands.

Wan, E. A. and Van Der Merwe, R. (2000). The unscented kalman filter for nonlinear estimation. In *Proceedings of the IEEE 2000 Adaptive Systems for Signal Processing, Communications, and Control Symposium (Cat. No. 00EX373)*, pages 153–158. Ieee.

Wang, C., Zhang, J., Tu, Y., Sabourova, N., Grip, N., Blanksvärd, T., and Elfgren, L. (2020a). Fatigue assessment of a reinforced concrete railway bridge based on a coupled dynamic system. *Structure and Infrastructure Engineering*, 16(6):861–879.

Wang, Q., Bathias, C., Kawagoishi, N., and Chen, Q. (2002). Effect of inclusion on subsurface crack initiation and gigacycle fatigue strength. *International Journal of Fatigue*, 24(12):1269–1274.

Wang, W., Hu, W., and Armstrong, N. (2017). Fatigue crack prognosis using bayesian probabilistic modelling. *Mechanical Engineering Journal*, 4(5):16–00702.

Wang, Y., Binaud, N., Gogu, C., Bes, C., and Fu, J. (2016). Determination of paris' law constants and crack length evolution via extended and unscented kalman filter: An application to aircraft fuselage panels. *Mechanical Systems and Signal Processing*, 80:262–281.

Wang, Y., Wang, W., Zhang, B., and Li, C.-Q. (2020b). A review on mixed mode fracture of metals. *Engineering Fracture Mechanics*, 235:107126.

Weibull, W. (2013). *Fatigue testing and analysis of results.* Elsevier.

Weng, S., Zhu, H., Xia, Y., Li, J., and Tian, W. (2020). A review on dynamic substructuring methods for model updating and damage detection of large-scale structures. *Advances in Structural Engineering*, 23(3):584–600.

Wu, M., Zhu, J., Heng, J., and Kaewunruen, S. (2019). Fatigue assessment on suspenders under stochastic wind and traffic loads based on in-situ monitoring data. *Applied Sciences*, 9(16):3405.

Xiao, Z.-G. and Yamada, K. (2004). A method of determining geometric stress for fatigue strength evaluation of steel welded joints. *International Journal of Fatigue*, 26(12):1277–1293.

Xiao, Z.-G., Yamada, K., Inoue, J., and Yamaguchi, K. (2006). Fatigue cracks in longitudinal ribs of steel orthotropic deck. *International Journal of Fatigue*, 28(4):409–416.

Xiongzi, C., Jinsong, Y., Diyin, T., and Yingxun, W. (2011). Remaining useful life prognostic estimation for aircraft subsystems or components: A review. In *Ieee 2011 10th international conference on electronic measurement & instruments*, volume 2, pages 94–98. IEEE.

Xu, X. and Chen, N. (2017). A state-space-based prognostics model for lithium-ion battery degradation. *Reliability Engineering & System Safety*, 159:47–57.

Yang, T., Liu, K., and Nie, G. (2021). Improved time domain substructural damage identification method on large-span spatial structure. *Shock and Vibration*, 2021.

Ye, X., Ni, Y. Q., Wong, K., and Ko, J. (2012). Statistical analysis of stress spectra for fatigue life assessment of steel bridges with structural health monitoring data. *Engineering Structures*, 45:166–176.

Ye, X., Su, Y., and Han, J. (2014). A state-of-the-art review on fatigue life assessment of steel bridges. *Mathematical Problems in Engineering*, 2014:1–13.

Yin, G.-a., Ding, F.-x., Wang, H.-b., Bai, Y., and Liu, X.-m. (2017). Connection performance in steel–concrete composite truss bridge structures. *Journal of Bridge Engineering*, 22(3):04016126.

Yuan, F.-G. (2016). *Structural health monitoring (SHM) in aerospace structures.* Woodhead Publishing.

Yuen, K.-V. and Huang, K. (2018). Real-time substructural identification by boundary force modeling. *Structural Control and Health Monitoring*, 25(5):e2151.

Yuen, K.-V. and Katafygiotis, L. S. (2006). Substructure identification and health monitoring using noisy response measurements only. *Computer-Aided Civil and Infrastructure Engineering*, 21(4):280–291.

Zghal, M., Mevel, L., and Del Moral, P. (2014). Modal parameter estimation using interacting kalman filter. *Mechanical Systems and Signal Processing*, 47(1-2):139–150.

Zhang, G. and Richter, B. (2000). A new approach to the numerical fatigue-life prediction of spot-welded structures. *Fatigue & Fracture of Engineering Materials & Structures*, 23(6):499–508.

Zhang, Q. and Jankowski, Ł. (2017). Damage identification using structural modes based on substructure virtual distortion method. *Advances in Structural Engineering*, 20(2):257–271.

Zhang, Q. and Zhang, L. (2018). State estimation for stochastic time varying systems with disturbance rejection. *IFAC-PapersOnLine*, 51(15):55–59.

Zhao, Y., Liu, H., Cai, S., and Sun, H. (2022). Mixed-mode fatigue crack growth analysis of i-shaped steel girders with trapezoidal corrugated-webs. *Journal of Constructional Steel Research*, 190:107153.

Zhao, Z. and Haldar, A. (1996). Bridge fatigue damage evaluation and updating using non-destructive inspections. *Engineering fracture mechanics*, 53(5):775–788.

Zhou, H., Liu, K., Shi, G., Wang, Y., Shi, Y., and De Roeck, G. (2013). Fatigue assessment of a composite railway bridge for high speed trains. part i: Modeling and fatigue critical details. *Journal of Constructional Steel Research*, 82:234–245.

Zhu, Q., Chen, L., Zhu, G., and Huo, X. (2019). Hysteresis energy based low cycle fatigue properties analysis in extruded al-7zn-2mg-1.5 cu-0.2 sc-0.1 zr alloy at low temperature. *Materials Research Express*, 6(11):116568.